HARMONIC ENTANGLEMENT
& PHOTON ANTI-BUNCHING

NICOLAI BERND GROSSE

a thesis submitted for the degree of
doctor of philosophy
THE AUSTRALIAN NATIONAL UNIVERSITY

APRIL 2009

Declaration

This thesis is an account of research undertaken between March 2004 and April 2009 at *The Department of Quantum Science, The Research School of Physical Sciences & Engineering, The Australian National University*, in Canberra, Australia.

Except where acknowledged in the customary manner, the material presented in this thesis is, to the best of my knowledge, original and has not been submitted in whole or part for a degree in any university.

Nicolai B. Grosse

15th April 2009

Acknowledgements

At last I can let my hair down and thank everybody who has helped me along the way. From the very first day I'd like to thank my supervisor Prof. Ping Koy Lam for welcoming me into his research group. It's here that I've enjoyed a wonderful combination of freedom and resources to pursue new directions and my own diversions; but also the supervision to keep me on track with sound advice when things became tough. The group's highly talented members kept their ideas circulating, and they've proved to be a vast store of knowledge. I'm grateful for having been given the opportunity to attend overseas conferences, and for having been permitted some quite lengthy stays in Germany. I especially thank Prof. Roman Schnabel for welcoming me into his group for all of those long stays, thereby making the Albert Einstein Institute (AEI) in Hannover, a home away from home. It's at the AEI that I've had the pleasure of getting to know the other PhD students over the years, and for improving my spoken German. Back in Australia, I'm indebted to Prof. Tim Ralph at the University of Queensland for initiating fruitful collaborations with Magdalena Stobińska, Dr. Hyunseok Jeong, and Christian Weedbrook. I've been delighted to work with Dr. Thomas Symul on several projects, where I much appreciated his thorough yet light-hearted pragmatic approach. I'd like to thank Prof. Hans Bachor, Prof. David McClelland and Prof. John Close for their advice during my initial orientation, and for their continued contact over the years. I'm indebted to Dr. Ben Buchler and Dr. Warwick Bowen for the foundations that they had laid down during the early days of the group, and for their readiness to engage with me in recent times. I thank Paul MacNamara, Paul Tant and Neil Devlin for their fine skills in the mechanical workshop; Neil Hinchey, Shane Grieves and James Dickson for their fine skills in the electronic workshop; Damien Hughes and Huma Cheema for sorting out the administrative side. I thank Dr. Steve Madden for providing access to the clean-room facility. I'm very grateful to Lorenzo Lariosa for his miraculous success in retrieving a lost invar cavity from the depths of the vapour degreasing tank. I also thank Roger Senior for alerting me to some crucial improvements in the photodetector designs. I've had the pleasure of working on many interesting projects with truly wonderful people. The midnight observing runs with Dr. Kirk McKenzie to search for low frequency squeezing; nutting out the OPA model and harmonic entanglement with Dr. Kirk McKenzie and Dr. Warwick Bowen; the quantum state engineering work with Dr. Hyunseok Jeong and Dr. Andrew Lance; the entanglement cloning with Christain Weedbrook; getting squeezed light to anti-bunch with Magdalena Stobińska and Dr. Thomas Symul; wrestling with the harmonic entanglement experiment together with Syed Assad and Moritz Mehmet. Each collaboration has left me with many fond memories. I've appreciated sharing time in the department with my colleagues (who I have not yet mentioned, and nearly all of whom have already earned their doctor titles): Dr. Simon Haine, Dr. Gabriel Hetet, Kate Wagner, Dr. Vincent Delaubert, Dr. Vikram Sharma, Guy Micklethwait, Dr. Jiri Janousek, Dr. Oliver Glöckl, Dr. Hongxin Zhou; and at the AEI: Nico Latzska, James Diguglielmo, Boris Hage, Daniel Friedrich, Dr. Alexander Franzen, Dr. Henning Vahlbruch. I feel that I've learned from everybody, not just in physics, but in all things. I've enjoyed the discussions and many interesting questions raised by Ken Li Chong, Daniel Alton and Ru Gway. I very much enjoyed the good humour and choice of music in the lab with Michael Stefszky in the days when we shared the same optics bench. I much appreciated the in-depth comments to the first draft that I had received from Dr. Ben Sheard, Michael Stefszky, Dr. Thomas Symul, Tobias Eberle, Dr. Magnus Hsu, Prof. Ping Koy Lam, and Prof. Roman Schnabel. I'm grateful to Aiko Samblowski for his friendship in and out of the lab, and for being so understanding during the times when I was under pressure from the thesis. I'm indebted to Syed Assad for his enormous commitment and equal contribution to the harmonic entanglement experiment, where his calm approach worked wonders with the stability of the setup. Saul, Aśka, Magnus and Ben have been to me like the most ancient and distant stars: helping me to navigate the often uncertain waters. Thank you Dr.-Ing. Joachim Westphal for your strong encouragement and generous help in so many ways. Thank you Oma for your faith in my abilities and for keeping my spirits high; Mama and Papa for your love, encouragement and support, not just during the PhD years, but ever since I can remember; Vio for always being there as my big sister; Olivia for your love, even over the greatest distances.

Abstract

Non-classical light and its observable properties can express many of the peculiar features that are unique to quantum mechanics. Furthermore, sources of non-classical light have applications in optical quantum computation, and in improving the sensitivity of optically-based measurement instruments. In this thesis, two sources of non-classical light were investigated theoretically, and tested experimentally. Methods were developed to observe the non-classical properties from measurements based in the continuous-variable regime.

Harmonic entanglement is the entanglement of a pair of light beams that are separated by an octave in optical frequency. We proposed that the degenerate optical parametric amplifier (OPA), which is a proven source of quadrature squeezed light, can also be used as a device to generate harmonic entanglement. From a linearised operator model of OPA, we found that this occurs when the OPA is coherently driven by a fundamental field (the seed) and its second-harmonic field (the pump), such that the OPA is operated in a regime of either pump depletion or enhancement. Our theoretical analysis showed that harmonic entanglement is observable on the quadrature amplitudes of the reflected seed and pump fields. The strength of entanglement, as quantified by the criteria of inseparability and Einstein-Podolsky-Rosen, is in principle limited only by the intra-cavity losses of the system, and the ability to drive the system above the threshold of optical parametric oscillation (OPO).

We built an experiment that was capable of testing the proposal that an OPA can be used as a source of harmonic entanglement. The OPA design was based on a second-order nonlinear crystal that was placed at the focus of a doubly-resonant optical cavity. The seed and pump light, which were derived from a laser and frequency-doubler, respectively, were injected into the OPA cavity. The reflected fundamental and second-harmonic fields were optically high-pass filtered to remove the bright carrier light while preserving the entanglement on the upper and lower sidebands. These were then received by two balanced homodyne detectors that acquired measurements of the amplitude and phase quadratures, from which the elements of the correlation matrix were calculated. Applying the inseparability

criterion to the matrix yielded a degree of 0.74 ± 0.01 which was less than one, and therefore satisfied the criterion of entanglement. Entanglement was also observed over a range of seed and pump powers. The experimental results supported the theoretical model of OPA that had been extended to include an excess phase noise in the form of guided acoustic wave Brillouin scattering occurring in the nonlinear crystal.

Photon anti-bunching is the tendency for photons to be detected apart from one another rather than together. It is characterised by the second-order coherence function of a single mode of light, which can be measured using a Hanbury-Brown–Twiss (HBT) intensity interferometer. The interferometer is based on a pair of single-photon counters that monitor the output ports of a symmetric beamsplitter. The phenomenon of anti-bunching is a clear signature of the quantum nature of light, and has no analogue in the classical and semi-classical theories. Displaced quadrature-squeezed states of light can in principle exhibit arbitrarily strong anti-bunching statistics, but in practice these sources are not easily measurable using discrete-variable techniques. We proposed a method for measuring the second-order coherence function using continuous-variable techniques alone, where a pair of balanced homodyne detectors replace the single-photon counters of the original HBT interferometer. By correlating the quadrature measurements from the homodyne detectors, it is possible to construct the second-coherence function and reveal the photon anti-bunching statistics.

We built an experiment that was capable of testing the proposal that photon anti-bunching can be observed from a source of displaced squeezed light using homodyne detection alone. Our source was based on an OPA that was optimised to deliver very weakly squeezed, and nearly pure, states of light. The displacement to the squeezed state was done by way of interference with an auxiliary amplitude modulated beam. The resulting displaced squeezed state was sent to a symmetric beamsplitter, where the light from the each output port was received by an independent homodyne detector. Measurements of the quadrature amplitudes were gathered and processed to construct the second-order coherence function, which at zero time delay, revealed a value of 0.11 ± 0.18 which was less than one, and thus confirmed the presence of photon anti-bunching. We also studied the second-order coherence function over a range of displacements of the squeezed state, and also for coherent states and biased thermal states. The experimental results supported the theory, and validated our continuous-variable technique of measuring the second-order coherence function.

Contents

Chapter 1

Introduction

1.1 Background themes

Two main themes tie my thesis together: ways of creating non-classical light, and ways of measuring that non-classicality. This kind of light is special because it has measurable properties that are counter-intuitive when viewed from the classical theoretical perspective. Probabilities can become negative (Wigner function), the Schwarz inequality can be violated (second-order coherence), or seemingly impossible correlations can be created between different observables (EPR entanglement). Both the wave and particle characteristics of light need to be carefully considered in order to fully understand these phenomena. If one adds to this the interaction of light with matter, one is overwhelmed with choices for creating, manipulating, and measuring these sources of light, or the interacting matter itself. The study of non-classical light thus becomes an immensely rich and rewarding subject, with far-reaching applications in many areas of modern physics.

Non-classical light is defined as having any measurable property that cannot be described within a theoretical framework that is built from Maxwell's equations of electromagnetism together with atoms that are described quantum mechanically:
[Jaynes and Cummings 1963]. This framework is often referred to as the semi-classical theory. It adequately describes the stimulated emission rates of atomic transitions (Einstein's A and B coefficients), the shot-noise that is recorded by a photo-ionisation detector, the 'single-photon' interference pattern (low-intensity Young's double-slit), and rather surprisingly, even the photo-electric effect [Lamb and Scully 1968]. But outside of its descriptive reach, lie non-classical states of light. These are described by the fully quantised theory of light, which essentially says that a quantum harmonic oscillator is assigned to every propagating mode of the electromagnetic field, and that the energy contained within each mode,

is restricted to having integer values (plus half) proportional to the optical frequency and scaled by Planck's constant. One result of this theory makes a radical departure from the semi-classical theory: empty space is not empty. Every mode of the electromagnetic field has a lowest nonzero energy state, the vacuum state, and this contributes to measurable effects such as the Casimir force between closely-spaced conductors [Casimir 1948], and the Lamb shift of atomic energy levels [Lamb and Retherford 1947].

Examples of non-classical states of light that have been created and observed in the laboratory environment are the rather exotically named: photon anti-bunched states[1], sub-Poissonian states[2], quadrature-squeezed states[3], quadrature-entangled states[4], Bell states[5], Fock states[6], N00N states[7], and coherent super-position states[8]. Each of these states exhibits at least one measurable property of the electromagnetic field that is a witness to the non-classicality. To be such a witness, a measurable property must have bounds associated with it that are set by the semi-classical theory, and these bounds are usually expressed as inequalities. For example, the semi-classical theory predicts that a photo-electric detector will produce a Poissonian distribution of the number of photo-ionisation events that are counted within a fixed time interval, provided that the detector is illuminated by a monochromatic source of light. The Poissonian distribution ensures that the mean and variance are equal and proportional to the intensity of the light. However, re-examining the problem with the fully quantised theory of light, shows that some sources of light can produce a sub-Poissonian counting distribution, which has a variance that is less than the mean. As this is something not possible in the semi-classical theory, experimentally observing a photo-counting variance less than the mean is evidence of non-classicality. The task of theoretically analysing sources of light for properties that have non-classical bounds, and finding practical ways to measure those properties in the laboratory, is repeated throughout my thesis.

Non-classical light is not just a curiosity, but can also be put to practical use. The most prominent example is the injection of quadrature-squeezed light into an interferometer-

---

[1] [Kimble *et al.* 1977]
[2] [Short and Mandel 1983]
[3] [Slusher *et al.* 1985]
[4] [Ou *et al.* 1992]
[5] [Kwiat *et al.* 1995]
[6] [Lvovsky *et al.* 2001]
[7] [Sun *et al.* 2006]
[8] [Ourjoumtsev *et al.* 2006]

based gravitational wave detector, with the aim of lowering the noise floor and thus allowing the detection of fainter and more distant astronomical sources of gravitational waves. Squeezed light in an interferometer allows one to make more sensitive differential phase measurements for the same optical power and detection time. This application was first suggested by Caves [Caves 1981], but only with recent advances in the bandwidth and strength of squeezed light sources, is this now becoming a reality for the GEO 600 detector and other observatories around the world [Schnabel 2008]. A similar approach with squeezed light has been used to demonstrate an improved sensitivity for other kinds of measurements which include frequency-modulation spectroscopy [Polzik *et al.* 1992], and beam position measurements [Treps *et al.* 2002]. These demonstrations however, have not revolutionised the field because those particular applications were not limited by the intensity of the light, which in most cases can be scaled up arbitrarily. Where non-classical light could make a key difference is with the goal of realising quantum computation. Here, light would play the role of a messenger between quantum logic gates that do the quantum information processing, which could be in the form of quantum dots [Li *et al.* 2003] or trapped ions [Cirac and Zoller 1995, Gulde *et al.* 2003]. Another proposal would be to engineer multimode entangled states of light upon which a specific set of measurements is made according to the scheme of cluster state quantum computing [Nielsen 2003]. This would have several advantages in robustness and scalability over the former scheme [Menicucci *et al.* 2006].

Non-classical states of light can be generated by a diverse range of physical systems that can be classed as being either macroscopic, or microscopic, depending on the number of interacting particles and the length-scale over which the interaction occurs. The microscopic class of systems includes the interaction of light with single atoms, ions, molecules, or artificial atoms in the form of nano-optical structures such as the colour centres that are created by defects within a crystal lattice. The length scale of these systems is many times smaller than the wavelength of light, and usually only one atomic particle is considered to interact at a time. For example, the first observed non-classical state of light was created in this way. Using resonance fluorescence from an ensemble of sodium atoms, Kimble demonstrated a violation of the Schwarz inequality, which was the first evidence for the quantisation of the electromagnetic field [Kimble *et al.* 1977, Walls 1979].

If the length scale of the interacting material is larger than the wavelength of light, it encompasses a macroscopic number of atoms, of the order of Avagadro's number, and an analysis of the system reduces to considering the bulk properties of the medium in response to light. Here, it is a medium's nonlinear response that can support the interaction and exchange of energy between light of different wavelengths, which under linear circumstances would not be possible. The interaction can also be enhanced by using optical feedback in the form of resonators/cavities. The nonlinear media can be in several forms: bulk media (crystals), optical fibres, micro-spheres, micro-toroids, or atomic gases (vapour cells). As an example, the first quadrature-squeezed state of light was measured using the four-wave mixing effect from the third-order nonlinearity in an atomic gas [Slusher *et al.* 1985]. This resulted in a sub-Poissonian distribution of photo-ionisation counts in the detector, which was a non-classical effect. Other macroscopic systems rely on a different interaction with matter, such as band-gap materials (semiconductor lasers, LEDs); or radiation pressure with micro-electromechanical systems (cantilevers, membranes). For my own research topics, I exclusively used the second-order nonlinear response of bulk media in the form of artificially grown crystals of potassium titanyl phosphate (KTP) and lithium niobate $(\mathrm{LiNbO_3})$.

The creation of a non-classical state of light is one thing, but without the verification of the non-classicality, the experiment is incomplete. The type of photodetector that is used, decides what properties of the light beam can be observed, and therefore what aspect of non-classicality can be investigated. It is generally said that an experimentalist can only detect the intensity of a beam of light. This is true for both types of available detector: single-photon counters, and PIN-junction photodiodes. But the information that can be extracted from each type of detector is different, and is also dependent on the source of light. The single-photon counter, say a photomultiplier tube, produces an electronic pulse for every photo-ionisation event. The intensity of the light must be kept low enough, such that the electronic pulses can be resolved in time. Note that the detector cannot distinguish between different (narrowly-spaced) wavelengths of light. Using this type of detector, it is a simple matter to measure correlations of photons that are collected at different places within the beam of light, or in other words, to measure the degree of second-order coherence of the light. Other properties can also be determined, such as the density matrix of the state of light. In general, using a single-photon counting detector limits the experimentalist to doing quantum optics in the discrete-variable (DV) regime, where 'discrete' refers to a photon either having been, or not having been detected.

In contrast to the DV regime, is the continuous-variable (CV) regime of quantum optics. The 'continuous' refers to the measurement of the electric field of the light itself, because the field can take on any value from a continuous distribution of values. In general, the detector used is a semiconductor PIN-junction photodiode, and the source of light is bright rather than dim. If the source of light contains a quasi-monochromatic component, the carrier, and if the carrier is bright ($\approx 10^{10}$ photons per second), then it will 'beat' against the components of the light at nearby wavelengths (the sidebands). The resulting electronic signal contains information that is wavelength dependent, in essence resolving the amplitude of the electric field for each nearby optical frequency. In this sense, it is the radio-frequency response of the detector that determines the range of optical wavelengths that are detectable. Several tricks can be used to shift the phase of the carrier component, and thus allow one to access the phase quadrature of the optical sidebands as well as the amplitude. Combining the data taken at many quadrature angles, from amplitude to phase, allows the mathematical reconstruction of the Wigner function of the state of the light at each optical sideband frequency [Leonhardt 1997, Schiller *et al.* 1996]. However, the detection times of individual photons can in practice never be resolved. This is because the electronic noise floor of the photodiode is already at the sensitivity level of the order of 10^8 photons per second, at best. For my own research topics, I exclusively used PIN photodiodes for detection, and so the experiments were completely within the realm of CV quantum optics.

A new direction in the field of quantum optics aims to close the gap between the CV and DV regimes. This is being accomplished by bringing together the techniques of single-photon detection and homodyne detection to simultaneously measure the same source of non-classical light. Such hybrid detection schemes have been used to create so-called Schrödinger kitten states, which are a super-position of two coherent states with different amplitudes [Ourjoumtsev *et al.* 2006]. The coherent amplitudes in that experiment were relatively small, hence the term 'kitten'. Such exotic states of light have no analogues in the semi-classical theory. They are wonderful examples of what is possible within the quantum theory of light.

1.2 Thesis topics

Of the many aspects of quantum optics that I brushed over in the last section, I had actually studied only one small part of it for my thesis. Gathered under the umbrella of non-classical light, my work examined two different hypotheses which I can dramatise in the following way:

- A pair of light beams of vastly different wavelengths, that are separated by an octave in the electromagnetic spectrum, can be made inseparable *(harmonic entanglement)*.
- The particulate nature of light can be revealed without ever having resolved a single particle during the measurement *(photon anti-bunching from squeezing)*.

Both phenomena highlight a different aspect of non-classicality that the electromagnetic field is capable of expressing. Next I will attempt to explain these ideas in a more accurate, but rather less dramatic way.

1.2.1 Harmonic entanglement

Entanglement is both a simple and complicated concept. In the full quantum theory of light, if the state of a two-mode field cannot be expressed as a product of two states with one for each mode, then the two modes are said to be inseparable or entangled. The inseparability has consequences for measurements that are made on some observables, such as the amplitude and phase quadratures of the electric field. When comparing quadrature measurements that are made on each mode individually, correlations between the two lists of random numbers in the data become apparent. Depending on the type of entanglement, the correlation can be stronger than that possible for any source of light that is based in the semi-classical theory. By *stronger* correlation, I mean that a single measurement result on one mode can be used to *better* predict a measurement made on the other mode, as characterised by the conditional variance. In the extreme case of perfect entanglement, the conditional variance would be zero for both observables, amplitude and phase, and the predictions made from one mode to the other would be without error. Such a result leads to an apparent violation of the uncertainty principle [Reid 1989]. The amplitude and phase observables are non-commuting, or incompatible, and therefore the uncertainty principle prohibits the measurement of both observables simultaneously for one mode with arbitrary precision. High precision in measurements of the phase can be sacrificed for a lack of precision in the amplitude, or vice versa.

Einstein, Podolsky and Rosen (EPR) used this kind of entangled state in their argument about whether quantum mechanics was actually a complete description of reality [Einstein *et al.* 1935]. Their argument was based on the principle that there must exist a corresponding *element of physical reality* for an observable, say amplitude, because a measurement of that observable made on one mode is perfectly correlated with the result of a similar measurement made on the other mode. The correlation does not diminish with a physical separation of both modes, and therefore is instantaneous. This is the famous 'spooky action at a distance'. Without that element of reality, the measurements cannot be correlated. In the same way, another element of reality exists for the non-commuting observable, phase. The paradox is that the Heisenberg uncertainty principle does not permit the simultaneous measurement of both observables with arbitrary precision, and therefore denies the simultaneous reality of both of those elements of reality. EPR chose to escape the paradox by concluding that it was the theory of quantum mechanics that was incomplete. A better theory would have a simultaneous description of both elements, perhaps with a set of variables that would decide the outcomes of measurements, but which would themselves remain inaccessible to the observer and thereby preserve the uncertainty principle. Whether such hidden variable theories existed or not, was thought for several decades to be an unmeasurable and undecidable problem. This changed when Bell proposed an experiment that could distinguish between a quantum theory with and without local hidden variables [Bell 1964]. The experiment was done by [Freedman and Clauser 1972, Fry and Thompson 1976, Aspect *et al.* 1982], the result of which confirmed that quantum mechanics is free of local hidden variables, and as such, retains its strange 'spooky action at a distance' character. Even today, the hidden variable theories are being tested with the Bell inequality measurements being repeated over ever greater distances [Ursin *et al.* 2007].

Aside from their role in probing the fundamentals of physics, entangled states are also the resource necessary for quantum logic gates and the functioning of quantum computers. This application motivates the search for sources of entangled light at various wavelengths that could access atomic transitions, or even multi-wavelength (muli-colour) entanglement to enable a connection between different atomic species.

One physical system that has proved to be a very flexible source of squeezed light and entangled light is the optical parametric amplifier (OPA). Under the name OPA, I include the processes of second-harmonic generation (SHG), and optical parametric oscillation (OPO), because they are all based on the same system but are operated under different conditions. The OPA relies on a medium with a second-order nonlinearity, that supports the interaction/conversion between light of one wavelength, the fundamental, and its second-harmonic. The interaction can be enhanced by introducing feedback in the form of an optical resonator/cavity. The OPA is then driven by the fundamental (seed) and second-harmonic (pump) fields, which are sourced from beams of coherent laser light. The pump beam is made much brighter than the seed beam, because the OPA can then operate in a regime that de-amplifies the seed, as measured on reflection from the OPA. When this happens, fluctuations in the amplitude of the seed beam are also de-amplified [Wu *et al.* 1986, Bachor and Ralph 2004]. Measuring these reduced fluctuations and comparing with the fluctuations from a coherent state, show that they are lower. The seed beam has been squeezed. Combining two such squeezed beams together on a 50:50 beamsplitter with the correct phase relation, then creates two beams that are EPR entangled. Such a source of entanglement has been demonstrated [Ou *et al.* 1992]. Similar sources have been used to demonstrate quantum information protocols like teleportation [Furusawa *et al.* 1998], [Bowen *et al.* 2003b] and secret-sharing [Lance *et al.* 2004]. A variation on the OPA theme, is to replace the monochromatic seed with a bichromatic seed (signal and idler), whose sum frequency matches exactly the second-harmonic frequency. Because the signal and idler are non-degenerate in frequency, they can be separated, and the result is that they as a pair can be entangled. Demonstrations of such two-colour entanglement have been made [Schori *et al.* 2002, Villar *et al.* 2005].

In many theoretical and experimental investigations of nonclassical light from the degenerate OPA, the role of the pump field was ignored in the sense that it was assumed to remain unaffected by the interaction with the seed field. This was only an approximation for the situation where the seed field carries much less optical power than the pump field. However, when the optical powers in both fields become comparable, it would be expected that a significant exchange would be possible between the two fields, and possibly with an associated change of amplitude/phase statistics on the pump. Following this idea, squeezed light on the reflected pump field from SHG was predicted, and subsequently observed [Paschotta *et al.* 1994]. An extension of this was the prediction [Horowicz 1989] and confirmation that correlations in the amplitudes of the reflected pump and seed fields were also produced by the SHG [Li *et al.* 2007, Cassemiro *et al.* 2007]. Based on these theoretical and experimental discoveries, one could propose that the reflected seed and pump fields share correlations in the phase as well as the amplitude, and perhaps that the state of light that is produced, is quadrature entangled. Since the entanglement would be between a fundamental field and its second-harmonic, we proposed the term *harmonic entanglement* for this phenomenon. These ideas can be summarised with the hypothesis that:

> Harmonic entanglement, which is the quadrature entanglement between a fundamental field and its second-harmonic field, is generated by a second-order nonlinear optical system in the form of an optical parametric amplifier, when it is coherently driven by those two fields.

The testing of this hypothesis, both theoretically and experimentally, forms the first main topic of my thesis.

1.2.2 Photon anti-bunching from squeezing

There is a simple experiment that goes to the heart of understanding the quantum nature of light. Hanbury-Brown and Twiss (HBT) looked at the situation of a single beam of light being divided into two beams by a 50:50 beamsplitter. They asked the question: would a correlation be observed between intensity measurements made on each beam of light after the beamsplitter? After doing the experiment they found that the answer was yes [Hanbury-Brown and Twiss 1956b]. This result encouraged them to scale up the experiment to astronomical proportions: they could directly determined the angular diameter of the star Sirius, and 31 other distant stars. [Hanbury-Brown and Twiss 1956a, Hanbury Brown 1974]. At the time of the first experiment, a debate raged as to whether the correlation, known as the HBT effect, should exist for thermal sources of light at all. The instrument is now called a HBT interferometer (or intensity interferometer), and what it probes, is the second-order coherence of light. Glauber developed the theoretical framework that describes the coherence of optical fields in the full quantum theory, and from this he could indeed find an explanation for the HBT effect, as a bunching together of the photons in the beam [Glauber 1963]. Furthermore, he showed that some optical fields could display a negative HBT effect that would be visible as an anti-correlation in the intensity measurements after the 50:50 beamsplitter. Such an effect would be impossible to obtain from the classical or even semi-classical theories of light, as it would violate the Schwarz inequality. The interpretation comes from the particulate nature of light, in the form of photon anti-bunching, which is the tendency for photons to arrive at the detector apart from one another. As this was a prediction unique to the quantum theory, it inspired the search for sources of light with photon anti-bunching statistics [Stoler 1974].

The light from resonance fluorescence emitted by a dilute gas of atoms was the first source to demonstrate photon anti-bunching statistics [Kimble *et al.* 1977]. Single-photon counters were used in the experiment to gather a histogram of time delayed coincidences. At zero time delay, the number of coincidence counts dropped, which was the anti-bunching effect, and the first demonstration of truly nonclassical light. Since then, photon anti-bunching has been observed in other sources of light such as conditioned measurements of parametrically down-converted light [Rarity *et al.* 1987, Nogueira *et al.* 2001], pulsed parametric amplification [Koashi *et al.* 1993, Lu and Ou 2001], quantum dots [Michler *et al.* 2000, Santori *et al.* 2002], and trapped single atoms or molecules [Lounis and Moerner 2000], [Darquie *et al.* 2005]. The detectors used in these experiments were of the single-photon counting type, because only these would have sufficient sensitivity and bandwidth to detect those dim sources. Therefore, all these experiments were operated with detectors in the regime of discrete-variable quantum optics.

In the continuous-variable regime, it was predicted from theoretical models that quadrature squeezed states of light could display anti-bunching statistics. However, in the laboratory, the sources of quadrature squeezed light were usually detected using homodyne detection. At first glance, it does not seem obvious that the amplitude and phase quadratures of the light will be able to yield the second-order coherence function, and therefore the measure of anti-bunching statistics. However, Magdalena Stobińska (who is a member of our collaboration group), took the creation-annihilation operator form of the equation for second-order coherence, and re-expressed it terms of quadrature operator measurements. The new measurement instrument looks very similar to the original HBT interferometer, but has a balanced homodyne detector in place of each single-photon detector. By measuring the four combinations of amplitude/phase, it is possible to construct the second-order coherence function. This enables the very pure sources of quadrature squeezed light to reveal their anti-bunching statistics, without ever resolving a single photon. These ideas can be summarised with the hypothesis that:

> Homodyne detection can replace the single-photon counters in a HBT interferometer to measure second-order coherence, which for the case of measuring a displaced-squeezed source of light, can be used to demonstrate photon anti-bunching statistics.

The testing of this hypothesis, both theoretically and experimentally, forms the second main topic of my thesis.

1.3 Thesis structure

I have organised my thesis into chapters that are largely self-contained, but they will seem more logical when they are read in sequence. The structure of my thesis is visualised in Figure 1.1. It breaks up into three parts. The first part is the background theoretical material which explains some of the key concepts and holds many terms and definitions. The second part deals with the topic of harmonic entanglement. The third part is devoted to the photon anti-bunching topic. The last chapter summarises the major theoretical and experimental results of this thesis. A brief overview of the content is give here:

- **Chapter 2:** *Theoretical Background*
  Later chapters rely on concepts and definitions like quadrature squeezing and entanglement. These are defined and explained in this chapter. I also present models for linear and nonlinear processes, and the detection of light in the two-mode formalism.

- **Chapter 3:** *Harmonic Entanglement: Theory*
  I extend a model of OPA, so that the fundamental and second-harmonic optical fields are analysed for harmonic entanglement. Next, I investigate how the strength and type of entanglement varies across the range of seed and pump field parameters.

- **Chapter 4:** *Harmonic Entanglement: Experiment*
  I present the experimental setup that we used to generate and measure harmonic entanglement. I place emphasis on the design, operation, and testing of the OPA, and the homodyne detection with optical carrier rejection.

- **Chapter 5:** *The GAWBS Hypothesis*
  Initial results from the harmonic entanglement experiment showed phase quadrature spectra that were plagued with sharp resonances. I show how a simple model of guided acoustic wave Brillouin scattering (GAWBS) can be used to explain the effect.

- **Chapter 6:** *Harmonic Entanglement: Results*
  The results of the harmonic entanglement experiment are presented and compared

with the theoretical model, both with and without GAWBS. The results cover a study of the ratio of pump and seed powers, as well as for a constant total input power.

- **Chapter 7:** *Photon Anti-Bunching from Squeezing: Theory*
  I give a derivation of how homodyne detection can be used to replace single-photon counters in a Hanbury-Brown–Twiss interferometer. Then I investigate the second-order coherence of displaced-squeezed states of light, and find photon anti-bunching.

- **Chapter 8:** *Photon Anti-Bunching from Squeezing: Experiment*
  I describe the experimental setup that we used to demonstrate that photon anti-bunching can be measured by using only homodyne detection. I present the results of photon anti-bunching statistic that were measured from a displaced-squeezed state.

- **Chapter 9:** *Summary and Outlook*
  Finally, I condense the most important theoretical and experimental results of the harmonic entanglement and photon anti-bunching topics. I also make suggestions for improvements and further studies that may yield interesting results.

Some suggestions for the reader: The background theory chapter (2) can be skimmed if one is already familiar with the material. The heavy experimental chapter (4) can also be skimmed if one is not keen on technical details. It is good however, to get an overview of the complicated experimental setup. Although the GAWBS chapter (5) seems to be a diversion from the main themes of this thesis, it was necessary to investigate the GAWBS hypothesis and supporting evidence separately, because the model of harmonic entanglement as produced from the OPA had to be modified accordingly. This is important when making comparisons between theory and the experimental results that are presented in Chapter 6. The bulk of my research topics can be found in Chapters: 3, 6, 7 and 8. While the summary and outlook chapter (9) is the place to go for the condensed knowledge that was gained during the research, and also for some ideas about where one could go from here.

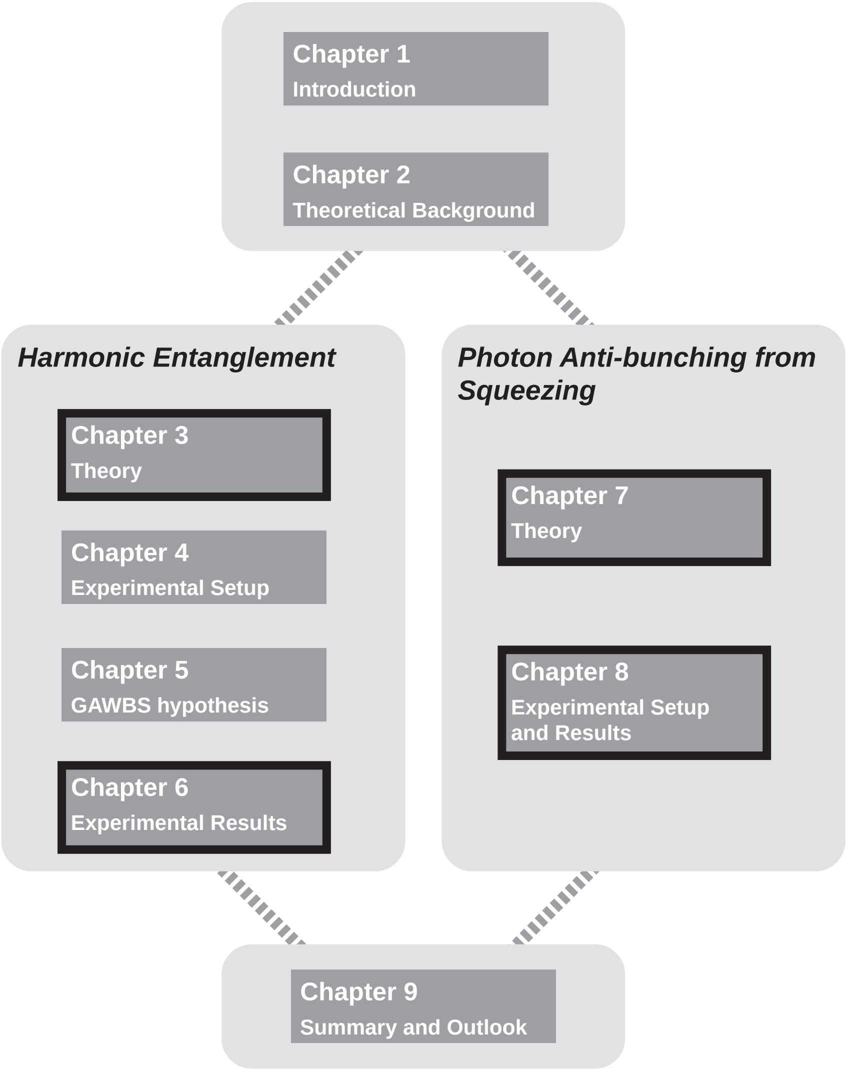

Figure 1.1: Thesis Structure.

1.4 List of publications

List of publications that were the main focus of my thesis:

- *Observation of entanglement between two light beams spanning an octave in optical frequency,*
  N. B. Grosse, S. Assad, M. Moritz, R. Schnabel, T. Symul and P. K. Lam,
  Phys. Rev. Lett. **100**, 243601 (2008).

- *Measuring Photon Antibunching from Continuous Variable Sideband Squeezing*
  N. B. Grosse, T. Symul, M. Stobińska, T. C. Ralph and P. K. Lam,
  Phys. Rev. Lett. **98**, 153603 (2007).

- *Harmonic Entanglement with Second-Order Nonlinearity,*
  N. B. Grosse, W. P. Bowen, K. McKenzie and P. K. Lam,
  Phys. Rev. Lett. **96**, 063601 (2006).

List of publications that were outside the main focus of my thesis:

- *Quantum Cloning of Continuous Variable Entangled States,*
  C. Weedbrook, N. B. Grosse, T. Symul, P. K. Lam and T. C. Ralph,
  Phys. Rev. A **77**, 052313 (2008).

- *Conditional quantum-state engineering using ancillary squeezed-vacuum states,*
  H. Jeong, A. M. Lance, N. B. Grosse, T. Symul, P. K. Lam and T. C. Ralph,
  Phys. Rev. A **74**, 033813 (2006).

- *Quantum-state engineering with continuous-variable postselection,*
  A. M. Lance, H. Jeong, N. B. Grosse, T. Symul, T. C. Ralph and P. K. Lam,
  Phys. Rev. A **73**, 041801(R) (2006).

- *Quantum Noise Locking,*
  K. McKenzie, E. E. Mikhailovm, K. Goda, P. K. Lam, N. Grosse, M. B. Gray, N. Mavalvala and D. E. McClelland,
  J. Opt. B **7**, 421 (2005).

- *Squeezing in the Audio Gravitational-Wave Detection Band,*
  K. McKenzie, N. Grosse, W. P. Bowen, S. E. Whitcomb, M. B. Gray, D. E. McClelland and P. K. Lam,
  Phys. Rev. Lett. **93**, 161105 (2004).

Chapter 2

Theoretical Background

Symbols and mathematical expressions can remain near meaningless without an explanation of how they relate to the physical world. As most of the chapters in this thesis rely on these representations, it makes sense to gather the main concepts and notation into a single chapter. My intention is not reproduce a textbook, but rather to provide only the minimum framework that is necessary to support the research topics that follow. I will lay particular emphasis on the quantisation of the EM field; direct and indirect measurement techniques; the linearisation technique and cavity rate equations; and finally the use of single- and two-mode states of light to illustrate squeezing and entanglement.

2.1 Quantisation of the EM field

The classical theory of the electromagnetic (EM) field as brought together in Maxwell's equations provides a highly accurate description of an astounding array of physical phenomena [Maxwell 1892]. At the beginning of the 20th century however, explanations of the phenomena of the photoelectric effect and blackbody radiation using the classical theory became problematic. The solutions were born in Planck's restriction of the energy in a blackbody oscillator to multiples of $\hbar\omega$; and Einstein's proposal that the energy of light itself was restricted to these steps, or quanta [Planck 1900, Einstein 1905]. These developments went hand in hand with new models of atoms having electrons orbiting the nucleus that were described by Schrödinger's equation [Schrödinger 1926]. A semi-classical theory with a classical electromagnetic field and quantised energy levels of an atom [Jaynes and Cummings 1963], proved adequate to describe the natural linewidths of atomic transitions and laser rate equations. This theory was also consistent with Young's double-slit experiment using very weak light [Aspect and Grangier 1987].

A full quantisation of the EM field was made by Dirac [Dirac 1947], and was further developed with Glauber's analysis of detection and coherence [Glauber 1963]. It can describe a broader range of phenomena that have no analogue in the classical or semi-classical theories. I want to show one of the ways of quantising the EM field. Colloquially, this means giving arguments for putting a hat on the electric field operator (from E to $\hat{E}$) and for the noncommutation of orthogonal quadrature operators. The derivation is not obvious. The method is to first find the plane wave solutions of the field using Maxwell's equations, and then quantise the energy of each according to a quantum harmonic oscillator. The quantised theory cannot be derived from the classical: a leap must be made. As we will see, this will come from comparing the energy of a harmonic oscillator, to that contained in the classical EM field. What follows is a concise version of the treatment that can be found in Loudon's textbook [Loudon 2000]. It breaks down into three steps: classical, quantum, and the comparison of each.

2.1.1 Step 1: The classical

The aim is to find travelling wave solutions of the EM field. The EM field is described by Maxwell's equations:

$$\nabla \times \mathbf{E} = -\frac{\partial \mathbf{B}}{\partial t} \tag{2.1}$$

$$\frac{1}{\mu_0}\nabla \times \mathbf{B} = \varepsilon_0 \frac{\partial \mathbf{E}}{\partial t} + \mathbf{J} \tag{2.2}$$

$$\varepsilon_0 \nabla \cdot \mathbf{E} = \sigma \tag{2.3}$$

$$\nabla \cdot \mathbf{B} = 0 \tag{2.4}$$

Where $\mathbf{J}$ is the current density and σ is the charge density. One method of finding the travelling wave solutions is to re-express the electric and magnetic fields in terms of a scalar potential ϕ and vector potential $\mathbf{A}$ [Jackson 1999]. These are both considerably abstract quantities. We will see later that $\mathbf{A}$ plays a pivotal role in the description of the quantisation.

For the moment consider them just as a tools to get to the solutions.

$$\mathbf{B} = \nabla \times \mathbf{A} \tag{2.5}$$

$$\mathbf{E} = \nabla\phi - \frac{\partial \mathbf{A}}{\partial t} \tag{2.6}$$

A further restriction is applied to the vector potential $\nabla \cdot \mathbf{A} = 0$, which is called the Coulomb gauge, which brings with it an implicit assumption that the system of field equations remains completely non-relativistic. The field equations then condense into

$$-\nabla^2 \mathbf{A} + \frac{1}{c^2}\frac{\partial}{\partial t}\nabla\phi + \frac{1}{c^2}\frac{\partial^2 \mathbf{A}}{\partial t^2} = \mu_0 \mathbf{J} \tag{2.7}$$

$$\nabla^2 \phi = \frac{1}{\varepsilon_0}\sigma \tag{2.8}$$

The current density $\mathbf{J}$ can be broken up into a transverse $\mathbf{J}_\mathrm{T}$ and longitudinal $\mathbf{J}_\mathrm{L}$ components, that have the properties: $\nabla \cdot \mathbf{J}_\mathrm{T} = 0$ and $\nabla \times \mathbf{J}_\mathrm{L} = 0$. This breaks up Equation 2.7 into two equations

$$-\nabla^2 \mathbf{A} + \frac{1}{c^2}\frac{\partial^2 \mathbf{A}}{\partial t^2} = \mu_0 \mathbf{J}_\mathrm{T} \tag{2.9}$$

$$\frac{1}{c^2}\frac{\partial}{\partial t}\nabla\phi = \mu_0 \mathbf{J}_\mathrm{L} \tag{2.10}$$

The solutions for each equation can be found independently. From now on we ignore the longitudinal component which corresponds to the non-propagating part of the EM field (the evanescent field). The transverse component corresponds to the propagating part of EM field, which is also called the radiation field. Consider the case of free space without current sources, so that $\mathbf{J}_\mathrm{T} = 0$, one then gets

$$-\nabla^2 \mathbf{A} + \frac{1}{c^2}\frac{\partial^2 \mathbf{A}}{\partial t^2} = 0 \tag{2.11}$$

which is the wave equation. To simplify the analysis, we first restrict the set of solutions to those obtained by applying a periodic boundary condition that is spaced at L. This is usually referred to as a *cavity*, but note that due to the periodicity of the boundary condition, travelling wave solutions are allowed. The general solution for $\mathbf{A}(\mathbf{r}, t)$ is then the sum over all travelling plane waves with wave vector $\mathbf{k}$ and two orthogonal polarisations labelled by

λ such that

$$\mathbf{A}(\mathbf{r},t) = \sum_{\mathbf{k}}\sum_{\lambda} \mathbf{e}_{\mathbf{k}\lambda} A_{\mathbf{k}\lambda}(\mathbf{r},t) \tag{2.12}$$

with

$$A_{\mathbf{k}\lambda}(\mathbf{r},t) = A_{\mathbf{k}\lambda}\exp(-\mathrm{i}\omega_k t + \mathrm{i}\mathbf{k}.\mathbf{r}) + A^*_{\mathbf{k}\lambda}\exp(\mathrm{i}\omega_k t - \mathrm{i}\mathbf{k}.\mathbf{r}) \tag{2.13}$$

The allowed $\mathbf{k}$ are given by vector components:

$$k_x = 2\pi\nu_x/L \quad , \quad k_y = 2\pi\nu_y/L \quad , \quad k_z = 2\pi\nu_z/L \tag{2.14}$$

with $\nu_{x,y,z}$ limited to $0, \pm1, \pm2, \pm3, ...$ The unit vector $\mathbf{e}_{\mathbf{k}\lambda}$ determines the polarisation, with the orthogonality condition $\mathbf{e}_{\mathbf{k}1}\cdot\mathbf{e}_{\mathbf{k}2} = 0$, and also being orthogonal to the direction of propagation $\mathbf{e}_{\mathbf{k}\lambda}\cdot\mathbf{k} = 0$. The angular frequency of the oscillation ω_k is proportional to the magnitude of the wave vector so that $\omega_k = c|\mathbf{k}| = c\sqrt{k_x^2 + k_y^2 + k_z^2} = ck$. One is free to choose any values for the complex coefficient $A_{\mathbf{k}\lambda}$ with its corresponding complex conjugate $A^*_{\mathbf{k}\lambda}$. Now that we have the vector potential, it is simple to calculate the electric or magnetic fields using $\mathbf{E}(\mathbf{r},t) = -\partial\mathbf{A}(\mathbf{r},t)/\partial t$ and $\mathbf{B}(\mathbf{r},t) = \nabla\times\mathbf{A}(\mathbf{r},t)$. I will not show their full forms here. What I want to do is to calculate the total radiative energy contained in the EM field. This is found by integrating the volume elements $\mathrm{d}V$ over the cavity volume V thus

$$\mathcal{E}_{\mathrm{R}} = \frac{1}{2}\int_V \mathrm{d}V \left[\varepsilon_0\mathbf{E}(\mathbf{r},t)\cdot\mathbf{E}(\mathbf{r},t) + \mathbf{B}(\mathbf{r},t)\cdot\mathbf{B}(\mathbf{r},t)\right] \tag{2.15}$$

This can also be expressed as a summation of the radiative energy from each of the allowed modes of the vector potential.

$$\mathcal{E}_{\mathrm{R}} = \sum_{\mathbf{k}}\sum_{\lambda}\mathcal{E}_{\mathbf{k}\lambda} \tag{2.16}$$

The simplification is tedious but with a neat end result, where each mode contributes the energy

$$\mathcal{E}_{\mathbf{k}\lambda} = \varepsilon_0 V\omega_k^2\left(A_{\mathbf{k}\lambda}A^*_{\mathbf{k}\lambda} + A^*_{\mathbf{k}\lambda}A_{\mathbf{k}\lambda}\right) \tag{2.17}$$

The terms are for the moment not combined (despite the fact that they commute), to leave them in a more suggestive form that we will compare with later.

2.1.2 Step 2: The quantum

Abandoning the EM field completely for the moment, we look at the quantum mechanical harmonic oscillator for a particle of mass m restricted to motion in one dimension in a quadratic potential. The system is described by the Hamiltonian [Griffiths 1995]:

$$\hat{\mathcal{H}} = \frac{1}{2m}\hat{p}^2 + \frac{1}{2}m\omega^2\hat{q}^2 \tag{2.18}$$

for position operator $\hat{q}$ and momentum operator $\hat{p}$ which obey the commutation relation

$$[\hat{p}, \hat{q}] = \mathrm{i}\hbar \tag{2.19}$$

It is the property that p and q do not commute, that leads to the Heisenberg uncertainty principle. The principle limits the precision to which the position and momentum of the particle can be measured. I will return to this concept later on. To continue the analysis, one usually makes the substitution to the dimensionless ladder operators:

$$\hat{a} \quad = \quad \sqrt{2m\hbar\omega}(m\omega\hat{q} + \mathrm{i}\hat{p}) \tag{2.20}$$

$$\hat{a}^\dagger \quad = \quad \sqrt{2m\hbar\omega}(m\omega\hat{q} - \mathrm{i}\hat{p}) \tag{2.21}$$

These are also called the creation operator $\hat{a}^\dagger$, and the annihilation operator $\hat{a}$. The commutation relation between them is

$$\left[\hat{a}, \hat{a}^\dagger\right] = \hat{a}\hat{a}^\dagger - \hat{a}^\dagger\hat{a} = 1 \tag{2.22}$$

which re-expresses the Hamiltonian as

$$\hat{\mathcal{H}} = \frac{1}{2}\hbar\omega\left(\hat{a}\hat{a}^\dagger + \hat{a}^\dagger\hat{a}\right) = \hbar\omega(\hat{a}^\dagger\hat{a} + \frac{1}{2}) \tag{2.23}$$

To see how the system works, we first propose an energy eigenstate of the system $|n\rangle$, such that $\hat{\mathcal{H}}|n\rangle = \mathcal{E}_n|n\rangle$. Next we apply the creation operator to both sides of the energy eigenvalue equation so that $\hat{a}^\dagger\hat{\mathcal{H}}|n\rangle = \hat{a}^\dagger\mathcal{E}_n|n\rangle$. After expanding the LHS and using Equation 2.22, we get a new energy eigenvalue equation: $\hat{\mathcal{H}}\hat{a}^\dagger|n\rangle = (\mathcal{E}_n + \hbar\omega)\hat{a}^\dagger|n\rangle$. We can interpret the application of the creation operator as bringing system into a new state $\hat{a}^\dagger|n\rangle = |n+1\rangle$ that has a higher energy level $E_{n+1} = \mathcal{E}_n + \hbar\omega$. Following the same

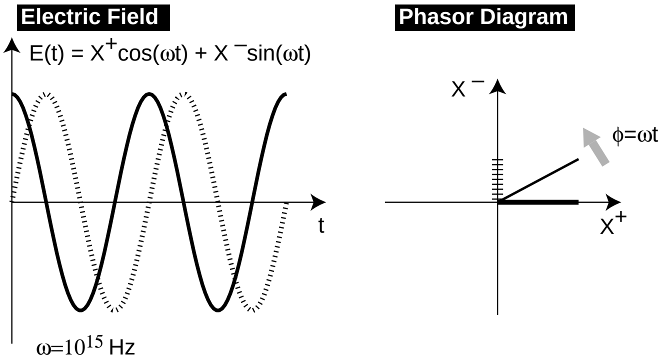

Figure 2.1: The EM wave is split up into a sum of sine and cosine components that are scaled by X^+ and X^- respectively. By convention, most of the amplitude is in the X^+ component (solid line), which means that the smaller X^- component (dashed line) essentially modifies only the phase.

procedure shows that the annihilation operators does the opposite $\hat{a}|n\rangle = |n-1\rangle$ and $\mathcal{E}_{n-1} = E_n - \hbar\omega$. What is missing now is the re-normalisation factor for these states $C_n|n\rangle$. We can get these by defining $\langle n|n\rangle = 1$ and noting for the annihilation operator that

$$\begin{aligned} \langle n-1|C^*_{n-1}C_{n-1}|n-1\rangle &= \langle n|\hat{a}^\dagger\hat{a}|n\rangle \\ |C_{n-1}|^2 &= n \end{aligned} \tag{2.24}$$

and similarly for the creation operator that

$$\begin{aligned} \langle n+1|C^*_{n+1}C_{n+1}|n+1\rangle &= \langle n|\hat{a}\hat{a}^\dagger|n\rangle \\ |C_{n+1}|^2 &= n+1 \end{aligned} \tag{2.25}$$

The re-normalisation factors are chosen to be real, which then shows that the creation and annihilation operators have the following effect on the energy eigenstates:

$$\hat{a}^\dagger|n\rangle = \sqrt{n+1}|n+1\rangle \tag{2.26}$$

$$\hat{a}|n\rangle = \sqrt{n}|n-1\rangle \tag{2.27}$$

There is a lowest energy level that the system can be in, the ground state $|0\rangle$, but the energy has the nonzero value of $\mathcal{E}_0 = \frac{1}{2}\hbar\omega$. The set of energy eigenstates of the system $|n\rangle$ are then labelled by $n = 0, 1, 2, 3, ...$ and they have the energy eigenvalues $\mathcal{E}_n = \mathcal{E}_0 + n\hbar\omega$. These states form a complete basis in which any state of the harmonic oscillator can be expressed as a suitably weighted superposition.

2.1.3 Step 3: The quantisation

The two parts of the puzzle a brought together. One begins by making the assumption that every classical mode of the EM field, labelled by subscripts $\mathbf{k}\lambda$, has a quantum harmonic oscillator associated with it. The creation and annihilation operators for each mode have the following effect on the nth energy eigenstate:

$$\begin{aligned} \hat{a}_{\mathbf{k}\lambda}|n_{\mathbf{k}\lambda}\rangle &= \sqrt{n_{\mathbf{k}\lambda}}|n_{\mathbf{k}\lambda}-1\rangle && (2.28) \\ \hat{a}^{\dagger}_{\mathbf{k}\lambda}|n_{\mathbf{k}\lambda}\rangle &= \sqrt{n_{\mathbf{k}\lambda}+1}|n_{\mathbf{k}\lambda}+1\rangle && (2.29) \end{aligned}$$

So in the mode $\mathbf{k}\lambda$, they create or destroy one unit of energy $\hbar\omega_k$, in other words, one photon. The commutation relation between the creation and annihilation operators is

$$\left[\hat{a}_{\mathbf{k}\lambda}, \hat{a}^{\dagger}_{\mathbf{k}\lambda}\right] = \hat{a}_{\mathbf{k}\lambda}\hat{a}^{\dagger}_{\mathbf{k}\lambda} - \hat{a}^{\dagger}_{\mathbf{k}\lambda}\hat{a}_{\mathbf{k}\lambda} = 1 \tag{2.30}$$

The combined state of the entire field is represented by the product notation

$$|\{n_{\mathbf{k}\lambda}\}\rangle = ...|n_{110,1}\rangle|n_{110,2}\rangle|n_{111,1}\rangle... \tag{2.31}$$

where the subscripts to n list first the mode number in three dimensions, followed by the choice of polarisation. The story of the quantisation does not end here because we need some way to relate the dimensionless creation and annihilation operators to the electric field in units of Newtons per Coulomb. We can do this by finding the Hamiltonian which represents the total energy of the system.

$$\hat{\mathcal{H}}_{\mathbf{k}\lambda} = \frac{1}{2}\hbar\omega\left(\hat{a}_{\mathbf{k}\lambda}\hat{a}^{\dagger}_{\mathbf{k}\lambda} + \hat{a}^{\dagger}_{\mathbf{k}\lambda}\hat{a}_{\mathbf{k}\lambda}\right) \tag{2.32}$$

By comparing this equation with the classical form of the total energy in Equation 2.17, we can make the plausible leap of faith in making the following replacements for the classical vector potential coefficients:

$$\begin{aligned} A_{\mathbf{k}\lambda} &\rightarrow (\hbar/2\varepsilon_0 V\omega_k)^{1/2}\hat{a}_{\mathbf{k}\lambda} && (2.33) \\ A^{*}_{\mathbf{k}\lambda} &\rightarrow (\hbar/2\varepsilon_0 V\omega_k)^{1/2}\hat{a}^{\dagger}_{\mathbf{k}\lambda} && (2.34) \end{aligned}$$

This step cannot be derived. It essentially becomes a definition for quantum optics theory, the predictions of which agree very well with experimental results, and so give us confidence that it is correct. The vector potential for the entire field is then

$$\hat{\mathbf{A}}(\mathbf{r},t) = \sum_{\mathbf{k}}\sum_{\lambda} \mathbf{e}_{\mathbf{k}\lambda}\hat{A}_{\mathbf{k}\lambda}(\mathbf{r},t) \tag{2.35}$$

where each mode contributes

$$\hat{A}_{\mathbf{k}\lambda}(\mathbf{r},t) = (\hbar/2\epsilon_0 V\omega_k)^{1/2}\left[\hat{a}_{\mathbf{k}\lambda}\exp(-\mathrm{i}\omega_k t + \mathrm{i}\mathbf{k}\cdot\mathbf{r}) + \hat{a}^{\dagger}_{\mathbf{k}\lambda}\exp(\mathrm{i}\omega_k t - \mathrm{i}\mathbf{k}\cdot\mathbf{r})\right] \tag{2.36}$$

From this one can calculate the electric field operator using $\hat{\mathbf{E}} = -\partial\hat{\mathbf{A}}/\partial t$. By convention the field is split up into positive and negative frequency components

$$\hat{\mathbf{E}}(\mathbf{r},t) = \hat{\mathbf{E}}^{(+)}(\mathbf{r},t) + \hat{\mathbf{E}}^{(-)}(\mathbf{r},t) \tag{2.37}$$

so that

$$\hat{\mathbf{E}}^{(+)}(\mathbf{r},t) = \sum_{\mathbf{k}}\sum_{\lambda} \mathbf{e}_{\mathbf{k}\lambda}(\hbar\omega_k/2\varepsilon_0 V)^{1/2}\hat{a}_{\mathbf{k}\lambda}\exp[-\mathrm{i}\Theta_{\mathbf{k}}(\mathbf{r},t)] \tag{2.38}$$

$$\hat{\mathbf{E}}^{(-)}(\mathbf{r},t) = \sum_{\mathbf{k}}\sum_{\lambda} \mathbf{e}_{\mathbf{k}\lambda}(\hbar\omega_k/2\varepsilon_0 V)^{1/2}\hat{a}^{\dagger}_{\mathbf{k}\lambda}\exp[\mathrm{i}\Theta_{\mathbf{k}}(\mathbf{r},t)] \tag{2.39}$$

The phase of the wavefronts is combined into a single phase term

$$\Theta_{\mathbf{k}}(\mathbf{r},t) = \omega_k t - \mathbf{k}\cdot\mathbf{r} - \frac{\pi}{2} \tag{2.40}$$

The offset $\frac{\pi}{2}$ is only a convention that absorbs a factor of i. We can group together the sine and cosine components of the complex exponentials, and organise the creation and annihilation operators into *quadrature operators*, thus giving

$$\hat{\mathbf{E}}(\mathbf{r},t) = \sum_{\mathbf{k}}\sum_{\lambda} \mathbf{e}_{\mathbf{k}\lambda}(2\hbar\omega_k/\varepsilon_0 V)^{1/2}\left\{\hat{X}^{+}_{\mathbf{k}\lambda}\cos[\Theta_{\mathbf{k}}(\mathbf{r},t)] + \hat{X}^{-}_{\mathbf{k}\lambda}\sin[\Theta_{\mathbf{k}}(\mathbf{r},t)]\right\} \tag{2.41}$$

Note that I have made a departure from the Loudon's notation [Loudon 2000], by removing the scaling factor $\frac{1}{2}$ in the definition of the quadrature operators, which for the remainder of this thesis become:

$$\hat{X}^{+}_{\mathbf{k}\lambda} := \left(\hat{a}^{\dagger}_{\mathbf{k}\lambda} + \hat{a}_{\mathbf{k}\lambda}\right) \quad , \quad \hat{X}^{-}_{\mathbf{k}\lambda} := \mathrm{i}\left(\hat{a}^{\dagger}_{\mathbf{k}\lambda} - \hat{a}_{\mathbf{k}\lambda}\right) \tag{2.42}$$

they correspond to the 'in-phase' and 'out-of-phase' components of the EM wave, respectively. By convention, it is assumed that most of the amplitude of the wave is in the X^+ component, hence it is called the amplitude quadrature. This means that X^- contributes essentially to a phase shift of the wave, and is therefore called the phase quadrature. This has been visualised in Figure 2.1 in the form of a phasor diagram. The amplitude and phase quadrature operators correspond to the position and momentum operators, respectively, as can be seen with the help of Equation 2.21. The quadrature operators are Hermitian, and are in principle directly measurable quantities. I will be using them throughout this thesis in calculations of the transfer functions of optical components, and in the evaluation of quadrature squeezing and entanglement. In addition, one is free to choose a new basis, which corresponds to a rotation by angle ϕ of the original basis, for example:

$$\hat{X}^{\phi}_{\mathbf{k}\lambda} = \hat{X}^{+}_{\mathbf{k}\lambda}\cos\phi + \hat{X}^{-}_{\mathbf{k}\lambda}\sin\phi \quad (2.43)$$

$$\hat{X}^{\phi+\frac{\pi}{2}}_{\mathbf{k}\lambda} = -\hat{X}^{+}_{\mathbf{k}\lambda}\sin\phi + \hat{X}^{-}_{\mathbf{k}\lambda}\cos\phi \quad (2.44)$$

To summarise the quantisation: what we now have is a ladder of energy eigenstates $|n_{\mathbf{k}\lambda}\rangle$ for each mode of the EM field; see Figure 2.2. The creation and annihilation operators add or subtract one quantum of energy $\hbar\omega_k$ from the mode, which is interpreted as a photon. Any single-mode state of the EM field can be expressed as a weighted superposition over the energy eigenstates:

$$|\psi\rangle = \sum_{n=0}^{\infty} c_n|n\rangle \quad (2.45)$$

with c_n the set of complex-valued coefficients. The electric field operator is expressed as a sum of the amplitude and phase quadrature operators, which themselves are the sum/difference of the creation and annihilation operators. The total energy contained in the EM field is found by applying

$$\hat{\mathcal{H}}|\{n_{\mathbf{k}\lambda}\}\rangle = (\mathcal{E}_{\mathrm{R}} + \mathcal{E}_0)|\{n_{\mathbf{k}\lambda}\}\rangle \quad (2.46)$$

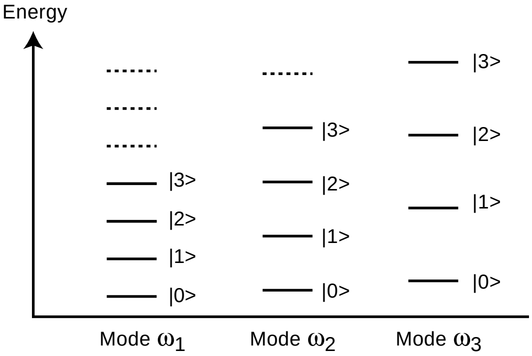

Figure 2.2: Each mode of the electromagnetic field can carry only a discrete amount of energy $(n+1/2)\hbar\omega_k$. A mode can be in a superposition state of many excitation levels at once (reminiscent of an atomic level scheme). Note that the lowest level still has $\hbar\omega_k/2$ of energy.

where

$$\mathcal{E}_0 = \frac{1}{2}\sum_{\mathbf{k}}\sum_{\lambda}\hbar\omega_k \tag{2.47}$$

$$\mathcal{E}_{\mathrm{R}} = \sum_{\mathbf{k}}\sum_{\lambda}\hbar\omega_k n_{\mathbf{k}\lambda} \tag{2.48}$$

The subscript 'R' stands for the radiative component, while the subscript '0' stands for the vacuum component. Note that even when all modes of the EM field are in their ground states, the summation for the vacuum component of the energy will still diverge to infinity. But this does not present a practical problem, since later it will be shown that a photo-ionisation detector is only sensitive to the radiative component, and therefore only to any excitation above the ground state. But it should be noted that the vacuum component is a measurable effect in experiments that investigate the Casimir effect of the attractive force between two perfectly conducting plates [Casimir 1948].

2.2 Observables, uncertainty, and quantum noise

Let us consider the amplitude and phase quadrature observables. The quadrature operators do not commute for a given mode of polarisation and propagation vector. The commutation relation is

$$\left[\hat{X}^{+}_{\mathbf{k}\lambda}, \hat{X}^{-}_{\mathbf{k}'\lambda'}\right] = 2\mathrm{i}\delta_{\mathbf{k},\mathbf{k}'}\delta_{\lambda,\lambda'} \tag{2.49}$$

If the modes are chosen to be degenerate, this leads to a Heisenberg uncertainty relation for the amplitude and phase quadratures. The uncertainty relation for a pair of arbitrary operators $\hat{O}_1$ and $\hat{O}_2$ depends on the commutation relation; see for example [Griffiths 1995]:

$$\sigma^2(\hat{O}_1)\,\sigma^2(\hat{O}_2) \geq \left(\frac{1}{2\mathrm{i}}\,\langle\left[\hat{O}_1,\hat{O}_2\right]\rangle\right)^2 \tag{2.50}$$

where the expectation value of the standard deviation of the operator has been defined by

$$\sigma^2(\hat{O}_1) = \left\langle\psi\middle|(\hat{O}_1)^2\middle|\psi\right\rangle - \left\langle\psi\middle|\hat{O}_1\middle|\psi\right\rangle^2 \tag{2.51}$$

where the inner product has been taken over an arbitrary state $|\psi\rangle$. Substituting in the commutation relation between the amplitude and phase quadrature operators then returns

$$\sigma^2(\hat{X}^+_{\mathbf{k}\lambda})\,\sigma^2(\hat{X}^-_{\mathbf{k}\lambda}) \geq \delta_{\mathbf{k},\mathbf{k}'}\delta_{\lambda,\lambda'} \tag{2.52}$$

This nonzero value for the minimum product of the variances tells us that there is a limit to the precision that one can simultaneously measure both quadratures for any given mode of the EM field. Note that the precision need not be equally distributed, as for example, the state may have a smaller variance in the amplitude quadrature but must then be compensated for by having a larger variance for the phase quadrature, such that the uncertainty relation is satisfied.

A somewhat bolder interpretation of the uncertainty principle is that the EM field itself cannot have a well-defined (or certain) value for the amplitude *and* phase quadrature. For example, a measurement of the amplitude quadrature will project the state into the $\hat{X}^+$ basis, and leave the phase quadrature completely uncertain.

An alternative view is that there is a noise penalty that is paid when one attempts to measure both quadratures simultaneously. But one should be careful here because our analysis has shown no time dependence of the field (other than the oscillation at the optical frequency ω_k). The thing to remember is that this noise refers only to the results of measurements that are made on an ensemble of identically prepared states. Since the measurement results will be drawn from a statistical distribution of values that fluctuate around a mean value, the sequence of randomly fluctuating values can be interpreted as noise. The more realistic case of a system that is not closed, and couples into a continuum of modes, will be treated in later sections.

Boson commutation relation:	$[\hat{a}, \hat{a}^\dagger]$	=	$\hat{a}\hat{a}^\dagger - \hat{a}^\dagger\hat{a} = 1$
Photon number:	$\hat{n}$	=	$\hat{a}^\dagger\hat{a}$
Amplitude quadrature:	$\hat{X}^+$	=	$(\hat{a}^\dagger + \hat{a})$
Phase quadrature:	$\hat{X}^-$	=	$\mathrm{i}(\hat{a}^\dagger - \hat{a})$
Mean of photon number:	$\mu(\hat{n})$	=	$\langle\psi\|\hat{n}\|\psi\rangle$
Variance of photon number:	$\sigma^2(\hat{n})$	=	$\langle\psi\|\hat{n}\hat{n}\|\psi\rangle - \langle\psi\|\hat{n}\|\psi\rangle^2$
Mean of amplitude quadrature:	$\mu(\hat{X}^+)$	=	$\langle\psi\|\hat{X}^+\|\psi\rangle$
Mean of phase quadrature:	$\mu(\hat{X}^-)$	=	$\langle\psi\|\hat{X}^-\|\psi\rangle$
Variance of amplitude quadrature:	$\sigma^2(\hat{X}^+)$	=	$\langle\psi\|\hat{X}^+\hat{X}^+\|\psi\rangle - \langle\psi\|\hat{X}^+\|\psi\rangle^2$
Variance of phase quadrature:	$\sigma^2(\hat{X}^-)$	=	$\langle\psi\|\hat{X}^-\hat{X}^-\|\psi\rangle - \langle\psi\|\hat{X}^-\|\psi\rangle^2$
Second-order coherence function:	$g^{(2)}(\tau)$	=	$\langle\psi\|\hat{a}^\dagger\hat{a}^\dagger\hat{a}\hat{a}\|\psi\rangle/\langle\psi\|\hat{a}^\dagger\hat{a}\|\psi\rangle^2$
			where $\|\psi\rangle$ is an arbitrary state

Table 2.1: A summary of definitions that will be applied to single-mode states of the EM field.

$\|n\rangle$	:=	$\hat{N}(n)\|0\rangle$
$\hat{N}(n)$	:=	$(\hat{a}^\dagger)^n/\sqrt{n!}$ where $n = 0, 1, 2, 3, ...$
$\hat{n}\|n\rangle$	=	$n\|n\rangle$
$\mu(\hat{n})$	=	n
$\sigma^2(\hat{n})$	=	0
$\mu(\hat{X}^+)$	=	0
$\mu(\hat{X}^-)$	=	0
$\sigma^2(\hat{X}^+)$	=	$2(n + \frac{1}{2})$
$\sigma^2(\hat{X}^-)$	=	$2(n + \frac{1}{2})$
$g^{(2)}(\tau)$	=	$1 - (1/n)$ for $n \geq 1$

Table 2.2: Properties of the number states.

$\|\alpha\rangle$	:=	$\hat{D}(\alpha)\|0\rangle$
$\hat{D}(\alpha)$	:=	$\exp(\alpha\hat{a}^\dagger - \alpha^*\hat{a})$ where $\alpha = \|\alpha\| \exp(\mathrm{i}\theta)$
$\hat{D}^\dagger(\alpha)\ \hat{a}\ \hat{D}(\alpha)$	=	$\hat{a} + \alpha$
$\hat{D}^\dagger(\alpha)\ \hat{a}^\dagger\ \hat{D}(\alpha)$	=	$\hat{a}^\dagger + \alpha^*$
$\hat{a}\|\alpha\rangle$	=	$\alpha\|\alpha\rangle$
$\langle\alpha\|\hat{a}^\dagger$	=	$\langle\alpha\|\alpha^*$
$\mu(\hat{n})$	=	$\|\alpha\|^2$
$\sigma^2(\hat{n})$	=	$\|\alpha\|^2$
$\mu(\hat{X}^+)$	=	$2\|\alpha\| \cos\theta$
$\mu(\hat{X}^-)$	=	$2\|\alpha\| \sin\theta$
$\sigma^2(\hat{X}^+)$	=	1
$\sigma^2(\hat{X}^-)$	=	1
$\|\alpha\rangle$	=	$\exp(-\|\alpha\|^2/2) \sum_{n=0}^{\infty}(\alpha^n/\sqrt{n!})\|n\rangle$
$P(n)$	=	$\exp(-\|\alpha^2\|)\|\alpha\|^{2n}/n!$
$g^{(2)}(\tau)$	=	1

Table 2.3: Properties of the coherent states.

$$
\begin{array}{rcl}
|\zeta\rangle & := & \hat{S}(\zeta)|0\rangle \\
\hat{S}(\zeta) & := & \exp(\frac{1}{2}\zeta^*(\hat{a})^2 - \frac{1}{2}\zeta(\hat{a}^\dagger)^2) \ \text{ where } \ \zeta = r\exp(\mathrm{i}\vartheta) \\
\hat{S}^\dagger(\zeta)\ \hat{a}\ \hat{S}(\zeta) & = & \hat{a}\cosh r - \hat{a}^\dagger\exp(\mathrm{i}\vartheta)\sinh r \\
\hat{S}^\dagger(\zeta)\ \hat{a}^\dagger\ \hat{S}(\zeta) & = & \hat{a}^\dagger\cosh r - \hat{a}\exp(-\mathrm{i}\vartheta)\sinh r \\
\mu(\hat{n}) & = & \sinh^2 r \\
\sigma^2(\hat{n}) & = & 2(\sinh^2 r + 1)\sinh^2 r \\
\mu(\hat{X}^+) & = & 0 \\
\mu(\hat{X}^-) & = & 0 \\
\sigma^2(\hat{X}^+) & = & \exp(2r)\sin^2(\vartheta/2) + \exp(-2r)\cos^2(\vartheta/2) \\
\sigma^2(\hat{X}^-) & = & \exp(2r)\cos^2(\vartheta/2) + \exp(-2r)\sin^2(\vartheta/2) \\
|\zeta\rangle & = & \sqrt{\operatorname{sech} r}\sum_{n=0}^{\infty}(\sqrt{(2n)!}/n!)(-\tanh r\exp(\mathrm{i}\vartheta)/2)^n|2n\rangle \\
P(n=2m) & = & (\operatorname{sech} r)((2m)!/(m!)^2)((\tanh r)/2)^{2m}\ , \\
P(n{=}2m{+}1) & = & 0 \ \text{ where } \ m = 0, 1, 2, 3, ... \\
g^{(2)}(\tau) & = & 3 + (1/\sinh^2 r)
\end{array}
$$

Table 2.4: Properties of the squeezed states.

$$
\begin{array}{rcl}
|\alpha,\zeta\rangle & := & \hat{D}(\alpha)\hat{S}(\zeta)|0\rangle \\
\hat{D}(\alpha) & := & \exp(\alpha\hat{a}^\dagger - \alpha^*\hat{a}) \ \text{ where } \ \alpha = |\alpha|\exp(\mathrm{i}\theta) \\
\hat{S}(\zeta) & := & \exp(\frac{1}{2}\zeta^*(\hat{a})^2 - \frac{1}{2}\zeta(\hat{a}^\dagger)^2) \ \text{ where } \ \zeta = r\exp(\mathrm{i}\vartheta) \\
\hat{D}^\dagger\hat{S}^\dagger\ \hat{a}\ \hat{S}\hat{D} & = & \hat{a}\cosh r - \hat{a}^\dagger\exp(\mathrm{i}\vartheta)\sinh r + \alpha \\
\hat{D}^\dagger\hat{S}^\dagger\ \hat{a}^\dagger\ \hat{S}\hat{D} & = & \hat{a}^\dagger\cosh r - \hat{a}\exp(-\mathrm{i}\vartheta)\sinh r + \alpha^* \\
\mu(\hat{n}) & = & |\alpha|^2 + \sinh^2 r \\
\sigma^2(\hat{n}) & = & |\alpha|^2\{\mathrm{e}^{2r}\sin^2(\theta{-}\frac{\vartheta}{2}){+}\mathrm{e}^{-2r}\cos^2(\theta{-}\frac{\vartheta}{2})\}{+}2(\sinh^2 r{+}1)\sinh^2 r \\
\mu(\hat{X}^+) & = & 2|\alpha|\cos\theta \\
\mu(\hat{X}^-) & = & 2|\alpha|\sin\theta \\
\sigma^2(\hat{X}^+) & = & \exp(2r)\sin^2(\vartheta/2) + \exp(-2r)\cos^2(\vartheta/2) \\
\sigma^2(\hat{X}^-) & = & \exp(2r)\cos^2(\vartheta/2) + \exp(-2r)\sin^2(\vartheta/2) \\
P(n) & = & (n!\cosh r)^{-1}(\frac{1}{2}\tanh r)^n\exp\{-|\alpha|^2 \\
 & & -\frac{1}{2}\tanh r((\alpha^*)^2\mathrm{e}^{\mathrm{i}\vartheta} + (\alpha)^2\mathrm{e}^{-\mathrm{i}\vartheta})\}|H_n(z)|^2 \\
 & & \quad \text{where } \ z = (\alpha + \alpha^*\mathrm{e}^{\mathrm{i}\vartheta}\tanh r)/\sqrt{2\mathrm{e}^{\mathrm{i}\vartheta}\tanh \mathrm{r}} \\
 & & \quad \text{and } \ H_n(z) \ \text{ are the Hermite polynomials} \\
g^{(2)}(\tau) & = & 1 + \{(2\alpha^2{+}\cosh(2r) - 2\alpha^2\coth r)\sinh^2 r\}/(\alpha^2 + \sinh^2 r)^2
\end{array}
$$

Table 2.5: Properties of the displaced-squeezed states.

$$
\begin{array}{rcl}
\hat{\rho}_{\mathrm{th}}(m) & := & \sum_{n=0}^{\infty}(m^n/(m+1)^{n+1})|n\rangle\langle n| \\
 & & \text{where } \ m = \{\exp(\hbar\omega/k_{\mathrm{B}}T) - 1\}^{-1} \\
\mu(\hat{n}) & = & m \\
\sigma^2(\hat{n}) & = & m^2 + m \\
\mu(\hat{X}^+) & = & 0 \\
\mu(\hat{X}^-) & = & 0 \\
\sigma^2(\hat{X}^+) & = & 2(m + \frac{1}{2}) \\
\sigma^2(\hat{X}^-) & = & 2(m + \frac{1}{2}) \\
P(n) & = & m^n/(m+1)^{n+1} \\
g^{(2)}(\tau) & = & 2
\end{array}
$$

Table 2.6: Properties of the thermal states.

2.3 The zoo of single mode states

My aim is to show how arbitrary states of light can be characterised according to the properties of photon number distribution, quadrature amplitudes, and second-order coherence. But to do this, I will first need to examine some specific states of light in order to illustrate these concepts. Table 2.1 is a list of the necessary definitions and short-hand notation. The relevant properties are listed in tables for each of the following states: number states (Table 2.2); coherent states (Table 2.3); squeezed states (Table 2.4); displaced squeezed states (Table 2.5); and thermal states (Table 2.6). I regret that there is insufficient space for me to give full derivations of the properties, nor for me to give convincing arguments for the correspondence of these states to those that can be produced in the laboratory. For better arguments in this regard, one can turn to [Loudon 2000].

2.3.1 Number states

We have already met the number states during the quantisation procedure: they are the energy eigenstates of a single mode of the EM field. The interpretation is that each eigenstate corresponds to n number of photons being contained in the mode. Following this idea, the photon number operator $\hat{n}$ is given by subtracting the contribution of the zero-point energy from the Hamiltonian of the system ($\mathcal{E}_0$ from eqn 2.46), such that $\hat{n} = \hat{a}^\dagger \hat{a}$. Applying the number operator then returns $\hat{n}|n\rangle = n|n\rangle$ as an eigenvalue. These *number states*, or *Fock states* as they are also referred to, form a complete basis in which an arbitrary state can be expressed as a complex-weighted superposition of number states. Properties of the number states are listed in Table 2.2.

All the states have a well defined photon number, in the sense that the variance of the photon number is zero. It is the state that has an absence of photons, the vacuum state $|n = 0\rangle$, that takes a special place amongst the set. It is a minimum uncertainty state in terms of the quadrature operator observables $\sigma^2(\hat{X}^+)\sigma^2(\hat{X}^-) = 1$. For the other states, the uncertainty product grows with the photon number, but the mean of the quadrature amplitude and phase remains at zero. In this sense, the number states do not seem to agree with the notion of a classical EM wave.

In the laboratory, photon number states can be prepared from a light source that is based on the mechanism of parametric down conversion. Pairs of photons are produced and separated, one of which is used as a trigger to temporally isolate the other photon with high probability.

2.3.2 Coherent states

The state that most resembles the classical EM wave which has a well-defined amplitude and phase, is the coherent state. The set of coherent states $|\alpha\rangle$ are parameterised by their *coherent amplitude* α. Note that α can be complex, where the real component shows up in the amplitude quadrature, and the imaginary component in the phase quadrature. The properties are listed in Table 2.3. The variances of the amplitude and phase quadratures are both equal to one, and form a minimum uncertainty product for all of the coherent states. The expansion of the coherent states in the basis of number states, follows a Poissonian distribution in the probability $P(n)$ of detecting the nth state. The mean and variance of the photon number are equal to each other, and proportional to the square of the coherent amplitude. For coherent amplitudes greater than one, the $P(n)$ distribution becomes approximately Gaussian.

The coherent states can be ‘grown’ out of the vacuum state by applying the displacement operator $\hat{D}(\alpha)$. This operator is also useful for unitarily transforming the creation and annihilation operators (and the observables that are built from these) instead of evolving the states, to enable one to work in the Heisenberg picture, which can simplify the calculation of quantities such as the second-order coherence.

A source of coherent states can be well approximated in the laboratory by a heavily attenuated source of laser light. The attenuation serves to reduce extraneous noise sources due to the lasing mechanism, and thereby prepare a nearly pure, coherent state.

2.3.3 Squeezed states

Unlike the coherent states, the squeezed states are free to take on unequal variances for the amplitude and phase quadratures while still preserving the minimum uncertainty product. The properties of the squeezed states are listed in Table 2.4. They can be grown out of the vacuum state by applying the squeeze operator $\hat{S}(\zeta)$, which is parameterised by $\zeta = r\mathrm{e}^{\mathrm{i}\vartheta}$ which the complex-valued squeezing parameter that determines the 'strength' of the squeezing. Choosing a value of $r = 0$ and $\vartheta = 0$ gives exactly the vacuum state, while $r > 0$ will cause one of the quadrature variances to drop below one, with larger deviations of the variance signifying stronger squeezing. The squeezed quadrature need not be aligned with the amplitude or phase quadratures. The arbitrary quadrature angle is determined by ϑ. Note that the mean values of quadrature amplitudes are zero, for this reason, the state is also called a squeezed *vacuum* state, but note that the state is no longer a true vacuum state, since the mean photon number is no longer zero. An expansion of the squeezed state in the Fock basis shows that only the even photon number states are present, and that the photon number variance always exceeds the mean photon number.

Squeezed states can be produced experimentally by a parametric down-converter that is driven to produce degenerate pairs of photons, such that the photon number distribution is populated only by even photon number states.

2.3.4 Displaced-Squeezed states

The squeezed state can be displaced in a similar fashion to the way that the vacuum state was displaced to form the coherent state. Applying the displacement operator to the squeeze operator then forms the displaced-squeezed states $|\alpha, \zeta\rangle$ when applied to the vacuum state. Their properties are listed in Table 2.5. One is free to choose the mean quadrature values via α, and also the squeezing of the quadrature variances via ζ. The mean photon number becomes the sum of a contribution from the square of the coherent amplitude and the squeezing operation. In contrast to a non-displaced-squeezed state (or vacuum squeezed state), the photon number variance may now become smaller or larger than the mean photon number depending on the amount of displacement and the strength of squeezing. Note that this is sometimes called photon number squeezing, which should not be confused with quadrature squeezing.

One way of preparing a displaced-squeezed state of light in a laboratory is to interfere a coherent source from a laser, with degenerate photon pairs from a parametric down-converter.

2.3.5 Thermal states

To write down the state of light that occurs in a single mode of the EM field under thermal equilibrium, we need to be able to describe a statistical mixture of number states, rather than a superposition. This is done by introducing the density operator $\hat{\rho}_{\mathrm{th}}(m)$ as parameterised by the mean photon number $m(T)$, which is given by the Planck thermal excitation function that depends on the temperature T. Both functions are given in the list of properties in Table 2.6. In a later section I will give the details of how the density function works, but for the moment let me just summarise the measurable properties of the thermal states.

The means of the amplitude and phase quadratures are zero, but the variances are proportional to the mean photon number. This is analogous to the case of the photon number states themselves, but where the parameter m can take on any positive value, rather than just integers. The value of m increases with increasing temperature T. Unlike for the number states, however, the variance of the photon number for the thermal states scales with $(m^2 + m)$. A variation on the original thermal state, is the *biased*-thermal state, where the variances for the amplitude and phase quadratures need not be equal. Although in this case, the analogy of the state arising from a condition of thermal equilibrium needs to be treated with caution.

2.4 Characterizing single-mode states

In the last section I had only introduced a few states of light, and listed some of their basic properties, but I have not yet brought the individual properties together into concepts that we can apply to arbitrary states. Each concept gives us not only another view into what a quantum state of light actually is, but also a way of deciding whether a state can be classed as being non-classical.

2.4.1 Expansion in the Fock basis: (sub-/super-Poissonian statistics)

The concept of photon statistics is most readily seen by expanding an arbitrary state in the Fock basis. We are interested in the probability of detecting each Fock state, as obtained by taking the modulus square of each expansion coefficient $P(n) = |c_n|^2$. In Figure 2.3,

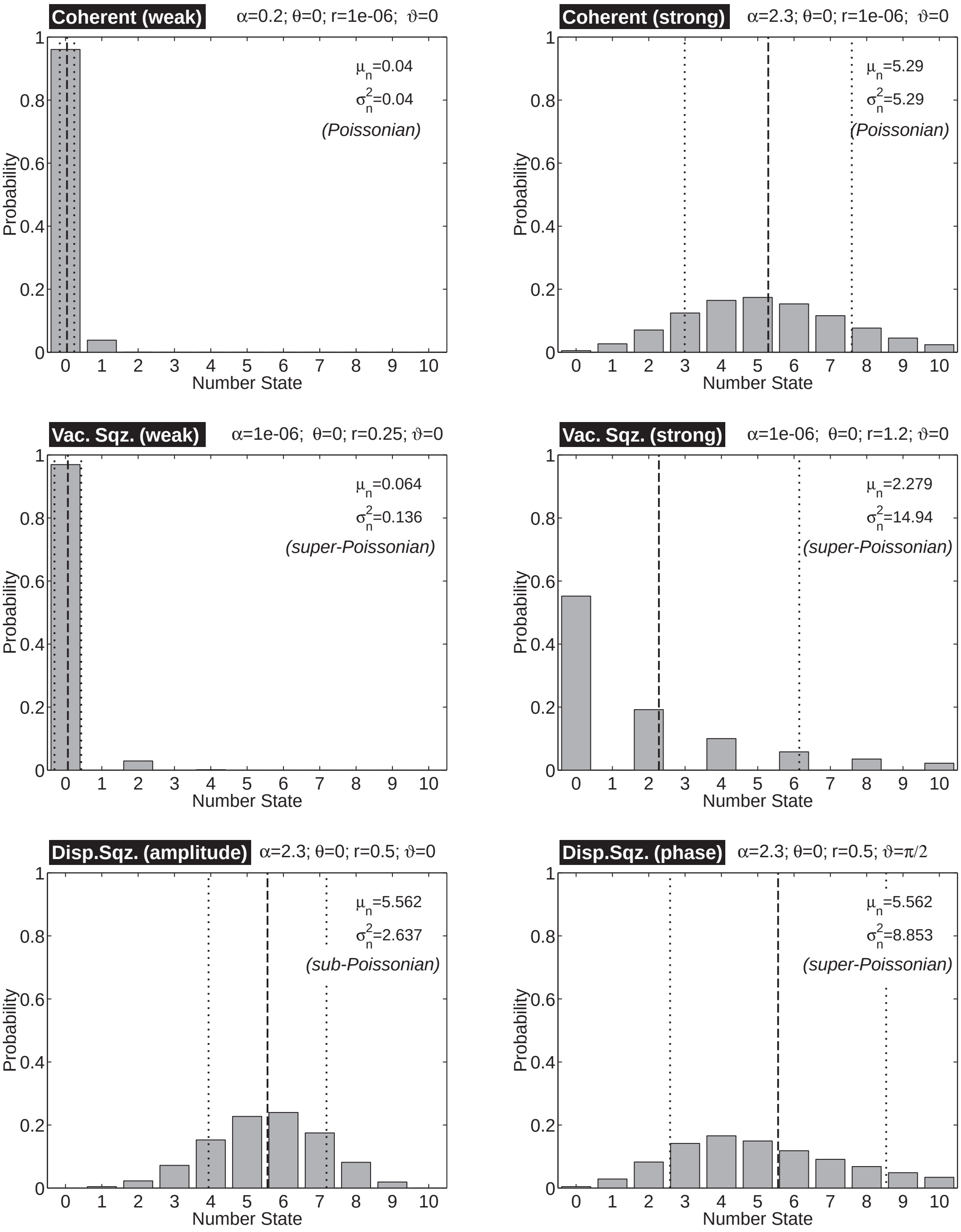

Figure 2.3: An expansion in the number state basis for coherent states and squeezed states. Note that for weak coherent state, essentially only the $n=1$ state contributes. For brighter coherent states, the distribution approaches a Gaussian. The weakly squeezed vacuum state begins as only an $n=2$ contribution, but increasing the squeezing parameter then begins to excite all even modes. The coherent state has Poissonian statistics, while the squeezed vacuum state has super-Poissonian statistics. However, by applying the correct displacement to the squeezed state, one can obtain sub-Poissonian statistics. The dashed lines are placed at the mean photon number. The dotted lines give the upper and lower edges that are set by the standard deviation of the photon number.

I have compared the examples of a weak and a strong coherent state, where the distribution function was taken from Table 2.3. For the case of a weak coherent amplitude, the distribution is dominated by the vacuum state, and the single photon Fock state. For larger coherent amplitudes, the distribution appears more Gaussian in shape. Although difficult to see directly, the mean equals the variance in each case, because they are both derived from a Poissonian distribution. This simple result from the Poissonian distribution can be used as a benchmark for deciding whether a state is nonclassical. The semi-classical theory of light only permits the detection of photons in a distribution that is either Poissonian, or 'broader' than Poissonian, in the sense of the variance exceeding the mean. The distribution itself can be arbitrarily shaped, but is nevertheless termed *super-Poissonian*. A clear signature of a non-classical state of light is therefore the observation of a photon number distribution that has a variance that is less than the mean, which is termed *sub-Poissonian*. An example is the displaced-squeezed state that has a large real coherent amplitude $\alpha \approx 1$, and a real and positive squeezing parameter $\zeta > 0$. An example is shown in Figure 2.3, where the variance is clearly less than the mean photon number.

Note that the converse of the sub-Poissonian criterion does not hold true for all states, i.e. a state that does not show sub-Poissonian statistics could still be nonclassical as witnessed by another criterion of non-classicality. The vacuum squeezed state, shown for instance in Figure 2.3, displays a super-Poissonian photon number distribution. The variance of the quadratures however, shows that one of them is squeezed below the level of a vacuum state, which is also a criterion of non-classicality.

2.4.2 Phasor diagram of quadrature statistics: (quadrature squeezing)

The quadrature statistics of an arbitrary state can be presented in a phasor diagram that is analogous to the classical representation of a wave that has a complex-valued amplitude (as shown in Figure 2.1). I will show the steps that go behind the drawing of such a phasor diagram, which is also called a 'ball-on-stick' diagram. First, let us consider measuring the amplitude quadrature of an ensemble of identically prepared coherent states. We would expect to observe a distribution of measured values that have a mean $\mu(\hat{X}^+)$ and standard deviation $\sigma(\hat{X}^-)$ as derived from Table 2.3. What the exact form of the distribution is, is

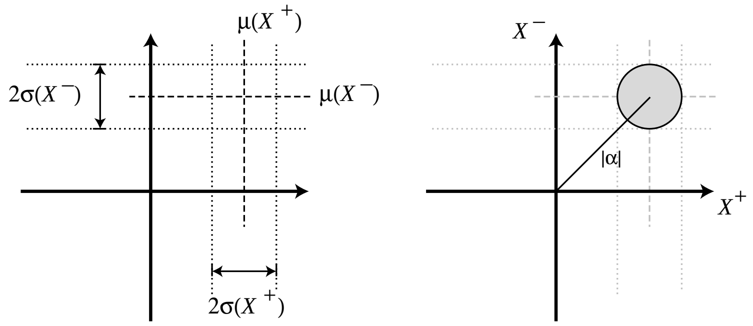

Figure 2.4: Phasor diagram of quadrature statistics. The 'ball-on-stick' diagram of a coherent state is constructed from the mean and standard deviations of separate measurements that are made on the amplitude and phase quadratures.

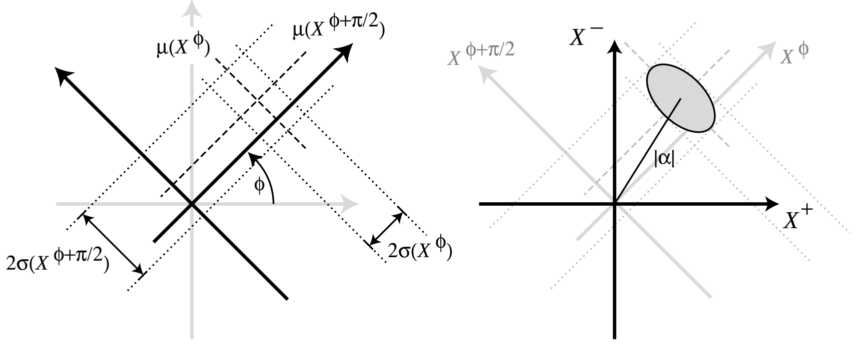

Figure 2.5: Phasor diagram of quadrature statistics. The 'ball-on-stick' diagram of a displaced-squeezed state is constructed from the mean and standard deviations of separate measurements that are made on the quadrature angles of ϕ and $\phi + \pi/2$. The angle is chosen to coincide with the major and minor axes of the ellipse that is derived from a contour of the Wigner function.

not important at the moment. The observed mean and standard deviation data are plotted as vertical lines in a two-dimensional Cartesian plane, that has been vaguely labelled with X^+ and X^-. Note that the hat notation has been dropped because the labels are only there to remind us of the measurement basis. We repeat the experiment, but measure instead the phase quadrature of the state, and collect the mean $\mu(\hat{X}^-)$ and standard deviation $\sigma(\hat{X}^-)$ information, which are then plotted as horizontal lines in the phasor diagram, as shown in Figure 2.4.

The next step in drawing the diagram involves making an assumption about the quadrature probability distribution of the state that is under investigation. For the case of the coherent state, as we will see later, the distribution is Gaussian along the amplitude and phase quadratures, and indeed for any quadrature angle in between. It is for this reason that it is customary to replace the rectangular 'construction' lines of the diagram with an ellipse that has major and minor axes that correspond to the standard deviation of the amplitude and phase quadratures (not necessarily respectively). The ellipse also corresponds to a contour of the two-dimensional (quasi-) probability distribution of the amplitude and phase quadratures, where the marginal distributions for each quadrature are derived from the Wigner function representation of the state.

Note that this method of constructing the ball-on-stick diagram will only work when I have chosen the quadrature angle that yields the major and minor axes of the two-dimensional quadrature distribution. I can illustrate this by constructing the ball-on-stick diagram for a displaced-squeezed state that is squeezed along an arbitrary quadrature angle ϑ. The relevant mean and standard deviations of the quadratures have been gathered from Table 2.5. The correct analysis is to choose a quadrature angle ϕ that is equal to the squeezing angle ϑ. This new quadrature basis is defined in Equation 2.44. The coordinates of the ellipse in the *rotated* quadrature basis can be drawn along a parameter t using: $x_{\text{ell}}^{\phi} = \mu(\hat{X}^{\phi}) + \sigma(\hat{X}^{\phi})\cos(t)$; $x_{\text{ell}}^{\phi+\frac{\pi}{2}} = \mu(\hat{X}^{\phi+\frac{\pi}{2}}) + \sigma(\hat{X}^{\phi+\frac{\pi}{2}})\sin(t)$. The construction diagram, and final ball-on-stick diagram are shown in Figure 2.5. The length of the 'stick' is equal to the absolute value of the displacement $|\alpha|$.

Now that I have gone through the method of drawing a ball-on-stick diagram, I can return to the concept of squeezing and its role as a witness to nonclassical states of light. If in the diagram, one finds that the minor axis of the ellipse has a value of less than that of a vacuum state (a value of one), then one can conclude that the state is 'squeezed' in that quadrature (whatever the angle may be). We may not however have necessarily observed a member of the family of squeezed state, since this would require fulfilling the definition as given in Table 2.4. The significance of observing squeezing is that it cannot occur in the semi-classical theory of light. The argument for this relies on the result that the semi-classical theory can only describe either coherent states of light, or statistical mixtures of them. Within these confines, it would not be possible to satisfy the criterion that a quadrature variances could be less than that of a coherent state (or vacuum state). Hence, the criterion of squeezing can be used as a witness for identifying nonclassical light.

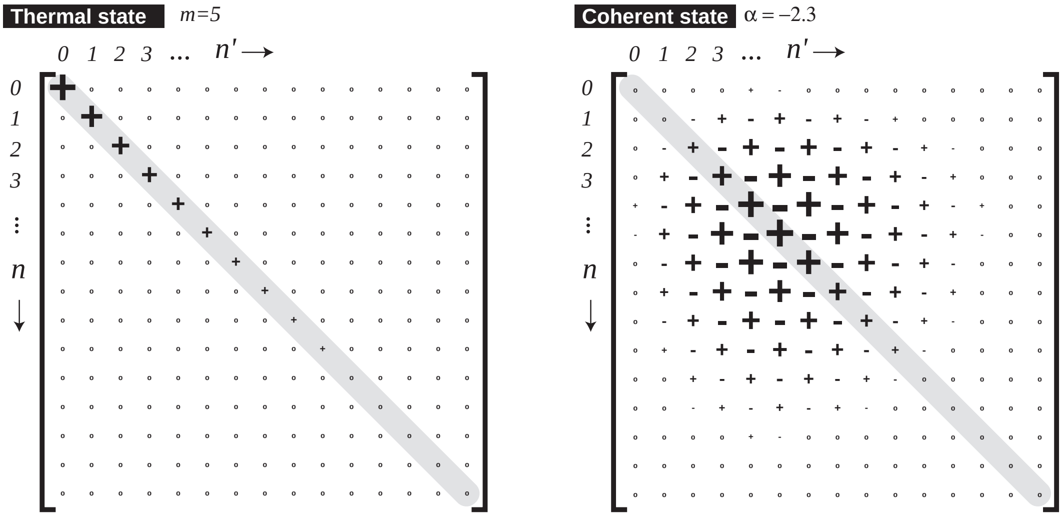

Figure 2.6: The density operator as expanded in the Fock basis and shown in matrix form with elements $\rho_{nn'}$. The value of each element has been replaced by a plus or minus symbol, where a larger size indicates a larger absolute value. Elements having values near to zero were replaced by a small 'o' symbol. The grey shading highlights the diagonal elements. The density matrices for a pure coherent state and a mixed thermal state are compared. The thermal state is completely mixed and does not show any off-diagonal elements.

2.4.3 The density operator: (pure/mixed states)

Pure states are states that can be expressed as a superposition of number states in the Fock basis. But for some physical systems that can only be described in a probabilistic theory, perhaps due to the large number of particles involved, then one may only have a limited knowledge of the state of light that is produced, and one would therefore need to find a way to describe a statistical mixture of states. The density operator is a short-hand notation that completely describes a mixed state as being made up of individual pure states, and the probabilities with which they are likely to be found.

The analysis begins by letting there be a discrete set of pure states $|R\rangle$ that are labelled with the variable R. We assume that we have knowledge of the probabilities P_R with which these states will occur. The probabilities need to sum to one: $\sum_R P_R = 1$. Each pure state can be expressed in terms of a discrete set of basis states $|S\rangle$ that are labelled by variable S. These states form a complete basis, such that $\sum_S |S\rangle\langle S| = 1$. The task at hand is to calculate the expectation value of some operator $\hat{O}$ for the statistical mixture of states. A way of doing this is apply the completeness property of the basis states, such that

$$\begin{aligned}
\langle\hat{O}\rangle &= \sum_R P_R \langle R|\hat{O}|R\rangle && (2.53)\\
&= \sum_R P_R \langle R|\hat{O}\Big(\sum_S |S\rangle\langle S|\Big)|R\rangle && (2.54)\\
&= \sum_R \sum_S P_R \langle R|\hat{O}|S\rangle\ \langle S|R\rangle && (2.55)\\
&= \sum_R \sum_S P_R \langle S|R\rangle\langle R|\hat{O}|S\rangle && (2.56)\\
&= \sum_S \langle S|\Big(\sum_R P_R |R\rangle\langle R|\Big)|\hat{O}|S\rangle && (2.57)
\end{aligned}$$

If we define the density operator as being

$$\hat{\rho} = \sum_R |R\rangle\langle R| \qquad (2.58)$$

then the expectation value of the operator $\hat{O}$ becomes

$$\begin{aligned}
\langle\hat{O}\rangle &= \sum_S \langle S|\hat{\rho}\hat{O}|S\rangle && (2.59)\\
&= \mathrm{Trace}\{\hat{\rho}\hat{O}\} && (2.60)
\end{aligned}$$

This seems rather abstract at the moment, but I think I can get around it by choosing the set $|S\rangle$ to be the Fock states, and by choosing to express the set $|R\rangle$ in the Fock basis. After doing this we get $\hat{\rho} = \sum_n \sum_{n'} P_{n,n'} |n'\rangle\langle n|$, for which $P_{n,n'}$. The coefficients $P_{n,n'}$ form a matrix. Note that I could also have chosen another basis, like the coherent states. To give a concrete example, let us refer to the density matrix of a thermal state (see Table 2.6). It is common to visualise the density matrix as a two-dimensional bar-graph plot, but an alternative is to highlight the structure of the matrix, as has been done in Figure 2.6. Note that the thermal state contains only diagonal elements. These correspond to the probabilities (or populations) of detecting the particular Fock state. Compare this with a pure coherent state, which has off-diagonal elements that can be interpreted as fixed phase relationship (or coherence) between the Fock states. The elements of the matrix were extracted from Table 2.3, by taking the product of the coefficients c_n of the Fock state expansion such that $c_n c_{n'}^* |n\rangle\langle n'|$. Some important properties of the density operator are the normalisation condition $\mathrm{Trace}\{\hat{\rho}\} = 1$, and the purity condition $\hat{\rho}^2 = \hat{\rho}$. The latter can be proved simply

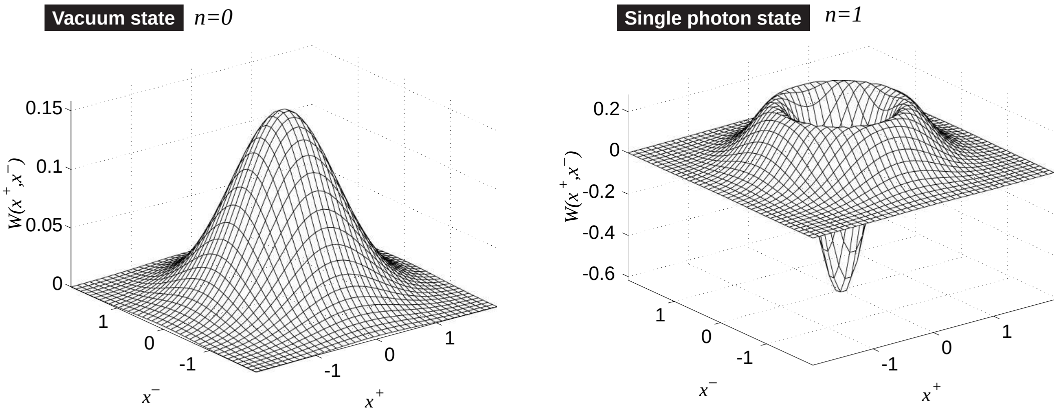

Figure 2.7: The Wigner functions of the vacuum state and single photon states are compared. Although being a member of the Fock state basis, the vacuum state differs from all other Fock states, in that its Wigner function is positive definite.

from the definition of a pure state $\hat{\rho}^2 = |R\rangle\langle R||R\rangle\langle R| = |R\rangle(1)\langle R| = \hat{\rho}$. Note that the purity condition does not give us a criterion for witnessing nonclassical states of light. For example, there exist states that are mixed, but still exhibit sub-Poissonian photon statistics, or quadrature squeezed light. A weakly phase-diffused, displaced-squeezed state can fulfil all of these conditions. The density operator contains all the information to describe pure and mixed states, but it is not a convenient tool for identifying nonclassical states of light.

2.4.4 The Wigner function: (negativity)

The density matrix can be converted into the Wigner function, which is a two-dimensional quasi-probability distribution over the quadrature observables. Like the density operator, the Wigner function contains all the information about the state of light, however, it is presented in a way that is more intuitive. The Wigner function in a sense fills in the shaded ellipse of the ball-on-stick diagram of quadrature statistics. It also reveals another nonclassical property of light: negativity of the Wigner function.

The definition of the Wigner function is not obvious at first glance,

$$W(x^+, x^-) = \frac{1}{\pi}\int_{-\infty}^{+\infty} \mathrm{d}z\ \exp(\mathrm{i}zx^-)\Big\langle x^+ - \frac{z}{4}\Big|\hat{\rho}\Big|x^+ + \frac{z}{4}\Big\rangle \tag{2.61}$$

nor at the second glance. More details about the origin of this equation and its setting in quantum optics can be found in the textbook of [Leonhardt 1997]. Nevertheless, I will attempt a brief discussion of the definition. Firstly, the density operator is evaluated over the eigenstates of the quadrature operators. These are defined by $\hat{X}^+|X^+\rangle = X^+|X^+\rangle$. The eigenstates are chosen as a pair that have a symmetric offset that is prescribed by the arbitrary variable z. The result is a function of z and x^+. If we consider that the phase-space variables (x^+ and x^-) are held fixed, then the integration performs a Fourier transform of the function in terms of z, into the space of x^-. Finally, the function is mapped out in terms of the variable x^+ to obtain a two-dimensional function.

The feature of the Wigner function, is that the marginalised distribution across one variable, say x^+, will return the probability distribution of measurements that are made in the corresponding quadrature basis ($\hat{X}^+$). This also works for any rotated quadrature basis. Like a traditional joint probability distribution, the Wigner function is normalised, as the integral over x^+ and x^- is equal to one. However, unlike a traditional joint probability distribution, the Wigner function has the freedom to become negative, even for Hermitian density operators. There is no problem in this, because an observer is only capable of (competently) measuring one quadrature of the light field at a time, and the marginalised distribution is guaranteed to be positive definite.

The Fock states beyond $n = 0$ turn out to have impressive looking Wigner functions. For example, the $n = 1$ Fock state has a Wigner function [Walls and Milburn 1994]:

$$W(x^+, x^-) = \frac{2}{\pi}(-1)^n L_n(4(x^+)^2 + 4(x^-)^2)\exp(-8(x^+)^2 - 8(x^-)^2) \tag{2.62}$$

where L_n are the Laguerre polynomials. This function is plotted for the case $|n = 1\rangle$, in Figure 2.7. The single photon Fock has a minimum at the origin of the phase space coordinates, of $W(0,0) = -2/\pi$. This is the smallest value possible for the Wigner function, and it clearly demonstrates the negativity possible in the Wigner function representation. The Wigner function of the vacuum state $|n = 0\rangle$ (which is also a zero amplitude coherent state), is shown in Figure 2.7. The function is Gaussian and so there is no negativity. However, here we can see that the contour of this function taken at the level $W = 1$, is concomitant to the ellipse of the ball-on-stick diagram of a coherent state in Figure 2.4. Indeed this is the more rigourous definition of the ellipse in the ball-on-stick diagram, and this applies for arbitrary states too.

The semi-classical theory can only describe pure coherent states, or mixtures of coherent states. These mixed states can never show negativity in the Wigner function. Negativity in the Wigner function is therefore a witness to nonclassical light. Because the Wigner function is highly analogous to a classical phase-space probability distribution, finding negativity in the ‘probability’ is quite a counterintuitive result.

I would also like to highlight the distinction between Gaussian and non-Gaussian states. This is most easily seen in the Wigner function. If the Wigner function has the form of two-dimensional Gaussian distribution, then the state is considered to be Gaussian. Any other form is considered non-Gaussian. Note that a Wigner function that shows negativity (and hence is a non-classical state) cannot possibly be a convolution over a set made up of only Gaussian states, and so such a state is necessarily non-Gaussian. But a state that is non-Gaussian does not necessarily need to have negativity, and hence is not guaranteed to be non-classical.

2.4.5 Second-order coherence: (photon anti-bunching)

I will reserve a full discussion of second-order coherence and the photon anti-bunching concept until Chapter 7. However, for completeness, I would like to introduce it at an earlier stage, and also motivate it from a slightly different perspective [Loudon 2000]. The question is: if I consider a single-mode state of the EM field, and extract one photon of energy from that mode, how ‘likely’ is it that I will be able to extract a second photon directly after the first one? The answer could perhaps be written down in the following way $\langle\psi|\hat{a}^\dagger\hat{a}^\dagger\hat{a}\hat{a}|\psi\rangle$, where two photons are first removed, and then restored. We can express this in terms of number operators, use the Boson commutation relation, and normalise the result to get

$$g^{(2)}(0) = \frac{\langle\hat{a}^\dagger\hat{a}^\dagger\hat{a}\hat{a}\rangle}{\langle\hat{a}^\dagger\hat{a}\rangle^2} \tag{2.63}$$

$$= \frac{\langle\hat{n}(\hat{n}-1)\rangle}{\langle\hat{n}\rangle^2} \tag{2.64}$$

$$= 1 + \frac{\sigma^2(\hat{n}) - \mu(\hat{n})}{\mu(\hat{n})^2} \tag{2.65}$$

where $g^{(2)}(0)$ is called the *degree of second-order coherence*. From Equation 2.64, we can deduce that a value of $g^{(2)}(0) = 0$ is consistent with a zero probability that two photons will be detected. We can interpret this as the tendency for photons to be detected one at a time (anti-bunched), rather than being detected together in groups (bunched). The criterion of $g^{(2)}(0) < 1$ becomes the definition of anti-bunched photon statistics.

We can look at this result from another perspective. In Equation 2.65, we can identify the criterion for sub-/super-Poissonian statistics. Therefore when the state has exactly a Poissonian photon number distribution, the second-order coherence function is at the boundary between bunching and anti-bunching (the state is then said to be second-order coherent). Furthermore, all sub-Poissonian states will fulfil the anti-bunching criterion. So in the discussion of non-classical light that follows, I will include photon anti-bunched states under the same umbrella as sub-Poissonian states of light.

2.4.6 Summary of criteria for non-classical light

In the last section I have shown a few different ways that states of light can be viewed in, and also a handful of criteria that can identify non-classical states of light. I have summarised these criteria in Table 2.7. Note that there exist states of light that can fulfil any logic combination of these criteria. Each criterion is sufficient to witness nonclassical light, but they are not necessary, i.e. there may exist other criteria of non-classicality that can identify non-classical light. Let me introduce abbreviations for the criteria: sub-Poissonian (P), quadrature squeezed (Q), and Wigner function negativity (W). An example of a state of light that fulfils the criteria (P&Q) is the displaced-squeezed state shown in Figure 2.3 where $|\alpha = 2.3, \zeta = 0.5\rangle$. A single photon state easily fulfils the condition (W), however applying squeezing operation to it would also satisfy (W&Q). An appropriate displacement operation applied to this state can then satisfy (W&Q&P). The definitions and properties of displaced squeezed single-photon states can be found in [Nieto 1997].

2.5 From discrete to continuous modes

The previous analysis of states of light was restricted to the case of a single mode of an ideal optical cavity (a closed system). This does not correspond to the type of experimental

Sub-Poissonian:	$\sigma^2(\hat{n}) - \mu(\hat{n})$	$<$	0
Quadrature squeezed :	$\{\sigma^2(\hat{X}^{\phi})\}_{\min(\phi)}$	$<$	1
Wigner function negativity:	$\{W(x^+, x^-)\}_{\min(x^+, x^-)}$	$<$	0

Table 2.7: A summary of criteria that will identify non-classical states of light. Note that all the criteria shown here are sufficient but not necessary criteria for non-classical light.

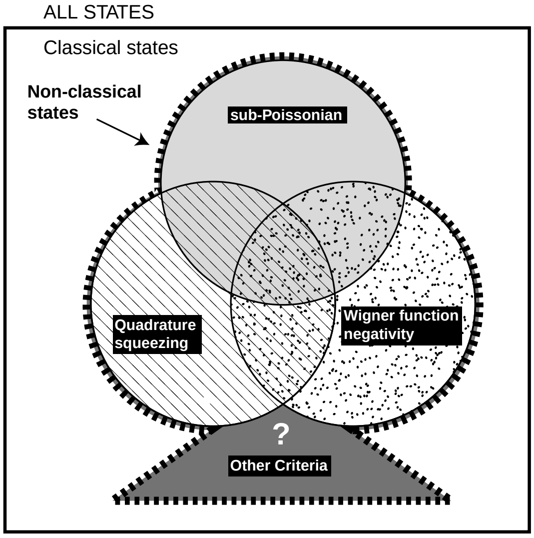

Figure 2.8: A Venn-type diagram of a selection of criteria for identifying nonclassical states of light. There exist states of light that occupy each overlap region, and also the multiple overlap regions. Note that other criteria of nonclassical light can still exist.

situation where laser beams freely propagate from source to detector. Although the closed system can be approached in experiments of cavity quantum electrodynamics (CQED), the experiments that I present in this thesis dealt with open systems. The consequence of opening the system, is that the modes become ever more closely spaced in frequency ω_k, such that it becomes necessary to describe a continuum of modes.

2.5.1 Continuum of modes

The spacing in frequency between neighbouring modes is given by $\Delta\omega = 2\pi c/L$, which depends on the length of the cavity (L) that was used in the quantisation procedure. As the length of the cavity is increased, the mode spacing will shrink to zero, and the electric field operator, which is a discrete sum over all modes, will become an integral $\sum_k \rightarrow \frac{1}{\Delta\omega}\int \mathrm{d}\omega$. The transverse spatial extent of the mode still has a finite area A. But some other properties change, like the Kronecker delta becoming a Dirac delta function, $\delta_{k,k'} \rightarrow \Delta\omega\delta(\omega-\omega')$. Note that the scaling of the delta function is important. We consider the case of waves propagating in only one direction, say along the z-axis, and having only the one polarisation. So the vector $\mathbf{k}$ just becomes the scalar k. We also restrict ourselves to the case of only positive frequency ω, i.e. for waves propagating in the positive z-axis direction.

As a consequence, the creation and annihilation operators become $\hat{a}_k \rightarrow \sqrt{\Delta\omega}\,\hat{a}(\omega)$ and $\hat{a}_k^\dagger \rightarrow \sqrt{\Delta\omega}\,\hat{a}^\dagger(\omega)$. This gives the new, but familiar looking commutation relation $[\hat{a}(\omega), \hat{a}^\dagger(\omega)] = \delta(\omega-\omega')$. With these new definitions, the electric field operator from Equation 2.39 becomes

$$\hat{E}^{(+)}(z,t) = +\mathrm{i}\int_0^\infty \mathrm{d}\omega \left(\frac{\hbar\omega}{4\pi\varepsilon_0 cA}\right)^{1/2} \hat{a}(\omega)\,\exp[-\mathrm{i}\omega(t-\frac{z}{c})] \qquad (2.66)$$

$$\hat{E}^{(-)}(z,t) = -\mathrm{i}\int_0^\infty \mathrm{d}\omega \left(\frac{\hbar\omega}{4\pi\varepsilon_0 cA}\right)^{1/2} \hat{a}^\dagger(\omega)\,\exp[+\mathrm{i}\omega(t-\frac{z}{c})] \qquad (2.67)$$

Note that the frequency spacing terms $\Delta\omega$ have cancelled, and that the cavity volume V has been replaced by transverse area A, by using $V = LA$.

2.5.2 Fourier transformed operators

One then makes a narrow-band assumption, where any excitation of the field is limited to small spread in frequency around the centre frequency ω_0. This is assumption valid for a laser sources, or atomic transitions that have narrow linewidths. As a consequence the integration range can then be extended without any harm, to include negative frequency, and the variable ω can be taken outside the integral as a constant ω_0 to give

$$\begin{aligned}\hat{E}^{(+)}(z,t) &= +\mathrm{i}\Big(\frac{\hbar\omega_0}{4\pi\varepsilon_0 cA}\Big)^{1/2}\int_{-\infty}^{\infty}\mathrm{d}\omega\,\hat{a}(\omega)\,\exp[-\mathrm{i}\omega(t-\frac{z}{c})] && (2.68)\\ \hat{E}^{(-)}(z,t) &= -\mathrm{i}\Big(\frac{\hbar\omega_0}{4\pi\varepsilon_0 cA}\Big)^{1/2}\int_{-\infty}^{\infty}\mathrm{d}\omega\,\hat{a}^\dagger(\omega)\,\exp[+\mathrm{i}\omega(t-\frac{z}{c})] && (2.69)\end{aligned}$$

These integrals are essentially performing a Fourier transformation to the creation annihilation operators. This motivates the definition of the time-domain operators. Note that they have been defined to be consistent with $\hat{a}^\dagger(t) = [\hat{a}(t)]^\dagger$, hence:

$$\begin{aligned}\hat{a}(t) &= \frac{1}{2\pi}\int_{-\infty}^{\infty}\mathrm{d}\omega\,\hat{a}(\omega)\,\exp(-\mathrm{i}\omega t) && (2.70)\\ \hat{a}^\dagger(t) &= \frac{1}{2\pi}\int_{-\infty}^{\infty}\mathrm{d}\omega\,\hat{a}^\dagger(\omega)\,\exp(+\mathrm{i}\omega t) && (2.71)\end{aligned}$$

where the propagation term will from now on be suppressed by letting $z = \pi c/2\omega$. The inverse Fourier transform of the operators is then defined as

$$\begin{aligned}\hat{a}(\omega) &= \int_{-\infty}^{\infty}\mathrm{d}t\,\hat{a}(t)\,\exp(+\mathrm{i}\omega t) && (2.72)\\ \hat{a}^\dagger(\omega) &= \int_{-\infty}^{\infty}\mathrm{d}t\,\hat{a}^\dagger(t)\,\exp(-\mathrm{i}\omega t) && (2.73)\end{aligned}$$

Using these definitions we get the time-domain electric field operator for positive and negative frequencies

$$\hat{E}^{(+)}(t) = \Big(\frac{\pi\hbar\omega_0}{\varepsilon_0 cA}\Big)^{1/2}\hat{a}(t) \quad , \quad \hat{E}^{(-)}(t) = \Big(\frac{\pi\hbar\omega_0}{\varepsilon_0 cA}\Big)^{1/2}\hat{a}^\dagger(t) \qquad (2.74)$$

Which add up to give the total electric field operator $\hat{E} = \hat{E}^{(+)} + \hat{E}^{(-)}$. Although the main result looks trivial, it appears as if I have just replaced the $\hat{a}(\omega)$ with $\hat{a}(t)$, but note that these definitions only apply for the case of a narrowband excitation of the EM field, and/or a narrowband photodetector.

2.6 Direct detection and the sideband picture

What does a photodiode measure? What part of the electromagnetic field does this correspond to? It turns out that there are two answers which depend to a large extent on the type of detector and the source of light that is used. At this point the discipline of quantum optics divides into two areas: discrete-variable (DV) and continuous-variable (CV) quantum optics. I will concentrate on CV quantum optics, because it applies to the experiments that I present in this thesis.

2.6.1 The two-mode formalism

The total electric field is the integral over the continuum of positive and negative propagating solutions of the EM field; see Equation 2.74. But this will not result in an intuitive interpretation of CV measurements. Such measurements are sensitive to modulations of the intensity (or amplitude) of the light, so it makes sense to analyse the electric field operator in terms of upper and lower sidebands [Caves and Schumaker 1985]. I will choose to perform the integral over pairs of modes that spaced around a central optical frequency, the *carrier*, at ω_0. Then we have the *upper sideband* mode at a frequency of $\omega_0 + \Omega$, while the *lower sideband* mode has a frequency of $\omega_0 - \Omega$. Using this new formalism, the total electric field becomes

$$\begin{aligned}
\hat{E}(t) \;=\; & \left(\frac{\hbar\omega_0}{4\pi\epsilon_0 c A}\right)^{1/2} \int_{\Omega_{\min}}^{\Omega_{\max}} \mathrm{d}\Omega \\
& \times\Bigg\{ \mathrm{i}\left(\frac{\omega_0-\Omega}{\omega_0}\right)^{1/2} \hat{a}(\omega_0-\Omega)\mathrm{e}^{-\mathrm{i}(\omega_0-\Omega)t} \\
& +\mathrm{i}\left(\frac{\omega_0+\Omega}{\omega_0}\right)^{1/2} \hat{a}(\omega_0+\Omega)\mathrm{e}^{-\mathrm{i}(\omega_0+\Omega)t} \\
& -\mathrm{i}\left(\frac{\omega_0-\Omega}{\omega_0}\right)^{1/2} \hat{a}^\dagger(\omega_0-\Omega)\mathrm{e}^{+\mathrm{i}(\omega_0-\Omega)t} \\
& -\mathrm{i}\left(\frac{\omega_0+\Omega}{\omega_0}\right)^{1/2} \hat{a}^\dagger(\omega_0+\Omega)\mathrm{e}^{+\mathrm{i}(\omega_0+\Omega)t} \Bigg\}
\end{aligned} \tag{2.75}$$

Fundamentally nothing has changed. It is only the way that the modes are now ‘counted’ that has changed. Note also, that I have not specified a range for the integration, other that $\Omega_{\max}, \Omega_{\min}$. There is of course a problem with double counting when $\Omega_{\min} = 0$, but for the moment lets keep it non-specific. In a typical quantum optics experiment, one often encounters values like $\omega_0 \approx 10^{15}$ Hz and up to $\Omega \approx 10^9$ Hz. So we can safely assume that $\Omega \ll \omega_0$, and hence that the $(\omega_0 - \Omega)/\omega_0$ scaling terms that appear in the equation above, can be assumed to equal one. This simplifies the expression enormously:

$$\begin{aligned}\hat{E}(t) &= \left(\frac{\hbar\omega_0}{4\pi\epsilon_0 cA}\right)^{1/2} \int_{\Omega_{\min}}^{\Omega_{\max}} \mathrm{d}\Omega \\ &\quad\times\Big\{ + \mathrm{i}\hat{a}(\omega_0 - \Omega)\mathrm{e}^{-\mathrm{i}(\omega_0-\Omega)t} + \mathrm{i}\hat{a}(\omega_0 + \Omega)\mathrm{e}^{-\mathrm{i}(\omega_0+\Omega)t} \\ &\quad -\mathrm{i}\hat{a}^\dagger(\omega_0 - \Omega)\mathrm{e}^{+\mathrm{i}(\omega_0-\Omega)t} - \mathrm{i}\hat{a}^\dagger(\omega_0 + \Omega)\mathrm{e}^{+\mathrm{i}(\omega_0+\Omega)t}\Big\} \qquad (2.76)\end{aligned}$$

The aim is now to simplify this expression further. The complex exponentials can be expanded into cosine and sine terms. The resulting arrangement of creation and annihilation operators then seem to naturally collect themselves into a set of four Hermitian operators to give

$$\begin{aligned}\hat{E}(t) &= \left(\frac{\hbar\omega_0}{4\pi\epsilon_0 cA}\right)^{1/2} \int_{\Omega_{\min}}^{\Omega_{\max}} \mathrm{d}\Omega \\ &\quad\times\Big\{ \sin(\omega_0 t)\Big[\cos(\Omega t)\hat{X}_c^+(\Omega) + \sin(\Omega t)\hat{X}_s^+(\Omega)\Big] \\ &\quad + \cos(\omega_0 t)\Big[\cos(\Omega t)\hat{X}_c^-(\Omega) + \sin(\Omega t)\hat{X}_s^-(\Omega)\Big]\Big\} \qquad (2.77)\end{aligned}$$

where the newly introduced *two-mode quadrature operators* have been defined as

$$\hat{X}_c^+(\Omega) := +\hat{X}^+(\omega_0 - \Omega) + \hat{X}^+(\omega_0 + \Omega) \qquad (2.78)$$

$$\hat{X}_s^+(\Omega) := -\hat{X}^-(\omega_0 - \Omega) + \hat{X}^-(\omega_0 + \Omega) \qquad (2.79)$$

$$\hat{X}_c^-(\Omega) := -\hat{X}^-(\omega_0 - \Omega) - \hat{X}^-(\omega_0 + \Omega) \qquad (2.80)$$

$$\hat{X}_s^-(\Omega) := -\hat{X}^+(\omega_0 - \Omega) + \hat{X}^+(\omega_0 + \Omega) \qquad (2.81)$$

and the *single-mode quadrature operators* a given by their usual definitions

$$\hat{X}^+(\omega_0 - \Omega) = \hat{a}^\dagger(\omega_0 - \Omega) + \hat{a}(\omega_0 - \Omega) \qquad (2.82)$$

$$\hat{X}^-(\omega_0 - \Omega) = \mathrm{i}\hat{a}^\dagger(\omega_0 - \Omega) - \mathrm{i}\hat{a}(\omega_0 - \Omega) \qquad (2.83)$$

$$\hat{X}^+(\omega_0 + \Omega) = \hat{a}^\dagger(\omega_0 + \Omega) + \hat{a}(\omega_0 + \Omega) \qquad (2.84)$$

$$\hat{X}^-(\omega_0 + \Omega) = \mathrm{i}\hat{a}^\dagger(\omega_0 + \Omega) - \mathrm{i}\hat{a}(\omega_0 + \Omega) \qquad (2.85)$$

Although not obvious at the moment, the set of two-mode quadrature operators describe amplitude and phase modulations at radio frequencies Ω of the oscillation at the optical carrier frequency ω_0. The superscript and subscript labels that I gave these operators is arbitrary, but in the next section we will see that $\hat{X}_c^+$ and $\hat{X}_s^+$ appear as modulations of the amplitude of the light as it would be measured on a photodiode. They correspond to two independent 'channels' of amplitude modulation on the light beam: the sine and cosine channels. The following commutation relations make this clear

$$\left[\hat{X}_c^+, \hat{X}_s^+\right] = \left[\hat{X}_c^+, \hat{X}_s^-\right] = \left[\hat{X}_c^-, \hat{X}_s^+\right] = \left[\hat{X}_c^-, \hat{X}_s^-\right] = 0 \tag{2.86}$$

which is independent of the choice of Ω. Within each channel, there are two non-commuting observables

$$\left[\hat{X}_c^+(\Omega), \hat{X}_c^-(\Omega')\right] = \left[\hat{X}_s^+(\Omega), \hat{X}_s^-(\Omega')\right] = 4\mathrm{i}\ \delta(\Omega - \Omega') \tag{2.87}$$

where $\delta(\Omega - \Omega' = 0) = 1$ and $\delta(\Omega - \Omega' \neq 0) = 0$. Each pair of incompatible observables then obeys the following uncertainty relations

$$\sigma^2\left(\hat{X}_c^+(\Omega)\right)\ \sigma^2\left(\hat{X}_c^-(\Omega')\right) \quad \geq \quad 4\ \delta(\Omega - \Omega') \tag{2.88}$$

$$\sigma^2\left(\hat{X}_s^+(\Omega')\right)\ \sigma^2\left(\hat{X}_s^-(\Omega')\right) \quad \geq \quad 4\ \delta(\Omega - \Omega') \tag{2.89}$$

Where the variance of an operator $\sigma^2(\hat{O})$ is defined in Table 2.1. The uncertainty product for the two-mode quadrature operators has a value of 4, which can be compared with a value of 1 for the single-mode quadrature operators.

2.6.2 Direct detection: Poynting vector

We have seen a representation of the electric field in a two-mode sideband formalism, but I want to make the connection with what a photodiode measures. The following derivation seems unusually long. This is because I wanted to clearly show the approximations (a strong and narrow-band excitation), that are needed to make the problem tractable. The rate of photo-ionisation of an atom is proportional to the Poynting vector operator of the light that the atom is being exposed to [Loudon 2000]. The Poynting vector is equal to the rate of energy per unit area that flows through a fixed plane. I begin the analysis in the single-mode formalism, before later changing to the two-mode formalism. In the continuum of single-modes, the Poynting vector operator becomes a double integral over the absolute frequencies ω and ω'. The negative and positive electric field operators from Equation 2.67 need to be written down in normal order, so that the Poynting vector operator becomes

$$\begin{align}
\hat{I}(t) &= 2\epsilon_0 c \hat{E}^{(-)}(t)\, \hat{E}^{(+)}(t) \tag{2.90}\\
&= \left(\frac{\hbar}{2\pi A}\right) \int_0^\infty \int_0^\infty \mathrm{d}\omega\, \mathrm{d}\omega'\, \sqrt{\omega\omega'}\, \hat{a}^\dagger(\omega)\, \hat{a}(\omega')\, \mathrm{e}^{\mathrm{i}(\omega-\omega')t} \tag{2.91}
\end{align}$$

The double integral cannot be simplified any further until I make an assumption about the excitation of the EM field. I would like to calculate what happens when a source of monochromatic laser light is incident on the detector. To simulate this situation, one can apply the displacement operator at the frequency ω_0 which establishes the carrier with a coherent amplitude α_0. In the Heisenberg picture this then transforms the creation and annihilation operators such that: $\hat{D}^\dagger \hat{a}(\omega) \hat{D} = \hat{a}(\omega) + \alpha_0\, \delta(\omega - \omega_0)$; $\hat{D}^\dagger \hat{a}^\dagger(\omega) \hat{D} = \hat{a}^\dagger(\omega) + \alpha_0^*\, \delta(\omega - \omega_0)$. For this discussion we set $\alpha_0^* = \alpha_0$. The displacement only applies to the frequency ω_0, which is the reason for introducing the delta function. The displacement transformation is then applied to the Poynting vector operator such that

$$\begin{align}
\hat{I}_\alpha(t) &= \hat{D}^\dagger(\alpha_0)\, \hat{I}(t)\, \hat{D}(\alpha_0) \tag{2.92}\\
&= \left(\frac{\hbar}{2\pi A}\right) \int_0^\infty \int_0^\infty \mathrm{d}\omega\, \mathrm{d}\omega'\, \sqrt{\omega\omega'}\, \mathrm{e}^{\mathrm{i}(\omega-\omega')t} \nonumber\\
&\quad \times \Big\{ \hat{a}^\dagger(\omega)\hat{a}(\omega') + \alpha_0^2\, \delta(\omega - \omega_0)\, \delta(\omega' - \omega_0) \nonumber\\
&\qquad \alpha_0\, \hat{a}^\dagger(\omega)\, \delta(\omega' - \omega_0) + \alpha_0\, \hat{a}(\omega')\, \delta(\omega - \omega_0) \Big\} \tag{2.93}
\end{align}$$

The double integral can be reduced to a single integral if we make the following assumption. Any terms in the integral that are not scaled by α_0 will not contribute significantly to the integral, and can therefore be neglected. The term that I will neglect is $\hat{a}^\dagger(\omega)\hat{a}(\omega')$. Since we have the freedom to choose the strength of the carrier by varying α_0, we can always enforce the validity of neglecting the cross-frequency terms. This is exactly the same as in classical optics where the sidebands ‘beat’ with the carrier to produce amplitude and phase modulations, whereas the beats between different sidebands are negligible. While keeping the approximation in mind, the expression for the Poynting vector can be broken up, and the integral over ω' can be evaluated such that

$$\begin{aligned}\hat{I}_\alpha(t) \;=\; & \left(\frac{\hbar\sqrt{\omega_0}}{2\pi A}\right)\left\{\alpha_0^2\int_0^\infty \mathrm{d}\omega\,\sqrt{\omega}\,\mathrm{e}^{+\mathrm{i}(\omega-\omega_0)t}\,\delta(\omega-\omega_0)\right.\\ & \left.+\alpha_0\int_0^\infty \mathrm{d}\omega\,\sqrt{\omega}\Big[\mathrm{e}^{+\mathrm{i}(\omega-\omega_0)t}\,\hat{a}^\dagger(\omega)+\mathrm{e}^{-\mathrm{i}(\omega-\omega_0)t}\,\hat{a}(\omega)\Big]\right\}\end{aligned}\tag{2.94}$$

The next step is to change the frequency variable such that $\omega = \omega_0 + \Omega$, where Ω is the sideband frequency relative to the carrier.

$$\begin{aligned}\hat{I}_\alpha(t) \;=\; & \left(\frac{\hbar\sqrt{\omega_0}}{2\pi A}\right)\left\{\alpha_0^2\int_{-\omega_0}^\infty \mathrm{d}\Omega\,\sqrt{\omega_0+\Omega}\,\mathrm{e}^{+\mathrm{i}\Omega t}\,\delta(\Omega-0)\right.\\ & \left.+\alpha_0\int_{-\omega_0}^\infty \mathrm{d}\Omega\,\sqrt{\omega_0+\Omega}\Big[\mathrm{e}^{+\mathrm{i}\Omega t}\,\hat{a}^\dagger(\omega_0+\Omega)+\mathrm{e}^{-\mathrm{i}\Omega t}\,\hat{a}(\omega_0+\Omega)\Big]\right\}\end{aligned}\tag{2.95}$$

The limits of the integration are then reduced from the half infinite plane, to covering just a small bandwidth B that extends above and below that carrier. The exact value of the bandwidth would depend on the type of detector, or in abstract terms, on the linewidth of the photo-ionisation process. However, we can assume that $B \ll \omega_0$. This ensures that we can make the approximation $\sqrt{\omega_0+\Omega} \approx \sqrt{\omega_0}$. The first integral can then be evaluated, thus leaving,

$$\hat{I}_\alpha(t) \;=\; \frac{\hbar\omega_0}{A}\left\{\alpha_0^2+\frac{\alpha_0}{2\pi}\int_{-B}^{+B}\mathrm{d}\Omega\Big[\mathrm{e}^{+\mathrm{i}\Omega t}\hat{a}^\dagger(\omega_0{+}\Omega)+\mathrm{e}^{-\mathrm{i}\Omega t}\hat{a}(\omega_0{+}\Omega)\Big]\right\}\tag{2.96}$$

This equation tells us that the detector is responsive to the constant photon flux $(\hbar\omega_0\alpha_0^2/A)$ from the coherent excitation at the carrier frequency, plus the contribution from the sideband quadrature amplitudes that are scaled by amplitude of the carrier. But to complete the measurement process, we need to define a time window over which the measurements takes place. This also determines what sideband frequencies will appear in the measurement. One way to implement this is to multiply the Poynting operator with a time window function and then integrate this over all time. I will consider two different window functions: one function $T_{\mathrm{DC}}(t)$ for measuring the steady-state intensity, and another function $T_{\mathrm{AC}}(t)$ for analysing fluctuations of the intensity at a specific frequency Ω_0. The measurement bandwidth is in both cases $\Delta\Omega$, which must be kept smaller than the detector bandwidth B.

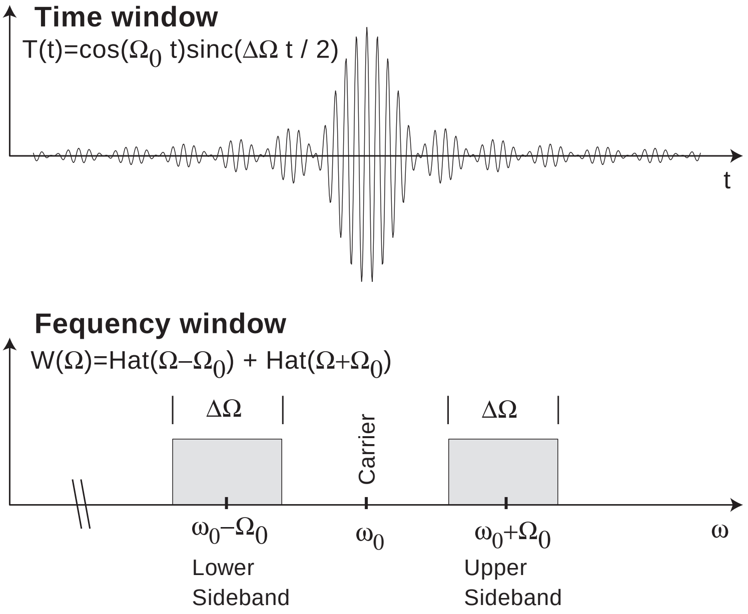

Figure 2.9: A method of getting into the sideband picture. In the time domain, one can choose to multiply the photocurrent by the cosine-sinc function. The resulting frequency window in the Fourier domain is a hat function on either side of the optical carrier ω_0, which corresponds to the two-mode sideband formalism.

The window functions are defined as

$$T_{\mathrm{DC}}(t) = \sin(\frac{1}{2}\Delta\Omega\, t)\Big/(\frac{1}{2}\Delta\Omega\, t) \tag{2.97}$$

$$T_{\mathrm{AC}}(t) = \cos(\Omega_0 t)\, \sin(\frac{1}{2}\Delta\Omega\, t)\Big/(\frac{1}{2}\Delta\Omega\, t) \tag{2.98}$$

The choice of these particular functions enables us to later get sharply defined frequency filters, which have been visualised in Figure 2.9. The Fourier transform of the time window functions, gives the corresponding frequency window functions:

$$W_{\mathrm{DC}}(\Omega) = \frac{2\pi}{\Delta\Omega}\begin{cases} 1 & , \quad (-\frac{1}{2}\Delta\Omega) < \Omega < (+\frac{1}{2}\Delta\Omega) \\ 0 & , \quad \text{elsewhere} \end{cases}$$

and

$$W_{\mathrm{AC}}(\Omega) = \frac{2\pi^2}{\Delta\Omega}\begin{cases} 1 & , \quad (-\Omega_0 - \frac{1}{2}\Delta\Omega) < \Omega < (-\Omega_0 + \frac{1}{2}\Delta\Omega) \\ 1 & , \quad (+\Omega_0 - \frac{1}{2}\Delta\Omega) < \Omega < (+\Omega_0 + \frac{1}{2}\Delta\Omega) \\ 0 & , \quad \text{elsewhere} \end{cases}$$

Note that for this to hold true we require that $\frac{1}{2}\Delta\Omega < \Omega_0$. Let us apply the T_{DC} window to the Poynting vector operator from Equation 2.96 and integrate over all time. This allows us to get the energy $\hat{\mathcal{E}}_{\mathrm{DC}}$ collected during the measurement window, therefore,

$$\begin{aligned}
\hat{\mathcal{E}}_{\mathrm{DC}} &= A\int_{-\infty}^{+\infty}\mathrm{d}t\, T_{\mathrm{DC}}(t)\,\hat{I}_\alpha(t) \\
&= \hbar\omega_0\alpha_0^2\Big(\frac{2\pi}{\Delta\Omega}\Big) + \frac{\hbar\omega_0\alpha_0}{2\pi}\int_{-B}^{+B}\mathrm{d}\Omega\,\Big\{\hat{a}^\dagger(\omega_0{+}\Omega)\int_{-\infty}^{+\infty}\mathrm{d}t\,T_{\mathrm{DC}}(t)\,\mathrm{e}^{+\mathrm{i}\Omega t} \\
&\quad +\hat{a}(\omega_0{+}\Omega)\int_{-\infty}^{+\infty}\mathrm{d}t\,T_{\mathrm{DC}}(t)\,\mathrm{e}^{-\mathrm{i}\Omega t}\Big\} \\
&= \hbar\omega_0\alpha_0^2\Big(\frac{2\pi}{\Delta\Omega}\Big) + \frac{\hbar\omega_0\alpha_0}{2\pi}\int_{-B}^{+B}\mathrm{d}\Omega\, W_{\mathrm{DC}}(\Omega)\Big\{\hat{a}^\dagger(\omega_0{+}\Omega) + \hat{a}(\omega_0{+}\Omega)\Big\} \\
&= \hbar\omega_0\alpha_0^2\Big(\frac{2\pi}{\Delta\Omega}\Big) + \frac{\hbar\omega_0\alpha_0}{\Delta\Omega}\int_{-\frac{1}{2}\Delta\Omega}^{+\frac{1}{2}\Delta\Omega}\mathrm{d}\Omega\,\hat{X}^+(\omega_0+\Omega) \qquad (2.99)
\end{aligned}$$

We can identify a characteristic time that corresponds to the duration of the time window, given by $\Delta t = 2\pi/\Delta\Omega$, which comes from the integral over all time of $T_{\mathrm{DC}}(t)$. With the time duration identified, we can then define the rate of energy collected, or power $\hat{P}_{\mathrm{DC}}$, that was detected

$$\begin{aligned}
\hat{P}_{\mathrm{DC}} &= \hbar\omega_0\alpha_0^2 + \frac{\hbar\omega_0\alpha_0}{2\pi}\int_{-\frac{\pi}{\Delta t}}^{+\frac{\pi}{\Delta t}}\mathrm{d}\Omega\,\hat{X}^+(\omega_0+\Omega) \qquad (2.100) \\
&= \hbar\omega_0\alpha_0^2\text{ , when } \Delta t \to \infty \qquad (2.101)
\end{aligned}$$

If we then keep extending the length of the time window to get a better average value, then range of the integral shrinks. Note that there is no anomalous result at $\Omega = 0$ because we are working in the Heisenberg picture, and the coherent state for the carrier was made by transforming the operator, not the state. So if I were to calculate the expectation value of the $\hat{P}_{\mathrm{DC}}$ operator, I would use a vacuum state for the $\Omega = 0$ mode (which would return a value of zero for the $\hat{X}^+$ operator). The main result is that in the limit of $\Delta t \to \infty$ we have $\hat{P}_{\mathrm{DC}} = \hbar\omega_0\alpha_0^2$. We can turn the argument on its head, and deduce that α_0^2 is in units of the mean number of photons per unit time. In SI units where $\hbar\omega_0$ is in Joules, the units of α_0^2 are in number per second $[\mathrm{s}^{-1}]$.

The procedure is similar for measurements that are made at the sideband frequencies that are centred at Ω_0. The idea of multiplying the Poynting operator with a temporal window function that looks like $T_{\mathrm{AC}}(t)$ is exactly the same as the experimental technique of demodulating an electronic signal, by multiplication with a reference frequency (an electronic local oscillator). I give the time window an additional freedom, which is the ability to be delayed by an amount t_0. Starting with Equation 2.96, the operator for energy collected by the detector becomes

$$\begin{aligned}
\hat{\mathcal{E}}_{\mathrm{AC}} &= A\int_{-\infty}^{+\infty}\mathrm{d}t\,T_{\mathrm{AC}}(t-t_0)\,\hat{I}_\alpha(t)\\
&= \frac{\hbar\omega_0\alpha_0}{2\pi}\int_{-B}^{+B}\mathrm{d}\Omega\left\{\hat{a}^\dagger(\omega_0+\Omega)\int_{-\infty}^{+\infty}\mathrm{d}t\,T_{\mathrm{AC}}(t-t_0)\,\mathrm{e}^{+\mathrm{i}\Omega t}\right.\\
&\qquad\left.+\hat{a}(\omega_0+\Omega)\int_{-\infty}^{+\infty}\mathrm{d}t\,T_{\mathrm{AC}}(t-t_0)\,\mathrm{e}^{-\mathrm{i}\Omega t}\right\}\\
&= \frac{\hbar\omega_0\alpha_0}{2\pi}\int_{-B}^{+B}\mathrm{d}\Omega\,W_{\mathrm{AC}}(\Omega)\\
&\qquad\times\left\{\mathrm{e}^{+\mathrm{i}\Omega t_0}\hat{a}^\dagger(\omega_0+\Omega)+\mathrm{e}^{-\mathrm{i}\Omega t_0}\hat{a}(\omega_0+\Omega)\right\}\\
&= \frac{\hbar\omega_0\alpha_0\pi}{\Delta\Omega}\int_{\Omega_0-\frac{1}{2}\Delta\Omega}^{\Omega_0+\frac{1}{2}\Delta\Omega}\mathrm{d}\Omega\left\{\mathrm{e}^{+\mathrm{i}\Omega t_0}\hat{a}^\dagger(\omega_0+\Omega)+\mathrm{e}^{-\mathrm{i}\Omega t_0}\hat{a}(\omega_0+\Omega)\right.\\
&\qquad\left.+\mathrm{e}^{-\mathrm{i}\Omega t_0}\hat{a}^\dagger(\omega_0-\Omega)+\mathrm{e}^{+\mathrm{i}\Omega t_0}\hat{a}(\omega_0-\Omega)\right\}\\
&= \frac{\hbar\omega_0\alpha_0\pi}{\Delta\Omega}\int_{\Omega_0-\frac{1}{2}\Delta\Omega}^{\Omega_0+\frac{1}{2}\Delta\Omega}\mathrm{d}\Omega\left\{\cos(\Omega t_0)\,\hat{X}_c^+(\Omega)+\sin(\Omega t_0)\,\hat{X}_s^+(\Omega)\right\}
\end{aligned}\tag{2.102}$$

Here we can see how the two-mode quadrature operators for the amplitude, as given by Equation 2.81, have appeared in the expression for the energy, as collected by the detector. If we divide the collected energy by the duration of the time window, again $\Delta t = 2\pi/\Delta\Omega$, then the operator for the average power that is detected becomes

$$\hat{P}_{\mathrm{AC}} = \frac{\hbar\omega_0\alpha_0}{2}\int_{\Omega_0-\frac{1}{2}\Delta\Omega}^{\Omega_0+\frac{1}{2}\Delta\Omega}\mathrm{d}\Omega\left\{\cos(\Omega t_0)\,\hat{X}_c^+(\Omega)+\sin(\Omega t_0)\,\hat{X}_s^+(\Omega)\right\}\tag{2.103}$$

Note that the two-mode quadrature operators carry the units of $[\mathrm{s}^{-1/2}]$. Let us calculate the expectation value of the mean and standard deviation of this operator, over the set of vacuum states $|\{0\}_\Omega\rangle$ for all Ω. We then get a mean $\mu(\hat{P}_{\mathrm{AC}}) = 0$, and standard deviation $\sigma(\hat{P}_{\mathrm{AC}}) = \hbar\omega_0\alpha_0\sqrt{\Delta\Omega/2}$. The former is to be expected, since we have made no coherent excitation at the sideband frequencies. The latter is scaled by the root of the bandwidth, therefore the larger the bandwidth, the more noise power is detected, which is consistent with a frequency independent power spectral density, or white noise. This is the derivation for the shot noise of a photodetector, when it is illuminated by a coherent state of light. The derivation of the shot noise using the semi-classical theory can be found in [Winzer 1997].

2.6.3 Two-mode coherent states produce AM and PM

The measured power of a photo-detector is neatly described in the two-mode formalism of Equation 2.103. An amplitude modulation (AM) and phase modulation (PM) can be produced on the light beam by applying a coherent excitation to the upper and lower sidebands. The two-mode displacement operator is defined by a pair of single-mode displacement operators:

$$\hat{D}_{\mathrm{m}} = \hat{D}(\alpha_-;\omega_0 - \Omega_{\mathrm{m}})\hat{D}(\alpha_+;\omega_0 + \Omega_{\mathrm{m}}) \tag{2.104}$$

It essentially creates a coherent state at the upper and lower sidebands at the modulation frequencies $\omega_0+\Omega_{\mathrm{m}}$ and $\omega_0-\Omega_{\mathrm{m}}$; and with the coherent amplitudes α_+ and α_-, respectively. It transforms the two-mode quadrature operators in the following way:

$$\hat{D}^\dagger_{\mathrm{m}}\,\hat{X}^+_{\mathrm{c}}\,\hat{D}_{\mathrm{m}} = \hat{X}^+_{\mathrm{c}}(\Omega) + 2\Big[+\Re\{\alpha_-\} + \Re\{\alpha_+\}\Big]\delta(\Omega-\Omega_{\mathrm{m}}) \tag{2.105}$$

$$\hat{D}^\dagger_{\mathrm{m}}\,\hat{X}^+_{\mathrm{s}}\,\hat{D}_{\mathrm{m}} = \hat{X}^+_{\mathrm{s}}(\Omega) + 2\Big[-\Im\{\alpha_-\} + \Im\{\alpha_+\}\Big]\delta(\Omega-\Omega_{\mathrm{m}}) \tag{2.106}$$

$$\hat{D}^\dagger_{\mathrm{m}}\,\hat{X}^-_{\mathrm{c}}\,\hat{D}_{\mathrm{m}} = \hat{X}^-_{\mathrm{c}}(\Omega) + 2\Big[-\Im\{\alpha_-\} - \Im\{\alpha_+\}\Big]\delta(\Omega-\Omega_{\mathrm{m}}) \tag{2.107}$$

$$\hat{D}^\dagger_{\mathrm{m}}\,\hat{X}^-_{\mathrm{s}}\,\hat{D}_{\mathrm{m}} = \hat{X}^-_{\mathrm{s}}(\Omega) + 2\Big[-\Re\{\alpha_-\} + \Re\{\alpha_+\}\Big]\delta(\Omega-\Omega_{\mathrm{m}}) \tag{2.108}$$

For example, to put an amplitude modulation on the cosine channel alone would require the condition that $\alpha_+ = \alpha_- = \alpha_{\mathrm{m}}$, where the modulation depth α_{m} is real. We choose the modulation frequency to be at the centre of the bandwidth, so $\Omega_{\mathrm{m}} = \Omega_0$, and the offset of the time window at $t_0 = 0$. Using Equation 2.103, together with the continuum of modes all in the vacuum state, we get the following measurement of the mean and standard deviation of the detected (AC) optical power: $\mu(\hat{P}_{\mathrm{AC}}) = \hbar\omega_0\alpha_0(2\alpha_{\mathrm{m}})$ and $\sigma(\hat{P}_{\mathrm{AC}}) = \hbar\omega_0\alpha_0\sqrt{\Delta\Omega/2}$. The signal-to-noise ratio is then simply $\mathcal{S} = 2\alpha_{\mathrm{m}}/\sqrt{\Delta\Omega/2}$. So if I would like to detect an amplitude modulation with a signal-to-noise ratio of one, then I would have to modulate the carrier light beam with enough depth to supply a rate of photons into the sidebands (α^2_{m}) that is equal to one eighth of the detection bandwidth. The noise, also called shot-noise, originates from the vacuum sidebands. In practice, the shot noise level becomes the calibration for the photodetector and subsequent spectral analysis. If one accurately knows the bandwidth of the spectrum analyser, then one can infer the mean number of photons in

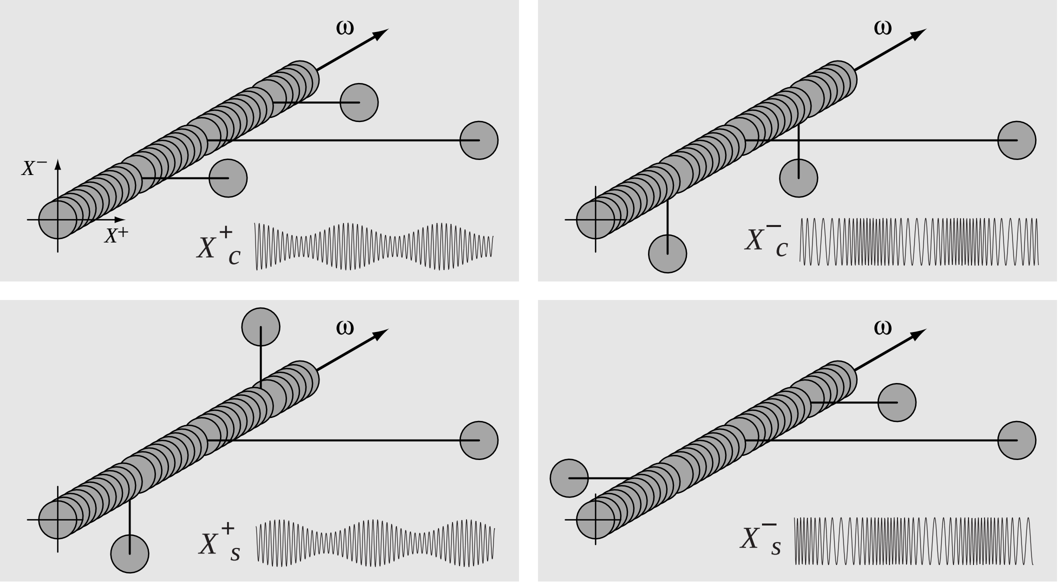

Figure 2.10: A visualisation of the two-mode coherent states which appear in two channels of amplitude modulation, and two channels of phase modulation. The two-mode coherent states are also presented as spectra that are made up of a ball-on-stick diagram drawn at each frequency. The frequency mode of the carrier is also shown. All other frequency modes are in the vacuum state.

the sidebands that make up the amplitude modulation [Webb *et al.* 2006].

The other channels of modulation are created in a similar manner by appropriately choosing the complex angles of α_- and α_+. These modulations of the light beam are shown graphically as an oscillation in Figure 2.10. Also shown is the spectrum as being made up of a ball-on-stick drawn at 'every' frequency. The phase relationships of the sidebands, relative to each other, determines what kind of modulation is produced.

2.6.4 A two-photon process produces two-mode squeezed states

We have seen that the vacuum sidebands are responsible for the shot noise in the form of a fluctuating optical power as measured by a photodetector. Looking at Equation 2.108, we know how to produce modulations on the light, but can we also remove them such that the light beam detected as a whole has a steady amplitude quadrature? If we lived inside a cavity in single-mode world, then the answer would be: yes, just apply the squeezed operator to the single mode. But in the world of photo-detection, which is inherently a two-mode process, we need to apply a two-mode squeeze operator in the form of:

$$\hat{S}(\zeta) = \exp\left\{\frac{1}{2}\zeta^*\hat{a}(\omega_0+\Omega)\,\hat{a}(\omega_0-\Omega) - \frac{1}{2}\zeta\hat{a}^\dagger(\omega_0-\Omega)\,\hat{a}^\dagger(\omega_0+\Omega)\right\} \tag{2.109}$$

Where the squeezing parameter is $\zeta = r\exp(\mathrm{i}\vartheta)$. One can readily see the similarity with the single-mode form in Table 2.4. If we choose to keep the squeezing parameter to be real $\zeta^* = \zeta = r$, then the two-mode squeezing operator works in the following way:

$$\hat{S}^\dagger(r)\,\hat{X}_{\mathrm{c}}^{+}(\Omega)\,\hat{S}(r) = \mathrm{e}^{-r}\hat{X}_{\mathrm{c}}^{+}(\Omega) \tag{2.110}$$

$$\hat{S}^\dagger(r)\,\hat{X}_{\mathrm{s}}^{+}(\Omega)\,\hat{S}(r) = \mathrm{e}^{-r}\hat{X}_{\mathrm{s}}^{+}(\Omega) \tag{2.111}$$

$$\hat{S}^\dagger(r)\,\hat{X}_{\mathrm{c}}^{-}(\Omega)\,\hat{S}(r) = \mathrm{e}^{+r}\hat{X}_{\mathrm{c}}^{-}(\Omega) \tag{2.112}$$

$$\hat{S}^\dagger(r)\,\hat{X}_{\mathrm{s}}^{-}(\Omega)\,\hat{S}(r) = \mathrm{e}^{+r}\hat{X}_{\mathrm{s}}^{-}(\Omega) \tag{2.113}$$

The squeezing operation acts like an amplification or de-amplification of the two-mode quadrature operators. The transformation is symplectic, in that the product of the phase and amplitude quadrature variances remains unchanged. The expression for the mean and standard deviation of the detected (AC) power becomes: $\mu(\hat{P}_{\mathrm{AC}}) = 0$ and $\sigma(\hat{P}_{\mathrm{AC}}) = \hbar\omega_0\alpha_0\mathrm{e}^{-r}\sqrt{\Delta\Omega/2}$. Compare this with the case before the squeezing operation was introduced. For positive values of the squeezing parameter, the measured noise, as given by the standard deviation, is lower by a factor of e^{-r} of the shot-noise level. Note that if we had applied only the single-mode squeezing operator, then this result would not have been possible. It is the correlation of the sidebands, as introduced by the two-mode squeezing operator, that enables the reduction of the measured amplitude noise of the light beam, to below that of shot noise.

2.6.5 A compact form of the two-mode formalism

The two-mode formalism is the most intuitive model for understanding what part of the EM field a photodetector detects. But it can be a bit clumsy when it comes to calculating the output of nonlinear optical components, such as an optical parametric amplifier. One way to get around this is to defining a new operator which contains both channels of the amplitude quadrature:

$$\hat{\mathbb{X}}_{\mathrm{cs}}^{+}(\Omega) := \frac{1}{2}\{\hat{X}_{\mathrm{c}}^{+}(\Omega) - \mathrm{i}\hat{X}_{\mathrm{s}}^{+}(\Omega)\} = \{\hat{a}(\omega_0 - \Omega) + \hat{a}^\dagger(\omega_0 + \Omega)\} \tag{2.114}$$

$$\hat{\mathbb{X}}_{\mathrm{cs}}^{-}(\Omega) := \frac{1}{2}\{\hat{X}_{\mathrm{c}}^{-}(\Omega) - \mathrm{i}\hat{X}_{\mathrm{s}}^{-}(\Omega)\} = \mathrm{i}\{\hat{a}(\omega_0 - \Omega) - \hat{a}^\dagger(\omega_0 + \Omega)\} \tag{2.115}$$

So what I have effectively done is to put the information of each real-valued channel into one complex-valued channel. The change of font for the new operators is to remind us that they are not Hermitian. When doing calculations, one must remember to take twice the real part $2\Re\{\hat{\mathbb{X}}^+_{\rm cs}(\Omega)\}$ to get the cosine channel, and twice the imaginary part $2\Im\{\hat{\mathbb{X}}^+_{\rm cs}(\Omega)\}$ to get the sine channel. The operators obey the commutation relation $[\hat{\mathbb{X}}^+(\Omega), \hat{\mathbb{X}}^-(\Omega')] = -2{\rm i}\,\delta(\Omega{-}0)\,\delta(\Omega'{-}0)$. The role that they play will be made clear in a moment after I define the Fourier transformed operators:

$$\hat{X}^+_{\rm cs}(t) = \frac{1}{2\pi}\int_{-\infty}^{+\infty}{\rm d}\Omega\ {\rm e}^{+{\rm i}\Omega t}\hat{\mathbb{X}}^+_{\rm cs}(\Omega) \tag{2.116}$$

$$\hat{X}^-_{\rm cs}(t) = \frac{1}{2\pi}\int_{-\infty}^{+\infty}{\rm d}\Omega\ {\rm e}^{+{\rm i}\Omega t}\hat{\mathbb{X}}^-_{\rm cs}(\Omega) \tag{2.117}$$

Note that I have returned to the original font for the time-domain operators because they are indeed Hermitian. The next step is to relate the time-domain operators to the detected AC power. I exploit the properties that $\hat{X}^+_{\rm c}(-\Omega) = \hat{X}^+_{\rm c}(\Omega)$ and $\hat{X}^+_{\rm s}(-\Omega) = -\hat{X}^+_{\rm s}(\Omega)$, which follow from their definitions. I also employ the convolution theorem of a Fourier transform to arrive at the following identity with Equation 2.103:

$$\hat{P}_{\rm AC} = \hbar\omega_0\alpha_0\,\hat{X}^+_{\rm cs}(t) * T_{\rm AC}(t)/\Delta t \tag{2.118}$$

where the convolution integral of the amplitude quadrature with the time window is

$$\hat{X}^+_{\rm cs}(t) * T_{\rm AC}(t) = \int_{-\infty}^{+\infty}{\rm d}t'\ \hat{X}^+_{\rm cs}(t')\,T_{\rm AC}(t-t') \tag{2.119}$$

and $T_{\rm AC}(t)$ is given in Equation 2.98, with the duration of the time window $\Delta t = 2\pi/\Delta\Omega$. Equation 2.118 tells us what we already knew: the fluctuations in the detected power are proportional to the amplitude quadrature of the sidebands and they are scaled by the coherent amplitude of the carrier. But the time-domain form that is presented here, is more general than Equation 2.103. It works for any choice of time window or frequency filter, as long as the convolution integral is re-evaluated. It is common practice in quick theoretical derivations to ignore the convolution integral, and even to ignore the scaling factor $\hbar\omega_0$. But one must remember that a time window must always be specified to allow one to make a quantitative comparison with experimental results. This concludes the section on the connection between the EM field and its detected power. The result is intuitive from its roots in classical optics, but buried beneath several layers of abstractions and operator definitions still lies the quantum harmonic oscillator.

2.7 Models of linear processes

Most experiments in quantum optics can be reduced to a few simple building blocks. We can model what happens to the optical field during its passage through each block, and therefore build an input-output transfer function for the relevant fields of the entire experiment [Bachor and Ralph 2004]. By far the most important component is the beamsplitter. From this we can develop models of optical loss, optical cavities, and homodyne detection.

2.7.1 Linearisation of operators in the time domain

The task of calculating transfer functions of optical components is greatly simplified by the technique of operator linearisation [Yurke 1984]. The idea is to break up an operator into time dependent, and time independent, components. For this to work, one has to make two transformations. Firstly, one must bring the operator into a rotating frame that removes the oscillation at the optical frequency ω_0 of the carrier. For example, the annihilation operator transforms according to $\hat{a}(t) \rightarrow \hat{a}(t)\exp(\mathrm{i}\omega_0 t)$, which changes the definition of the Fourier transformed operators of Equation 2.71 in terms of the sideband frequency Ω such that

$$\hat{a}_{\mathrm{rot}}(t) = \frac{1}{2\pi}\int_{-\infty}^{+\infty}\mathrm{d}\Omega\ \hat{a}(\omega_0+\Omega)\exp(-\mathrm{i}\Omega t) \tag{2.120}$$

Secondly, we must apply a displacement operation to the carrier mode, which makes a coherent state at the carrier frequency. In the rotating frame, this looks like $\hat{D}^{\dagger}\,\hat{a}_{\mathrm{rot}}(t)\,\hat{D} = \hat{a}_{\mathrm{rot}}(t)+\alpha$. We therefore get the original operator plus the scalar from the coherent amplitude of the carrier. As we are working in the Heisenberg picture, we must remember that the initial state of the carrier mode must be kept in a vacuum state when calculating the expectation values of operators. If we abide by this rule, then the annihilation operator in the rotating frame (and prior to the displacement operation) will be guaranteed to have have a time-averaged expectation value of zero: $\langle 0|\int_{-\infty}^{+\infty}\mathrm{d}t\ \hat{a}_{\mathrm{rot}}(t)|0\rangle = \langle 0|\hat{a}(\omega_0)|0\rangle = 0$. In the notation, one removes the 'rot' subscript and places a delta symbol in front of the rotating-frame operator $\hat{a}_{\mathrm{rot}}(t) \rightarrow \delta\hat{a}(t)$, to show that its mean value is zero: $\langle\delta\hat{a}(t)\rangle = 0$.

To summarise these steps so far: α is the component for the steady-state classical amplitude of the carrier mode; and $\delta\hat{a}(t)$ is the component that holds the quantum fluctuations. We have therefore made the transformation: $\hat{a}(t) \rightarrow \alpha + \delta\hat{a}(t)$. One can follow a similar procedure of transformation for the creation operator to get: $\hat{a}^{\dagger}(t) \rightarrow \alpha^{*} + \delta\hat{a}^{\dagger}(t)$. Note that my argument here has been subtle. I have not invoked a time-average of the operator in the definition, but rather, I have relied on the displacement operation to bring about a scalar offset of the creation and annihilation operators.

The final step in the linearisation procedure comes when one removes any terms that appear in expressions of operators, that are proportional to the products of two or more fluctuating terms. For example, applying the rotating frame and displacement transformations to the creation and annihilation operators, the number operator in the time domain becomes

$$\begin{aligned} \hat{a}^{\dagger}(t)\,\hat{a}(t) &= \alpha^{*}\alpha + \alpha^{*}\delta\hat{a}(t) + \alpha\delta\hat{a}^{\dagger}(t) + \delta\hat{a}^{\dagger}(t)\,\delta\hat{a}(t) && (2.121) \\ &= |\alpha|^{2} + |\alpha|\left[\mathrm{e}^{-\mathrm{i}\phi}\delta\hat{a}^{\dagger}(t) + \mathrm{e}^{+\mathrm{i}\phi}\delta\hat{a}(t)\right] + \delta\hat{a}^{\dagger}(t)\,\delta\hat{a}(t) && (2.122) \\ &= |\alpha|^{2} + |\alpha|\delta\hat{X}_{a}^{\phi_{\alpha}}(t) + \delta\hat{a}^{\dagger}(t)\,\delta\hat{a}(t) && (2.123) \\ &\approx |\alpha|^{2} + |\alpha|\delta\hat{X}_{a}^{\phi_{\alpha}}(t) && (2.124) \end{aligned}$$

where in the last step I have assumed that the second-order fluctuation term will be much smaller than the terms scaled by α. Which will be valid for the case of a strong excitation of $|\alpha| \gg 1$. The quadrature operator for arbitrary angles $\delta\hat{X}_{a}^{\phi_{\alpha}}$ from Equation 2.44 was introduced to accommodate the complex-valued coherent amplitude. The angle is $\phi_{\alpha} = \mathrm{Arg}\{\alpha\}$. For $\phi_{\alpha} = 0$ and $\phi_{\alpha} = \pi/2$ we have the amplitude and phase quadratures respectively.

As a comment, one can immediately see the usefulness of the linearisation approach. The result here can be compared with the 'DC' and 'AC' measurements of the Poynting vector in Equation 2.101 and Equation 2.103. By using the linearisation procedure for the time domain operators, one can avoid a lengthy digression into defining time and frequency windows, while still getting essentially the same result.

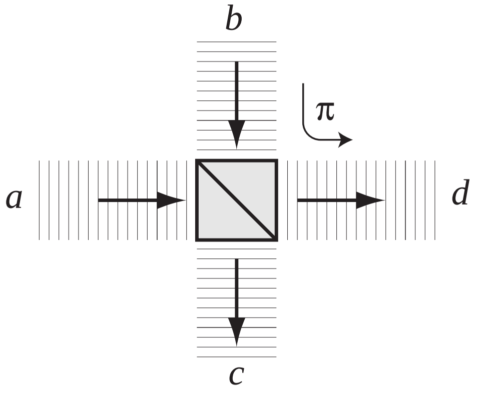

Figure 2.11: A diagram showing how two independent modes, for the plane waves labelled by a and b, can interfere on a beamsplitter of intensity reflectivity η, to create two new modes c and d. Note the π phase shift on the path from b to d.

2.7.2 The beam splitter

Consider a set of modes that are plane waves with propagation vectors $\mathbf{k}$ pointing in different directions, but that have all the same magnitude $|\mathbf{k}|$. A beamsplitter is a device that allows two of these input modes (a and b) to interfere to produce two output modes (c and d). The beamsplitter can be described as a matrix of complex transmitivity and reflectivity factors [Saleh and Teich 1991]. But for the moment, let us assume that the beamsplitter has an intensity reflectivity of η, and that it introduces a π phase shift on reflection from the path b to d, and no phase shift on all the other paths. A diagram is shown in Figure 2.11. The beamsplitter transforms the creation and annihilation operator in the following way:

$$\hat{c}^\dagger = \sqrt{\eta}\,\hat{a}^\dagger + \sqrt{1-\eta}\,\hat{b}^\dagger \quad , \quad \hat{c} = \sqrt{\eta}\,\hat{a} + \sqrt{1-\eta}\,\hat{b} \tag{2.125}$$

$$\hat{d}^\dagger = \sqrt{1-\eta}\,\hat{a}^\dagger - \sqrt{\eta}\,\hat{b}^\dagger \quad , \quad \hat{d} = \sqrt{1-\eta}\,\hat{a} - \sqrt{\eta}\,\hat{b} \tag{2.126}$$

These equations are equally valid for the time-domain operators as the frequency-domain operators, so an explicit dependence will be dropped from the notation. The amplitude and phase quadrature operators for the output modes c and d simply become

$$\hat{X}_c^\pm = \sqrt{\eta}\,\hat{X}_a^\pm + \sqrt{1-\eta}\,\hat{X}_b^\pm \quad , \quad \hat{X}_d^\pm = \sqrt{1-\eta}\,\hat{X}_a^\pm - \sqrt{\eta}\,\hat{X}_b^\pm \tag{2.127}$$

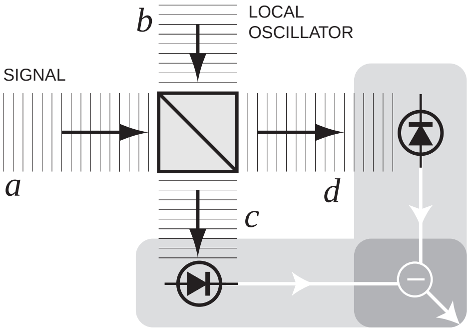

Figure 2.12: The technique of homodyne detection. The signal beam is interfered with a bright local oscillator. The two output ports are detected, and the photocurrents are subtracted from one another. The resulting current is proportional to the quadrature of the signal beam, where the angle is selected by the phase of the local oscillator.

Because the modes a and b are assumed to be independent and share no prior correlations, the mean and variances of the quadrature operators for modes c and d simplify to

$$\mu(\hat{X}_c^{\pm}) = \sqrt{\eta}\,\mu(\hat{X}_a^{\pm}) + \sqrt{1-\eta}\,\mu(\hat{X}_b^{\pm}) \tag{2.128}$$

$$\mu(\hat{X}_d^{\pm}) = \sqrt{1-\eta}\,\mu(\hat{X}_a^{\pm}) - \sqrt{\eta}\,\mu(\hat{X}_b^{\pm}) \tag{2.129}$$

$$\sigma^2(\hat{X}_c^{\pm}) = \eta\,\sigma^2(\hat{X}_a^{\pm}) + (1-\eta)\,\sigma^2(\hat{X}_b^{\pm}) \tag{2.130}$$

$$\sigma^2(\hat{X}_d^{\pm}) = (1-\eta)\,\sigma^2(\hat{X}_a^{\pm}) + \eta\,\sigma^2(\hat{X}_b^{\pm}) \tag{2.131}$$

I want to model the situation where one is interested in detecting mode a, but the mode suffered optical attenuation, or loss, along the path from source to detector. The beamsplitter of reflectivity η will accurately describe the effect of attenuation. Note that in the case of scattering or absorption, one would need to model a continuum of beamsplitters, but the end result is the same. If we take the case that input mode b is in the vacuum state, then we get: $\mu(\hat{X}_c^{\pm}) = \sqrt{\eta}\,\mu(\hat{X}_a^{\pm})$ and $\sigma^2(\hat{X}_c^{\pm}) = \eta\,\sigma^2(\hat{X}_a^{\pm}) + (1-\eta)$. We find that not only is the mean field attenuated, but that the vacuum state on mode b increases the quadratures variances on the output mode c. It is for this reason that experiments involving quadrature squeezed light, where $\sigma^2(\hat{X}_a^{+}) < 1$, that the detected amount of squeezing is degraded by the level of optical attenuation, and that detectors of high quantum efficiency are desirable.

2.7.3 Homodyne detection

So far we have been limited to measuring the amplitude quadrature of a light beam. This is the only part of the field that a single detector is sensitive to. One way to make the measurement phase sensitive is to interfere the beam of interest (the signal) on a beamsplitter with an auxiliary beam (the local oscillator); see Figure 2.12. For this to work, one must choose the splitting ratio to be symmetric $\eta = 1/2$, and the local oscillator in mode b to be in a bright coherent state $|\beta\rangle_b$ that is much greater than the mean field of the signal in mode a that is in the arbitrary state $|\psi\rangle_a$. The two output ports c and d of the beamsplitter are detected, and the photocurrents are subtracted from one another. Using the technique of linearisation, I can write down the difference of the number operators to give

$$\begin{aligned} \hat{n}_{\text{dif}} &= \hat{c}^\dagger\hat{c} - \hat{d}^\dagger\hat{d} && (2.132)\\ &= |\beta|\hat{X}_a^{\phi_\beta} + |\alpha|\hat{X}_b^{\phi_\alpha} && (2.133)\\ &\approx |\beta|\hat{X}_a^{\phi_\beta} \quad \text{when } \alpha \ll \beta && (2.134) \end{aligned}$$

where $\phi_\alpha = \text{Arg}\{\alpha\}$ and $\phi_\beta = \text{Arg}\{\beta\}$. The contribution of the quadrature amplitudes of the local oscillator to the difference current is negligible in the case of a strong local oscillator $\beta \gg \alpha$. Hence, one does not even require the local oscillator to be in a coherent state, it could for example be a squeezed state. The main requirement however, is that the phase of the local oscillator (relative to the signal) can be controlled. It is this phase which selects which quadrature angle of the signal beam is detected. This technique is called homodyne detection, because the optical frequency of the local oscillator was chosen to be the same as the signal beam. Indeed, for the technique to work efficiently, one must ensure that the two modes are well matched in the transverse-spatial functions and polarisation degrees of freedom.

From an experimental point of view, one strength of homodyne detection is that it allows measurement results to be calibrated to the vacuum state. The chain of electronic devices from photodiode to spectrum analyser can be so long that it makes an absolute measurement very challenging. This means that at the front of Equation 2.134 there is a constant factor, G, that depends on trans-impedance gain, bandwidth, and so on. This problem is side-stepped if one takes a calibration measurement by simply blocking the signal beam. This puts mode a into a vacuum state, thus giving a variance of the difference current: $\sigma^2(\hat{n}_{\text{dif}}) = G^2|\beta|^2$. Since the factor G is unchanged, it therefore cancels out. Homodyne detection forms the cornerstone of most continuous-variable quantum optics experiments, where squeezing and quadrature correlations between modes can be verified. Furthermore, from homodyne mea-

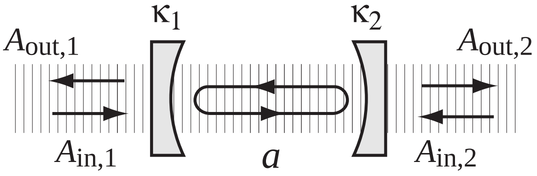

Figure 2.13: Schematic of a standing-wave cavity consisting of two mirrors with coupling coefficients κ_1 and κ_2. The intra-cavity field is labelled a, while the input fields are labelled $A_{\mathrm{in},1}$ and $A_{\mathrm{in},2}$.

surements taken over 2π of quadrature angles, it is for example possible to mathematically reconstruct the Wigner function of the state $|\psi\rangle_a$; see for example [Leonhardt 1997].

2.7.4 Optical cavities

We can make a light beam periodically interfere with itself by letting it reflect back and forth between two partially reflective mirrors. If the light exactly retraces its steps, in the sense that the transverse profile is preserved, then the setup becomes a stable optical resonator, or optical cavity. The applications of optical cavities are ubiquitous. For example, an optical cavity is the element of feedback in a laser system.

To model the cavity, we start by defining two coupling mirrors of reflectivity η_1 and η_2, that have decay rates $\kappa_1 = (1-\eta_1)/2\tau$ and $\kappa_2 = (1-\eta_2)/2\tau$, where $\tau = c/d$ is the round-trip time that is determined by the round-trip optical path length d. The total coupling rate is $\kappa = \kappa_1 + \kappa_2$, where all the coupling rates are in SI units of $[\mathrm{s}^{-1}]$. A diagram is shown in Figure 2.13. The intra-cavity field is described by the dimensionless annihilation operator $\hat{a}(t)$, while the input fields are described by $\hat{A}_{\mathrm{in},1}(t)$ and $\hat{A}_{\mathrm{in},2}(t)$ which have the units $[\mathrm{s}^{-\frac{1}{2}}]$. Similarly, the output fields are $\hat{A}_{\mathrm{out},1}(t)$ and $\hat{A}_{\mathrm{out},2}(t)$. The upper-case operators are to remind us that they have different units to the lower-case intra-cavity operators. We can now start to describe the evolution of the fields. The intra-cavity field decays with a rate that is proportional to $-\kappa\hat{a}$, but the intra-cavity field is also built up by the input fields according to $\sqrt{2\kappa_1}\hat{A}_{\mathrm{in},1}(t)$ and $\sqrt{2\kappa_1}\hat{A}_{\mathrm{in},2}(t)$; see for example [Collett and Gardiner 1984]. Combining both processes gives:

$$\frac{\mathrm{d}\hat{a}(t)}{\mathrm{d}t} = -\kappa\hat{a}(t) + \sqrt{2\kappa_1}\hat{A}_{\mathrm{in},1}(t) + \sqrt{2\kappa_2}\hat{A}_{\mathrm{in},2}(t) \tag{2.135}$$

My aim is to solve this differential equation to get the intra-cavity field in terms of the input fields. The linearisation transformation can be applied to the operators. This means that the annihilation operator is transformed into the rotating frame and a carrier is displaced according to $\hat{a}(t) \rightarrow [\alpha + \delta\hat{a}(t)]\exp(\mathrm{i}\omega_0 t)$ and similarly for the creation operator $\hat{a}^\dagger(t) \rightarrow [\alpha^* + \delta\hat{a}^\dagger(t)]\exp(-\mathrm{i}\omega_0 t)$. A similar transformation is given to the input and output fields. By substituting these into Equation 2.135 and remembering the definition of the time domain operators in Equation 2.71, we can peel off an equation for the carrier field and solve it immediately to get

$$\alpha = \frac{1}{\kappa}\left[\sqrt{2\kappa_1}\alpha_{\mathrm{in},1} + \sqrt{2\kappa_2}\alpha_{\mathrm{in},2}\right] \tag{2.136}$$

The rate equation for the sidebands become

$$\begin{aligned}\frac{\mathrm{d}}{\mathrm{d}t}\,\delta\hat{a}(t) &= -\kappa\,\delta\hat{a}(t) + \sqrt{2\kappa_1}\,\delta\hat{A}_{\mathrm{in},1}(t) + \sqrt{2\kappa_2}\,\delta\hat{A}_{\mathrm{in},2}(t)\\ \frac{-\mathrm{i}\Omega}{2\pi}\int\!\mathrm{d}\Omega\,\mathrm{e}^{-\mathrm{i}\Omega t}\,\hat{a}(\omega_0{+}\Omega) &= \frac{1}{2\pi}\int\!\mathrm{d}\Omega\,\mathrm{e}^{-\mathrm{i}\Omega t}\Big[-\kappa\,\hat{a}(\omega_0{+}\Omega)\\ &\quad+\sqrt{2\kappa_1}\,\hat{A}_{\mathrm{in},1}(\omega_0{+}\Omega) + \sqrt{2\kappa_2}\,\hat{A}_{\mathrm{in},2}(\omega_0{+}\Omega)\Big]\end{aligned}$$

Following through with an inverse Fourier transform we get

$$-\mathrm{i}\Omega\hat{a}(\omega_0{+}\Omega) = -\kappa\hat{a}(\omega_0{+}\Omega) + \sqrt{2\kappa_1}\hat{A}_{\mathrm{in},1}(\omega_0{+}\Omega) + \sqrt{2\kappa_2}\hat{A}_{\mathrm{in},2}(\omega_0{+}\Omega)$$

solving for the intra-cavity field, gives

$$\hat{a}(\omega_0{+}\Omega) = \frac{\kappa + \mathrm{i}\Omega}{\kappa^2 + \Omega^2}\left[\sqrt{2\kappa_1}\hat{A}_{\mathrm{in},1}(\omega_0{+}\Omega) + \sqrt{2\kappa_2}\hat{A}_{\mathrm{in},2}(\omega_0{+}\Omega)\right] \tag{2.137}$$

following the same steps for the creation operator, and changing the sign of Ω in the annihilation operator gives

$$\hat{a}(\omega_0{-}\Omega) = \frac{\kappa - \mathrm{i}\Omega}{\kappa^2 + \Omega^2}\left[\sqrt{2\kappa_1}\hat{A}_{\mathrm{in},1}(\omega_0{-}\Omega) + \sqrt{2\kappa_2}\hat{A}_{\mathrm{in},2}(\omega_0{-}\Omega)\right] \tag{2.138}$$

$$\hat{a}^\dagger(\omega_0{+}\Omega) = \frac{\kappa - \mathrm{i}\Omega}{\kappa^2 + \Omega^2}\left[\sqrt{2\kappa_1}\hat{A}^\dagger_{\mathrm{in},1}(\omega_0{+}\Omega) + \sqrt{2\kappa_2}\hat{A}^\dagger_{\mathrm{in},2}(\omega_0{+}\Omega)\right] \tag{2.139}$$

The sum of these two operators is exactly the definition of the *compact* form of the two-mode amplitude and phase quadrature operators given in Equation 2.115, hence

$$\hat{\mathbb{X}}^\pm_a(\Omega) = \frac{\kappa - \mathrm{i}\Omega}{\kappa^2 + \Omega^2}\left[\sqrt{2\kappa_1}\hat{\mathbb{X}}^\pm_{\mathrm{in},1}(\Omega) + \sqrt{2\kappa_2}\hat{\mathbb{X}}^\pm_{\mathrm{in},2}(\Omega)\right] \tag{2.140}$$

However, it is the reflected fields that are more interesting. One can get them from the input-output relation for the annihilation operator $\hat{A}_{\mathrm{out},2} = \sqrt{2\kappa_1}\hat{a} - \hat{A}_{\mathrm{in},2}$; and similarly for the quadrature operators $\hat{\mathbb{X}}^{\pm}_{\text{out},2} = \sqrt{2\kappa_2}\hat{\mathbb{X}}^{\pm}_{a} - \hat{\mathbb{X}}^{\pm}_{\text{in},2}$. Although this result appears simple, its derivation is nontrivial [Collett and Gardiner 1984]. Using the input-output relation, the transfer function for the fields that leave the cavity from the first and second mirrors become

$$\hat{\mathbb{X}}^{\pm}_{\text{out},1}(\Omega) = \left[\frac{2\kappa_1(\kappa - \text{i}\Omega)}{\kappa^2 + \Omega^2} - 1\right]\hat{\mathbb{X}}^{\pm}_{\text{in},1}(\Omega) + \left[\frac{2\sqrt{\kappa_1\kappa_2}(\kappa - \text{i}\Omega)}{\kappa^2 + \Omega^2}\right]\hat{\mathbb{X}}^{\pm}_{\text{in},2}(\Omega) \tag{2.141}$$

$$\hat{\mathbb{X}}^{\pm}_{\text{out},2}(\Omega) = \left[\frac{2\sqrt{\kappa_1\kappa_2}(\kappa - \text{i}\Omega)}{\kappa^2 + \Omega^2}\right]\hat{\mathbb{X}}^{\pm}_{\text{in},1}(\Omega) + \left[\frac{2\kappa_2(\kappa - \text{i}\Omega)}{\kappa^2 + \Omega^2} - 1\right]\hat{\mathbb{X}}^{\pm}_{\text{in},2}(\Omega) \tag{2.142}$$

In a similar fashion, the output carrier fields simplify to

$$\alpha_{\text{out},1} = \left[\frac{\kappa_1 - \kappa_2}{\kappa_1 + \kappa_2}\right]\alpha_{\text{in},1} + \left[\frac{2\sqrt{\kappa_1\kappa_2}}{\kappa_1 + \kappa_2}\right]\alpha_{\text{in},2} \tag{2.143}$$

$$\alpha_{\text{out},2} = \left[\frac{2\sqrt{\kappa_1\kappa_2}}{\kappa_1 + \kappa_2}\right]\alpha_{\text{in},1} - \left[\frac{\kappa_1 - \kappa_2}{\kappa_1 + \kappa_2}\right]\alpha_{\text{in},2} \tag{2.144}$$

Note that the real and imaginary components of the sideband field transfer function correspond to twice the sine and cosine channels. This means that the cavity has the ability to map one channel into the other channel depending on the sideband frequency. Note, that this is not the same as a phase shift, i.e. the amplitude quadrature is not mapped onto the phase quadrature. This only happens for the case when the carrier field is off-resonance with the cavity (i.e. the cavity is de-tuned).

In most quantum optics experiments, one is interested in the transfer function of the variances of these fields. However, a spectrum analyser essentially measures the sum of the individual variances for the sine and cosine channels (subscript ‘s’ and ‘c’ respectively), which corresponds to the noise power. To do this mathematically, I can define a new type of variance $V^{\pm}$ according to the expectation value of the compact quadrature operator multiplied by its Hermitian conjugate such that

$$V^{\pm} := \mu\Big((\hat{\mathbb{X}}^{\pm}_{\text{cs}})^{\dagger}\hat{\mathbb{X}}^{\pm}_{\text{cs}}\Big) \tag{2.145}$$

$$= \frac{1}{4}\sigma^2(\hat{X}^{+}_{\text{c}}) + \frac{1}{4}\sigma^2(\hat{X}^{\pm}_{\text{s}}) \tag{2.146}$$

Where these operators have their definitions in Equation 2.81 and Equation 2.115. As an example, one can choose to put all the input modes into a vacuum states (for all Ω), which have the property that $\sigma^2(\hat{X}^{\pm}_{\text{c,in},1}) = \sigma^2(\hat{X}^{\pm}_{\text{s,in},1}) = 2$ which then gives $V^{\pm}_{\text{in},1} = 1$, and similarly $V^{\pm}_{\text{in},2} = 1$. These variances for the vacuum state become the reference against

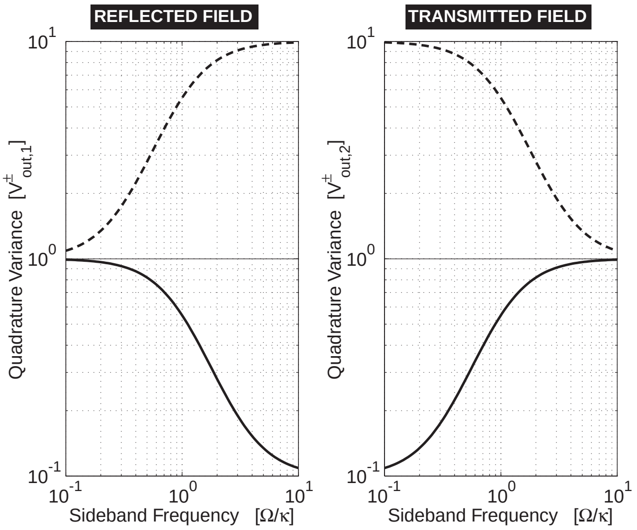

Figure 2.14: Transfer function of an impedance-matched cavity for an input mode in a broadband squeezed state having $V^+_{\rm in,1} = 0.1$ and $V^-_{\rm in,1} = 10$. The second input mode is in a vacuum state $V^{\pm}_{\rm in,2} = 1$. The solid and dashed lines are the variances of the amplitude and phase quadratures, respectively. The frequency axis is normalised to the cavity bandwidth κ. At low frequencies, the cavity is transparent and transmits the squeezed state. As the frequency increases, the cavity reflects the squeezed state.

which other states, such as squeezed states, are compared. The cavity transfer functions in terms of the newly-defined variance become

$$V^{\pm}_{\rm out,1}(\Omega) = \left[\frac{(\kappa_1-\kappa_2)^2+\Omega^2}{\kappa^2+\Omega^2}\right]V^{\pm}_{\rm in,1}(\Omega) + \left[\frac{4\kappa_1\kappa_2}{\kappa^2+\Omega^2}\right]V^{\pm}_{\rm in,2}(\Omega) \tag{2.147}$$

$$V^{\pm}_{\rm out,2}(\Omega) = \left[\frac{4\kappa_1\kappa_2}{\kappa^2+\Omega^2}\right]V^{\pm}_{\rm in,1}(\Omega) + \left[\frac{(\kappa_1-\kappa_2)^2+\Omega^2}{\kappa^2+\Omega^2}\right]V^{\pm}_{\rm in,2}(\Omega) \tag{2.148}$$

To illustrate the cavity transfer functions, I will choose the case of an impedance matched cavity, where $\kappa_1 = \kappa_2$. In this case, the cavity becomes completely transparent to the carrier field, such that $\alpha_{\rm out,2} = \alpha_{\rm in,1}$. The variances of the sidebands however, become filtered as a function of the sideband frequency. For $\Omega = 0$ the cavity is completely transparent. For $\Omega \gg \kappa$ the cavity is completely reflective. This is plotted in Figure 2.14, which shows the quadrature variances of transmission and reflection of the cavity when a broadband two-mode squeezed state is incident on the first input. The cavity has the transfer function of a frequency-dependent beamsplitter. Hence, it can be used to either low-pass or high-pass optical frequencies, with a cut-off frequency that is set by the cavity bandwidth $\Omega = \kappa$. The low-pass filtering characteristics of cavities are used in quantum optics experiments to prepare shot-noise-limited coherent states from laser sources that are dominated by technical noise sources.

2.8 Models of nonlinear processes

It is not possible to transform classical states of light into nonclassical states using linear processes such as beamsplitters and optical cavities. Nonlinear optical media, however, support the mixing of waves of different wavelengths, and it is via this effect that nonclassical states of light can be produced.

2.8.1 Second-order nonlinearity

A transparent solid material is quite a marvellous thing. One way of looking at it is that a single photon must fight its way past an enormous number of atoms, each of which could either absorb the photon, or scatter it in a new direction. The remarkable thing is that the scattered paths add coherently in the forward propagating direction, and for an ideal material, the light is not attenuated, but only slowed in its speed of propagation. This situation changes when the intensity of the light field has a strength that is comparable to the inter-atomic fields. The polarisation density of the material then begins to respond nonlinearly to the electric field. The response of the material can be written down as a polynomial expansion

$$\mathcal{P} = \epsilon_0 \left(\chi^{(1)} E + \chi^{(2)} E^2 + \chi^{(3)} E^3 + ... \right) \tag{2.149}$$

where ϵ_0 is the permitivity of free space, and $\chi^{(1)}$ is the linear susceptibility of the material (which for vacuum is equal to zero). The second-order nonlinear susceptibility $\chi^{(2)}$ supports three-wave mixing, which is used in devices such as optical parametric oscillators and second-harmonic generators for the purpose of frequency conversion. The third-order susceptibility $\chi^{(3)}$ is responsible for the Kerr-effect, which is where the refractive index of the material is dependent on the intensity of the light. This supports four-wave mixing and devices such as phase-conjugating mirrors. For my thesis, I have primarily used second-order nonlinear materials. There are at least two ways to understand the three-wave mixing effect that is supported by the second-order nonlinearity: (1) With a classical analysis of the propagating waves; (2) In the picture of interacting photons.

(1) The classical wave analysis of the second-order nonlinearity has a rough analogy

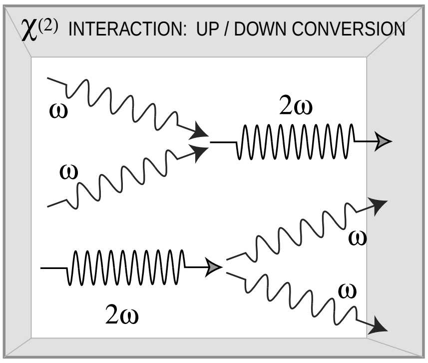

Figure 2.15: A diagram of photon interactions in a second-order nonlinear material. Only the degenerate pairs have been considered. Both the up-conversion and down-conversion processes occur, but it is the net conversion that decides whether the overall process is second-harmonic generation or optical parametric oscillation.

with sound and music. If one turns up the volume knob too high on a cheap radio, then the music begins to sound harsh and distorted. This happens because higher harmonics are generated from the original sound source, as sine waves become square waves due to clipping in the electronic circuitry. The difference with optics is that this effect is both desirable and expensive to manufacture. Let us send a single mode of light $E = E_0 \sin(\omega t)$ into the second-order nonlinear material and see how the polarisation density responds:

$$\mathcal{P} = \epsilon_0 \left[\chi^{(1)} E_0 \sin(\omega t) + \chi^{(2)} E_0^2 \sin^2(\omega t) + ...\right] \tag{2.150}$$

$$= \epsilon_0 \left[\chi^{(1)} E_0 \sin(\omega t) + \chi^{(2)} E_0^2 \Big(\frac{1}{2} - \frac{1}{2}\cos(2\omega t)\Big) + ...\right] \tag{2.151}$$

The result is that the polarisation density now oscillates at the second-harmonic frequency of 2ω, which will in turn radiate an electromagnetic wave at 2ω. The nonlinear medium has acted as a second-harmonic generator (SHG). To maximise the conversion efficiency of an SHG, one must ensure that the second-harmonic light produced at one location in the material, interferes constructively with the light that is produced further along, otherwise the net conversion can cancel out completely. This consideration means that one must choose a material that has a refractive index for the fundamental n_ω that exactly matches the refractive index of the second-harmonic $n_{2\omega}$, which is called phase matching. Much effort goes into developing materials that have a high second-order nonlinear susceptibility, and are transparent and phase-matched at both wavelengths.

Several techniques can be used to bring about the phase-matching condition. Angle-tuning relies on the birefringence of the material, where the refractive index and dispersion is angle-dependent. This has the disadvantage that for wide angles, the fundamental and

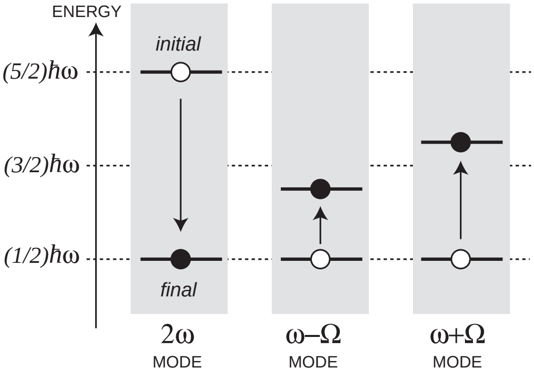

Figure 2.16: An energy level diagram of three modes that are involved in a non-degenerate down-conversion process. A photon in mode 2ω is removed and a photon each is deposited in the modes $\omega{+}\Omega$ and $\omega{-}\Omega$. Energy and momentum (depending on the medium) are still conserved.

second-harmonic beams very rapidly lose their spatial-overlap (also called walk-off) and hence reduce the conversion efficiency. The dispersion of a material depends weakly on the temperature, and provided that the phase-matching temperature is not extreme, this technique is quite effective, and it is often used in conjunction with the other phase-matching techniques. There is a way to cancel out the effect of a non-phase-matched material, by manufacturing the material so that the sign of the nonlinearity $\pm\chi^{(2)}$ alternates along its length at a certain rate (the poling rate). This so-called *quasi-phase matching* technique enables a wider range of materials, temperatures, and wavelengths to be used for frequency conversion.

(2) One can look at second-order nonlinear interaction in a simplified photon picture, as in the Feynman type of diagram in Figure 2.15. Two photons of frequency ω_1 and ω_2 combine to make a new photon of frequency ω_3. The interaction must conserve energy and momentum. The two conditions are

$$\hbar\omega_3 = \hbar\omega_1 + \hbar\omega_2 \tag{2.152}$$

$$\hbar\mathbf{k}_3 = \hbar\mathbf{k}_1 + \hbar\mathbf{k}_2 \tag{2.153}$$

where the latter equation must of course hold true for each component of the momentum vector, and the magnitude depends on the refractive index of the material n_1, so that $|\mathbf{k}_1| = n_1\omega_1/c$. For the case of second-harmonic generation $\omega_3 = 2\omega_1 = 2\omega_2$, and therefore $n_1 = n_2$, one gets back the result of the classical wave analysis: with the phase-matching condition $n_3 = n_1$. What is missing in this picture is the scattering rate of the interaction, indeed even the direction of the reaction is reversible. Hence the processes of up- and down-conversion can occur simultaneously in a nonlinear medium, and it is the net conversion that decides whether the process is up-conversion (SHG), or down-conversion (degenerate OPO). To go further, one needs a detailed model of a particular system. Here one can choose between a travelling-wave analysis through a medium, or an analysis of well-defined modes in an optical resonator that enclosed the non-linear material.

The degenerate process is not the only one that is allowed. Energy and momentum can still be conserved for the case that ω_1 and ω_2 are not equal. An example is depicted in Figure 2.16, where a photon of energy can be removed from the mode $\omega_3 = 2\omega$, and deposited in the modes $\omega_1 = \omega - \Omega$ and $\omega_2 = \omega + \Omega$. Where Ω is an offset frequency. It turns out that it is exactly this process that produces two-mode squeezed states at the sideband frequency Ω around the carrier ω. I will proceed with modelling such a process in the next section.

2.8.2 A basic model of OPO

An optical parametric oscillator (OPO), is a device that uses the three-wave mixing effect to convert a high optical frequency (the pump) into two lower frequencies (signal and idler). The OPO is usually built by enclosing a second-order nonlinear medium in an optical cavity. The cavity is made resonant for either one, or both of the lower frequencies which significantly enhances the conversion efficiency. I am interested in the quantum states that are generated by the degenerate OPO when it is driven by a coherent pump field. The signal and idler frequencies are also restricted to be degenerate, which defines them as the fundamental frequency, while the pump must be the second-harmonic. The OPO can be modelled using a pair of rate equations that are similar to the cavity equations that were described earlier, but are now modified to include the interaction between the fundamental and second-harmonic fields. A schematic is shown in Figure 2.17. The derivation of the nonlinear interaction terms is quite involved and non-trivial. Here I can give only a reference where such a derivation can be found [Collett and Gardiner 1984]. From [Drummond *et al.* 1980], the rate equations for the annihilation operators of the fundamental $\hat{a}$ and the second-harmonic

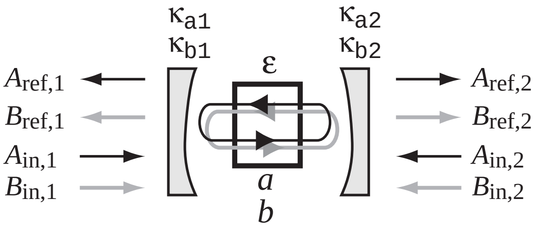

Figure 2.17: Schematic of a simple OPO cavity consisting of two mirrors with coupling coefficients κ_{a1} and κ_{a2} for the fundamental and κ_{b1} and κ_{b2} for the second-harmonic. The nonlinear optical medium is placed between mirrors, where the intra-cavity fields are labelled a and b. All the input and output fields for the fundamental and second-harmonic are included in the model.

$\hat{b}$ intra-cavity fields are

$$\frac{\mathrm{d}\,\hat{a}(t)}{\mathrm{d}t} = -\kappa_a\,\hat{a}(t) + \epsilon\,\hat{a}^\dagger(t)\,\hat{b}(t) + \hat{A}_{\mathrm{in}} \tag{2.154}$$

$$\frac{\mathrm{d}\,\hat{b}(t)}{\mathrm{d}t} = -\kappa_b\,\hat{b}(t) - \frac{1}{2}\epsilon\,\hat{a}(t)\,\hat{a}(t) + \hat{B}_{\mathrm{in}} \tag{2.155}$$

Where all operators and labels involving a and b correspond to the fundamental and second-harmonic fields, respectively. The total cavity decay rates are $\kappa_a = \kappa_{a1} + \kappa_{a2}$ and $\kappa_b = \kappa_{b1} + \kappa_{b2}$. The input operators are actually the sum for all input fields, such that $\hat{A}_{\mathrm{in}} = \sqrt{\kappa_{a1}}\,\hat{A}_{\mathrm{in},1}(t) + \sqrt{\kappa_{a2}}\,\hat{A}_{\mathrm{in},2}(t)$ and $\hat{B}_{\mathrm{in}} = \sqrt{\kappa_{b1}}\,\hat{B}_{\mathrm{in},1}(t) + \sqrt{\kappa_{b2}}\,\hat{B}_{\mathrm{in},2}(t)$. The intra-cavity operators are dimensionless, while the individual input operators $\hat{A}_{\mathrm{in},1}$, etc., have the SI units $[s^{-\frac{1}{2}}]$. The strength of the nonlinear interaction is governed by ϵ, which can be complex-valued (depending on the phase-matching condition), but which I will set to be real from now on. I will make two further assumptions: the second-harmonic input field at the first mirror (the pump field) is displaced to be in a coherent state $\beta_{\mathrm{in},1}$ at the carrier frequency $2\omega_0$; while all other input fields are in the vacuum states at all frequencies. The second assumption is that the pump field will neither be enhanced nor depleted. This is reasonable, only when no coherent excitation at the fundamental is produced (which corresponds to OPO below threshold). With these assumptions in mind, we can easily solve the coupled set of equations using the linearisation technique. The fundamental field is brought into the rotating frame $\hat{a}(t) \rightarrow \delta\hat{a}(t)\,\mathrm{e}^{\mathrm{i}\omega_0 t}$, where $\langle\delta\hat{a}(t)\rangle = 0$. And the second-harmonic is rotated and displaced according to $\hat{b}(t) \rightarrow \beta + \delta\hat{b}(t)\,\mathrm{e}^{\mathrm{i}2\omega_0 t}$, where $\langle\delta\hat{b}(t)\rangle = 0$, and the value of β is yet to be determined from the corresponding coherent amplitude of the input

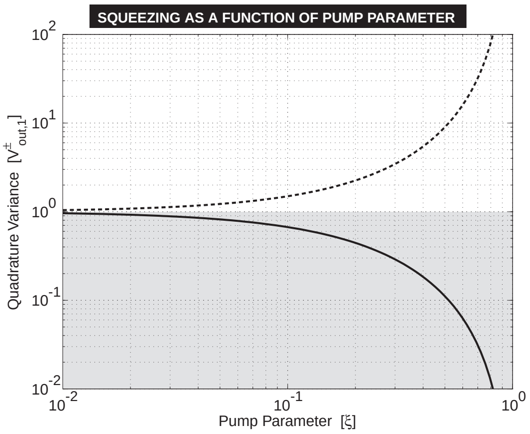

Figure 2.18: Squeezing from an ideal OPO cavity. The quadrature variances are plotted as a function of the pump parameter ξ. The sideband frequency is set to $\Omega = 0$. The solid and dashed lines are the amplitude and phase quadratures respectively. Squeezing is present in the shaded area. The squeezing becomes arbitrarily strong as the OPO threshold is approached at $\xi = 1$. The linearisation approximations in the model however, break down at this point.

field $\beta_{\mathrm{in},1}$. In the frequency domain, the operators become

$$\hat{a}(t) = \frac{1}{2\pi}\int d\Omega\, e^{-i\Omega t}\, \hat{a}(\omega_0+\Omega) \tag{2.156}$$

$$\hat{a}^\dagger(t) = \frac{1}{2\pi}\int d\Omega\, e^{+i\Omega t}\, \hat{a}^\dagger(\omega_0+\Omega) \tag{2.157}$$

$$\hat{b}(t) = \beta + \frac{1}{2\pi}\int d\Omega\, e^{-i\Omega t}\, \hat{b}(2\omega_0+\Omega) \tag{2.158}$$

$$\hat{b}^\dagger(t) = \beta^* + \frac{1}{2\pi}\int d\Omega\, e^{+i\Omega t}\, \hat{b}^\dagger(2\omega_0+\Omega) \tag{2.159}$$

where ω_0 is the carrier frequency of the fundamental field, and Ω is the sideband frequency. Similar definitions apply to the input and output fields. These definitions are substituted into Equation 2.155, where the steady-state component for the second-harmonic is peeled off and solved to give $\beta = (\sqrt{2\kappa_{b1}}/\kappa_b)\beta_{\mathrm{in}}$. I can choose to set $\beta^* = \beta$. By definition, the steady-state fundamental field has zero amplitude, and will not be considered any further. The analysis of the fluctuations of the fundamental field proceeds by taking the inverse Fourier transform, neglecting the fluctuation-fluctuation terms, and solving for the input fields to give

$$\hat{A}_{\mathrm{in}}(\omega_0+\Omega) = (\kappa_a - i\Omega)\,\hat{a}(\omega_0+\Omega) + \epsilon\beta\,\hat{a}^\dagger(\omega_0-\Omega) \tag{2.160}$$

$$\hat{A}^\dagger_{\mathrm{in}}(\omega_0-\Omega) = (\kappa_a - i\Omega)\,\hat{a}^\dagger(\omega_0-\Omega) + \epsilon\beta\,\hat{a}(\omega_0+\Omega) \tag{2.161}$$

From this pair, I can form the compact amplitude and phase quadrature operators (see Section 2.6.5):

$$\hat{\mathbb{X}}^{\pm}_{\mathrm{Ain}}(\Omega) = (\kappa_a \pm \epsilon\beta - i\Omega)\,\hat{\mathbb{X}}^{\pm}_a(\Omega) \tag{2.162}$$

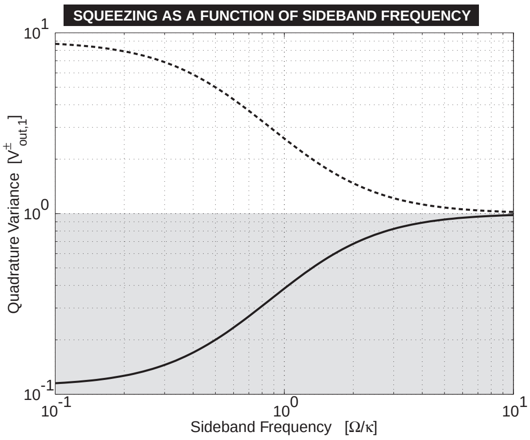

Figure 2.19: Squeezing from an ideal OPO cavity. The quadrature variances are plotted as a function of the sideband frequency Ω normalised to the cavity bandwidth κ_a. The pump parameter is set to $\xi = 0.5$. The solid and dashed lines are the amplitude and phase quadratures respectively. Squeezing is present in the shaded area. The squeezing becomes weaker as the sideband frequency is increased beyond the cavity linewidth. Note that the purity of the state produced by the OPO, as given by the product of the amplitude and phase variances, remains constant.

The input-output relation is applied to get the field exiting the cavity from the first mirror.

$$\hat{\mathbb{X}}^{\pm}_{\text{Aout1}}(\Omega) \quad = \quad \left[\frac{2\kappa_{a1}}{\kappa_a \pm \epsilon\beta - \mathrm{i}\Omega} - 1\right]\hat{\mathbb{X}}^{\pm}_{\text{Ain1}}(\Omega) + \left[\frac{2\sqrt{\kappa_{a1}\kappa_{a2}}}{\kappa_a \pm \epsilon\beta - \mathrm{i}\Omega}\right]\hat{\mathbb{X}}^{\pm}_{\text{Ain2}}(\Omega) \quad (2.163)$$

We can compare the transfer function of the OPO to that of the linear cavity in Equation 2.142. Here, the term $\epsilon\beta$ is an additional parameter that can vary the transmission coefficient of the cavity for both input modes. The sign of the coefficient however, depends on whether the quadrature is amplitude or phase.

2.8.3 OPO as a source of squeezed light

From the transfer function of the OPO, I can calculate the variance of the compact quadrature operator according to Equation 2.146. They become:

$$V^{\pm}_{\text{Aout1}}(\Omega) \quad = \quad \left[\frac{(\kappa_a - 2\kappa_{a1} \pm \epsilon\beta)^2 + \Omega^2}{(\kappa_a \pm \epsilon\beta)^2 + \Omega^2}\right]V^{\pm}_{\text{Ain1}}(\Omega) + \left[\frac{4\kappa_{a1}\kappa_{a2}}{(\kappa_a \pm \epsilon\beta)^2 + \Omega^2}\right]V^{\pm}_{\text{Ain2}}(\Omega)$$

If the term $\epsilon\beta$ is positive, then the amplitude quadrature will show squeezing ($V^{+}_{\text{Aout1}} < 1$). This can be enhanced by making the cavity completely over-coupled such that $\kappa_{a2} = 0$, which means that input mode 2 is not transmitted at all. The strongest squeezing occurs when the pump amplitude approaches OPO-threshold at $\beta = \kappa_a/\epsilon$. At exactly OPO-threshold, the model breaks down. The problem is that the linearisation procedure is no longer valid, and one needs to use perturbation techniques to model the transition to OPO threshold [Chaturvedi *et al.* 2002]. Nevertheless, the simple model that is presented here, is quite adequate for describing the behaviour below-threshold. I make the replacement to a dimensionless pump parameter $\xi = \epsilon\beta/\kappa_a$ which equals one for the OPO threshold case.

The output variance is then

$$V^{\pm}_{\mathrm{Aout1}}(\Omega) \;=\; \left[\frac{(1 \mp \xi)^2 + (\Omega/\kappa_a)^2}{(1 \pm \xi)^2 + (\Omega/\kappa_a)^2}\right] V^{\pm}_{\mathrm{Ain1}}(\Omega) \tag{2.164}$$

where the input variance has been assumed to be in a vacuum state ($V^{\pm}_{\mathrm{Ain1}} = 1$). The output variance is plotted in Figure 2.18 as a function of the pump parameter for a sideband frequency set to zero. The remarkable thing is that only a finite pump power is needed for the model to produce arbitrarily strong squeezing. This model is of course simplified in the sense that no loss mechanisms have been included. Figure 2.18 shows the output variance as a function of sideband frequency (and for the pump parameter set to $\xi = 0.5$). The best squeezing occurs well within the cavity bandwidth κ_a. The reason is that for high frequencies, the upper and lower sidebands acquire a large phase shift for each round-trip in the cavity, which essentially lowers the effective nonlinear interaction.

2.9 Two-mode entanglement

So far we have seen that single-mode states are capable of exhibiting non-classical statistical properties such as quadrature squeezing or sub-Poissonian counting distributions. An extension to these ideas are the two-mode states that show non-classical properties only when the measurements made individually on each mode, are compared. The prime example is the two-mode entangled state which can in principle show completely noise-free correlations between quadrature measurements made on one mode when compared with the other mode. This type of state goes back to the arguments of Einstein-Podolsky-Rosen (EPR). To simplify the following analysis I will abandon the continuous-mode formalism, and return to the discrete-mode case. I want to show that two-mode states of light can exhibit the EPR type of entanglement. I will present the ideas in two ways, firstly with field operators, and secondly with expansions in the Fock state basis. My approach is unusual because I start with the specific cases and work my way up to the general description that is provided by the inseparability criterion.

2.9.1 Quantum correlation

This section serves as a precursor to introducing the idea of entanglement. A naive way to create a two-mode nonclassical state would be perhaps to take a single-mode nonclassical state and send it onto a symmetric beamsplitter. Lets us consider a quadrature squeezed state that enters on port 1, and a vacuum state that enters on port 2. The input state can therefore be written as $|\psi\rangle = |\zeta\rangle_1 \otimes |0\rangle_2$, where ζ is the complex squeezing parameter $\zeta = r\exp(\mathrm{i}\vartheta)$. The transfer function of a beamsplitter is given in Equation 2.131, this time with a change of subscript labels. The quadrature operators for the output ports a and b are therefore

$$\hat{X}_a^{\pm} = \frac{1}{\sqrt{2}}\left(\hat{X}_1^{\pm} + \hat{X}_2^{\pm}\right) \quad , \quad \hat{X}_b^{\pm} = \frac{1}{\sqrt{2}}\left(\hat{X}_1^{\pm} - \hat{X}_2^{\pm}\right) \tag{2.165}$$

I would now like to analyse the output ports for correlations in the quadrature operators. The most straightforward way is to calculate the expectation value of the correlation coefficient between modes a and b, which are shown here for the amplitude quadrature:

$$\begin{aligned} C_{ab}^{++} &= \langle\psi|\hat{X}_a^{+}\hat{X}_b^{+}|\psi\rangle && (2.166)\\ &= [\sigma^2(\hat{X}_1^{+}) - \sigma^2(\hat{X}_2^{+})]/2 && (2.167)\\ &= [\exp(2r) - 1]/2 && (2.168) \end{aligned}$$

For the case of no squeezing, no correlation is evident: $r = 0 \implies C_{ab}^{++} = 0$. This is because one essentially couples in two independent vacuum states, for which the quadrature amplitudes add together in port a, and subtract in port b. However, for the case of arbitrarily strong squeezing, one sees an anti-correlation: $r \to -\infty \implies C_{ab}^{++} = -1/2$. The field that actually contributes to the anti-correlation comes not from the squeezed state in mode 1, but from the vacuum state in mode 2. The fact that there is a correlation is nothing special, because I could have sent in a classical state, such as a thermal state, and I also would have seen a correlation. I want to class the correlation as being either classical or nonclassical, to do this, one needs to use a related quantity: the conditional variance. The definition of the conditional variance in terms of the quadrature operators is

$$V_{a(b)}^{+(+)} = \sigma^2(\hat{X}_a^+) - \frac{|C_{ab}^{++}|^2}{\sigma^2(\hat{X}_b^+)} \tag{2.169}$$

One interpretation is that it is a measure of the reduced uncertainty in mode a when one is given the information in mode b. This is why mode b is shown in parentheses in the subscript of $V_{a(b)}^{+(+)}$. For zero correlation, the variance of mode a remains unchanged. However, if there is a correlation, then it means that there are components within X_a^+ and X_b^+ that are identical, and therefore measurements made on mode b can be used to cancel out those components on mode a, thereby reducing the variance in mode a. This can be shown explicitly by re-writing the conditional variance in the equivalent form:

$$V_{a(b)}^{+(+)} = \left\{\sigma^2(\hat{X}_a^+ - g\hat{X}_b^+)\right\}_{\min(g)} \tag{2.170}$$

where g is a gain parameter which is adjusted until the variance is at a minimum. I will now go back to the specific case of the squeezed state on a beamsplitter. The result for the conditional variance is

$$\begin{aligned} V_{a(b)}^{+(+)} &= \frac{2\,\sigma^2(\hat{X}_1^+)\,\sigma^2(\hat{X}_2^+)}{\sigma^2(\hat{X}_1^+) + \sigma^2(\hat{X}_2^+)} && (2.171) \\ &= 1 + \tanh(r) && (2.172) \end{aligned}$$

Note that the conditional variance in this expression is symmetric for modes a and b, but this was only because we had chosen a symmetric beamsplitter. If we examine the case where the input modes are not squeezed, then the conditional variance of a is equal to its ‘simple’ variance: $r = 0 \implies V_{a(b)}^{+(+)} = 1$ and $\sigma^2(\hat{X}_a^+) = 1$. This means that it was not possible to reduce the variance in a by using measurements from b. This particular case of two vacuum states as inputs to the beamsplitter is identical to the smallest conditional variance that can be achieved in the semi-classical theory of optics. The semi-classical theory of detection implies that a measurement of the amplitude quadrature using a single detector, will be shot-noise-limited, which produces a variance that is exactly the same level that is set by a coherent state, and hence also for a vacuum state in a homodyne-type measurement. Since the semi-classical theory also implies that the shot-noise originates independently from within each detector, one cannot expect to see correlations between them, and hence the conditional variance is strictly limited to unity (appropriately normalised to the intensity of the light). The consequence is that if one sees a conditional variance that is less than unity in the fully-quantised theory, then that two-mode state can be classed as being non-classical.

Returning again to the special case, as the squeezing parameter is turned on and made arbitrarily strong, the conditional variance approaches zero: $r \rightarrow -\infty \implies V^{+(+)}_{a(b)} = 0$. We can also see for weaker squeezed states that provided $r < 0$ then $V^{+(+)}_{a(b)} < 1$. Hence, a squeezed state and a vacuum state sent onto a beamsplitter produces a two-mode nonclassical state, where the correlation produced is usually referred to as a quantum-correlation. The paper of [Treps and Fabre 2004] supports these arguments on more rigourous grounds. The next question is, what has happened to the phase quadrature? Similar definitions of the conditional variance apply to the phase quadrature. For the case of squeezed light on the beamsplitter, the conditional variance is: $V^{-(-)}_{a(b)} = 1 - \tanh(r)$. Therefore if there is a quantum correlation in one quadrature, there is only a classical correlation in the other. We will see in the next section that by interfering two squeezed beams on a beamsplitter, that it is possible to see quantum correlations in both quadratures.

2.9.2 Dual Quantum correlation and EPR entanglement

The next simplest experiment is to combine two squeezed beams on a symmetric beamsplitter. We can recycle the conditional variance equations from the previous section. This time however, we start with the state $|\psi\rangle = |\zeta_1\rangle_1 \otimes |\zeta_2\rangle_2$, where $\zeta_{1,2}$ are the complex squeezing parameters $\zeta_{1,2} = r_{1,2}\exp(i\vartheta_{1,2})$. I choose the squeezing in each beam to be equal in strength but in orthogonal quadratures: $r_1 = -r_2 = r$. From Equation 2.169 and Equation 2.172 one can obtain the conditional variance for the amplitude and phase quadratures:

$$V^{+(+)}_{a(b)} = V^{-(-)}_{a(b)} = \mathrm{sech}(2r) \tag{2.173}$$

For no squeezing $r = 0$, this function has a value of one, and there is no correlation at all. As r is increased, either in the positive or negative direction, the conditional variance approaches zero. This means that for any non-zero value of r, the two-mode state that exits the beamsplitter shows quantum correlations in both the amplitude and phase quadratures. This can be called a dual quantum correlation. I will spend some time discussing the significance of this result.

In view of the classical theory of electromagnetism, the two light beams that exit a beamsplitter when one light beam is incident, are always perfectly correlated in amplitude and phase. In contrast, for the semi-classical theory, as discussed earlier, the correlations can never be free of noise, due to the shot-noise in the detection process. However, as we have seen, the full quantum theory allows for perfect correlations to be established between the two beams of light. And these correlations can be observed for both the amplitude and phase quadratures, despite the fact that they are non-commuting observables. But how can we reconcile this with the Heisenberg uncertainty principle? The principle limits the precision with which the non-commuting observables can be measured for a single mode, and not the correlations between two independent modes; see Equation 2.52. So in this formalism, there is not a problem. From a historical perspective however, this same result (but in a related system) concerned Einstein, Podolsky and Rosen (EPR) in their famous paper [Einstein *et al.* 1935]. They objected to the inherent non-local character of the correlations to the extent that they questioned whether quantum mechanics indeed even offered a complete description of physical reality.

EPR examined the situation of parent particle undergoing fission into two particles. The reaction must conserve energy and momentum, and this leads to a perfect correlation in the position and momentum of the two particles. The particles are allowed to separate from one another after travelling some distance, before the measurements are performed at station A and station B. The measurement events are completed within a time interval that is shorter than the time it takes for light to travel from A to B. Therefore the measurement events are space-like and causally separated. How is it then that correlations can appear when one later compares the measurements from A and B? Without super-luminal communication, the conclusion is that the two particles must have had either well defined position and momenta at the time of creation, or the particles had the potential to develop those position and momenta from a common hidden variable. The former is forbidden in quantum mechanics because it violates the Heisenberg uncertainty principle. The latter is not described by quan-

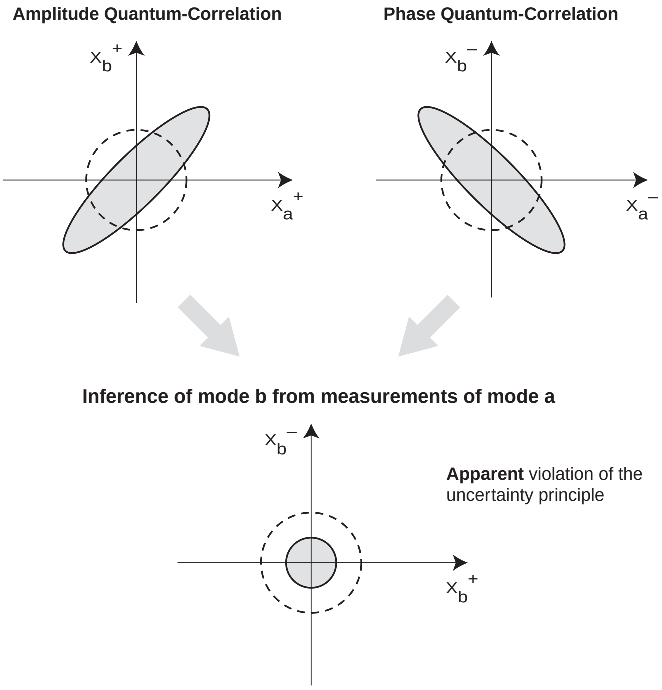

Figure 2.20: EPR entanglement visualised as dual quantum correlations. Two squeezed states are interfered on a symmetric beamsplitter. The ellipses mark a contour of the resulting two-dimensional Gaussian distribution when the quadrature measurements for each mode are plotted against each other. The resulting quantum correlations would allow an observer of the amplitude quadrature of mode a, to infer what mode b measures, to a precision better than one unit of quantum noise. This can also be done for the phase quadrature, which gives the apparent violation of the uncertainty principle. The violation is only apparent because both measurements could not be made simultaneously without paying a noise penalty.

tum mechanics at all. Hence, if one is to preserve locality, then one must reject quantum mechanics as a theory. This is the EPR paradox. The correlations are referred to as EPR correlations, or EPR entanglement.

EPR entanglement in continuous-variables was observed in an optical system by [Ou *et al.* 1992]. After this result, one must either accept that quantum mechanics is non-local, or that it is incomplete. But given the successes of quantum theory in describing the electronic structure of atoms and molecules, the philosophical debate about non-locality was put aside. Many years later, Bell proposed an experiment that could accept or reject the entire class of local hidden-variable theories [Bell 1964]. Freedman and Clauser, and Aspect *et al.* did the experiment using entangled light, and found results that were consistent with an absence of local hidden-variable theories [Freedman and Clauser 1972, Aspect *et al.* 1982]. Hence, one must accept that quantum mechanics inherently has a non-local character to it. Quantum mechanics may still be incomplete however, as the experiments did not rule out non-local hidden-variable theories.

The position and momentum of a particle are analogous to the amplitude and phase quadratures of a mode of the electromagnetic field. They share the same definition in terms of the creation-annihilation operators. A formal comparison was made by Reid in reference [Reid 1989], who also defined a criterion that could be applied to detect EPR entangled states of light based on quadrature measurements. The EPR criterion is defined as the product of the conditional variances for the amplitude and phase quadratures. There are actually two criteria, because there are two directions of inference possible in the conditional variances:

$$\varepsilon_{ab} = V_{a(b)}^{+(+)} \, V_{a(b)}^{-(-)} < 1 \tag{2.174}$$

$$\varepsilon_{ba} = V_{b(a)}^{+(+)} \, V_{b(a)}^{-(-)} < 1 \tag{2.175}$$

If the entanglement is identical in both inference directions then one simply writes the criterion as $\varepsilon < 1$. When the criterion is fulfilled, the state is in an EPR entangled state. The form of these equations are very similar to the form of the Heisenberg uncertainty principle in Equation 2.52. If we think of the conditional variance $V_{a(b)}$ as being the variance of mode a reduced by information gathered from mode b, then we can interpret the expression of the EPR criterion as an apparent violation of the uncertainty principle. The violation is only apparent because it is not possible to simultaneously measure the correlations in amplitude and phase without changing the states, by for example introducing more vacuum modes via beamsplitters. This apparent violation is illustrated in Figure 2.20, where the correlations, and their remaining uncertainty, are shown as the major and minor axes of the ellipses, respectively. The ellipse represents the contour of a two-dimensional Gaussian probability distribution. Note that the correlation diagram should not be confused with the ball-on-stick diagram for a single mode. The example shown is that of EPR entanglement made by sending two squeezed states (and squeezed in orthogonal quadratures) onto a beamsplitter.

I would like to compare our two sources of two-mode nonclassical light: one squeezed state input to a beamsplitter; and two squeezed states input to a beamsplitter. The simplified expressions are taken from Equation 2.172 and Equation 2.173 and become

$$\varepsilon_{\text{one}} = \text{sech}^2(r) \tag{2.176}$$

$$\varepsilon_{\text{two}} = \text{sech}^2(2r) \tag{2.177}$$

So we can see for $\varepsilon_{\rm one}$, that even if the state shows quantum correlations in only one quadrature, it is still possible to show EPR entanglement when r is non-zero. But the apparent violation is much stronger for the dual quantum correlation case of $\varepsilon_{\rm two}$. This makes sense. If one thinks of squeezed light as being a resource for demonstrating nonclassical effects, then having two squeezed states will give a larger effect than if one has only one squeezed state available. An argument like this leads one to considering the EPR criterion as a measure of entanglement strength. I address the idea of entanglement measures in the next section.

2.9.3 Wavefunction inseparability and entanglement measures

EPR entanglement is just one form of entanglement. The term entanglement is synonymous with wave-function *inseparability*. A wave-function that describes two or more modes is considered *separable* when it can be expressed as a product of wave-functions for each individual mode: $|\psi\rangle = |\psi_1\rangle_1 \otimes |\psi_2\rangle_2 \otimes ... \otimes |\psi_n\rangle_n$. If it is not possible to express the wave-function in this way, in at least one choice of basis states, then the wave-function is inseparable, and the state is said to be entangled. We can see how this works by taking an example from the EPR entanglement that is generated by interfering a squeezed state with a vacuum state on a symmetric beamsplitter. To simplify the analysis, I will choose to keep the strength of the squeezing small, such that the squeezed state in the Fock state expansion is approximately: $|\zeta\rangle \approx |0\rangle + \xi|2\rangle$, where $\xi \ll 1$ and can be taken from Table 2.4 for a given complex squeezing parameter ζ. The wave-function prior to the beamsplitter interaction is then

$$|\psi_{12}\rangle_{12} \approx \Big(|0\rangle_1 \, + \xi|2\rangle_1\Big) \otimes |0\rangle_2 \tag{2.178}$$

where the subscripts refer to the two input modes. The symmetric beamsplitter transforms the initial Fock states into the output modes a and b in the following way [Leonhardt 1997]:

$$|n\rangle_1 \otimes |0\rangle_2 \rightarrow \sum_{k=0}^{n} \sqrt{\mathcal{B}(n,k)}\, 2^{-n/2}\, |k\rangle_a \otimes |n-k\rangle_b \tag{2.179}$$

where n is the Fock state number and $\mathcal{B}(n,k)$ is the binomial of k objects selected from a set of n objects. The final state can then be approximated as

$$\begin{aligned}|\psi_{ab}\rangle_{ab} &\approx |0\rangle_a \otimes |0\rangle_b + \frac{\xi}{\sqrt{2}}|1\rangle_a \otimes |1\rangle_b + \frac{\xi}{2}|0\rangle_a \otimes |2\rangle_b + \frac{\xi}{2}|2\rangle_a \otimes |0\rangle_b \quad (2.180)\\ &\neq |\psi_a\rangle_a \otimes |\psi_b\rangle_b \quad (2.181)\end{aligned}$$

This state cannot be expressed as a product of states for the modes a and b, and hence the state is inseparable and therefore entangled. Although EPR correlations in the quadrature amplitudes are not as obvious to see as in Equation 2.176, one can immediately see a simple form of discrete-variable entanglement. The measurement of two photons in mode a guarantees that no photons will be detected in mode b. Although Equation 2.181 serves as a criterion/definition to detect entanglement, is it possible to quantify the strength of the entanglement in some way? The inseparability criterion of Duan and others allows one to compute a number $\mathcal{I}$ from the entire class of two-mode Gaussian entangled states [Duan *et al.* 2000]. Gaussian states are those typically produced by interfering squeezed light sources on beamsplitters. The Gaussian label refers to the form of the (four-dimensional) Wigner function that describes the two-mode state. The criterion $\mathcal{I} < 1$ then detects those entangled states. To compute $\mathcal{I}$ one needs to have access to the first-order correlation matrix of the quadrature amplitudes, which means writing down all combinations of the correlation coefficients $C_{ab}^{\pm\pm}$, as defined in Equation 2.166. The coefficients are usually arranged into a matrix M that is made up of other matrices such that

$$M = \begin{bmatrix} G_{11} & G_{12} \\ (G_{12})^T & G_{22} \end{bmatrix} \quad (2.182)$$

where

$$G_{11} = \begin{bmatrix} C_{aa}^{++} & C_{aa}^{+-} \\ C_{aa}^{-+} & C_{aa}^{--} \end{bmatrix} \quad (2.183)$$

and

$$G_{22} = \begin{bmatrix} C_{bb}^{++} & C_{bb}^{+-} \\ C_{bb}^{-+} & C_{bb}^{--} \end{bmatrix} \quad (2.184)$$

and

$$G_{12} = \begin{bmatrix} C_{ab}^{++} & C_{ab}^{+-} \\ C_{ab}^{-+} & C_{ab}^{--} \end{bmatrix} \quad (2.185)$$

and $(G_{12})^T$ is the transpose of G_{12}. Before the inseparability can be calculated, one needs to perform local unitary operations to each mode, in order to bring the correlation matrix into *Standard Form I*. This removes any cross-quadrature correlations, and since the operations are local, they in no way influence the inseparability of the state, but rather only optimise how well the entanglement is measured. The allowed operations are the squeezing operator in Table 2.4, and quadrature rotation as shown in Equation 2.44. When the operations are done properly, the correlation matrix will have the form

$$M'=\begin{bmatrix} n & 0 & c & 0 \\ 0 & n & 0 & c' \\ c & 0 & m & 0 \\ 0 & c' & 0 & m \end{bmatrix} \tag{2.186}$$

Those new elements can be found by using the following identities with the determinants: $\det(G_{11}) = n^2$, $\det(G_{22}) = m^2$, $\det(G_{12}) = cc'$, and $\det(M) = (nm - c^2)(nm - c'^2)$ as given in [Duan *et al.* 2000]. The rotation operation has removed the cross-quadrature terms, and the squeezing operation has equalised the amplitude and phase quadrature variances.

The next step in the optimisation is to apply local squeezing operations r_1 and r_2 to bring the matrix into *Standard Form II*. When in this form, the elements satisfy the following two conditions:

$$\frac{n/r_1 - 1}{nr_1 - 1} = \frac{m/r_2 - 1}{mr_2 - 1} \tag{2.187}$$

and

$$|c|\sqrt{r_1 r_2} - |c'|/\sqrt{r_1 r_2} = \sqrt{(nr_1 - 1)(mr_2 - 1)} - \sqrt{(n/r_1 - 1)(m/r_2 - 1)} \tag{2.188}$$

These two equations must be solved for r_1 and r_2. In general there are eight solutions, and one must select the one that returns the lowest value of inseparability. The matrix in standard form II then looks like

$$M''=\begin{bmatrix} nr_1 & 0 & c\sqrt{r_1 r_2} & 0 \\ 0 & n/r_1 & 0 & c'/\sqrt{r_1 r_2} \\ c\sqrt{r_1 r_2} & 0 & mr_2 & 0 \\ 0 & c'/\sqrt{r_1 r_2} & 0 & m/r_2 \end{bmatrix} \tag{2.189}$$

The elements of the correlation matrix in standard form II can then be entered into the expression for inseparability:

$$\mathcal{I} = \frac{1}{2}\left(C_I^+ + C_I^-\right) / \left(k + 1/k\right) \tag{2.190}$$

where

$$\begin{aligned} C_I^+ &= k(nr_1) + (1/k)(mr_2) - 2|c\sqrt{r_1 r_2}| && (2.191) \\ C_I^- &= k(n/r_1) + (1/k)(m/r_2) - 2|c'/\sqrt{r_1 r_2}| && (2.192) \end{aligned}$$

and

$$k = \sqrt{\frac{mr_2 - 1}{nr_1 - 1}} = \sqrt{\frac{m/r_2 - 1}{n/r_1 - 1}} \tag{2.193}$$

The variables $C_I^\pm$ are similar to the conditional variances used in the EPR criterion. The factor k is there to correct for any imbalance between the sub-systems, which is related to the direction of inference for the conditional variances. The inseparability criterion using the definition in Equation 2.190 is given by

$$\begin{aligned} \mathcal{I} &< 1 \quad \text{(inseparable)} && (2.194) \\ \mathcal{I} &\geq 1 \quad \text{(separable)} && (2.195) \end{aligned}$$

The inseparability criterion is a necessary and sufficient criterion for Gaussian entanglement. If the optimisation procedure on the correlation matrix was performed correctly (giving the standard form II), then the inseparability criterion will detect even the smallest amount of entanglement. This is in contrast to the EPR criterion which is only a sufficient criterion for detecting entanglement, and misses out on detecting some entangled states, for example those that have been severely optically attenuated.

There is an equivalent way of representing inseparability: the *product form* given by $\mathcal{I} = \sqrt{C_I^+ C_I^-}/(k + 1/k)$. It is shown in [Bowen *et al.* 2004] that provided the conditions in Equation 2.187 and Equation 2.188 are met, that the product form is equivalent to the original *sum form* in Equation 2.190. There is another form of inseparability that is commonly used by experimentalists because the measurement is much simpler than recording all the elements of the correlation matrix:

$$\mathcal{I}_{\mathrm{unopt}} = \langle\psi|(\hat{X}_a^+ \pm \hat{X}_b^+)^2|\psi\rangle + \langle\psi|(\hat{X}_a^- \mp \hat{X}_b^-)^2|\psi\rangle \tag{2.196}$$

The quadrature amplitudes measured on each subsystem are simply added or subtracted from one another before the variance is calculated. The sign of the sum is chosen to minimise the inseparability. It should be noted that this method is equivalent to setting $r_1 = r_2 = k = 1$ in the definition of the original form of the inseparability, and hence:

$$\mathcal{I}_{\mathrm{unopt}} = \frac{1}{4}\left(C_{aa}^{++} + C_{bb}^{++} + C_{aa}^{--} + C_{bb}^{--} - 2|C_{ab}^{++}| - 2|C_{ab}^{--}|\right) \geq \mathcal{I} \tag{2.197}$$

From this we can deduce that $\mathcal{I}_{\mathrm{unopt}} < 1$ is a sufficient but not necessary condition for entanglement. Hence, $\mathcal{I}_{\mathrm{unopt}}$, or the *unoptimised* inseparability, can be indeed be used to detect entanglement, but not all kinds of entanglement will be caught. These ideas naturally lead to the idea of measuring the entanglement based on the EPR and inseparability criteria.

2.9.4 Entanglement measures

A good measure of entanglement would increase or decrease monotonically with the ‘strength’ of the entanglement, and ideally would respond linearly too. How to define the ‘strength’ however, is largely subjective. It is for this reason that there is no one measure, but many measures that each respond to a different aspect of entanglement. For example: inseparability of the state [Duan *et al.* 2000, Horodecki 1997], logarithmic negativity [Plenio 2005], and the EPR criterion [Reid 1989]. The EPR criterion for entanglement, as defined in Equation 2.175 and discussed in Section 2.9.2, can be extended to a measure of entanglement. This is in the sense that the smaller the value of ϵ, the greater the apparent violation of the Heisenberg uncertainty principle, as seen by the shrinking area formed by the inferred quadrature variances, as shown in Figure 2.20. The relationship is monotonically decreasing, and at $\epsilon = 0$ the two subsystems are perfectly correlated in amplitude and phase. But as the EPR criterion is only sufficient, it can only be used as a measure of *EPR* entanglement, and not other forms of entanglement.

Although the inseparability criterion has its roots in the simple idea of separability of the wave-function, the calculation itself is less transparent. One interpretation is that $\mathcal{I}$

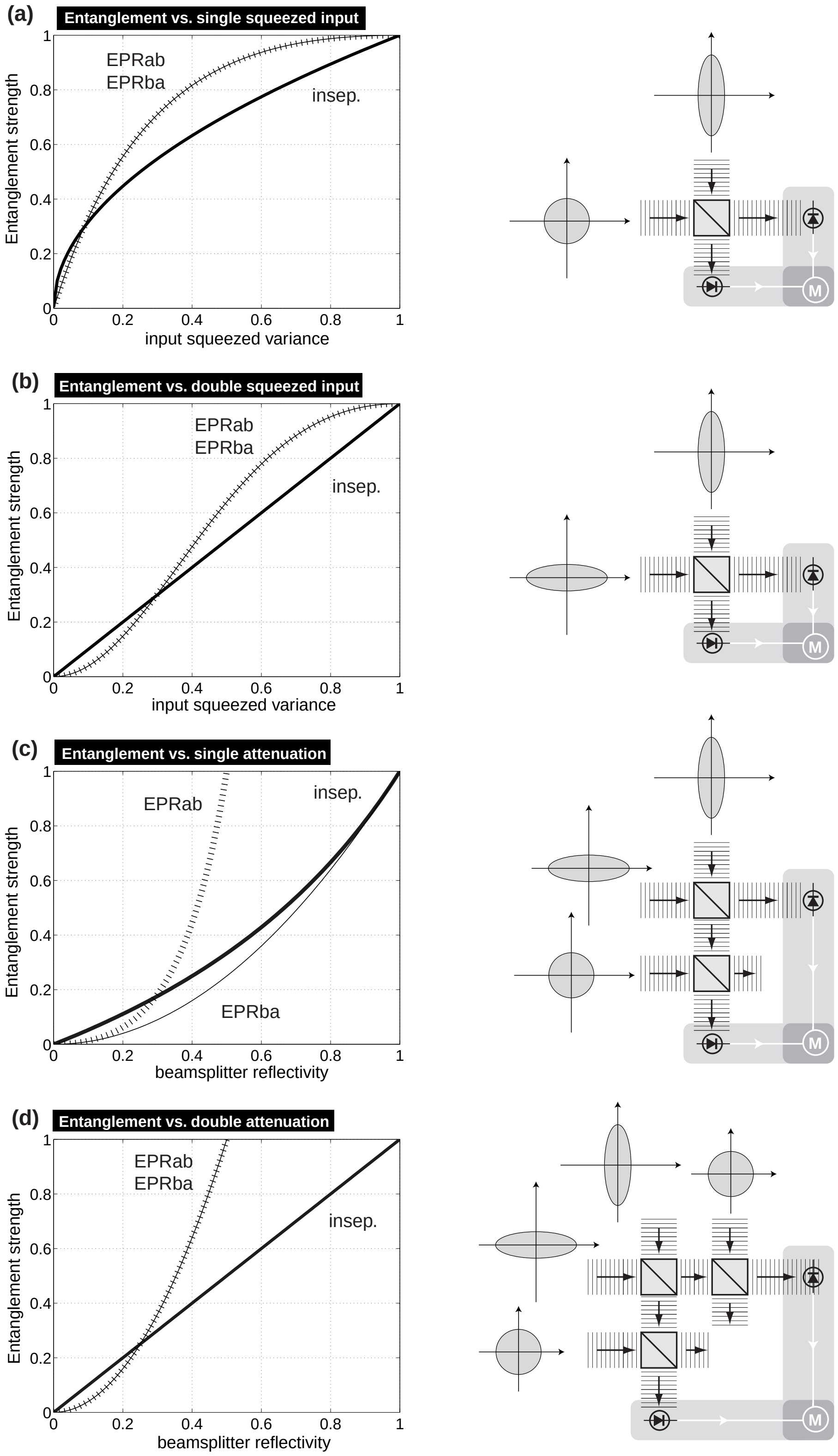

Figure 2.21: EPR and inseparability are examined in four different entanglement 'experiments'. The entanglement is generated by interfering one or two squeezed states on a symmetric beamsplitter. 'M' represents the measurement of the correlation matrix. (a) and (b) are functions of the input squeezed variance $\sigma^2(\hat{X}^+_{1,2}) \in \{0,1\}$. (c) and (d) are functions of the beamsplitter reflectivity $\eta \in \{0,1\}$ that is used to model the attenuation, while the input squeezing is held constant: $\sigma^2(\hat{X}^+_{1,2}) = 0$.

can be used as a measure of 'how separable' the state is. Given for example a two-mode Gaussian entangled state described by the Wigner function $W_{\text{insep}}(x_a^+, x_a^-, x_b^+, x_b^-)$, how good can the overlap integral with another state that is separable $W_{\text{sep}}(x_a^+, x_a^-, x_b^+, x_b^-)$ be? The overlap integral would be taken over all the coordinates of the Wigner functions, and the entire space of Wigner functions for separable states W_{sep} would be searched such that the integrand (F) is maximised. In this sense we can see that F would behave similarly to $\mathcal{I}$. If the state under test is separable then a separable state can be found such that $F = 1$ while $\mathcal{I} \geq 1$. If the state is inseparable then no separable state can have a perfect overlap, hence $F < 1$ for all $\mathcal{I} < 1$. The inseparability is therefore qualitatively consistent with a measure of how separable a state is.

Further evidence that EPR and inseparability are good measures of entanglement, is how they behave as functions of the squeezed light resources that are used to generate the entangled states, and also as a function of optical attenuation applied to those states. An example of this is made in four 'experiments' in Figure 2.21. The calculational building blocks have already been covered in Sections: 2.7.2; 2.9.2; 2.9.3. I will not show the analytical results here. From graphs (a) and (b), one can see that low values of $\mathcal{I}$ and ϵ are consistent with the notion that strong entanglement is generated by strong squeezing. In (c) and (d), the entangled state is attenuated by one or two beamsplitters which has the effect of increasing the values of $\mathcal{I}$ and ϵ. This is consistent with the notion that entanglement strength should be reduced by attenuation because uncorrelated vacuum states are introduced during the process, and these degrade the quantum correlations. Note that EPR and inseparability are not analogous to the Fahrenheit and Celsius temperature scales. There is no one-to-one correspondence between the two. The correspondence changes depending on the details of how the entanglement was produced and detected.

A further refinement to characterising entanglement is the *bias* property. The easiest way to see this is to compare the entanglement sources that are based on either one, or two, sources of squeezed light; see Section 2.9.2. For the case of entangled light based on a single source of squeezed light, a quantum correlation will only be observed in one quadrature and not the other, hence the entanglement is *biased* in that observable. Whether a source of entanglement is biased or not affects the efficacy of some quantum information protocols, such as teleportation. The concept of biased entanglement is put on a more rigourous footing in [Bowen *et al.* 2003a]. Another property unique to the EPR measure, is the fact that there are really two measures, one for each direction of inference. For the remainder of this thesis, I will refer to this difference as the *balance* between the subsystems. There have also been other ways of characterising Gaussian entangled states according to various classes [DiGuglielmo *et al.* 2007]. One of the most recent proposals for an entanglement measure is *logarithmic negativity*. This measure gives a value for the number of entangled bits of information that could be extracted from the entangled state [Plenio 2005]. For the remainder of this thesis however, I will solely use the EPR and inseparability measures to characterise entangled states.

With this section I conclude the chapter on quantum optics theory. The material covered is by far not representative of the true breadth and depth that the field of quantum optics has acquired. But I hope that it is complete enough to serve as a reference to support the thesis topics that follow.

Chapter 3

Harmonic Entanglement: Theory

The main message of this chapter is that a degenerate optical parametric amplifier (OPA) is capable of producing harmonic entanglement. I build on this by explaining how the classical behaviour of the OPA influences the strength and type of harmonic entanglement. The story splits up into an analysis of the classical field and an analysis of the quantum fluctuations, before combining again to give an interpretation of the harmonic entanglement phenomenon. This work forms part of a collaboration that was initiated by W. P. Bowen and K. McKenzie. It has been published under the following reference:

- *Harmonic Entanglement with Second-Order Nonlinearity,*
  N. B. Grosse, W. P. Bowen, K. McKenzie and P. K. Lam,
  Phys. Rev. Lett. **96**, 063601 (2006).

3.1 Background

We have already encountered the method of generating quadrature entanglement by using a beamsplitter to interfere two squeezed states; see Section 2.9.2. The entanglement that is generated, is between two modes that are equal in optical frequency. But what if my aim was now to generate entanglement between two different optical frequencies? Could I do this in a similar way? The answer is no, because the beamsplitter can only interfere two modes that have the same magnitude of the propagation vector. What we need is a 'nonlinear beamsplitter' that would allow the interaction of two different wavelengths. Fortunately, a medium that has a second-order nonlinear response, does indeed allow such an interaction between two modes of light: the *fundamental* and *second-harmonic*. The presence of quadrature entanglement between these two modes is referred to as *harmonic entanglement*.

Harmonic entanglement is a special case of the more general two-colour entanglement. One of the first sources of entangled light was actually two-colour entanglement between 423 nm and 551 nm [Kocher and Commins 1967]. The entanglement was measured in the polarisation correlations of the light emitted in a two-photon cascade from the energy levels in a gas of Calcium atoms. A similar source was used to test Bell's theorem for local hidden-variables [Freedman and Clauser 1972, Fry and Thompson 1976, Aspect *et al.* 1982]. The atomic-based sources were later replaced by nonlinear BBO or KTP crystals [Kwiat *et al.* 1995]. When these were pumped with intense light pulses and operated under the correct phase matching conditions, they could produce entanglement between colours that were separated by up to 740 nm in wavelength [Pelton *et al.* 2004]. Although the physical process is similar to the non-degenerate optical parametric oscillator (OPO), the conversion is done only in a single-pass for which the conversion rate is so weak that single photons can be resolved, and the entanglement verified, in the discrete-variable (DV) regime.

In contrast, entangled light sources that were designed to be measured in the continuous-variable (CV) regime, were usually limited to the case of degenerate or near-degenerate $(\approx 1\,\mathrm{GHz})$ optical parametric oscillation [Schori *et al.* 2002]. The main reason is that in order to verify entanglement in the CV regime, one needs to be able to measure the amplitude *and* phase quadratures. Without some form of reference beam that is coherent with the entanglement source, access to the phase quadrature is not possible. One way around this is to reflect the entangled light from an under-coupled narrow-linewidth optical resonator. When the resonator is de-tuned, the phase quadrature can be rotated into the amplitude quadrature. This method was used to demonstrate entanglement for colours that were separated by up to 1 nm [Villar *et al.* 2005, Su *et al.* 2006].

The aim was to further increase the separation of the wavelengths in two-colour entanglement. Quantum correlations between the fundamental and second-harmonic fields in second-harmonic generation (SHG) had been proposed by [Horowicz 1989] and were later observed by [Li *et al.* 2007, Cassemiro *et al.* 2007]. But the necessary phase information was lacking to confirm the presence of harmonic entanglement. That harmonic entanglement should be measurable in a travelling-wave SHG was proposed by [Olsen 2004]. The strength of the entanglement according to the inseparability criterion was however fundamentally limited in this system. This is a similar result to the limitation of squeezed light generation via SHG, where 3 dB is the best squeezing level obtainable [White *et al.* 1997]. Systems where the squeezing level is not limited in this way, are the degenerate OPO and OPA; see [Wu *et al.* 1986]. The current record for squeezing is 10 dB from OPO [Vahlbruch *et al.* 2008].

We chose to study the degenerate OPA in a cavity environment as a candidate for producing harmonic entanglement because it was already a proven source of strong levels of squeezing on the fundamental field, and because in certain regimes of operation, large conversions between the fundamental and second-harmonic fields can occur. To summarise, the hypotheses that I would like to test in this chapter are:

- A model of degenerate OPA can produce harmonic entanglement.
- To produce entanglement, the OPA must support an exchange of energy between the fundamental and second-harmonic fields.
- The strength of harmonic entanglement in the OPA region is only limited by intracavity losses.

Provided that these hypotheses can agree with our model of OPA, then one can begin to speculate on the possible applications for such a source of harmonic entanglement. Central to modern techniques in optical metrology has been the ability to make connections between light beams that span an octave in optical frequency. This development has realised the optical-comb whose offset-frequency can be directly linked to the SI definition of the second [Udem *et al.* 2002]. As such, spectroscopic measurements can now be made with an absolute accuracy beyond one part in 10^{15} [Holzwarth *et al.* 2000], and have enabled unprecedented testing of fundamental quantum mechanical effects [Fischer *et al.* 2004]. Harmonic entanglement has the potential to be applied to the heterodyne stabilisation of optical-combs used in metrology [Diddams *et al.* 2000]. In the heterodyne scheme, a fraction of the frequency comb is tapped off, and interfered with two reference (local oscillator) beams, the fundamental and second-harmonic field produced by a Nd:YAG laser and SHG. The SHG guarantees the harmonic relationship between the two local oscillator beams. The two resulting beat notes with the frequency comb are compared by taking their difference, and this error signal is used to stabilise the offset frequency of the comb to an atomic clock standard. If one were to replace the local oscillators with harmonically entangled local oscillators, then the difference signal will be quantum correlated, and will therefore show a noise floor that is reduced below the shot-noise-limit. This would in principle ensure a better signal-to-noise ratio for the desired error signal, and would allow better locking of the frequency comb to the atomic clock standard.

3.2 Advanced model of OPA (with pump-depletion)

The OPA model that I will present here is an extension to the simple OPO model that was derived in Section 2.8.2. Although the equations of motion for the fields are identical, it is the removal of some assumptions in the calculation that introduces another level of complexity. The classical behaviour and quantum statistics of the fields was already analysed in [Drummond *et al.* 1980], but the authors did not analyse the correlations between the fields. In the next sections, I will analyse the correlations between the seed and pump fields and show that they meet the EPR and inseparability criteria of entanglement, and therefore for harmonic entanglement.

The system under analysis consists of a second-order nonlinear medium enclosed within an optical resonator as shown in Figure 3.1. The resonator is coupled to the environment through two partially reflective mirrors. One mirror represents an input/output coupler, while the other represents uncontrollable coupling (loss) to all other environmental modes. The non-linear medium induces an interaction between the two intra-cavity fields. The aim here is to investigate the level of harmonic entanglement that this interaction can achieve between the reflected output fields. The system is described by the following equations of motion [Drummond *et al.* 1980]:

$$\frac{\mathrm{d}\hat{a}}{\mathrm{d}t} = -\kappa_a\hat{a} + \epsilon\hat{a}^\dagger\hat{b} + \hat{A}_{\mathrm{in}} \tag{3.1}$$

$$\frac{\mathrm{d}\hat{b}}{\mathrm{d}t} = -\kappa_b\hat{b} - \frac{1}{2}\epsilon\hat{a}^2 + \hat{B}_{\mathrm{in}}, \tag{3.2}$$

where $\hat{a}$ and $\hat{b}$ are Heisenberg picture annihilation operators describing the intra-cavity fundamental and second harmonic fields respectively; κ_a and κ_b are the associated total resonator decay rates; ϵ is the nonlinear coupling strength between the fields; and $\hat{A}_{\rm in}$ and $\hat{B}_{\rm in}$ represent the accumulated input fields to the system. The partially reflective mirrors modelling input/output coupling and loss are distinguished with the subscripts '1' and '2', respectively; while the input and reflected fields are denoted by the subscripts 'in' and 'ref'. Using this terminology $\kappa_a = \kappa_{a1} + \kappa_{a2}$, $\kappa_b = \kappa_{b1} + \kappa_{b2}$, $\hat{A}_{\rm in} = \sqrt{2\kappa_{a1}}\hat{A}_{1,{\rm in}} + \sqrt{2\kappa_{a2}}\hat{A}_{2,{\rm in}}$, and $\hat{B}_{\rm in} = \sqrt{2\kappa_{b1}}\hat{B}_{1,{\rm in}} + \sqrt{2\kappa_{b2}}\hat{B}_{2,{\rm in}}$.

The solutions to Equation 3.1 and Equation 3.2 are obtained through the technique of linearisation, where operators are expanded in terms of their coherent amplitude and quantum noise operator, so that $\hat{a} = \alpha + \delta\hat{a}$ and $\hat{b} = \beta + \delta\hat{b}$ with $\langle\delta\hat{a}\rangle = \langle\delta\hat{b}\rangle = 0$, and second-order terms in the quantum noise operators are neglected. By isolating just the coherent amplitude part, one gets the classical OPA equations of motion:

$$\frac{{\rm d}\alpha}{{\rm d}t} = -\kappa_a\alpha + \epsilon\alpha^*\beta + \alpha_{\rm in} \tag{3.3}$$

$$\frac{{\rm d}\beta}{{\rm d}t} = -\kappa_b\beta - \frac{1}{2}\epsilon\alpha^2 + \beta_{\rm in} \tag{3.4}$$

The classical equations are readily solved using analytical techniques. The quantum fluctuations of the intra-cavity fields can be obtained from Equation 3.1 and Equation 3.2 by applying the linearisation, and neglecting the second order terms in the quantum noise operators, thereby giving:

$$\frac{{\rm d}\,\delta\hat{a}}{{\rm d}t} = -\kappa_a\,\delta\hat{a} + \epsilon(\alpha^*\,\delta\hat{b} + \beta\,\delta\hat{a}^\dagger) + \delta\hat{A}_{\rm in} \tag{3.5}$$

$$\frac{{\rm d}\,\delta\hat{b}}{{\rm d}t} = -\kappa_b\,\delta\hat{b} - \epsilon\alpha\,\delta\hat{a} + \delta\hat{B}_{\rm in} \tag{3.6}$$

These quantum operator equations can be solved by taking the Fourier transformation, and by supplying the classical intra-cavity field solutions α, β. In this sense, it is then the classical behaviour of the system that drives the quantum statistical behaviour. Although the classical and quantum models can be solved analytically, I must use a case study approach to visualise the behaviour of the system in graphs. The OPA model parameters that I used are given in Table 3.1. Note that the scale of the values were chosen to allow the numerical evaluation to proceed with minimal error. The nonlinear interaction strength ϵ is in most experiments much weaker ($\approx 10^{-4}$ of typical κ_a). However, in the diagrams to follow, the input seed and pump fields are re-scaled to their respective threshold levels, $\alpha_{\mathrm{in,c}}$ and $\alpha_{\mathrm{in,c}}$, and the final diagrams turn out to be invariant to any changes in ϵ, and choosing a particular value of ϵ is made redundant. A similar scale-invariance applies to the cavity decay rates: κ_a and κ_b, but only if their *ratio* is preserved. The ratio was chosen to be strongly resonant for the seed field, and weakly resonant for the pump field.

3.3 Classical OPA behaviour

Although based on the same equations of motion as the OPO in Section 2.8.2, the removal of several simplifying assumptions creates a great deal of complex behaviour in the advanced OPA. A diagram labelling the input and output fields is shown in Figure 3.1. I will begin with the classical equations of motion as given in Equation 3.3 and Equation 3.4. For convenience, I have collected all the definitions of the variables into Table 3.1. Later I will explain where the definitions of the critical seed and pump fields come from. The aim now is to solve these equations for the intra-cavity fundamental and second-harmonic fields in the steady state: $\frac{\mathrm{d}\alpha}{\mathrm{d}t} = \frac{\mathrm{d}\beta}{\mathrm{d}t} = 0$. By appropriately choosing the cavity parameters $\kappa_b \gg \kappa_a$, we can make sure that the second-harmonic field inside the cavity decays much more quickly than the fundamental field. This allows us to solve for β in Equation 3.4:

$$\beta = -\frac{\epsilon}{2\kappa_b}\alpha^2 + \frac{\beta_{\mathrm{in}}}{\kappa_b} \tag{3.7}$$

and substitute it into Equation 3.3 to get:

$$0 = -\kappa_a\alpha + \frac{\epsilon\beta_{\mathrm{in}}}{\kappa_b}\alpha^* - \frac{\epsilon^2}{2}|\alpha|^2\alpha + \alpha_{\mathrm{in}} \tag{3.8}$$

The problem then reduces to solving Equation 3.8 for α. I will start by treating the special cases of OPO, SHG, and OPA separately, before combining them into one diagram.

Having the solution is not enough, because the stability must also be checked. This is determined by calculating the four eigenvalues taken from a perturbation analysis of Equation 3.3 and Equation 3.4. I will simply take these from the derivation as found in

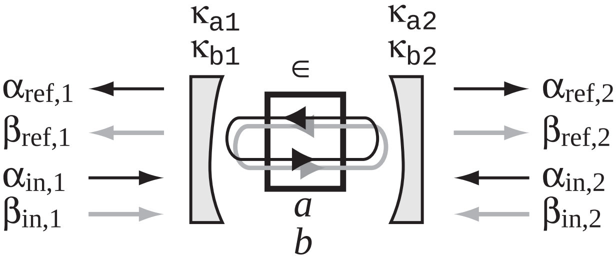

Figure 3.1: The OPA model consists of a second-order nonlinear medium enclosed by an optical resonator. Mirror 1 acts as the input/output coupler, while mirror 2 represents loss to the environment.

OPA MODEL PARAMETERS:			
nonlinear coupling constant:	ϵ	=	$1.0\ [\mathrm{s}^{-1/2}]$
mirror 1 coupling rate for seed:	κ_{a1}	=	$1.0\ [\mathrm{s}^{-1}]$
mirror 1 coupling rate for pump:	κ_{b1}	=	$10.0\ [\mathrm{s}^{-1}]$
mirror 2 coupling rate for seed:	κ_{a2}	=	$0.01\ [\mathrm{s}^{-1}]$
mirror 2 coupling rate for pump:	κ_{b2}	=	$0.1\ [\mathrm{s}^{-1}]$
seed driving field (normalised):	α_{d}	=	$\pm$ variable $[\#]$
pump driving field (normalised):	β_{d}	=	$\pm$ variable $[\#]$
SOLVE FOR THESE VARIABLES:			
intra-cavity fundamental field:	α	=	$[\#]$
intra-cavity second-harmonc field:	β	=	$[\#]$
OTHER DEFINITIONS:			
total cavity decay rate for seed:	κ_a	=	$\kappa_{a1} + \kappa_{a2}$
total cavity decay rate for pump:	κ_b	=	$\kappa_{b1} + \kappa_{b2}$
critical input seed field on mirror 1:	$\alpha_{\mathrm{in,1,c}}$	=	$(2\kappa_a + \kappa_b)[2\kappa_b(\kappa_a + \kappa_b)]^{1/2}/(\epsilon\sqrt{2\kappa_{a1}})$
critical input pump field on mirror 1:	$\beta_{\mathrm{in,1,c}}$	=	$\kappa_a\kappa_b/(\epsilon\sqrt{2\kappa_{b1}})$
critical intra-cavity fundamental:	$\alpha_{\mathrm{in,c}}$	=	$(2\kappa_a + \kappa_b)[2\kappa_b(\kappa_a + \kappa_b)]^{1/2}/\epsilon$
critical intra-cavity second-harmonic:	$\beta_{\mathrm{in,c}}$	=	$\kappa_a\kappa_b/\epsilon$
input seed field on mirror 1:	$\alpha_{\mathrm{in,1}}$	=	$\alpha_{\mathrm{d}} \times \alpha_{\mathrm{in,1,c}}\ [\mathrm{s}^{-1/2}]$
input pump field on mirror 1:	$\beta_{\mathrm{in,1}}$	=	$\beta_{\mathrm{d}} \times \beta_{\mathrm{in,1,c}}\ [\mathrm{s}^{-1/2}]$
input seed field on mirror 2:	$\alpha_{\mathrm{in,2}}$	=	$0\ [\mathrm{s}^{-1/2}]$
input pump field on mirror 2:	$\beta_{\mathrm{in,2}}$	=	$0\ [\mathrm{s}^{-1/2}]$
total input seed field:	α_{in}	=	$\sqrt{2\kappa_{a1}}\alpha_{\mathrm{in,1}} + \sqrt{2\kappa_{a2}}\alpha_{\mathrm{in,2}}\ [\mathrm{s}^{-1}]$
total input pump field:	β_{in}	=	$\sqrt{2\kappa_{b1}}\beta_{\mathrm{in,1}} + \sqrt{2\kappa_{b2}}\beta_{\mathrm{in,2}}\ [\mathrm{s}^{-1}]$
reflected seed field on mirror 1:	$\alpha_{\mathrm{ref,1}}$	=	$\sqrt{2\kappa_{a1}}\alpha - \alpha_{\mathrm{in,1}}$
reflected pump field on mirror 1:	$\beta_{\mathrm{ref,1}}$	=	$\sqrt{2\kappa_{b1}}\beta - \beta_{\mathrm{in,1}}$
reflected seed field on mirror 2:	$\alpha_{\mathrm{ref,2}}$	=	$\sqrt{2\kappa_{a2}}\alpha - \alpha_{\mathrm{in,2}}$
reflected pump field on mirror 2:	$\beta_{\mathrm{ref,2}}$	=	$\sqrt{2\kappa_{b2}}\beta - \beta_{\mathrm{in,2}}$

Table 3.1: Fixed and variable parameters used for the OPA model. The appropriate SI units are given. The $\#$ symbol is dimensionless.

[Drummond *et al.* 1980]. The eigenvalues are:

$$\lambda_1, \lambda_2 = -\frac{1}{2}\{-|\epsilon\beta| + \kappa_a + \kappa_b\} \pm \frac{1}{2}\{(-|\epsilon\beta| + \kappa_a - \kappa_b)^2 - 4|\epsilon\alpha|^2\}^{1/2} \quad (3.9)$$

$$\lambda_3, \lambda_4 = -\frac{1}{2}\{|\epsilon\beta| + \kappa_a + \kappa_b\} \pm \frac{1}{2}\{(|\epsilon\beta| + \kappa_a - \kappa_b)^2 - 4|\epsilon\alpha|^2\}^{1/2} \quad (3.10)$$

If the real components of all four eigenvalues are negative, then the solutions are stable. Having a nonzero imaginary component means that the solutions are damped oscillations. The fields that exit/reflect from the cavity mirrors, $\alpha_{\mathrm{ref},1}$ and $\beta_{\mathrm{ref},1}$, can be obtained via the input-output relation [Collett and Gardiner 1984]. Their definitions are given in Table 3.1.

3.3.1 The phase-space diagram

I am interested in seeing how the intra-cavity fields behave as a function of the input seed and pump fields. If I only allow α_{in} and β_{in} to take on real values, then it makes sense to plot a quantity of interest as a function of these two variables in a phase-space diagram. The result is a map that shows where (in the sense of what values of $\alpha_{\mathrm{in}}, \beta_{\mathrm{in}}$) one can expect to find interesting properties, such as large amplification. This method was used successfully by [Drummond *et al.* 1980] to locate much of the interesting OPA behaviour in the two-dimensional space. I continue investigating the phase-space diagram in this way, but I also ensure that the scaling is equal for both axes, such that all points on a circle correspond to the same total optical power going into the OPA. This helps when one is trying to make comparisons with an experimental setup or with experimental results.

In the phase-space diagram, the seed field occupies the horizontal axis which represents the SHG process. The pump field occupies the vertical axis which is the OPO process. Figure 3.2(a) shows all of the stability regions that will be discussed in this chapter. The range of seed and pump field amplitudes is however much larger than is currently accessible by experimentalists. The stability regions that I will concentrate on are shown in Figure 3.2(b); these include bi-stable and complex-valued OPA. I have also distinguished between OPA amplification and OPA de-amplification regions. The circle shows a total input power that is equal to OPO threshold power. I will now examine each of these regions in detail.

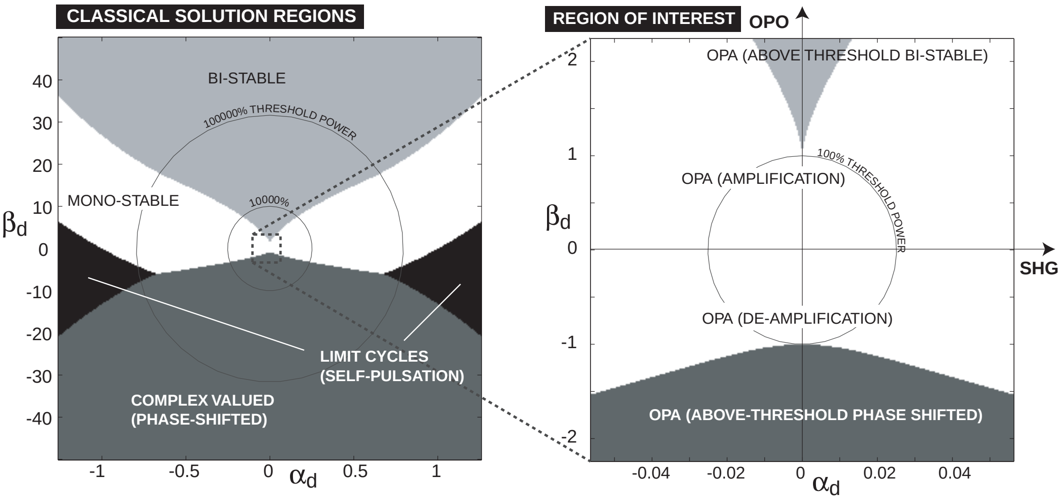

Figure 3.2: A stability analysis of the OPA solutions reveals a range of behaviour: mono-stability, bi-stability, out-of-phase (complex-valued) mono-stability, and self-pulsation. The driving fields are normalised to the critical amplitude for self-pulsation in SHG, and the threshold amplitude for OPO. Circles mark the total input power to the system. Left: large scale structure. Right: regions that are accessible by current experimental techniques.

3.3.2 OPO

The first case is where only the pump field is driving the system, such that $\alpha_{\rm in} = 0$. There are three possible solutions. Which of them is stable depends on the value of the pump amplitude:

$$\alpha = 0 \quad , \quad \beta = \beta_{\rm in}/\kappa_b \quad , \quad |\beta_{\rm in}| < \beta_{\rm in,c} \tag{3.11}$$

$$\alpha = \pm\left[\frac{2}{\epsilon}(|\beta_{\rm in}| - \beta_{\rm in,c})\right]^{1/2} \quad , \quad \beta = \kappa_a/\epsilon \quad , \quad |\beta_{\rm in}| \geq \beta_{\rm in,c} \tag{3.12}$$

$$\alpha = \pm {\rm i}\left[\frac{2}{\epsilon}(|\beta_{\rm in}| - \beta_{\rm in,c})\right]^{1/2} \quad , \quad \beta = \kappa_a/\epsilon \quad , \quad |\beta_{\rm in}| \leq -\beta_{\rm in,c} \tag{3.13}$$

The threshold/critical value is $\beta_{\rm in,c}$, which is used to define the normalised driving field $\beta_{\rm d}$; see Table 3.1. When operated below OPO threshold $(|\beta_{\rm in}| < \beta_{\rm in,c})$, there is no light produced at the fundamental frequency. But the quantum fluctuation analysis in Section 2.8.2 showed that it was in this regime that strong squeezing is produced. The classical OPO model produces light at the fundamental only when the pump field is above the threshold level; see Figure 3.3(a). Interestingly, the intra-cavity second-harmonc field remains at a constant value, even if the input pump field is increased. Note that there are two solutions for the fundamental field: one for each sign of the pump field. The meaning of the sign is a relative phase shift between the fundamental and second-harmonic fields. But below threshold, the meaning of relative phase is denied because $\alpha = 0$. One interpretation is that a kind of symmetry breaking has to occur along the transition from below- to above-threshold. These solutions are stable and have negative real eigenvalues. However for the above-threshold solutions, they have only pure real eigenvalues when the following set of criteria are met:

$$|\beta_{\rm in}| \quad > \quad \beta_{\rm in}^{c} + \kappa_b^2/8\epsilon \tag{3.14}$$

$$|\beta_{\rm in}| \quad > \quad \beta_{\rm in}^{c} + (2\kappa_a - \kappa_b)^2/8\epsilon \tag{3.15}$$

When the OPO is driven with a pump field above either of these criteria, the solutions for α, β become spiral-stable. A small perturbation shows a damped oscillation. The oscillations should appear as sidebands in the spectrum of the fluctuation analysis; see [Drummond *et al.* 1981], although as of yet, they have not been experimentally observed. However, the non-degenerate OPO that is driven well above threshold is a commonly used source of frequency-tuneable light for applications such as molecular spectroscopy.

3.3.3 SHG

For the SHG case, one drives the system only with the seed field, while the input pump field is set to zero: $\beta_{\rm in} = 0$. The system then converts fundamental light into the second-harmonic. The solution for the second-harmonic field is found by solving the cubic equation:

$$-2\kappa_b(\epsilon\beta)^3 + 4\kappa_a\kappa_b(\epsilon\beta)^2 - 2{\kappa_a}^2\kappa_b(\epsilon\beta) = |\epsilon\alpha_{\rm in}|^2 \tag{3.16}$$

The cubic has three analytical solutions but by reasoning with the conservation of energy for the fundamental field, two of them can be ruled out, thereby just leaving the real solution [Drummond *et al.* 1980]. The formula itself is too lengthy to include here. The expression for the intra-cavity fundamental field is found by plugging the solution for β into Equation 3.7 and solving resulting the quadratic equation for α. By analysing the resulting eigenvalues for the solutions α, β, one finds a threshold that is associated with SHG:

$$|\alpha_{\rm in,c}| = \frac{1}{\epsilon}(2\kappa_a + \kappa_b)\left[2\kappa_b(\kappa_a + \kappa_b)\right]^{1/2} \tag{3.17}$$

When the SHG is driven above this threshold $\alpha_{\rm in} > \alpha_{\rm in,c}$, the eigenvalues become pure imaginary. This means that the system has un-damped oscillations, which are also called self-pulsation. The threshold value for self-pulsation $\alpha_{\rm in,c}$ is used as a reference to define the dimensionless driving field α_d; see Table 3.1. In the regime of self-pulsation, the stored energy in the intra-cavity field is periodically shuffled from the fundamental to the second-harmonic and back. I am forced to keep my quantum fluctuation analysis away from the self-pulsation regime because the linearisation assumption breaks down. Setting this limit is reasonable from an experimental point of view because to reach self-pulsation in typical SHG setups would require seed powers in excess of 1 kW continuous-wave. At these powers, thermal (oscillation) effects would surely dominate. In contrast, the case for SHG below the self-pulsation threshold is quite simple; see Figure 3.3(b). It is characterised by a monotonic increase in the intra-cavity second-harmonic field as the input seed power is increased. There is a point for which the seed field is completely converted into the second-harmonic. The required amplitude for the total input seed field for which this happens is: $\alpha_{\rm in} = \sqrt{8\kappa_a^3\kappa_b/\epsilon^2}$, which depends only on the fixed cavity parameters. This is the optimum point at which to operate an SHG for the purpose of efficient frequency doubling. The SHG is a commonly used experimental technique for creating laser light at very short wavelengths (into the ultra-violet spectrum) for which many lasing media typically lose their efficiency.

3.3.4 OPA (general)

The usual sense of the term OPA is when the input seed field is much weaker than the input pump field. However, I bend the definition to include the case of arbitrary $\alpha_{\rm in}$ and $\beta_{\rm in}$. There are several solutions to Equation 3.8, and also three main regions where the solutions are stable. We cannot rule out *a priori* that the solutions for α could be complex-valued. So to make the problem tractable, we let $\alpha = r\ \exp({\rm i}\phi)$, where r is strictly real. The equation then reduces to solving a cubic, and a trigonometric identity:

$$r^3 - \left(\frac{2\beta_{\rm in}}{\epsilon}\right) r\ \cos(2\phi) + \left(\frac{2\kappa_a\kappa_b}{\epsilon^2}\right) r - \left(\frac{2\kappa_b\alpha_{\rm in}}{\epsilon^2}\right)\cos(\phi) = 0 \qquad (3.18)$$

$$\sin(2\phi) + \left(\frac{\kappa_b\alpha_{\rm in}}{\epsilon\beta_{\rm in} r}\right)\sin(\phi) = 0 \qquad (3.19)$$

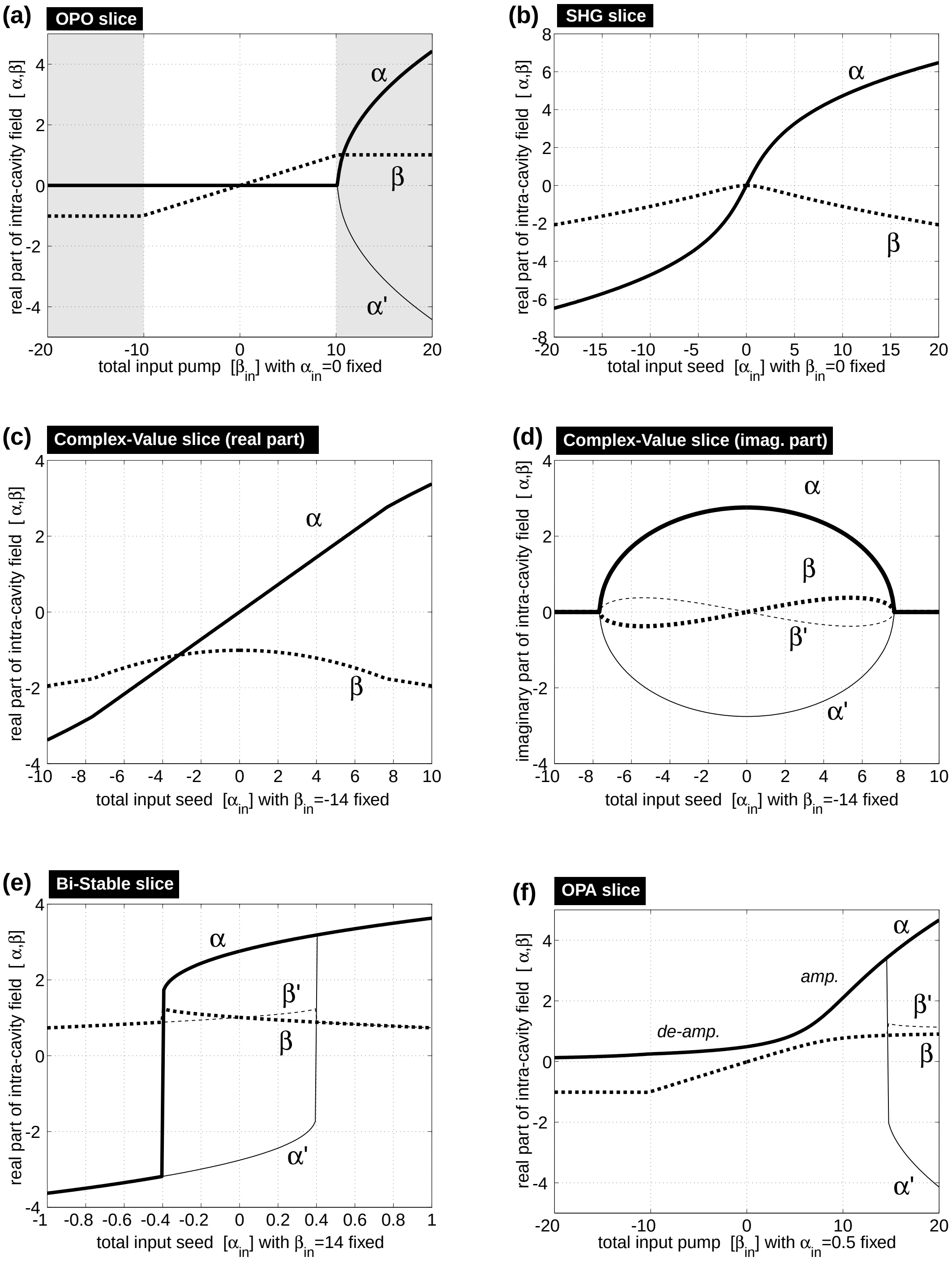

Figure 3.3: Various case studies of the classical OPA system. The parameters are from Table 3.1. Solid and dashed lines are the steady-state solutions to the fundamental and second-harmonic intra-cavity fields, respectively. Heavy and light lines correspond to the different stable solution sets (bi-stability).

The method of [Drummond *et al.* 1980] was to split up the problem into a so-called 'in-phase' solution set ($\phi = 0$) and an 'out-of-phase' set ($\phi \neq 0$). Finding the in-phase set reduces to solving the cubic:

$$r^3 - \left(\frac{2\beta_{\text{in}}}{\epsilon}\right) r + \left(\frac{2\kappa_a\kappa_b}{\epsilon^2}\right) r - \left(\frac{2\kappa_b\alpha_{\text{in}}}{\epsilon^2}\right) = 0 \tag{3.20}$$

for r, while $\phi = 0$. The out-of-phase set requires r to satisfy:

$$r^3 + \left(\frac{2\beta_{\text{in}}}{\epsilon} + \frac{2\kappa_a\kappa_b}{\epsilon^2}\right) r \quad = \quad 0 \tag{3.21}$$

and therefore also for ϕ to satisfy:

$$\cos(\phi) \quad = \quad \frac{-\kappa_b\alpha_{\text{in}}}{2\epsilon\beta_{\text{in}}r} \tag{3.22}$$

In total there are five possible solutions. When the stability of the solutions are analysed, the 'in-phase' set gives rise to the OPA mono-stable, and OPA bi-stable regions, while the 'out-phase' set leads to the OPA-complex-value region.

3.3.5 OPA (complex-value)

In the complex-value region, a phase shift is induced onto the intra-cavity fields. The phase shift is non-trivial in the sense that it is not simply a copy of the phase of the input fields. The complex-valued solutions are stable proved that the following conditions are met:

$$\beta_{\text{in}} \quad < \quad -\beta_{\text{in,c}} \tag{3.23}$$

$$(\alpha_{\text{in}})^2 \quad \leq \quad \frac{8\epsilon}{{\kappa_b}^2}|\beta_{\text{in}}|^2\left(|\beta_{\text{in}}| - \beta^c_{\text{in}}\right) \tag{3.24}$$

An example of this is shown in Figure 3.3. In graph (c) the real part of the intra-cavity fields is plotted as a function of the input seed. In graph (d) the imaginary part is plotted. Note that there are two stable solutions for the fundamental field α and α' which differ in sign only. The magnitude of the two solutions is the same. This prediction has not yet been confirmed experimentally.

3.3.6 OPA (bi-stable)

As the name suggests, there are two stable solutions for the fields in this region. The two solutions do not have the same magnitude, and as such they can be considered truly distinct. The bi-stable region is defined by a bound on the pump field that depends on the seed field:

$$\beta_{\rm in} \quad > \quad \beta_{\rm in,c} + \frac{3}{2}\left(\frac{\kappa_b \alpha_{\rm in}}{\epsilon^2}\right)^{2/3} \tag{3.25}$$

This means that the total input power to the system must exceed the OPO threshold power. An example of the bi-stable region is made in Figure 3.3(e). Here one can see an abrupt change in slope in the fundamental field α (heavy solid line), as the seed amplitude is reduced. If one were to increase the amplitude again, the solution would switch to the α' solution (thin solid line). It was suggested in [Drummond *et al.* 1980] that such behaviour could be used for building an optical switch or (classical) memory. This is another prediction of the model that has not yet been confirmed experimentally.

3.3.7 OPA (mono-stable)

The mono-stable region occupies those areas of the phase-space diagram that are not occupied by the complex-valued and bi-stable regions; see Figure 3.2. Although not strictly limited to the case of a weak seed field and a strong pump field, it is for this case that the amplifying property of the OPA is most apparent. An example of this is made in Figure 3.3(f). Depending on the sign (phase) of the input pump field, the intra-cavity field is either amplified or de-amplified in comparison to the case with the pump field set to zero. If however the pump field is increased beyond the OPO threshold (in this model $|\beta_{\rm in}| \approx 10$), then the system enters into either the complex-value region or the bistable region. The amplifying property of the OPA in the below OPO-threshold regime is a well-established experimental result. In the quantum fluctuation analysis, it is the phase-dependent amplification that is the mechanism responsible for the system transforming coherent seed light into squeezed light. The OPA operating in this regime is a well established source of squeezed light.

3.3.8 The input-output gain maps

A good way to visualise the classical behaviour is to map out the gain of the OPA as a function of the driving fields. I have defined the gain in the following way: $\mathcal{G}_a = |\alpha_{\mathrm{ref},1}|^2/|\alpha_{\mathrm{in},1}|^2$ and $\mathcal{G}_b = |\beta_{\mathrm{ref},1}|^2/|\beta_{\mathrm{in},1}|^2$. This is the optical power of the reflected light from mirror 1 divided by the input light incident on the same mirror. I have to be careful with this definition of gain, because it includes linear loss of the cavity as well as the gain due to the nonlinear interaction. But provided that I use an over-coupled cavity for the model $\kappa_{a1} \gg \kappa_{a2}$, then the dominant effect is gain due to the nonlinear interaction.

The colour-coded graphs in Plate 3 show the gain mapped as a function of the pump and seed fields which have been normalised to their respective thresholds given in Table 3.1. The horizontal axis corresponds to SHG. This can be seen by the depletion of the fundamental field, and strong amplification of the second-harmonic field in the area immediate to the horizontal axis. The vertical axis corresponds to OPO. When above OPO threshold, the second-harmonic field is depleted, while the fundamental field is strongly amplified. Bistability has been presented in the diagram by plotting one solution on the right hand side, and the other solution on the left hand side. The loss of symmetry in the seed field amplitude is thus only apparent. Hence any differences in left-right symmetry is evidence of bi-stability. There is another phenomenon that has not been discussed so far. There are two parabolic-like lines where the gain for both the fundamental and second-harmonic fields is zero. I refer to these lines as neutral-point solutions, because the rate of the two competing nonlinear processes, up-conversion and down-conversion, are equal. Later, we will see that the neutral point plays a key role in the interpretation of harmonic entanglement.

3.3.9 The input-output phase maps

The phase behaviour of the OPA system also exhibits interesting results when plotted as a map of the driving fields. I have defined the phase as being the argument of the complex-valued amplitude of the reflected field from mirror 1: $\phi_a = \arg(\alpha_{\mathrm{ref},1})$ and $\phi_b = \arg(\beta_{\mathrm{ref},1})$. I have to be careful with the interpretation, because this definition of the phase includes the trivial phase-flip that occurs on the horizontal and vertical axes of the map due to the change of sign of the driving fields.

The colour-coded graphs in Plate 4 show the phase of the reflected fields as a function of the normalised pump and seed fields. There are two prominent non-trivial phase shifts to be seen. The complex-value region in the lower section of the graphs is readily apparent. There is an interesting phase anomaly for the second-harmonic field along the vertical OPO axis. When the system is driven by the pump only, at exactly twice the OPO threshold amplitude, and in a small vicinity around this point, the phase shift can take on any value. If we look at the corresponding gain map in Plate 3, then the second-harmonic field is completely depleted at this point, and the field has zero amplitude, which means that the phase is not a well defined property anyway. A similar effect occurs on the other lines of depletion for both the second-harmonic and fundamental fields. Here however, the jump in phase is restricted to exactly 180°. Later we will see that the non-trivial phase shift in the complex-value region also plays a key role in interpreting the phenomenon of harmonic entanglement.

3.4 Quantum fluctuation analysis

The quantum fluctuation analysis begins with Equation 3.5 and Equation 3.6 whose operators are defined in the time domain. The aim is to get the intra-cavity field operators in terms of the input field operators. The first step is to bring the equations into the frequency domain with Ω the sideband frequency away from ω_0 the carrier; see Section 2.7.4. The result for the annihilation and creation operators is:

$$\mathrm{i}\Omega\,\delta\hat{a} = -\kappa_a\,\delta\hat{a} + \epsilon(\alpha^*\,\delta\hat{b} + \beta\,\delta\hat{a}^\dagger) + \delta\hat{A}_{\mathrm{in}} \tag{3.26}$$

$$\mathrm{i}\Omega\,\delta\hat{a}^\dagger = -\kappa_a\,\delta\hat{a}^\dagger + \epsilon(\alpha\,\delta\hat{b}^\dagger + \beta^*\,\delta\hat{a}) + \delta\hat{A}_{\mathrm{in}}^\dagger \tag{3.27}$$

$$\mathrm{i}\Omega\,\delta\hat{b} = -\kappa_b\,\delta\hat{b} - \epsilon\alpha\,\delta\hat{a} + \delta\hat{B}_{\mathrm{in}} \tag{3.28}$$

$$\mathrm{i}\Omega\,\delta\hat{b}^\dagger = -\kappa_b\,\delta\hat{b}^\dagger - \epsilon\alpha^*\,\delta\hat{a}^\dagger + \delta\hat{B}_{\mathrm{in}}^\dagger \tag{3.29}$$

Where the operators have had their following functional forms suppressed for compactness: $\delta\hat{a}(\omega_0 - \Omega)$ and $\delta\hat{a}^\dagger(\omega_0 + \Omega)$. The equations are solved for the input fields, before the sum and differences are taken. The sum for the seed field operators gives the amplitude quadrature: $\delta\hat{X}^{+}_{\rm Ain} = \delta\hat{A}^{\dagger}_{\rm in} + \delta\hat{A}_{\rm in}$. The difference gives the phase quadrature $\delta\hat{X}^{-}_{\rm Ain} = {\rm i}(\delta\hat{A}^{\dagger}_{\rm in} - \delta\hat{A}_{\rm in})$. Similar definitions apply for the pump field. Note that these quadrature operators, are the compact two-mode quadrature operators, as discussed in Section 2.6.5. The results are:

$$\begin{aligned}
\delta\hat{X}^{+}_{\rm Ain} &= (\kappa_a - {\rm i}\Omega)(\delta\hat{a}^{\dagger} + \delta\hat{a}) - \epsilon(\alpha\,\delta\hat{b}^{\dagger} + \alpha^{*}\,\delta\hat{b}) - \epsilon(\beta^{*}\,\delta\hat{a} + \beta\,\delta\hat{a}^{\dagger}) && (3.30)\\
\delta\hat{X}^{-}_{\rm Ain} &= (\kappa_a - {\rm i}\Omega)\,({\rm i}\delta\hat{a}^{\dagger} - {\rm i}\delta\hat{a}) - \epsilon({\rm i}\alpha\,\delta\hat{b}^{\dagger} - {\rm i}\alpha^{*}\,\delta\hat{b}) - \epsilon({\rm i}\beta^{*}\,\delta\hat{a} - {\rm i}\beta\,\delta\hat{a}^{\dagger}) && (3.31)\\
\delta\hat{X}^{+}_{\rm Bin} &= (\kappa_b - {\rm i}\Omega)(\delta\hat{b}^{\dagger} + \delta\hat{b}) + \epsilon(\alpha^{*}\,\delta\hat{a}^{\dagger} + \alpha\,\delta\hat{a}) && (3.32)\\
\delta\hat{X}^{-}_{\rm Bin} &= (\kappa_b - {\rm i}\Omega)({\rm i}\delta\hat{b}^{\dagger} - {\rm i}\delta\hat{b}) + \epsilon({\rm i}\alpha^{*}\,\delta\hat{a}^{\dagger} + {\rm i}\alpha\,\delta\hat{a}) && (3.33)
\end{aligned}$$

The arrangement of the intra-cavity creation and annihilation operators suggests that they can be combined into quadrature operators. It helps if I make the following transformations to the classical solutions: $\alpha \to |\alpha|\exp({\rm i}\theta_{\alpha})$ and $\beta \to |\beta|\exp({\rm i}\theta_{\beta})$; where $\theta_{\alpha} = {\rm Arg}(\alpha)$ and $\theta_{\beta} = {\rm Arg}(\beta)$. I can then use the definition of the generalised quadrature operator: $\hat{X}^{\theta} = \hat{a}^{\dagger}\exp({\rm i}\theta) + \hat{a}\exp(-{\rm i}\theta)$ and $\hat{X}^{\theta} = \hat{X}^{+}\cos\theta + \hat{X}^{-}\sin\theta$. Now the input field quadrature operators can be expressed in terms of the intra-cavity quadrature operators, and the result can be displayed in matrix form:

$$\begin{bmatrix} \delta X^{+}_{A,{\rm in}} \\ \delta X^{-}_{A,{\rm in}} \\ \delta X^{+}_{B,{\rm in}} \\ \delta X^{-}_{B,{\rm in}} \end{bmatrix} = \begin{bmatrix} A & B & C & D \\ B & A' & -D & C \\ -C & D & E & 0 \\ -D & -C & 0 & E \end{bmatrix} \begin{bmatrix} \delta X^{+}_{a} \\ \delta X^{-}_{a} \\ \delta X^{+}_{b} \\ \delta X^{-}_{b} \end{bmatrix} \qquad (3.34)$$

where

$$\begin{aligned}
A &= \kappa_a - i\omega - \epsilon|\beta|\cos\theta_{\beta} && (3.35)\\
A' &= \kappa_a - i\omega + \epsilon|\beta|\cos\theta_{\beta} && (3.36)\\
B &= -\epsilon|\beta|\sin\theta_{\beta} && (3.37)\\
C &= -\epsilon|\alpha|\cos\theta_{\alpha} && (3.38)\\
D &= -\epsilon|\alpha|\sin\theta_{\alpha} && (3.39)\\
E &= \kappa_b - i\omega, && (3.40)
\end{aligned}$$

The matrix has to be inverted to obtain the solution for the intra-cavity field in terms of the input fields. Let us call the *inverted* matrix $\mathcal{M}$ that has the elements m_{ij} organised into rows i and columns j. Actually, we are not interested so much in the intra-cavity fields, but rather the fields that reflect/exit from the OPA cavity. The reflected fields can be directly obtained by using the input-output formalism [Collett and Gardiner 1984], such that $\hat{X}^{\pm}_{\rm Aref,1} = \sqrt{2\kappa_{a1}}\hat{X}^{\pm}_{a} - \hat{X}^{\pm}_{\rm Ain,1}$ and $\hat{X}^{\pm}_{\rm Bref,1} = \sqrt{2\kappa_{b1}}\hat{X}^{\pm}_{b} - \hat{X}^{\pm}_{\rm Bin,1}$. And where one must be careful to use the definition of the individual input fields, as opposed to the accumulated input fields. The final expression for each reflected field is simply a weighted linear sum of all the input fields. It is easiest to see how this works if I take an example:

$$\begin{aligned}
\delta\hat{X}^{+}_{\rm Aref,1} \;=\;& (2m_{11}\sqrt{\kappa_{a1}\kappa_{a1}} - 1)\,\delta\hat{X}^{+}_{\rm Ain,1} + 2m_{11}\sqrt{\kappa_{a1}\kappa_{a2}}\,\delta\hat{X}^{+}_{\rm Ain,2} \\
& + 2m_{12}\sqrt{\kappa_{a1}\kappa_{a1}}\,\delta\hat{X}^{-}_{\rm Ain,1} + 2m_{12}\sqrt{\kappa_{a1}\kappa_{a2}}\,\delta\hat{X}^{-}_{\rm Ain,2} \\
& + 2m_{13}\sqrt{\kappa_{a1}\kappa_{b1}}\,\delta\hat{X}^{+}_{\rm Bin,1} + 2m_{13}\sqrt{\kappa_{a1}\kappa_{b2}}\,\delta\hat{X}^{+}_{\rm Bin,2} \\
& + 2m_{14}\sqrt{\kappa_{a1}\kappa_{b1}}\,\delta\hat{X}^{-}_{\rm Bin,1} + 2m_{14}\sqrt{\kappa_{a1}\kappa_{b2}}\,\delta\hat{X}^{-}_{\rm Bin,2} \qquad (3.41)
\end{aligned}$$

Another example is

$$\begin{aligned}
\delta\hat{X}^{+}_{\rm Bref,1} \;=\;& 2m_{31}\sqrt{\kappa_{b1}\kappa_{a1}}\,\delta\hat{X}^{+}_{\rm Ain,1} + 2m_{31}\sqrt{\kappa_{b1}\kappa_{a2}}\,\delta\hat{X}^{+}_{\rm Ain,2} \\
& + 2m_{32}\sqrt{\kappa_{b1}\kappa_{a1}}\,\delta\hat{X}^{-}_{\rm Ain,1} + 2m_{32}\sqrt{\kappa_{b1}\kappa_{a2}}\,\delta\hat{X}^{-}_{\rm Ain,2} \\
& + (2m_{33}\sqrt{\kappa_{b1}\kappa_{b1}} - 1)\,\delta\hat{X}^{+}_{\rm Bin,1} + 2m_{33}\sqrt{\kappa_{b1}\kappa_{b2}}\,\delta\hat{X}^{+}_{\rm Bin,2} \\
& + 2m_{34}\sqrt{\kappa_{b1}\kappa_{b1}}\,\delta\hat{X}^{-}_{\rm Bin,1} + 2m_{34}\sqrt{\kappa_{b1}\kappa_{b2}}\,\delta\hat{X}^{-}_{\rm Bin,2} \qquad (3.42)
\end{aligned}$$

where the details are in the subscripts, but also in the location of the ‘minus one’ term. The expressions for the other reflected fields are obtained in a similar manner.

What we are interested in, are the correlation coefficients of the quadrature operators between the reflected fundamental and second-harmonic fields. The correlation coefficient is generally defined as: $C_{ab} = \frac{1}{2}\langle\hat{O}_a\hat{O}_b + \hat{O}_b\hat{O}_a\rangle - \langle\hat{O}_a\rangle\langle\hat{O}_b\rangle$, where $\hat{O}_a$ and $\hat{O}_b$ are two arbitrary operators. Because I have employed the compact two-mode quadrature operators in my analysis, I must use a variation on the definition of the correlation coefficient. The explanation for this is based on the ‘compact’ quadrature variance, as given in Section 2.7.4. The compact quadrature variance is what is measured on the envelope detector of an electronic spectrum analyser, which is the device typically used in quantum optics experiments to record the quadrature noise measurements. As we are working with fluctuation operators, the modified correlation coefficient then becomes: $C_{ab} = \langle (\hat{O}_a)^\dagger \hat{O}_a \rangle$. The task is greatly simplified by the fact that operator products between two independent input modes will have expectation values of zero. The terms that do indeed contribute, will be shown in the following example:

$$\begin{aligned}
C_{\mathrm{Aref1,Bref1}} &= (2m_{11}\sqrt{\kappa_{a1}\kappa_{a1}} - 1)^*(2m_{31}\sqrt{\kappa_{b1}\kappa_{a1}})\,\langle(\delta\hat{X}^+_{\mathrm{Ain,1}})^\dagger\delta\hat{X}^+_{\mathrm{Ain,1}}\rangle \\
&\quad + (2m_{11}\sqrt{\kappa_{a1}\kappa_{a2}})^*(2m_{31}\sqrt{\kappa_{b1}\kappa_{a2}})\,\langle(\delta\hat{X}^+_{\mathrm{Ain,2}})^\dagger\delta\hat{X}^+_{\mathrm{Ain,2}}\rangle \\
&\quad + (2m_{12}\sqrt{\kappa_{a1}\kappa_{a1}})^*(2m_{32}\sqrt{\kappa_{b1}\kappa_{a1}})\,\langle(\delta\hat{X}^-_{\mathrm{Ain,1}})^\dagger\delta\hat{X}^-_{\mathrm{Ain,1}}\rangle \\
&\quad + (2m_{12}\sqrt{\kappa_{a1}\kappa_{a2}})^*(2m_{32}\sqrt{\kappa_{b1}\kappa_{a2}})\,\langle(\delta\hat{X}^-_{\mathrm{Ain,2}})^\dagger\delta\hat{X}^-_{\mathrm{Ain,2}}\rangle \\
&\quad + (2m_{13}\sqrt{\kappa_{a1}\kappa_{b1}})^*((2m_{33}\sqrt{\kappa_{b1}\kappa_{b1}} - 1))\,\langle(\delta\hat{X}^+_{\mathrm{Bin,1}})^\dagger\delta\hat{X}^+_{\mathrm{Bin,1}}\rangle \\
&\quad + (2m_{13}\sqrt{\kappa_{a1}\kappa_{b2}})^*(2m_{33}\sqrt{\kappa_{b1}\kappa_{b2}})\,\langle(\delta\hat{X}^+_{\mathrm{Bin,2}})^\dagger\delta\hat{X}^+_{\mathrm{Bin,2}}\rangle \\
&\quad + (2m_{14}\sqrt{\kappa_{a1}\kappa_{b1}})^*(2m_{34}\sqrt{\kappa_{b1}\kappa_{b1}})\,\langle(\delta\hat{X}^-_{\mathrm{Bin,1}})^\dagger\delta\hat{X}^-_{\mathrm{Bin,1}}\rangle \\
&\quad + (2m_{14}\sqrt{\kappa_{a1}\kappa_{b2}})^*(2m_{34}\sqrt{\kappa_{b1}\kappa_{b2}})\,\langle(\delta\hat{X}^-_{\mathrm{Bin,2}})^\dagger\delta\hat{X}^-_{\mathrm{Bin,2}}\rangle \qquad (3.43)
\end{aligned}$$

The other correlation coefficients are calculated in a similar way. We now need to choose what states the input fields are in. Since the input states are either coherent states (the seed and pump fields into mirror 1), or vacuum states (all other input fields), I can be sure that the compact variances will equal one; see Section 2.7.4. For example:

$$\langle\alpha_{\mathrm{in,1}}|(\delta\hat{X}^+_{\mathrm{Ain,1}})^\dagger\delta\hat{X}^+_{\mathrm{Ain,1}}|\alpha_{\mathrm{in,1}}\rangle = 1 \qquad (3.44)$$

$$\langle 0|(\delta\hat{X}^+_{\mathrm{Ain,2}})^\dagger\delta\hat{X}^+_{\mathrm{Ain,2}}|0\rangle = 1 \qquad (3.45)$$

We now have all the tools required to calculate the entire matrix of correlation coefficients. We can proceed to investigate the presence of entanglement between the output fundamental and second harmonic fields. A bi-partite Gaussian entangled state is completely described by its correlation matrix [Duan *et al.* 2000] which has the following arrangement of elements:

$$M_{ab}=\begin{bmatrix} C^{++}_{aa} & C^{+-}_{aa} & C^{++}_{ab} & C^{+-}_{ab} \\ C^{-+}_{aa} & C^{--}_{aa} & C^{-+}_{ab} & C^{--}_{ab} \\ C^{++}_{ba} & C^{+-}_{ba} & C^{++}_{bb} & C^{+-}_{bb} \\ C^{-+}_{ba} & C^{--}_{ba} & C^{-+}_{bb} & C^{--}_{bb} \end{bmatrix} \tag{3.46}$$

Note that to keep the notation simple, I have made the following change of subscripts: $_{\mathrm{Aref},1} \rightarrow_{a}$ and $_{\mathrm{Bref},1} \rightarrow_{b}$. Once I have calculated the elements of this matrix, I can then analyse it for either the inseparability criterion or the EPR criterion for entanglement; see Section 2.9.3.

3.4.1 Numerical methods

Given the rather large expression involved in calculating harmonic entanglement from the correlation matrix, it was simpler to break up the calculation into three steps, where each step returned a numerical value. The model parameters that were used are given in Table 3.1. The first step in the calculation was to find the values of the intra-cavity fields for a given pump and seed field using the classical model, for example from Equation 3.13. This value was then fed into the quantum fluctuation model, to get the values of the correlation matrix elements, such as in Equation 3.43. Finally, the correlation matrix was analysed using a numerical algorithm to find the standard form II of the matrix, and hence to find the optimised inseparability, which is a necessary and sufficient criterion for entanglement.

3.4.2 Initial testing of the model

Every new theoretical model should be treated with caution. Analytical errors, numerical errors or over-stretched approximations will cause the model to make inaccurate predictions. For this reason, it is wise to invest some time to gain some confidence in the model by testing it against a well-established result. One result that has been confirmed by many experiments, is the ability of the OPA in the weak seed limit to produce quadrature squeezed light on the fundamental field, and also the ability of the OPA in the SHG limit to produce squeezing on the second-harmonic field. Both of these results can be seen in Plate 5, where the quadrature variances have been mapped as a function of the input seed and pump fields. There is a wealth of information here, but I want to first concentrate on the squeezing of the fundamental field as a function of pump power. This corresponds to the immediate vicinity of the vertical (OPO) axis in the diagram. Depending on the sign of the pump field as it approaches OPO threshold, the amplitude quadrature of the fundamental field takes on either $-15\,\mathrm{dB}$ or $+15\,\mathrm{dB}$, which is squeezing and anti-squeezing, respectively. For a pump amplitude of zero, the quadrature variance is as expected 0 dB (that of a coherent state). A further investigation of the model (not shown), is that the level of squeezing becomes arbitrarily strong as the intra-cavity losses of the OPA are reduced ($\kappa_{a2} \rightarrow 0$). These results are in agreement with predictions from other OPA models [Wu *et al.* 1986, Walls and Milburn 1994].

Another test is the production of SHG squeezing. If we follow the horizontal (SHG) axis in Plate 5 for the second-harmonic amplitude quadrature, then the variance changes from $0\,\mathrm{dB}$ at the origin, to $-3\,\mathrm{dB}$ at the extreme end. The squeezing strength seems to clamp, even when intra-cavity losses are reduced. This result is consistent with the SHG squeezing predictions in other SHG models [Mandel 1982]. A rather simple check is to see whether the fields are violating the Heisenberg uncertainty principle anywhere on the map. With quadrature variances, one simply calculates the product of the variances. Although not shown explicitly in Plate 5, if one adds (in dB scale) the amplitude and phase quadrature maps for the fundamental field, then one does not find a value that is less than unity at any point on the map. A similar test for the second-harmonic field gives the same result. Another test is to turn off the nonlinearity in the model by letting $\epsilon = 0$. In doing this, one removes the nonlinear gain in the system, and even though there may be intra-cavity loss in the system, the input coherent and vacuum states, should remain unchanged with a quadrature variance of one. Although not shown in the graphs, the OPA model confirms this result. Since the OPA model has survived the key tests, it should be safe to continue with analysing the quantum correlations between the fundamental and second-harmonic fields, and therefore to look for harmonic entanglement.

3.4.3 Entanglement is all over the map of driving fields

If I map out the EPR entanglement measure as a function of the driving fields in Plate 6, the first thing that strikes me qualitatively, is that there is at least some entanglement to be seen almost everywhere. The second thing is that the strongest entanglement seems to coincide along the boundaries, i.e. the boundaries where there is a change of the stability

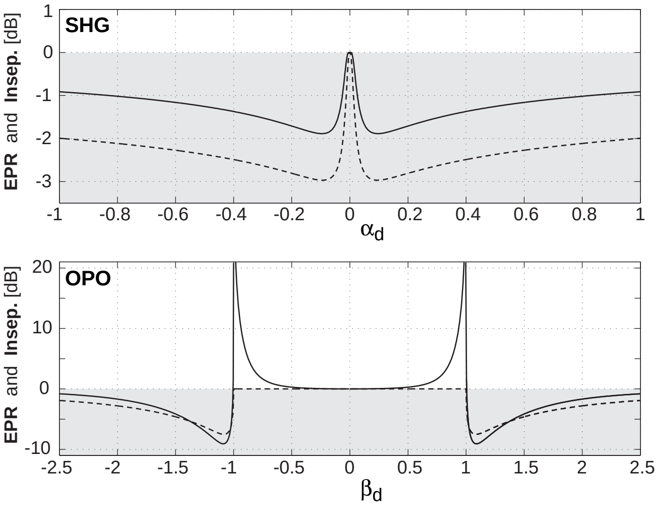

Figure 3.4: (a) Second-harmonic generation produces harmonic entanglement for all non-zero pump powers. But the strength is limited to $\varepsilon_o = 1.9\,\mathrm{dB}$, even for the case of 100% escape efficiency. (b) Optical parametric oscillation can only produce harmonic entanglement when driven above threshold. The best value reads $\varepsilon_o = 9.1\,\mathrm{dB}$, located just beyond threshold. This value can be arbitrarily improved by increasing the escape efficiency. Solid line is the EPR criterion, while the dashed line is inseparability. The shaded area is entangled.

of the classical solutions. I have some cause for celebration, because I have already shown my main hypothesis: a model of OPA can entangle the fundamental and second-harmonic fields. But I want to go further than this, and try to get an understanding of how the strength and type of entanglement depends on the underlying classical behaviour of the system.

3.4.4 SHG produces harmonic entanglement, but it’s not the best

I first examine the case of taking a slice in the map of driving fields along the SHG axis. Figure 3.4(a) plots the EPR and inseparability entanglement measures as a function of the normalised seed amplitude from zero up to the onset of self-pulsation (which is the limit of the OPA model, but not the system itself). We can see that for SHG, there is at least some level of entanglement to be found for all values of the seed field. There is an optimum of $-2\,\mathrm{dB}$ of EPR entanglement at $\alpha_d = 0.1$. This result is reminiscent of the $3\,\mathrm{dB}$ squeezing limit for SHG. The cause may be that the pair absorption process for SHG only allows a single sideband of squeezing or entanglement to be generated, the other sideband is occupied by a vacuum state. The strength of entanglement does not improve if I reduce the intra-cavity losses, and so the harmonic entanglement generation in SHG appears to be fundamentally limited.

3.4.5 OPO above threshold makes harmonic entanglement, but none below

The strongest experimental sources of squeezed light have, to date, used below-threshold OPO to make 10dB squeezed light [Vahlbruch *et al.* 2008]. I therefore would have expected that OPO would also produce the strongest harmonic entanglement. Figure 3.4(b) takes a slice along the OPO axis of the map. The EPR and inseparability measures are plotted as a function of the normalised pump amplitude. The result for below OPO threshold is that there is no entanglement, as shown by EPR being greater than one, and inseparability closely hugging the unity line. However, when the pump field is increased beyond threshold, the entanglement strength rapidly finds an optimum ($9.1\,\mathrm{dB}$), before then gradually easing off with increasing pump power. If one observes the optimum point as the intra-cavity losses are reduced arbitrarily, the strength of entanglement also increases arbitrarily and moves ever closer to the OPO threshold point. The strength of harmonic entanglement in above-threshold OPO is therefore not fundamentally limited as in the SHG case.

3.4.6 OPA near the boundaries makes the best harmonic entanglement

Even on the classical gain plots we can see that there are discontinuities in the reflected classical field amplitudes across the borders where one solution becomes unstable, and makes the transition to the next solution. One can expect that the quantum effects will be especially strong here, because a small fluctuation in one field, say the pump, can transfer to a large fluctuation in the seed, thereby producing strong correlations. The best way to study these boundary regions is to perhaps set the total input power to a constant value, and only trace out a circle in the map of driving fields. In Figure 3.5(a), I chose a total input power of 90% OPO threshold power. The polar plot follows the circle in the entanglement map of Plate 6, where the path is parameterised by the angle θ_R that is defined by $\alpha_d = (\beta_{\mathrm{in,1,c}}/\alpha_{\mathrm{in,1,c}})\sqrt{2\xi}\sin\theta_R$, and $\beta_d = \sqrt{\xi}\cos\theta_R$. Where ξ is the ratio of the total input power to the OPO threshold power. The ratio of the pump to seed powers is $R = |\beta_{\mathrm{in},1}|^2/(\frac{1}{2}|\alpha_{\mathrm{in},1}|^2 + |\beta_{\mathrm{in},1}|^2)$. In the polar plot, points closer to the origin signify more EPR entanglement. We can see two regions—one in the OPA amplification region, and the other in the OPA de-amplification region—where the EPR entanglement finds an optimum

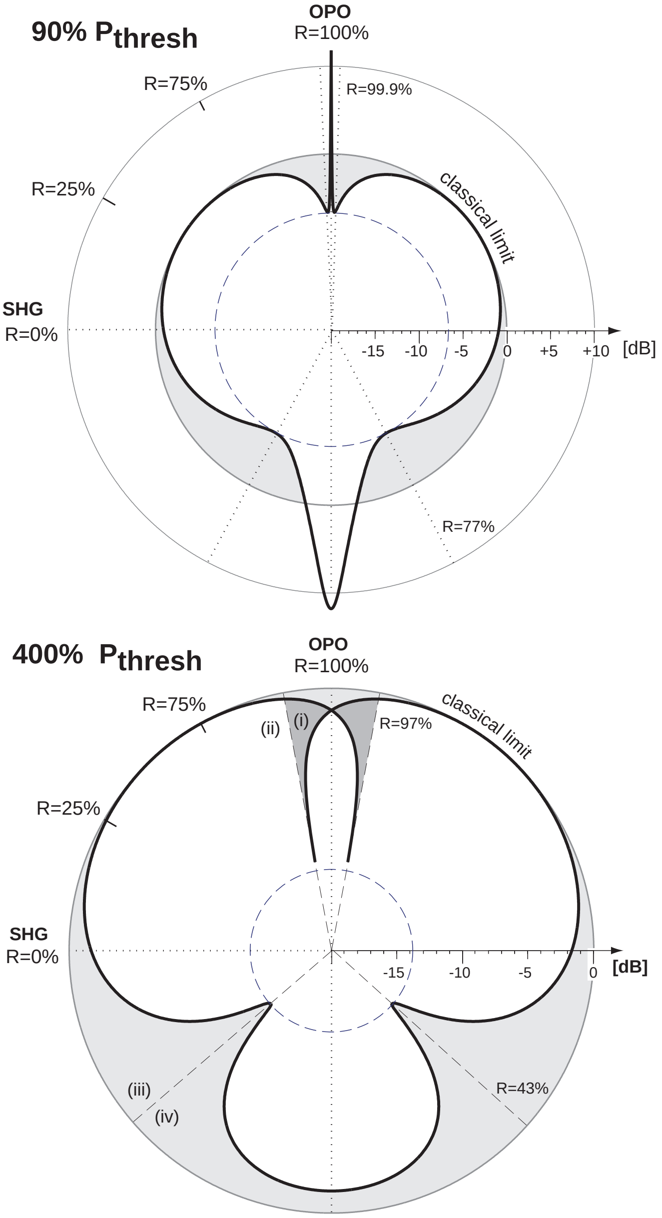

Figure 3.5: The total input power is held constant, but is split between α_{d} and β_{d}. The splitting fraction R is varied. EPR entanglement strength is displayed radially. (a) The 90% case is optimally entangled in the regime of moderately pump-depleted OPA, and reaches $\varepsilon_o \approx 6.5\ \mathrm{dB}$. (b) The 400% case shows the region of bi-stability. Optimal entanglement occurs on the edges of solutions; $\varepsilon_o \approx 14\ \mathrm{dB}$.

of $-6.5\,\mathrm{dB}$. Note though, that since we are in the OPA mono-stable solution set, that no solution boundaries have been crossed yet. This changes when I set the total input power to 400% of OPO threshold power. Once again there are two optimum settings for the seed and pump fields. And these indeed correspond to the boundaries between the mono-stable OPA region and the bi-stable regions; or the boundary between the mono-stable and complex-valued regions. The optimum EPR entanglement turns out to be $-14\ \mathrm{dB}$ for both boundary crossings. This result suggests that perhaps the total input power is akin to a resource for the production of harmonic entanglement.

3.5 Interpretation

We have seen harmonic entanglement mapped across the input driving fields, and we have looked at several case studies. But I would like to draw some generalisations of the OPA system from this overload of information. In the next following sections I will attempt to interpret the theoretical results.

3.5.1 Harmonic entanglement requires an exchange of energy or phase

What I want to answer is, why is harmonic entanglement stronger for some combinations of seed and pump amplitudes, and not for others? How does the OPA produce harmonic entanglement? The answer is probably easier to find for the converse: for which seed and pump amplitudes is there no entanglement and why? If we look on the map, there are only two regions that have no entanglement: OPO below threshold, and the neutral path within the OPA mono-stable region (upper half of Plate 3). What they have in common is that the classical gain for the fundamental and second-harmonic are exactly zero along these paths. There is no exchange of energy. So if one field, say the pump, has a fluctuation, then it is impossible for it to be mapped onto the seed. And without at least some correlation, or anti-correlation, there cannot be any entanglement.

If we look closely at the classical gain maps, then we can see another neutral path of seed and pump amplitudes (this time in the lower half of the diagrams in Plate 3). But along this path, there is indeed a generous amount of entanglement to be seen, at least $-6\,\mathrm{dB}$ according to the EPR measure in Plate 6. The difference here is that although there is no exchange of power between the fundamental and second-harmonic fields, there is indeed an exchange of phase shifts acquired by the reflected fields. The two fields are therefore correlated according to their phases, and not their intensities. And it is this correlation that allows harmonic entanglement to be generated along an otherwise ‘neutral’ path.

3.5.2 Biased entanglement is the rule and not the exception

When looking at the map of entanglement in Plate 6, it is hard to get a feeling for the kind of entanglement that is being produced. I have therefore chosen a few examples, or case-studies, at various points in the map, so that one can see what is happening to both the real and imaginary parts of the classical amplitudes, and also the amplitude and phase quadrature variances. The states are represented by ball-on-stick diagrams, where the stick is the classical amplitude, and the major and minor axes of the ball correspond to the quadrature standard deviations. The state is represented in this way for the fields both before and after their interaction in the cavity.

Case 1 in Plate 6 is a strongly driven SHG. The seed field is almost completely depleted, i.e. it has been converted into the second-harmonic. One can see weak squeezing on the amplitude quadrature of the fundamental field, and also weak harmonic entanglement between the fields. The entanglement is biased, because the states produced for the fundamental and second-harmonic fields show squeezing; see Section 2.9.4.

Case 2: is below-threshold OPO in the de-amplification regime. There is no pump-depletion, and the squeezing on the fundamental field is very strong. But there is no entanglement. This is because there has been no exchange of energy between the pump and seed fields, as witnessed by the coherent amplitude ‘stick’ in the diagram not having changed.

Case 3: is below-threshold OPA, and in a region of moderate pump-enhancement. This means that the squeezing on the fundamental field is slightly degraded, but due to the significant exchange of energy between pump and seed, a moderate level of harmonic entanglement is produced. As in Case 1, we see that the entanglement is biased.

Case 4: is clearly above-threshold OPO. A fundamental field has been created, but so much so, that the pump field is almost completely depleted. The exchange of energy has been perhaps too great, and this has limited the strength of correlations between the two fields. Hence the entanglement is only moderate compared to other regions of similar total input power (400% of OPO threshold). The fundamental field is squeezed in the phase quadrature. So we have another example of biased entanglement in the collection.

Case 5: is a neutral point. Here there is no net exchange of energy between the fundamental and second-harmonic fields. As a result, there is no squeezing to be seen, nor harmonic entanglement.

Case 6: is in the complex-value region of the map. As a result, the reflected fields gather non-trivial phase shifts. The pump depletion or enhancement is very weak for this point, as can be seen by the lengths of the amplitude sticks not having changed much. But the change in phase is significant. As a result, small fluctuations in the seed field intensity are transferred onto the phase of the second-harmonic, and vice versa. The entanglement that is produced is quite strong when compared with other points along the 400% total input power line. It should also be noted that the entanglement that is produced is biased.

These case studies have shown two things. Firstly the important role that pump depletion or enhancement plays in producing harmonic entanglement. And secondly, that harmonic entanglement as produced by the OPA system is inherently biased, regardless of the choice of seed and pump fields. The ‘biasedness’ is evident in an analysis of the quadrature variances for the fundamental or second-harmonic fields, which show squeezing.

3.5.3 Optimum entanglement occurs at 7 times threshold power

If we look at the polar plots in Figure 3.5, we can see that the amount of harmonic entanglement is the same in both the amplification and de-amplification regions. The 400% case also has stronger entanglement than the 90% total input power case. This seems to suggest that the total input power is a resource that decides how much entanglement can be generated. If this is true, then more power should mean stronger entanglement. But there turns out to be an optimum level for the total input power.

To study this, I stepped through several orders of magnitude of total input power. For each step, I took a circular path in terms of the pump and seed amplitudes, and recorded the strongest value of entanglement. I repeated this procedure until I had the optimal EPR measure as a function of total input power. This is plotted in Figure 3.6. I have repeated the

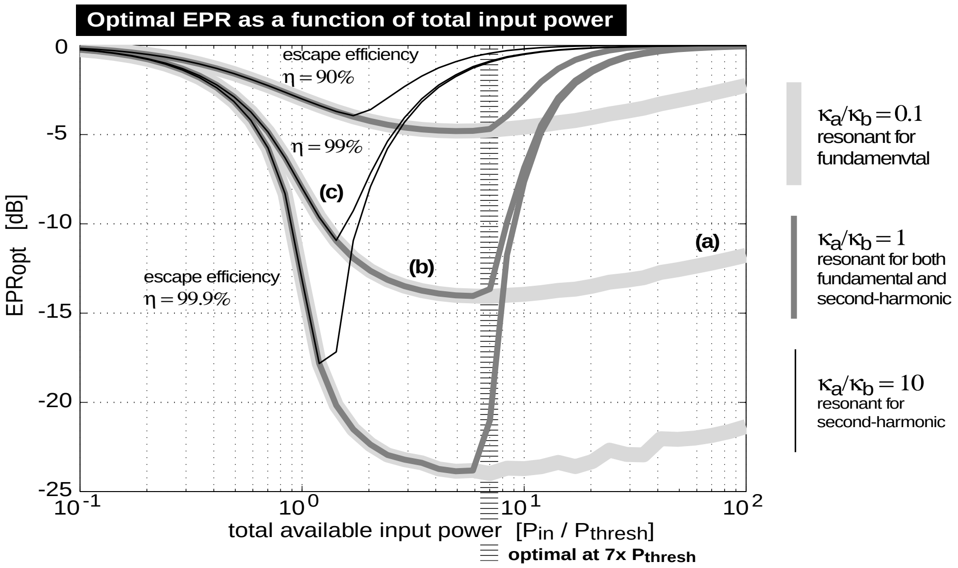

Figure 3.6: The optimal entanglement is found as a function of total input power, and plotted for several coupling ratios κ_a/κ_b. The best strategy is to keep $\kappa_a/\kappa_b \leq 1$, i.e. preferably singly-resonant on mode a, after which the total input power of $7\times$ threshold will generate the strongest entanglement, largely independent of the escape efficiency $\eta_{\rm esc}{=}\kappa_{a,1}/\kappa_a{=}\kappa_{b,1}/\kappa_b$.

study for three different ratios of input-output couplers, and also three different settings for the intra-cavity losses. But let me start with the standard case as given by the parameters in Table 3.1, which is shown here in line (a) in Figure 3.6. As the total input power is increased, the entanglement strength finds an optimum at about 7 times the OPO threshold power. But for higher total input powers, the entanglement begins to weaken.

In the case of a doubly-resonant cavity along line (b), where the fundamental and second-harmonic decay rates are equal, one also sees an optimum entanglement point at 7 times OPO threshold power; line (b). But the entanglement weakens much more quickly than for the previous case. If I then make the OPA cavity effectively singly-resonant for the second-harmonic field, as in line (c), the optimum at 7 times threshold power is not even reached. But note that my OPA model could break down at this point, because the approximation used in the derivation to adiabatically remove the second-harmonic field no longer applies.

3.5.4 In principle, OPA can make arbitrarily strong harmonic entanglement

If the escape efficiency of the OPA cavity is increased from 90% to 99.9%, which is done by reducing the intra-cavity losses ($\kappa_{a2} \rightarrow 0$), the level of optimal EPR entanglement also increases. But the total input power at which this occurs, moves only very little away from the 7 times threshold value; see Figure 3.6. Hence, when designing an experimental setup, one would not require more than this total input power in order to get the most entanglement out of the system. Having the potential for arbitrary strength in the system is a huge motivation to build up an experiment and start measuring in the lab. It means that one does not need to overcome a hurdle that is already imposed by the OPA system itself.

3.5.5 Squeezed driving fields enhance entanglement

So far I have considered driving the system with a seed and pump that are in coherent states. It is then interesting to ask the question whether the fluctuations on those states map to the entangled states. The quantum fluctuation model easily allows me to change the input states to squeezed states, just by changing the value of the compact quadrature variances. I tried several combinations of squeezing on the seed and pump fields, and found the strongest results for the orthogonal combinations: for example, $6\,\mathrm{dB}$ squeezed on the seed amplitude, but $6\,\mathrm{dB}$ on the pump phase. Or vice versa. The harmonic entanglement map is plotted for these two cases in Plate 7. The first impression is that there is more entanglement, in the sense of being both stronger, and beginning closer toward the origin, i.e. for lower total input powers. The inset plot compares the entanglement map at the $-3\,\mathrm{dB}$ contour for the coherent and squeezed input states. Clearly visible is that the regions appear to have moved, so that for one particular combination of pump and seed squeezing, 3dB of entanglement can now be accessed at only a few percent of total input power.

We can also look at individual cases. I have chosen to examine a point on the SHG axis. Looking at the ball-on-stick picture and comparing the squeezed and coherent models, we can see that the kind of entanglement has changed from being biased, to being nearly symmetric (biased entanglement is discussed in Section 2.9.4). The general message is clear. Squeezed driving fields can enhance harmonic entanglement and compensate for bias that is inherent in the OPA system.

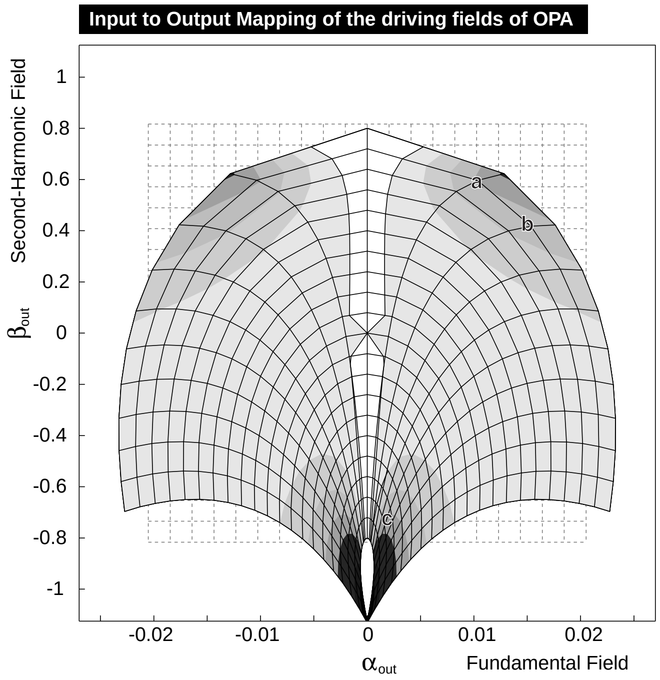

Figure 3.7: Intuitive interpretation of harmonic entanglement generation in OPA. The input seed and pump fields are represented by a dashed-grey grid. The nonlinear process then exchanges energy between the fields, thereby distorting the grid (dark solid grid), upon which the EPR measure of harmonic entanglement is plotted, where darker ink signifies stronger entanglement. The cells that are most distorted and at angles give rise to strong correlations between the fundamental and second-harmonic fields, which are the basis for forming harmonic entanglement.

3.5.6 An intuitive interpretation using co-ordinate transformations

Despite having examined various aspects of the harmonic entanglement that is generated by OPA, there is perhaps one thing that is missing. I would like to have an intuitive picture for how the entanglement is created in the OPA. For squeezed light, there is a simple picture for how it is created in an OPA. One can imagine that the OPA de-amplification process that happens to the classical amplitude of the seed field, likewise happens to the quantum fluctuations in the amplitude quadrature. The output light therefore has a quadrature variance that is squeezed in comparison to a coherent state of light that has the same optical power. For harmonic entanglement, the picture is complicated by the fact that we need to consider two fields at once, and the correlations between them.

For classical fields, one consider the role of the OPA system as mapping a set of input fields, into a set of output fields. I can represent this mapping as distortion in a grid of equally spaced points. Figure 3.7 shows a set of equally spaced input fields as a light-grey two-dimensional grid. The region that has been plotted is within the mono-stable OPA region. The OPA system then maps the input seed and pump fields into new values of the output seed and pump fields, which are represented by the dark-grey grid. The distortion is severe, but note that for some regions, there is a $180°$ phase shift involved, which means that the change in power is not as large as it looks initially. I have then plotted the EPR measure of harmonic entanglement on top of the distorted grid, which enables us to see the relationship between distortion of the mapping and the entanglement.

We can then see that harmonic entanglement only occurs when a particular cell of the grid has changed its angle from the original cell. A change in angle means is that the seed and pump fields have become coupled. Another effect is then the stretching/compression of the cell. Stretching represents anti-squeezing, while compression represents squeezing of the amplitude quadrature. As an example, I could choose to set the input seed and pump to lie at the corner of the cell marked (a). If I then bring a small fluctuation in the seed field, so that the system now rests on the corner (b), one can see that the small fluctuation has been amplified and has caused a coupling between the fundamental and second-harmonic fields. Thus a correlation has been produced. A similar argument applies to a cell that is considered at point (c). Although difficult to see, the fluctuation has been de-amplified (squeezed), while still allowing coupling between the fundamental and second-harmonic fields. This particular cell therefore demonstrates a quantum correlation between the fundamental and second-harmonic fields, and it is this quantum correlation that is at the heart of the harmonically entangled state.

3.6 Summary

Harmonic entanglement is the quadrature entanglement between a fundamental optical field and its second-harmonic. By extending an advanced model of OPA, I was able to analyse the quadrature correlations between the reflected fundamental and second-harmonic fields. The correlations were characterised according to the EPR and inseparability criteria of entanglement. The OPA system supports a range of classical processes: mono-stable, bi-stable, complex-valued, SHG, and OPO. In all but two cases (the neutral path, and below-threshold OPO) the system exhibited harmonic entanglement on the reflected fields. By reducing intra-cavity losses, the strength of the entanglement could in principle be made arbitrarily strong. The optical power levels that are required to see moderate levels of harmonic entanglement, of order $3\,\mathrm{dB}$ in the EPR measure, are quite reasonable, where only a total input power of 50 to 90% of OPO threshold is needed. This suggests that the OPA system is an excellent candidate for a source of harmonic entanglement.

Chapter 4

Harmonic Entanglement Experiment: Materials and Methods

In the preceding chapter, I presented a theoretical model and its predictions that harmonic entanglement could be produced by an optical parametric amplifier (OPA). The aim of the experiment presented in this chapter was to test those predictions. What looked simple on paper ended up covering a three metre long optical table tethered to a rack of electronics. This chapter explains why the experiment became complicated, and details the design and testing of its key components. The construction and operation of the experiment was a collaboration with Syed Assad, Moritz Mehmet and myself. Along the way, we developed the technique of optical carrier rejection for the purpose of measuring the phase quadrature of bright light; and we also found evidence of guided acoustic wave Brillouin scattering occurring in the nonlinear crystal of the OPA (see Chapter 5). Our attention to building an OPA of sufficiently high escape efficiency and low threshold power was rewarded with a series of observations of harmonic entanglement that are presented in Chapter 6.

4.1 Overall Design Considerations

The design of the experiment is very simple in principle. A laser provides a source of coherent light at $1064\,\mathrm{nm}$ (red). A fraction of the light is frequency doubled to $532\,\mathrm{nm}$ (green) using a second-harmonic generator. Both driving fields—the red seed and green pump—are then combined and injected into an OPA, which consists of a $\chi^{(2)}$ nonlinear crystal placed within an optical resonator. The fields reflected from the OPA are separated, and each wavelength (colour) is received by a homodyne detector that measures the phase and amplitude quadratures. The quadrature data is recorded as a time-series, from which

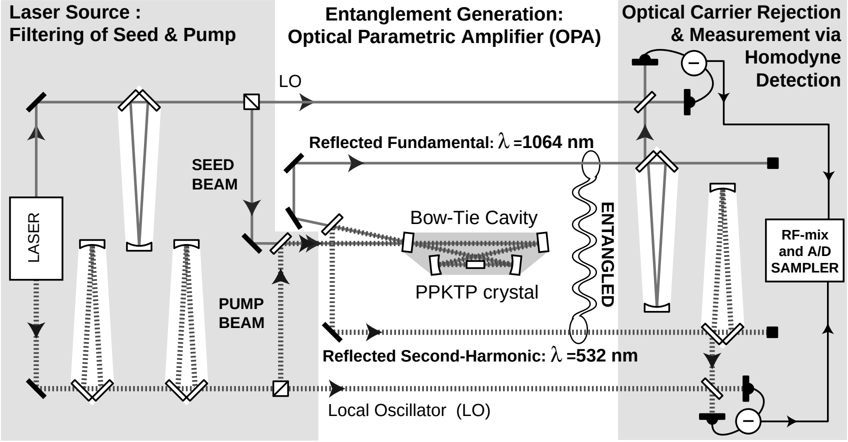

Figure 4.1: Overall design of the experiment. Entanglement was generated between the reflected fundamental and second-harmonic fields of an optical parametric amplifier. Optical carrier rejection allowed the verification of entanglement via homodyne detection. Dashed lines are the 532 nm (green) light beams. Solid lines are the 1064 nm (red) light beams.

the elements of the correlation matrix are calculated. Finally, the presence of harmonic entanglement is verified by analysing the matrix according to the inseparability criterion.

In practice, the design of the experiment needed some modification; see Figure 4.1. The reason was that only bright driving fields, on the order of OPO threshold power ($P_{\rm th}$), can yield strong harmonic entanglement. Bright light brings with it two challenges. Firstly, the driving fields must be close to shot-noise-limited at the sideband frequency of measurement, which in our case was $\Omega \sim 10\,{\rm MHz}$. Any excess noise on the driving fields would couple directly into the fields reflected from the OPA, thereby degrading the entanglement. This problem is more significant at higher laser powers. The solution was to filter the light by transmitting it through an optical cavity having a linewidth $\delta\nu$, where the excess noise at the sideband frequencies is stripped from the carrier. For frequencies above the cavity linewidth, the transfer function follows a $1/f$ roll-off for the noise power, which means that the linewidth could be chosen to suite the filtering needs.

The second challenge was that of measuring the phase quadrature of the light, which is necessary to verify entanglement. Measuring the phase quadrature is most readily done using the technique of balanced homodyne detection. The requirement however, is that the local oscillator be at least $\sim$ 30 times brighter than the signal beam. If for example $P_{\rm th} = 100\,{\rm mW}$, and for the case that the OPA is driven at this level, then one could expect an entangled signal beam of up to $100\,\mathrm{mW}$. Homodyne detection would then a require a local oscillator in excess of $3\,\mathrm{W}$, which would be difficult for a single photodiode to detect (and survive). The literature reports two different techniques that have been applied to effectively rotate the phase quadrature into the amplitude quadrature (at a given sideband frequency), thereby making it possible to measure the phase quadrature using just a single photodetector (or two detectors in a self-homodyne setup). One method used the phase shift acquired by the carrier after reflection from an under-coupled cavity that was de-tuned [Villar *et al.* 2006]. The scheme of [Glöckl *et al.* 2004] was based on an unequal arm length Mach-Zehnder interferometer. We used a different technique, that of optical carrier rejection, which reduced the optical power in the signal beam without significantly affecting the sidebands. The signal beam was aligned onto an (ideally) impedance-matched cavity that would transmit the carrier light when on resonance. The sidebands lying outside the cavity linewidth were reflected. Using this method, we were able to reduce the carrier light by up to $25\,\mathrm{dB}$, and perform homodyne detection on the sidebands.

The problems associated with producing bright shot-noise limited light, and detecting the phase quadrature of bright light, could in principle be avoided entirely by just reducing P_{th} of the OPA. One must be careful however, to avoid introducing additional losses which would degrade entanglement. The simplest method is to decrease the total cavity decay rates. Our solution was to make the OPA cavity doubly resonant, i.e. resonant at both the fundamental and second-harmonic fields. This ensured that the losses were roughly equally distributed over both colours, while keeping $P_{\mathrm{th}} < 100\,\mathrm{mW}$.

A schematic of the entire experiment is shown in Figure 4.1. Here we can see the implementation of filtering of the seed and pump light to ensure that they are shot-noise limited. These cavities also cleaned the spatial mode into a TEM_{00} profile. They are labelled as mode-cleaners to contrast them from the filter-cavities which are installed at the homodyne detection end, where they perform their role in optical carrier rejection. Although performing different roles, their design and construction were identical. The OPA cavity was built according to a bow-tie geometry, primarily to allow unrestricted access to the reflected entangled beams. A dispersion compensation plate was used to neutralise the

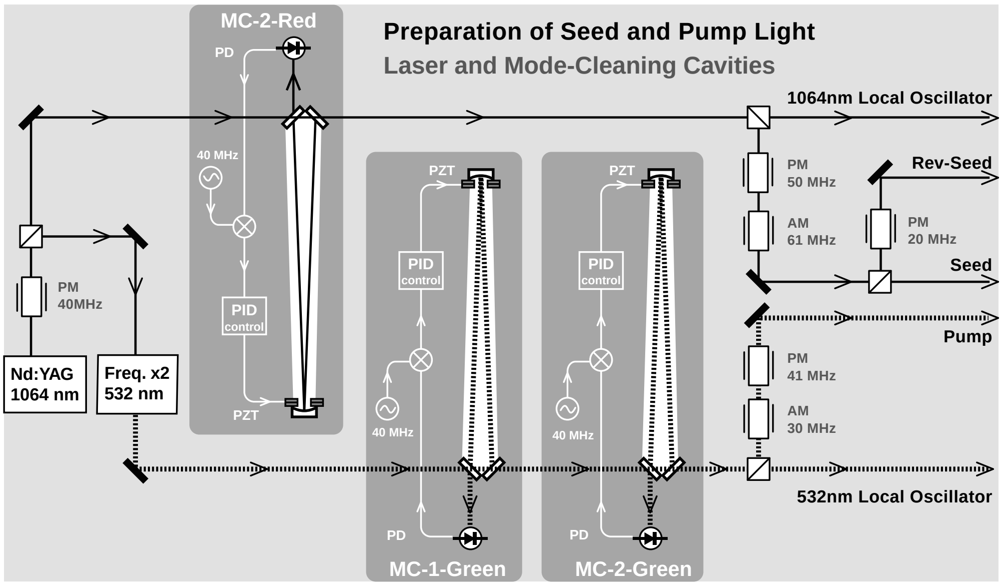

Figure 4.2: Schematic of the laser preparation stage. Light from a Nd:YAG laser was frequency doubled. Dashed lines are 532 nm; solid lines are 1064 nm. Both colours were filtered by optical cavities. Reference beams (local oscillators) were tapped-off before modulation sidebands were applied to the seed, pump, and reverse-seed beams. Electronic components used for servo-control are outlined in white.

dispersion that was acquired per-round-trip (from AR and HR coatings), which is essential for keeping P_{th} low in the doubly-resonant design.

4.2 Preparation of seed and pump light

Laser source: A schematic is shown in Figure 4.2. A Nd:YAG laser (*Diabolo model from Innolight GmbH.*) was the only source of light for the whole experiment. It emitted $1064\,\mathrm{nm}$ (red), and also $532\,\mathrm{nm}$ (green) coherent light from an internal frequency doubler. The maximum power output of continuous-wave (CW) light was $400\,\mathrm{mW}$ for red and $800\,\mathrm{mW}$ for green. The laser linewidth was quoted from the manufacturer as $1\,\mathrm{kHz}$. The laser also had an internal intensity noise-eater which was switched on for taking measurements because it reduced the noise-power of the relaxation oscillation by $30\,\mathrm{dB}$. A Faraday isolator was placed in the red path (not shown), as a precaution against possible feedback from the retro-reflecting optics. In the experiment, there were no such optics placed intentionally, although there may have been stray alignment from the AR-coatings of flat optical components like waveplates.

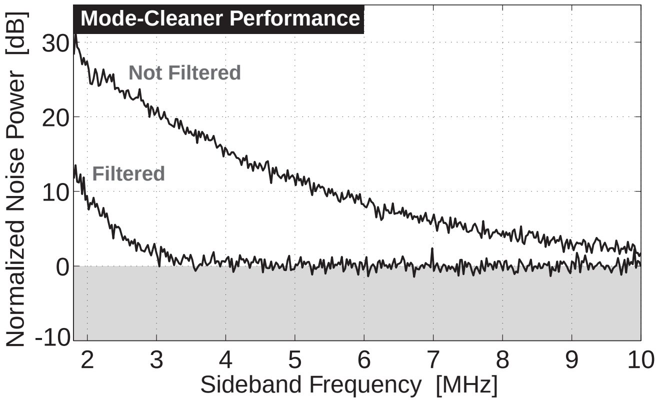

Figure 4.3: Filtering performance of the second green mode-cleaner (MC-2G). 1 mW of light was sent to the cavity. The noise-power spectrum of the transmitted light was measured using a self-homodyne setup for calibration to the vacuum state (grey upper boundary). The filtered light had reduced noise-power, and was shot-noise limited beyond 4 MHz.

Initially, a cascade of two mode-cleaning cavities for each colour was installed in the beam paths. But limited optical power meant that the first red cavity was not used. All three remaining cavities were of the same mechanical design by K. McKenzie: 3 mirror triangular geometry, $800\,\mathrm{mm}$ optical path length, PZT actuated end-mirror. The important parameters to note at this stage are the linewidths of the first and second green mode-cleaners (MC-1G and MC-2G), $1.0\,\mathrm{MHz}$ and $1.9\mathrm{MHz}$, respectively; and the second red mode-cleaner (MC-2R), of $0.4\,\mathrm{MHz}$. Total transmission for each colour was moderate to good: $\sim 95\%$ for red; $\sim 95\%$ and $\sim 78\%$ for green.

Mode-cleaner performance: Here, one of the green mode-cleaners (MC-2G) was tested for how well it could suppress the relaxation oscillation of the laser. The method was to use a self-homodyne technique to get the noise spectra calibrated to the shot-noise-limit. Spectra were taken with and without the locked cavity in place, such that the power on the detectors was kept the same ($1\,\mathrm{mW}$). The results are shown in Figure 4.3. The roll-off remnant of the relaxation oscillation above $2\,\mathrm{MHz}$ was suppressed by up to 20dB, which ensured that the green light was shot-noise-limited beyond $4\,\mathrm{MHz}$. We decided to install another green mode-cleaner because higher powers would later be used for driving the OPA. The addition of another cavity provides another factor of $1/f$ filter response, thereby leading to additional noise suppression. The red mode-cleaning cavity had a sufficiently narrow linewidth to negate the need for a second red mode-cleaner.

After filtering, some of the light was diverted for the local oscillators, before preparing the seed, pump, and reverse-seed beams with AM and PM sidebands. The sidebands were used later for servo-control purposes. The frequencies (and possible beat frequencies) were

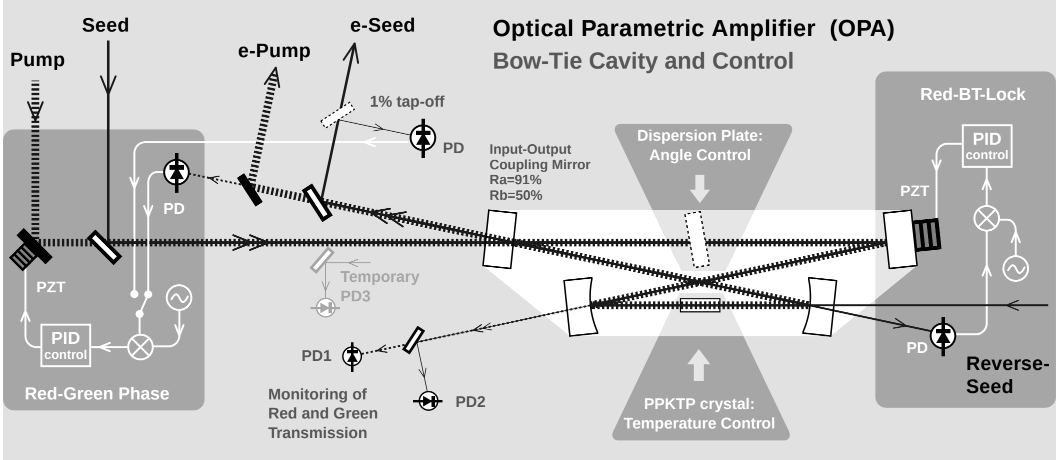

Figure 4.4: Schematic of the OPA setup. Seed and pump beams are injected into the 4-mirror bow-tie cavity. The reflected/emitted e-seed and e-pump are sent on for detection and verification of entanglement. The cavity has closed control loops for the cavity length, crystal temperature, and seed-pump relative phase. The dispersion plate angle is adjusted to minimise OPO threshold power.

chosen to lie outside the anticipated measurement range $5 \rightarrow 10\ \mathrm{MHz}$ to avoid potential interference with the entanglement measurements. The amount of power diverted to each beam was adjustable using polarisation optics. The seed, pump, and local oscillator beams had their polarisation cleaned using Glan-Thomson prisms. The beams were brought to a waist size radius $\sim 1\,\mathrm{mm}$ thus ensuring near-collimation for the length of the $3\,\mathrm{m}$ optical table.

4.3 OPA setup in detail

Because the OPA was the entangling agent, it played the most important role in the experiment. The most important requirements, were those of high escape efficiency and low threshold power. Stability and control were also very important, as an entanglement measurement could take many minutes to complete. These requirements influenced several aspects of the design and construction of the OPA which will now be addressed. A schematic of the OPA is shown in Figure 4.4 together with the photograph and diagram in Plate 1 and Plate 2.

Cavity geometry: It is the reflected pump and seed fields from the OPA that were predicted to be entangled, and so we needed efficient access to these fields without using a Faraday isolator (which typically induces a $\sim 5\%$ loss). We therefore chose a travelling-wave, four-mirror, bow-tie geometry. The bow-tie cavity can be made quite compact without introducing a significant amount of astigmatism (an elliptical transverse mode shape). We wanted the most compact cavity possible (offering a large bandwidth), that had a small angle of incidence for the beam path, yet without the angle being so small as to cause clipping of the beam at the edges of the crystal (keeping a gap the size of a factor 20 of the beam width). A compromise was reached for a 6° angle of incidence, and radii of curvature for the inner mirrors of $38\,\mathrm{mm}$ which were spaced at $44\,\mathrm{mm}$. The flat outer mirrors were spaced at $90\,\mathrm{mm}$. This ensured a stable resonator geometry, with a waist radius in the KTP crystal of $W_0 = 40\,\mu\mathrm{m}$. Which was only $10\,\mu\mathrm{m}$ larger than the Boyd-Kleinman optimum waist for the $10\,\mathrm{mm}$ long KTP crystal. The total optical path length for a round-trip was $285\,\mathrm{mm}$. Note that compared to a standing wave cavity, a travelling wave cavity is sensitive to a back-scattering loss mechanism. We measured a back-scatter of 5 parts per million at $1064\,\mathrm{nm}$ with the cavity on resonance. This level of back-scatter was a negligible source of intra-cavity loss overall.

Optical properties: With the cavity geometry fixed, the next step was to determine the optimum reflectivities of the input-output coupling mirror. No other component has such a strong effect on the OPO threshold power, and more importantly, the accessible entanglement for a fixed total input power. Here, intra-cavity losses also played a role. Rather than leaving the design to heuristic arguments, both parameters R_a and R_b were scanned, while the model of OPA and harmonic entanglement was tested for every combination of pump and seed powers that were available from a maximum of $200\,\mathrm{mW}$ for red and $400\,\mathrm{mW}$ for green. From now on I will use a compact notation like $200/\!\!/400\,\mathrm{mW}$ to describe cavity parameters in the order of red-green. The best value of EPR harmonic entanglement was found in the parameter space and recorded. This result is plotted in Fig. 4.5. Note that the nonlinear coupling strength of the material $\mathrm{LiNbO_3}$ was used in the model, and this generally gives higher OPO threshold powers than for PPKTP. We ordered several mirrors for the experiment such that various combinations of R_a and R_b could be tested. The mirror having the design specifications of $R_a = 90\%$ and $R_b = 40\%$ was chosen for the OPA, with predicted finesse $60/\!\!/8$ (red/\!\!/green). Note that the actual mirrors deviated from these nominal values, which is discussed further in Section 4.4.

Nonlinear crystal: The ideal nonlinear crystal would have a high nonlinearity to loss ratio, and a high damage threshold. The nonlinear material that was chosen was an artificially grown crystal of potassium titanyl phosphate (KTP). This material meets the requirements of high transparency at $1064\,\mathrm{nm}$ and $532\,\mathrm{nm}$. It is birefringent and dispersive, having refractive indices at room temperature at 1064 nm: $n_x = 1.738$; $n_y = 1.746$; $n_z = 1.830$; and at 532 nm: $n_x = 1.779$; $n_y = 1.789$; $n_z = 1.889$. The material has a second-order nonlinear coefficient in pico-metres per volt in the various axes to the principle optic axis: $d_{31} = 6.5$; $d_{32} = 5.0$; $d_{33} = 13.7$; $d_{34} = 7.6$; $d_{35} = 6.1$; see for example [Dmitriev *et al.* 1995]. During the manufacturing process, the use of periodic-poling techniques while growing the crystal, where the sign of the nonlinearity is periodically flipped (but no change to the refractive index), allows the higher nonlinear coefficient to be used (d_{33}) while being quasi-phase-matched at room temperature. Periodically-poled KTP is called PPKTP. A 10 mm long crystal and 1.5 mm by 1.5 mm across was obtained from the manufacturer *Raicol*. The ends were polished flat and AR coated to $< 0.1\%$. The temperature of the crystal had to be actively controlled to $\sim 10\,\mathrm{mK}$, in order to maintain the condition that the red and green fields were co-resonant in the cavity. The phase-matching condition itself was several degrees wide.

The optical properties of the KTP material, and the material's utilisation for nonlinear optics has been reviewed in [Bierlein and Vanherzeele 1989]. The manufacturing technique for the periodic poling of KTP, which is covered in [Chen and Risk 1994], enabled the d_{33} nonlinear coefficient (which is higher than for the other crystal axes) to be used in the quasi-phase-matched configuration and at room temperatures. The application of PPKTP to the task of efficient optical parametric oscillation (OPO) was reviewed in [Myers *et al.* 1995], which culminated in the observation of quadrature squeezed light from a PPKTP based OPO [Suzuki *et al.* 2006], and from a PPKTP based OPA [Hirano *et al.* 2005]. These experimental results established PPKTP as an excellent material for the production of nonclassical light. In comparison to $\mathrm{MgO:LiNbO_3}$ it shows reduced absorption at the $1064\,\mathrm{nm}$ and $532\,\mathrm{nm}$ wavelengths, and a higher effective nonlinearity (which lowers the OPO thresh-

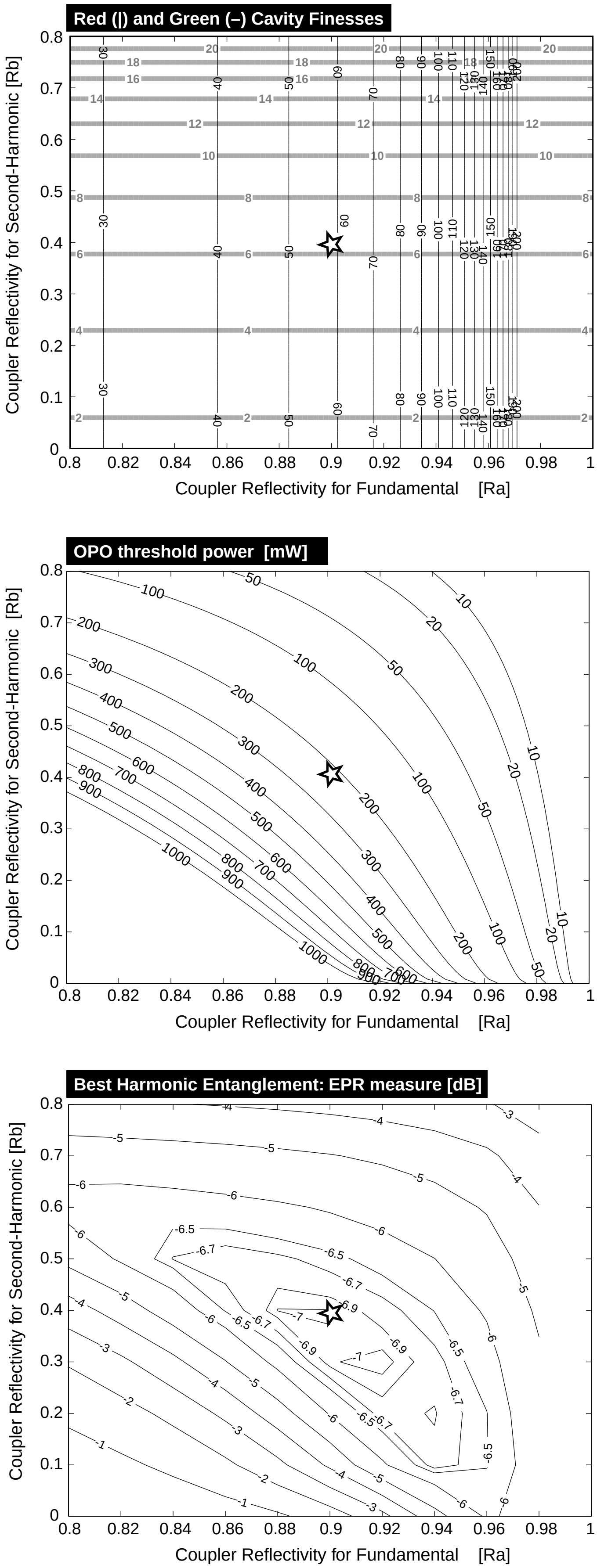

Figure 4.5: A search in the parameter space of the input-output coupler for the best combination of red and green mirror reflectivities. Using the theoretical OPA and entanglement model, with a maximum seed and pump power of $200/\!/400\,\mathrm{mW}$. The best point is marked by the star. This point meets the compromise of minimal cavity finesses (and therefore large cavity linewidths), an OPO threshold power that is easily attainable, and strong harmonic entanglement.

old). However, grey-tracking, which is a photo-refractive damage to the material, can occur at blue-coloured wavelengths and high intensities, which can lead to markedly increased optical losses.

OPA construction: All of the OPA optics were mounted on a single A4 size aluminium block that was $50\,\mathrm{mm}$ high. This kept the feet of the individual optical components under $25\,\mathrm{mm}$ in height, thus helping with mechanical stability. Each of the four mirrors of the bow-tie cavity could have their angles changed by a fine 3-axis control, or be translated in position by $\sim 10\,\mathrm{mm}$. This modular concept was also applied to the crystal and its temperature controller, which could easily be removed in one piece. A perspex lid was placed over the entire assembly to reduce air currents and temperature fluctuations. Holes were left open for the in-coming and out-going seed and pump beams.

OPA control: Four parameters needed to be controlled in the OPA: cavity resonance for red field (closed loop via reverse seed); cavity resonance for green field (open loop via crystal temperature); phase matching condition (open loop via dispersion plate); and the relative phase between the in-coming seed and pump fields (measured via a 1% tap-off on reflection from the OPA).

Red cavity: Since the OPA was resonant for both the red and green fields, the cavity resonance condition had to be met for both colours. Ignoring the green cavity for the moment (I speak as if there were two cavities, but they were geometrically identical) one could lock the red cavity by actuating the position of one mirror that was attached to a piezo electric actuator (PZT) which was driven by a high voltage amplifier $0 \rightarrow 200\,\mathrm{V}$. The position of the mirror was adjusted by a closed-loop control system, which consisted of a proportional integrator controller with a low-pass filter pole located at the high voltage input to the PZT stage. The error signal was extracted using the Pound-Drever-Hall (PDH) method [Drever *et al.* 1983] from an auxiliary beam at $1064\,\mathrm{nm}$, called a 'reverse-seed' beam which was transmitted through one of the HR mirrors and travelled in the reverse direction to the seed and the pump. This meant that the reverse-seed experienced a severely under-coupled cavity, which reduced the size of an extractable error signal, and was also sensitive to residual AM from the phase modulator (which led to offsets that depended on the intensity of the reverse-seed). However, using a reverse-seed that carried its own PM sidebands had a big advantage over an error signal extracted from the seed or pump. This was because the (forward) seed beam would undergo phase-dependent amplification, and this would occur irrespective of whether the PM sidebands were on the pump or the seed. The resulting derived error signal would be the sum of two error signals, one for the cavity length and the other for the seed-pump relative phase. Nevertheless, at the highest seed and pump powers used, a similar kind of dependence was noticeable in the error signal derived from the reverse-seed. This can be attributed to back-scattered intra-cavity light (from the forward to the reverse direction), since the (forward-)seed and reverse-seed relative phases was not controlled. The proportional gain and pole of the low-pass filter were optimised to suppress disturbances from DC up to the unity gain point at $10\,\mathrm{kHz}$.

Green cavity: Although the cavity resonance for the red field was now locked, this did not guarantee co-resonance with the green field. The reason is that all the components in the optical path are dispersive, especially transmission through the PPKTP crystal. In practice we adjusted the temperature of the crystal to bring the green on to co-resonance with the red. The temperature had to be held at about $10\,\mathrm{mK}$ stability. A large temperature range however, was planned (up to 200 degrees Celsius). This was achieved by using a Peltier element attached to a copper heat reservoir that was heated with a resistive element. A thermistor temperature sensor on the small copper crystal cell was read by a NewPort temperature controller. The crystal was enclosed by an adjustable-sized copper cell that gave thermal contact to three sides of the crystal. The thermal reservoir was a 25mm copper cube. The cell and peltier were held onto the cube via stainless steel clamp, as stainless steel is a relatively poor conductor of heat. The reservoir cube was placed on a stainless steel foot which effectively insulated it from the recess built into the aluminium A4-size block. The entire oven assembly was attached to a fine XYZ-axis mount which was bolted onto the optical bench. The XYZ control allowed us to effectively move the waist of the cavity eigenmode around in the crystal to find the best operating point that avoided scattering centres/defects and therefore minimise losses.

Phase-matching: Tuning the temperature to bring the green and red cavities on co-resonance however, brought the crystal away from its optimum phase matching condition. Therefore by turning the dispersion plate, one could adjust the relative phase-shift that was acquired by a round-trip of the red and green fields, and thus compensate for the change in temperature. In this way it was possible to satisfy both the phase-matching condition of the PPKTP, and also the red-green co-resonance condition. The dispersion plate was a slightly wedged piece of BK7 glass with high-quality AR coatings ($< 0.1\%$ for red and green). The glass has a refractive index of $n = 1.501$ for red and $n = 1.502$ for green. Changing the angle at which light travels through the plate, changed the optical path length difference for red and green light. In practice, only about one degree was necessary to sweep through a full red wavelength.

Relative phase: The final control loop was the relative phase between the seed and pump fields. The theoretical analysis assumed that the relative phase was either $\phi = 0$ or $\phi = \pi$. To ensure that this condition was met, a PZT-actuated mirror was placed in the pump path. The error signal for the control loop could be detected on a photodiode that was placed either on the reflected seed or reflected pump beams (via a 1% tap-off). Which signal was used depended on which of the two was larger, and this depended on the particular choice of driving field powers. The error signal was extracted by de-modulating the photocurrent with one of the PM sideband frequencies, either the frequency on the pump field, or the frequency on the seed field, which-ever provided the larger error signal. In practice, the SNR of the error-signal depended on the how much parametric gain was occurring, i.e. more gain meant a larger error signal. By just changing the polarity of the error signal, it was possible to lock to either amplification or de-amplification.

Optical alignment: Good mode-matching of the seed and pump beams into the OPA were vital to avoid coupling significant optical power into higher-order TEM modes. The AM and PM modulator units introduced wave-front distortions. This limited the mode matching of the s-polarised light for seed and pump to 98% and 99%, respectively. The task of mode-matching was made easier because the larger waist of the OPA cavity was $200\,\mu\mathrm{m}$ across. Compare this to the reverse-seed, which was mode-matched to the smaller $40\,\mu\mathrm{m}$ waist of the cavity. For the reverse-seed, it was only possible to get 75% mode-

	Units	Rev. Seed	Pump	Forw. Seed
Wavelength	[nm]	1064±1	532±1	1064±1
Mode-Matching	[%]	76.0±2.2	99.5±0.2	98.9±1.4
Ref.coeff.	[%]	98.8±0.2	69.8±0.9	74.0±0.5
Ref.coeff.corr.	[%]	98.5±0.2	69.6±0.9	73.7±0.7
Linewidth	[MHz]	18.32±0.23	120±3	18.32±0.23
FSR	[MHz]	1047±17	1050±20	1047±17
Finesse	[—]	57.2±1.2	8.74±0.50	57.2±1.2

Table 4.1: Measured properties of the OPA cavity. The reflection coefficient is corrected for the limited mode-matching efficiency.

matching, because the effect of diffraction expanded the beam size beyond the size of the first alignment mirror. The mode-matching and alignment were made while observing the DC photocurrent on detectors PD1, PD2, and PD3; see Figure 4.4. Note that D3 for the reverse-seed was introduced only temporarily by a flipper mirror.

4.4 OPA testing

Before searching for harmonic entanglement, it was good to test some basic classical properties of the OPA. The quantum noise property of squeezing from the OPA in the OPO limit was also tested.

Cavity characterisation: The cavity parameters that we measured here will be used later in the theoretical OPA model. We studied the transmitted and reflected light of the cavity by monitoring the output of several photodetectors while scanning the cavity length. We used the PDH error signal as a frequency ruler to directly determine the cavity linewidth which is defined as a full-width half-maximum (FWHM) of the transmitted Airy function. The accuracy of the free spectra range measurement (and therefore finesse) was boosted by using the technique of counting Guoy phase shifts with the beam slightly misaligned. The results are summarised in Table 4.1. The linewidth for red at $18\,\mathrm{MHz}$ was much narrower than for green. This determined the highest frequency that we could expect to measure entanglement. From the finesse and the corrected reflection coefficients, we could deduce the input-output coupler reflectivity $90/\!\!/53\%$ (red//green); as well as the combined loss of all the other components per round-trip $0.7/\!\!/7.7\%$. The loss for green was surprisingly high. Note that this was the combined loss that included transmission through the PPKTP crystal

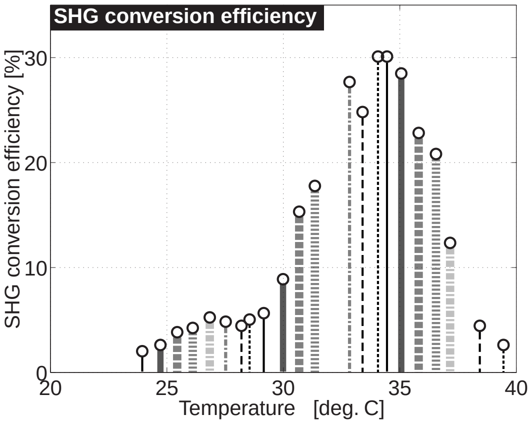

Figure 4.6: SHG conversion efficiency as a function of temperature and different angles of the dispersion plate. The points correspond to maximum conversion efficiency which was found at the red-green co-resonance condition. Vertical lines of the same pattern belong to measurements taken at the same angle of the dispersion plate.

and dispersion plate, and reflections from their AR coatings. Similar measurements that we had made half a year earlier had yielded only half the loss for green. This may be evidence for the phenomenon of grey-tracking, where the KPT material is exposed to bright light for long periods of time and accumulates photo-refractive defects. It is well known that the rate of damage, and the strength of the scattering effect, is more pronounced for light at shorter wavelengths.

SHG efficiency: The simplest test for checking the nonlinear interaction was to observe second-harmonic generation (SHG). The method was to hold the cavity on resonance using the reverse seed. The (forward) seed was then set at a given input power of $10\,\mathrm{mW}$. The temperature of the cavity was swept (which periodically brought the green co-resonant with the red). The SHG output was monitored on the green reflection photodetector. The temperature was recorded at which the conversion was maximum, as well as the optical power which gave an estimate of the SHG conversion efficiency. Typically three peaks could be recorded within a $20°\mathrm{C}$ temperature range. Then the angle of the dispersion plate was adjusted by a few tenths of a degree, and the temperature scan was repeated. The result is that the expected sinc-squared dependence of conversion efficiency on phase-matching is clearly seen in Fig. 4.6. For our PPKTP crystal, the width of the central peak is about $5°\mathrm{C}$. Which is quite broad compared to the co-resonance condition which is only $\sim 0.1°\mathrm{C}$ across. This meant that meeting the co-resonance condition was more critical than meeting the phase-matching temperature. Through this measurement process we were able to find the optimum angle of the dispersion plate, and also the optimum operating temperature, that gave the largest effective nonlinearity.

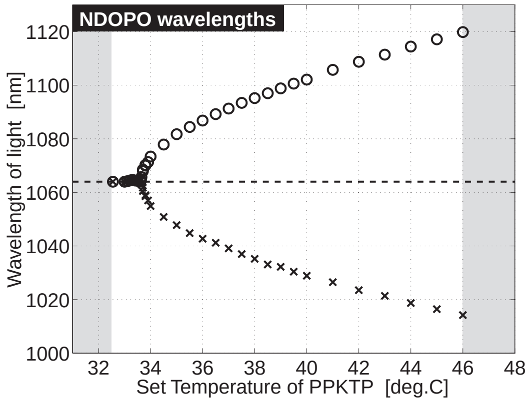

Figure 4.7: The wavelengths of light emitted from the system that was driven above OPO threshold. The non-degeneracy increased with increasing crystal temperature. The grey-zones mark the limitation set by the maximum pump power ($320\,\mathrm{mW}$).

OPO threshold power: The critical pump power at which optical parametric oscillation (OPO) begins, is the most defining property of the OPA system. We measured it by monitoring the power on the reflected red detector, while holding the cavity locked on resonance using the reverse-seed. The crystal temperature was adjusted to bring the green cavity on co-resonance. The pump power was increased until a signal was observed in the red reflection detector. After the optimisation procedure outlined in the SHG section, the OPO threshold power was typically observed to be $P_{\rm thr} = 85 \pm 5$ mW. Where the uncertainty in our estimate is attributed to the absolute accuracy of the independent power meter used. This threshold power was deemed sufficiently low so that we could continue with the harmonic entanglement experiment, i.e. there was no need to change the output coupler for one of higher reflectivity. By knowing the threshold power, and the cavity reflectivities, one can work backwards from the theory to obtain the effective nonlinearity. In our case we got $\epsilon = 1500\,\sqrt{\rm Hz}$ which was the value to be used later in the theoretical modelling. An independent estimate of the OPO threshold pump power can be made using the Boyd-Kleinman theory [Kleinman *et al.* 1966]. Here, the value strongly depends on the estimate of the waist size of the cavity eigenmode. Using the value $40\,\mu\mathrm{m}$ we arrived at a threshold power of $70\,\mathrm{mW}$ assuming that the PPKTP material had the optimal poling rate. This is in reasonable agreement with the observed value.

NDOPO above-threshold: Having found the OPO threshold power, we took the opportunity to study the light that was produced above this threshold. The light turned out not to have exactly the $1064\,\mathrm{nm}$ wavelength, but was rather produced in two beams, above and below in wavelength, hence the term non-degenerate OPO (NDOPO).

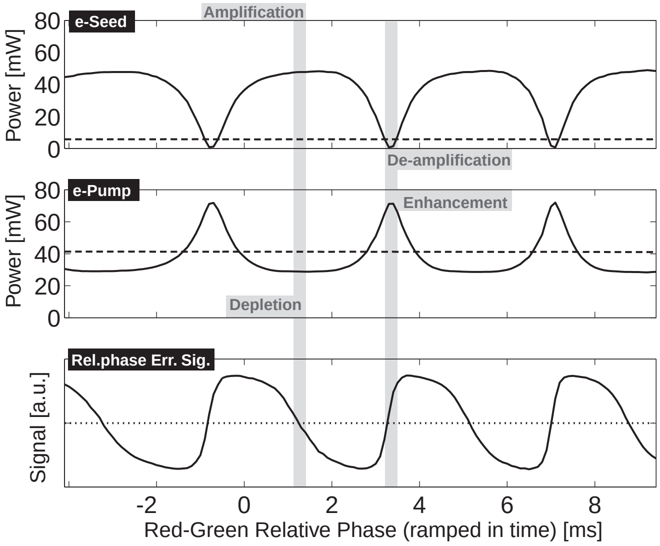

Figure 4.8: A demonstration of OPA seed gain and pump depletion. The input seed power was $36\,\mathrm{mW}$; input pump power $64\,\mathrm{mW}$. The relative phase was ramped over time, showing the exchange of energy between the two fields. The total reflected power remained nearly constant at $75 \pm 5\,\mathrm{mW}$. Dashed lines show the level of the reflected field with the absence of the other input field.

A commercial optical spectrum analyser was used to observe the wavelength of the light emitted by the OPA cavity, when the pump power was increased above threshold. The cavity was held on resonance using the reverse-seed. The measurements were repeated at different phase-matching temperatures, that also ensured red-green co-resonance. The results are plotted in Figure 4.4. One can see that below a certain temperature, the OPO is operating degenerately at $1064\,\mathrm{nm}$. As the temperature is increased, the wavelengths separate, because the phase-matching of the PPKTP is now matched for those two particular wavelengths and also the pump field. Note the pump power had to be increased to reach the wider non-degeneracy, until the limits were reached which are shown as grey zones. This test demonstrated that the OPA system was also capable of behaving as a NDOPO that could have a non-degeneracy of up to $100\,\mathrm{nm}$.

OPA seed gain and pump depletion: The purpose here was to test whether a significant amount energy could be exchanged between the red and green fields via their interaction in the OPA cavity. This is important because one prediction from the model is that an exchange of energy needs to occur to produce harmonic entanglement. The method was to lock the cavity length on the red and green co-resonance. The seed power was held constant at $36\,\mathrm{mW}$ and the pump power at $64\,\mathrm{mW}$. The seed-pump relative phase was then ramped over time, while monitoring the reflected power for both colours, and also the PDH-derived error signal. The results showed a repeating pattern of seed amplification and de-amplification that was concomitant with the pattern of pump depletion and enhancement, respectively; see Figure 4.8. The dashed line show the reflected seed power for when the pump was blocked, and vice-versa the dashed line for the reflected pump power plot. The total optical power of the reflected fields remained constant at about $75\,\mathrm{mW}$, which meant that $25\,\mathrm{mW}$ was being scattered or leaked out of the cavity. The error signal showed a zero-crossing for both amplification and de-amplification, thereby allowing us to lock the relative phase in both regimes. The exchange of energy was significant, as the power could be transferred almost completely from red to green, or green to red. Whichever occurred depended only on the relative-phase.

OPO squeezing: The simplest test of the quantum noise properties of the OPA system, was to check for squeezed light produced by driving the system in the OPO regime. The method was to lock the cavity length onto red-green co-resonance. The reflected seed was aligned on a balanced homodyne detector, the LO phase was ramped over time, and the noise power was measured at a sideband frequency of $7.8\,\mathrm{MHz}$. The homodyne detector had a total detection efficiency of about 85%. The seed was then blocked, and the pump power fixed at $81\,\mathrm{mW}$ which was about 95% of OPO threshold power. Figure 4.9 shows the resulting squeezing and anti-squeezing as the local oscillator phase was ramped. The best squeezing shows $-4\,\mathrm{dB}$, and the anti-squeezing $+6\,\mathrm{dB}$. We also repeated the measurements for a range of pump powers (from 10 mW to 94 mW). The trend of larger squeezing with larger pump powers can be seen in Figure 4.10. The limitation of $-4\,\mathrm{dB}$ squeezing is consistent with a homodyne total detection efficiency of 85% and a cavity escape efficiency of 86%. The observation of squeezed light meant that the system passed a key test for harmonic entanglement observations.

Conclusion: The OPA system had proved itself in terms of exhibiting the wide range of classical behaviour expected of it (SHG, OPO, NDOPO, OPA). And also gave a first hint at the nonclassical squeezed states of light produced by OPO, which are prerequisites for the generation of harmonic entanglement.

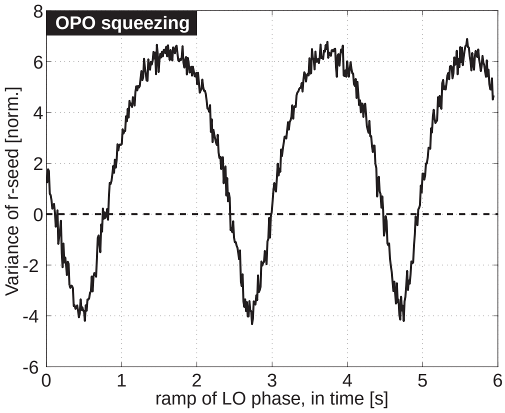

Figure 4.9: Squeezed light from an OPO. Quadrature variances are in decibel scale and normalised to the vacuum state. The pump power was fixed at $81\,\mathrm{mW}$. The local oscillator phase was scanned.

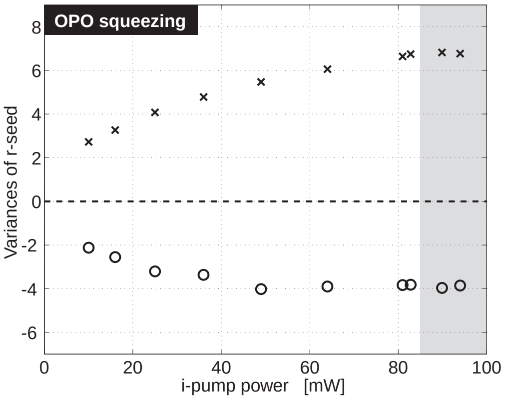

Figure 4.10: Squeezing and anti-squeezing from the OPO for a range of pump powers. Quadrature variances are in decibel scale and normalised to the vacuum state. The grey shaded area marks the above-threshold regime.

4.5 Optical Carrier Rejection

Harmonic entanglement was predicted to occur on the sidebands of bright optical fields ($>100\,\mathrm{mW}$) reflected from the OPA. It was not practical to use homodyne detection directly, which requires the local oscillator (LO) to be much brighter than the signal beam. We used the method of optical carrier rejection (OCR), with a near-impedance-matched filter cavity, to transmit the unwanted carrier light, and efficiently reflect the desired sidebands ready for homodyne detection. The schematic is shown in Figure 4.11. For the filter cavity to be successful as an optical carrier rejector, it had to meet some requirements: (1) be nearly impedance-matched to suppress as much carrier as possible; (2) have a sufficiently narrow bandwidth such that the sidebands are not attenuated; (3) have an excellent mode-matching capability, i.e. be relatively astigmatism-free. The filter cavities that we built met all of these requirements.

Construction: The cavity had a 3-mirror ring geometry with an $800\,\mathrm{mm}$ round-trip path length and $4°$ angle of incidence on the $2\,\mathrm{m}$ curved end mirror. The original design was by K. McKenzie. We modified the end-cap that housed the PZT actuator and mirror assembly to allow one to tilt the curved mirror and therefore allow centering of the spatial eigenmode. The cavity was held on resonance by a PDH error signal that was derived from a $150\,\mathrm{kHz}$ dither of the end mirror. The error signal was extracted from a detector that

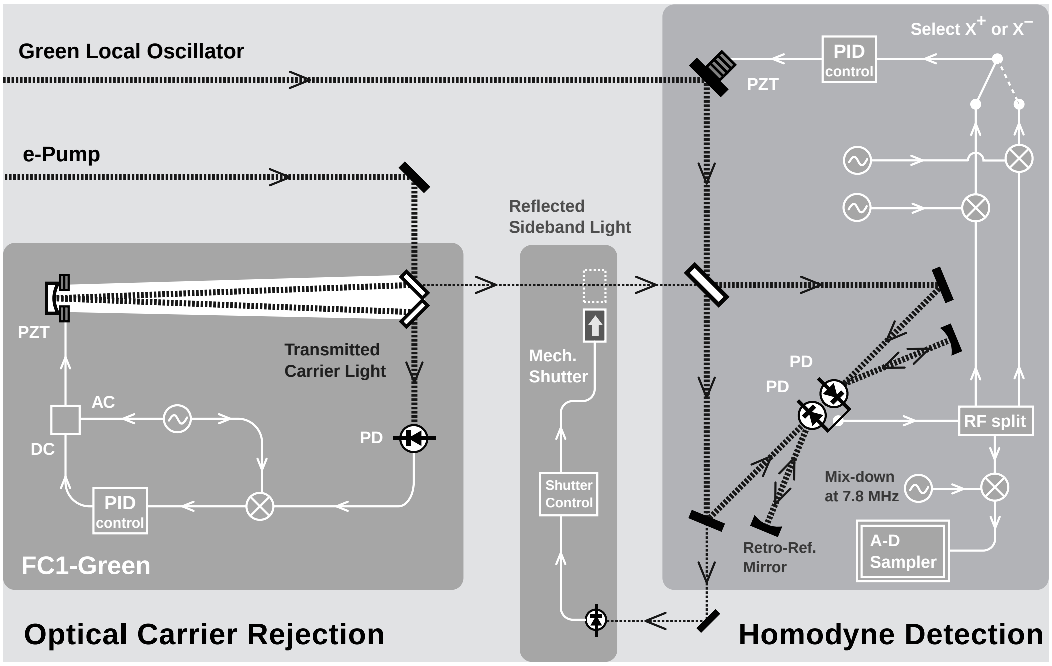

Figure 4.11: Schematic of the application of optical carrier rejection, and homodyne detection for measuring the quadrature amplitudes of bright light beams. Outlined in white are the servo-control electronics.

was placed in transmission (with suitable attenuation). The dither depth was set somewhere between 0.01% and 0.1% of the maximum transmitted power, with the level depending on the amount of available light. Excellent mode-matching was achieved by performing the alignment with the appropriate eigenmode that was emitted by the OPA cavity. For example, we would use the OPA system as an SHG to align the green filter cavity; and then use the OPA system in an OPA amplification regime (with gain ~ 10), to align the red filter-cavity. Final values for the mode-matching were typically $99.8 \pm 0.1 /\!\!/ 99.9 \pm 0.1\%$ for (red$/\!\!/$green), which satisfy the mode-matching requirements.

Performance: The filter cavities were characterised for their gross optical properties. The methods used here have already been described in the OPA section. The results are summarised in Table 4.2. The measured linewidths were $980\,\mathrm{kHz}$ for red, and $370\,\mathrm{kHz}$ for green. With the filter cavities locked onto resonance, the attenuation of the carrier was up to $22\,\mathrm{dB}$ for red and $26\,\mathrm{dB}$ for green. This level of attenuation of the carrier would in principle be sufficient to allow the homodyne detection of a $100\,\mathrm{mW}$ signal beam using only a $30\,\mathrm{mW}$ local oscillator, thus satisfying the attenuation requirement.

From the data we could also create theoretical models of the filter cavities, to predict

	Units	MC1G	MC2G	MC2R	FC1G	FC1R
Mode-Match.	[%]	98.1±0.1	98.0±0.4	98.8±0.4	99.9±0.1	99.8±0.1
Ref.coeff.	[%]	5.0±0.2	21.9±0.4	3.1±0.4	0.24±0.05	0.73±0.05
Ref.coeff.corr.	[%]	3.2±0.6	20.3±0.5	1.9±0.6	0.13±0.10	0.53±0.11
Linewidth	[kHz]	1010±30	1850±50	418±5	980±40	373±14
FSR	[MHz]	347±10	345±10	346±7	347±10	346±7
Finesse	[—]	344±10	186±10	828±19	351±9	928±31

Table 4.2: Measured properties of the mode-cleaners and filter cavities. ‘Ref.coeff.corr’ is the reflectance coefficient of the cavity when in a locked state on the TEM00 mode, and with a correction for the measured mode-matching.

what attenuation and phase-shift the upper and lower sidebands would experience upon reflection from the cavity. The cavities were modelled as simple two-mirror cavities, with the red having mirrors 99.64% and 99.69% (the former being the input-output coupler); and the green 99.08% and 99.14%. Figure 4.6 shows that for sideband frequencies greater than $5\,\mathrm{MHz}$, the attenuation should be less than $0.05\,\mathrm{dB}$ and a phase shift less than $6°$. This is small when compared to the specified AR coating reflectivity of $< 0.5\%$, therefore the filter cavity satisfied all three requirements for deployment in the optical carrier rejection scheme.

Additional construction notes: Extra precautions were taken to avoid dust settling on the mirror surfaces during construction. We assembled the cavities in one of the clean rooms made available by Dr. Steve Madden at the Australian National University. The Invar cavities (actually split in two halves), were de-greased using at a vapour de-greasing facility. Before installing the mirrors, the surfaces were inspected under a microscope for any surface defects or dust particles. Only a clean nitrogen gas jet was applied over the surface to remove the dust. The two halves of the invar spacer were bolted together and sealed with vacuum compatible epoxy. The mirrors were glued onto the invar spacer using UV-curing adhesive, which had the advantage of allowing us to completely seal the cavity within only a couple of hours. We believe that this procedure was necessary, because the second green mode-cleaning cavity (MC-2G) had been assembled without these precautions. After a period of 12 months of operation, its finesse dropped from about 350 to 186 ± 10, which was an indication of continuing contamination/damage of the intra-cavity mirror surfaces.

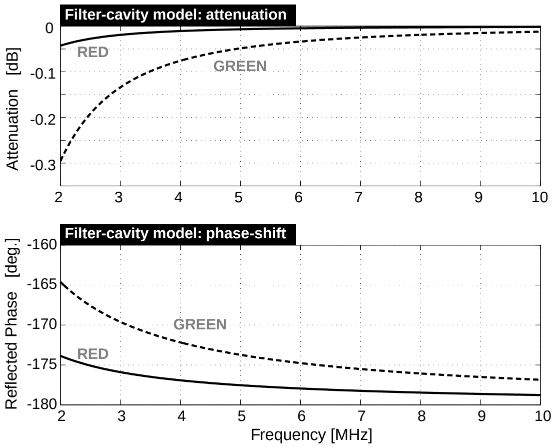

Figure 4.12: A model of the transfer functions of light reflected from the filter cavities. The minimal attenuation and phase-shift experienced by the reflected sideband fields indicate that the cavities will perform well as an optical carrier rejector.

4.6 Homodyne detection

The role of the homodyne detector was to convert into an electronic signal, the quadrature amplitudes that resided on the upper and lower sidebands that were centred around the carrier of an optical beam. In a balanced homodyne detector, the local oscillator (LO) serves as a phase reference and effectively amplifies the quadrature amplitudes, with the noise on the LO itself suppressed (because the noise is common mode). The homodyne detector should ideally have a high total detection efficiency. This relies on having good mode overlap between the signal and LO beams, and on finding photodiodes with high quantum efficiency. Also desirable, are photodiodes with a large bandwidth and low dark-noise, i.e. good shot-noise clearance above dark-noise. The homodyne detector must also demonstrate a linear noise response to the LO power.

Red homodyne detector: The LO and signal beam were incident on a beam splitter with close to 50/50 splitting ratio (adjustable using polarisation angle). Eight degrees of freedom of the LO were matched to those of the signal beam. These were the four degrees of freedom for the position and direction of the beam; two for the Gaussian beam waist size and waist position; and two for the polarisation. Measurements of the fringe visibility with the seed amplified by the OPA by a factor of ten (which corresponds to the OPA cavity eigenmode), typically yielded 99.0%. The light from each output port was directed onto an InGaAs photodiode (ETX500, *Epitaxx* now *JDS-Uniphase*) having an estimated quantum efficiency of $95 \pm 2\%$. The photodiodes were arranged back-to-back on the circuit board, such that the photocurrents were directly subtracted from one another before the trans-impedance amplifier. The photodiodes did not have their protection windows removed. It was possible to vary the photodiode response by about 2% by tweaking the angle of the light beam incident on the detector. This may have been the result of parasitic interference fringes from the AR coatings of the window and/or the semiconductor layers and coatings. Care was taken to fill the maximum amount of photodiode surface before the onset of clipping of the beam. We noticed a problem in the experiment when the photodiode was aligned in such a way as to retro-reflect light back into the OPA cavity. This tended to cause the lock of the seed-pump relative phase to become unstable. We therefore selected a nearby high response fringe that was not precisely retro-reflecting.

The first test was to check the common mode rejection (CMR) capability of the homodyne detector, i.e. the suppression of intensity noise on the LO. For this, the laser noise-eater was disengaged, and the relaxation oscillation at $1\,\mathrm{MHz}$ was observed on an electronic spectrum analyser. A typical value for the CMR was $35\,\mathrm{dB}$. The clearance of shot-noise above dark-noise was typically $15\,\mathrm{dB}$, from the $2 \rightarrow 20\,\mathrm{MHz}$ range, with a LO power of $20\,\mathrm{mW}$. The linear response of the homodyne detector was tested by measuring the response of RF noise power (and also DC response) to an increasing LO power that was calibrated to a commercial power meter. We chose an RF sideband at $7.8\,\mathrm{MHz}$ with a bandwidth of $30\,\mathrm{kHz}$. The LO power was varied from zero up to $12.5\,\mathrm{mW}$ over 20 measurements. There was no indication of nonlinearity (saturation) occurring at high powers. Nevertheless, we cautiously chose to operate the homodyne detector with a LO power of 70% of the maximum power tested.

Green homodyne detector: The green homodyne detector was built in the same way as the red one, except that a silicon photodiode was used instead (s5973-02, *Hamamatsu*) that had an estimated quantum efficiency of $89 \pm 5\%$. We found that the photodiodes reflected $8 \rightarrow 10\%$ of the incident light over a wide range of angles ($0 \rightarrow 15^\circ$). We therefore installed small concave mirrors (ROC=$15\,\mathrm{mm}$), to retro-reflect the light back onto the photodiodes. This boosted the detected power by a measurable 7%. We saw only minor interference effects between the forward and retro-reflected light ($< 0.1\%$).

An array of tests were performed on the green homodyne detector. The fringe visibility

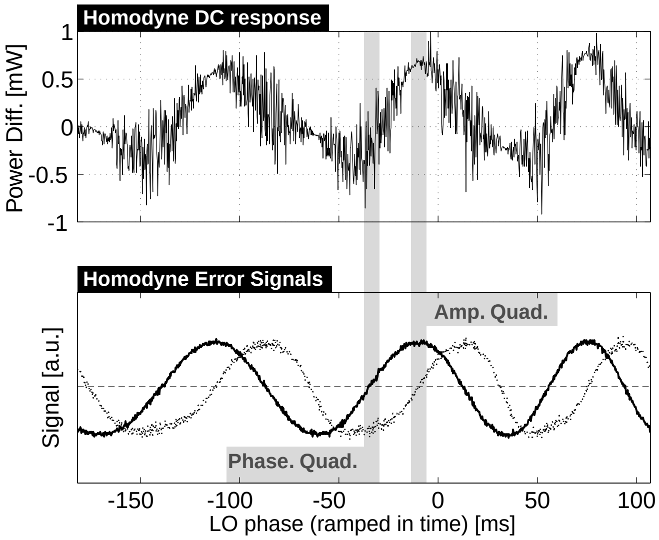

Figure 4.13: DC response of the green homodyne detector with optical carrier rejection engaged. An original signal beam of $30\,\mathrm{mW}$ was rejected by a factor of $-20\,\mathrm{dB}$. The LO phase was ramped, and the error signals for amplitude and phase observed.

with the second-harmonic light produced by the OPA in the SHG regime (which corresponds to the OPA cavity eigenmode), was typically at the 99.4% level. The CMR of the laser relaxation oscillation was typically $30\,\mathrm{dB}$. Clearance above dark noise was $15\,\mathrm{dB}$ across the range $2 \rightarrow 20\,\mathrm{MHz}$. The linearity of the RF response as a function of LO optical power was tested from zero up to $8.8\,\mathrm{mW}$. There was no indication of nonlinearity (saturation) occurring at high powers. Nevertheless, we cautiously chose to operate the homodyne detector with a LO power of 80% of the maximum power tested.

LO phase control: The phase of the LO had to be actively controlled to measure either the phase or amplitude quadratures. This is most important for verifying the presence of entanglement. When measuring the elements of the correlation matrix, the quadratures must for each sub-system (in our case colour) must be orthogonal to one another. Our method was to control the phase using an error signal derived from the AM and PM sidebands that were present on the seed and pump beams. These modulations were recovered in the homodyne photodetector signals, which were then demodulated and filtered using standard techniquies.

An example of the error signals and DC response of the homodyne detector is given in Fig. 4.13 where the LO phase was ramped over time. The RF error signals proved to be very stable in comparison to the DC response of the homodyne detector for frequencies below the linewidth of the OCR filter cavities. This is evidence that the filter cavities were performing their role, i.e. the sideband frequencies above the bandwidth of the filter

	# Red	Trans. (each→total) [%]	# Green	Trans. (each→total) [%]
Dichroic Ref. s-pol.	1	99.6	—	—
Dichroic Trans. p-pol	—	—	1	99.0
1% tap-off	1	99.0	1	99.0
HR mirror	10	$99.8 \rightarrow 98.0$	11	$99.8 \rightarrow 97.8$
Lens 2AR	7	$99.75 \rightarrow 98.3$	7	$99.75 \rightarrow 98.3$
Waveplates 2AR	5	$99.5 \rightarrow 97.5$	4	$99.5 \rightarrow 98.0$
FC1R in Ref. at 7.8 MHz	1	99.4	—	—
FC1G in Ref. at 7.8 MHz	—	—	1	99.0
Beamsplitter AR	1	99.5	1	99.5
Homodyne efficiency	1	97.9	1	98.8
Photodiode efficiency	1	95 ± 2	1	89 ± 5
Total Efficiency	—	85	—	80

Table 4.3: An estimate of the optical losses along the path from the OPA to the photodiodes in the homodyne detectors. The contribution to the total loss made by each optical component is shown. Note that the homodyne efficiency is equal to the square of the fringe visibility.

cavity were insensitive to fluctuations in de-tuning. The locking points are where the error signal crosses the zero point. The apparent noise on the DC response was the remnant of the dither oscillation of the OCR filter cavity ($150\,\mathrm{kHz}$). Note that we had the freedom to choose the polarity of the error signal. This meant that the sign of the quadrature data was arbitrary. The sign of the time-series quadrature data was later processed to conform to a standard given by the so-called calibration point of input power $81\,\mathrm{mW}$ for the seed, and $9\,\mathrm{mW}$ for the pump (locked in the regime of seed de-amplification). Prior to performing entanglement measurements, the offset of the locking point was adjusted to coincide with the appropriate maximum/minimum of the noise variance of the measured state. This ensured the orthogonality of the quadrature being measured.

Homodyne protection system: If during a harmonic entanglement run, the filter-cavities were to fall out of lock, then more than $100\,\mathrm{mW}$ of light would fall on the photodiodes of the homodyne detector. These would quickly heat the diodes and destroy them. To prevent this, we constructed a shutter system in the signal beam path, that was triggered by small auxiliary photodiodes, where a fraction of the light on the path toward each homodyne detector was tapped-off from the transmission through a HR mirror ($< 0.1\%$). A control system with an adjustable threshold then triggered a shutter to close the signal beam.

Total detection efficiency: An estimate of the total detection efficiency of the entire experiment is important for the purpose of getting an accurate model of the experiment.

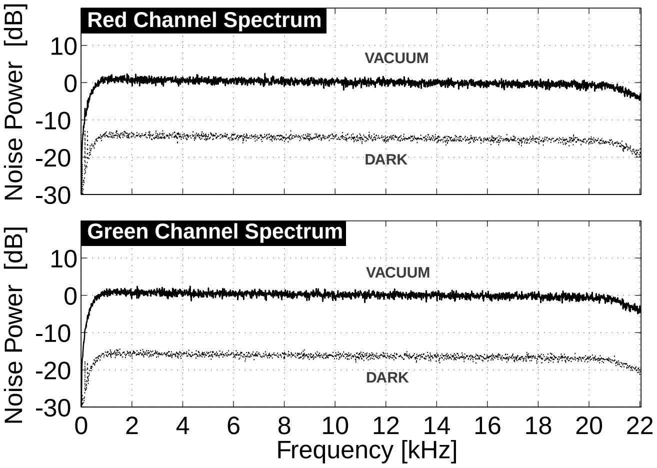

Figure 4.14: Spectra of the sampled data for a vacuum state and for detector dark noise. Clearance of dark-noise above shot-noise is $15\,\mathrm{dB}$.

Here we attempt to catalogue all the loss mechanisms along optical path from the OPA cavity to the photodiode in the homodyne detector. The estimated losses from the optical components and their surfaces are listed in Table 4.3. The total detection efficiency was then estimated to be $85 \pm 4\%$ for the red path, and $80 \pm 6\%$ for the green path.

4.7 Signal processing

Independent electronic channels were built to filter and amplify the photocurrents from each homodyne detector. Each channel could then be observed on an electronic spectrum analyser, or recorded on a separate RF mix-down circuit with digital sampler. The spectrum analyser was used primarily for diagnostics and checking the locking points of the homodyne detector (amplitude and phase). The RF mix-down and sampler were used to record a time-series to allow the direct calculation of the correlation coefficient, and subsequent evaluation of the correlation matrix.

Electronic channels: The photodetector circuits were built from a trans-impedance stage whose output was connected to a DC-coupled buffer stage. The signal was filtered between $1.8\,\mathrm{MHz}$ and $10\,\mathrm{MHz}$. This was done to remove the modulations present at higher frequencies that were left over from the LO phase locks. At this point onwards, one could measure the signal either on the spectrum analyser directly, or it could be sent on for further processing. The processing continued with a $+17\,\mathrm{dB}$ amplification stage before being mixed down with an electronic local oscillator at $\Omega = 7.8\,\mathrm{MHz}$. The resulting signal was low-passed into the audio band and amplified by $+60\,\mathrm{dB}$ using a low-noise audio ampli-

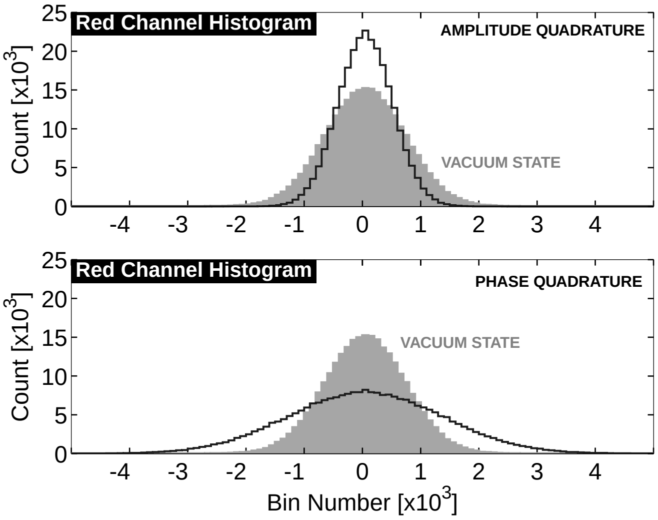

Figure 4.15: Histograms of the sampled channel data. A vacuum state measurement is shown by the grey-filled histogram which conforms to a Gaussian distribution according to a chi-square test and 99.9% confidence interval. The black-outlined histogram is from an amplitude squeezed state, that was produced with seed and pump power of $5\,\mathrm{mW}$ and $60\,\mathrm{mW}$, respectively.

fier. A high-pass filter with a pole at $80\,\mathrm{Hz}$ was used to remove residual line noise (mostly $50\,\mathrm{Hz}$), before being sampled by a sound card in the computer. The paths for red and green channels were kept physically separate until the sound card. A test of the cross-talk between the two channels was made acquiring a shot-noise trace. It revealed a cross-talk (correlation) of $-30\,\mathrm{dB}$ of the level of the shot-noise level itself, which was negligible. During each step of the measurement sequence, 2^{18} points were acquired at a sampling rate of $44.1\,\mathrm{kHz}$ with a $16\,\mathrm{bit}$ resolution. Figure 4.14 shows the resulting spectrum of the sampled data for both a dark noise and shot noise measurement. The $15\,\mathrm{dB}$ clearance of shot noise above dark noise is visible. Note also, that the spectrum is essentially flat, with the exception of the high-pass pole at $80\,\mathrm{Hz}$, and the beginning of the anti-aliasing filter at $20\,\mathrm{kHz}$. It was important to check that the sampled data was indeed Gaussian distributed. A histogram of a measured vacuum state is shown in Figure 4.15. A chi-square analysis confirmed that the data adhered to a Gaussian distribution with a confidence level of 99.9%. Also shown is an example of the distribution of a squeezed state.

Data analysis: For an entanglement measurement, several sets of data must be sampled. While the entangler was operating, all four combinations of amplitude and phase for each colour were recorded $(X_R^+, X_G^+); (X_R^+, X_G^-); (X_R^-, X_G^+); (X_R^-, X_G^-)$. Then the reference for vacuum states $(X_R^{\mathrm{v}}, X_G^{\mathrm{v}})$ were recorded. These were necessary to normalise the previous data to the vacuum state, i.e. such that a quadrature variance of 1 signifies a vacuum state. The signal beams alone (without local oscillators) were then recorded $(X_R^{\mathrm{s}}, X_G^{\mathrm{s}})$, which showed the noise power of the carrier light in higher-order spatial modes. This excess light came from pump and seed light that was not mode-matched into the bow-tie cavity and the OCR filter-cavities. Given that the homodyne detector visibilities were in excess of 99%, and the OCR was suppressing 26 dB of carrier light, it is reasonable to assume that the excess noise was acting like a local-oscillator for higher-order spatial modes in the true LO beam. And since these were occupied by vacuum states, it is safe to assume that the excess noise was independent of the entanglement itself. Indeed, there was only very little correlation ($-20\,\mathrm{dB}$ of the shot-noise level) between any pairs of signal beam measurements. With both the signal and LO beams blocked, the dark noise of the homodyne detectors was also recorded $(X_R^{\mathrm{d}}, X_G^{\mathrm{d}})$.

Each recorded measurement is therefore hypothesised to be made up of several independent noise components that add linearly:

$$X_R^{\mathrm{d}} = g_1(d_1) \quad , \quad X_G^{\mathrm{d}} = g_2(d_2) \tag{4.1}$$

$$X_R^{\mathrm{v}} = g_1(d_1 + v_1) \quad , \quad X_G^{\mathrm{v}} = g_2(d_2 + v_2) \tag{4.2}$$

$$X_R^{\mathrm{s}} = g_1(d_1 + s_1) \quad , \quad X_G^{\mathrm{s}} = g_2(d_2 + s_2) \tag{4.3}$$

$$X_R^{+} = g_1(d_1 + s_1 + p_1) \quad , \quad X_G^{+} = g_2(d_2 + s_2 + p_2) \tag{4.4}$$

where the subscripts 1 and 2 refer to the red and green fields, respectively; g_1 is a gain term that depends on the gain of the electronics; d_1 is the detector dark noise; v_1 is the vacuum state; s_1 is the vacuum state contribution from the signal beam acting as a local oscillator for higher order modes; p_1 is the ‘plus’ or amplitude quadrature of the signal beam as scaled by the true local oscillator. Note that prior to processing, the mean value of the entire recording was calculated and subtracted from each set.

The data was processed in two streams: one with, and one without, corrections for the excess noise from the optical carrier rejection technique. Because of the Gaussian statistics involved, it was possible to simply subtract those particular contributions from the appropriate averaged quantities. The formula for the corrected and uncorrected variances are:

$$V^{+}_{R,\mathrm{uncorr}} := \frac{\overline{(X^{+}_{R})^2} - \overline{(X^{\mathrm{d}}_{R})^2}}{\overline{(X^{\mathrm{v}}_{R})^2} - \overline{(X^{\mathrm{d}}_{R})^2}} = \frac{\overline{(p_1)^2} + \overline{(s_1)^2}}{\overline{(v_1)^2}} \tag{4.5}$$

$$V^{+}_{R,\mathrm{corr}} := \frac{\overline{(X^{+}_{R})^2} - \overline{(X^{\mathrm{s}}_{R})^2}}{\overline{(X^{\mathrm{v}}_{R})^2} - \overline{(X^{\mathrm{d}}_{R})^2}} = \frac{\overline{(p_1)^2}}{\overline{(v_1)^2}} \tag{4.6}$$

where the overbar indicates the average over all data points, and the vacuum state variance is $\overline{(v_1)^2} = 1$. These definitions deliver the quadrature variance of the signal beam which is free of any electronic gain terms. The correlation coefficient between the red and green fields is given by the formula:

$$C^{++}_{RG} := \frac{\overline{(X^{+}_{R} X^{+}_{G})}}{\left[\overline{(X^{\mathrm{v}}_{R})^2} - \overline{(X^{\mathrm{d}}_{R})^2}\right]^{1/2}\left[\overline{(X^{\mathrm{v}}_{G})^2} - \overline{(X^{\mathrm{d}}_{G})^2}\right]^{1/2}} = \frac{\overline{(p_1 p_2)}}{\left[\overline{(v_1)^2 (v_2)^2}\right]^{1/2}} \tag{4.7}$$

Due to the non-correlation of the dark noise and signal beam noise sources between the red and green fields, this formula delivers the correlation coefficient that is free of those terms. The correlation coefficient is also free of any electronic gain terms, because it is normalised to the vacuum state. By applying this method to the other combinations of amplitude and phase quadratures, it is possible to build up the elements of the correlation matrix which can then be analysed according to the inseparability criterion.

4.8 Procedure

The following just serves to give an overview of the daily alignment procedure that was necessary even before measurements of entanglement could begin.

- The laser and frequency doubler were given at least one hour to stabilise after being switched on. The light was aligned onto the mode-cleaners, which were locked and the offset of the locking point from resonance was nulled.
- The reverse-seed was aligned onto the OPA, and the error signal was checked for any AM, i.e. an optical contribution to the offset of the error signal. This was removed by adjusting the polarisation optics. The OPA was locked and the offset was nulled.
- The pump and seed beams were aligned onto the OPA cavity. The mode-matching was measured.
- The green eigenmode of the OPA cavity was produced by locking the OPA and using it as an SHG. The green was mode-matched into the filter cavity. The mode-matching was measured.

- The FC-1G was left to drift, while the LO was aligned to the signal beam. The visibility was measured.
- The LO power was set, and the CMR checked on the spectrum analyser.
- A similar procedure was performed for the red eigenmode of the cavity, using the OPA as an amplifier of a weak seed (by a factor of 10). The mode-matching into the red filter cavity was optimised, as well as the homodyne visibility and CMR.
- The homodyne protection system was checked by increasing the LO power of each colour until the shutters triggered at the 12 volt level. The LO powers were returned to the standard 10 volt level.
- The system was ready for a measurement run. Starting with the calibration: seed power 81 mW, pump power 9 mW, locked to de-amplification.
- The quadratures of each colour were scanned, and the LO phase lock was checked to coincide with either the max. or min. noise power as appropriate.
- The four combinations of quadratures were measured, followed by measurements of the vacuum, dark, and OCR excess noises.
- Then the procedure was repeated for another set of pump and seed powers.
- The data was later analysed according to the method outlined in the previous sections.

4.9 Summary

In this chapter, I have given an account of the design, construction, and operation of an experiment to measure harmonic entanglement from an OPA. The key components of the experiment: the laser source, the mode-cleaning cavities, the OPA, the optical-carrier-rejection system, and the homodyne detectors, were described and characterised in detail. The components worked together in a sufficiently stable manner to enable the testing of the theoretical predictions of the OPA model.

Chapter 5

Harmonic Entanglement Experiment: The GAWBS Hypothesis

Our first attempts at measuring harmonic entanglement were plagued by a set of narrow peaks in the phase quadrature spectra of the reflected seed and pump fields from the optical parametric amplifier (OPA). We hypothesised that these peaks came from the phenomenon of guided acoustic wave Brillouin scattering (GAWBS)[1] that was occurring in the nonlinear crystal. We observed that the frequency and amplitude of the narrow peaks depended on the crystal temperature. We extended our OPA model to accommodate this effect and found good agreement with a set of measurements that were made over a wide range of input seed and pump powers.

5.1 Initial observations

The aim was to test the apparatus by attempting to measure entanglement from the OPA, but with the second-order nonlinearity effectively switched off. We did this by setting the crystal temperature several tens of degrees Celsius above the optimal phase matching condition, but still ensuring co-resonance for the fundamental (1064 nm, red) and second-harmonic (532 nm, green) fields. The OPA system should then reduce to a simple doubly-resonant cavity. From the model, we expected to see a featureless spectrum at the level of shot-noise, for both the amplitude and phase quadratures of the red and green fields.

---

[1] Note that the acronym GAWBS can be pronounced as a word that rhymes with the word ‘gauze’

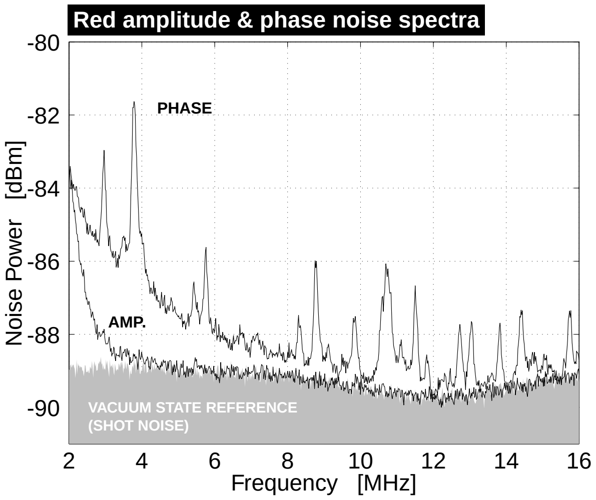

Figure 5.1: Red only, amplitude and phase spectra. The peaks visible in the phase spectrum are absent in the amplitude. RBW is set to $100\,\mathrm{kHz}$. Dark noise is approx. $10\,\mathrm{dB}$ below shot noise.

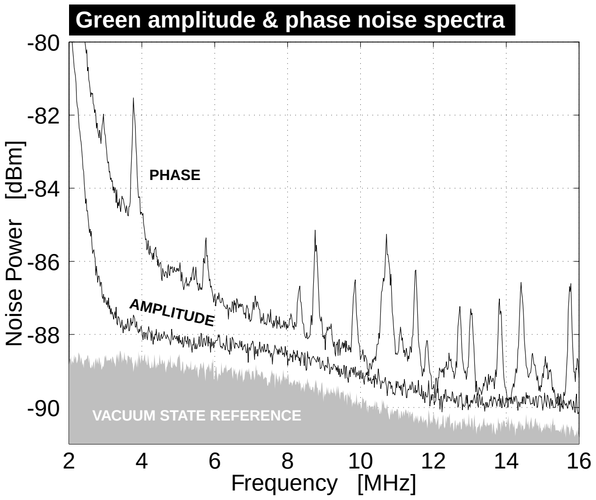

Figure 5.2: Green only, amplitude and phase spectra. The phase noise peaks are similar to the ones seen in the red spectrum. RBW is set to $100\,\mathrm{kHz}$. Dark noise is approx. $10\,\mathrm{dB}$ below shot noise.

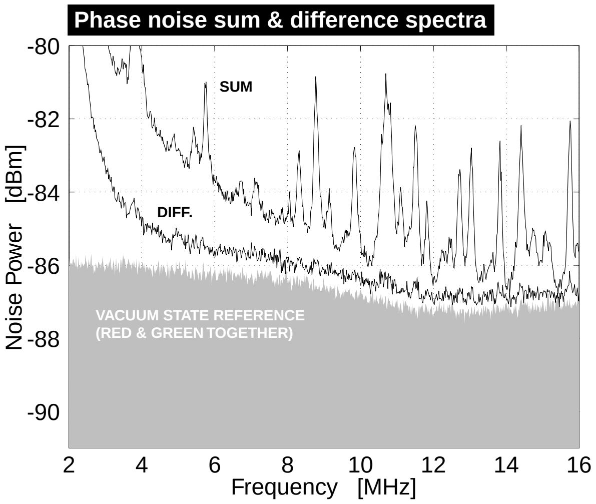

Figure 5.3: Spectra of the sum and difference photocurrents of the red and green homodyne detectors while measuring the phase quadrature. Note the excellent cancellation of the phase noise. RBW is set to $100\,\mathrm{kHz}$. Dark noise is approx. $10\,\mathrm{dB}$ below shot noise.

Phase spectra: We began by setting the seed and pump powers to $4\,\mathrm{mW}$ and $36\,\mathrm{mW}$, respectively. The OPA cavity length was locked to co-resonance. Note that despite fact that the crystal temperature was far away from the phase-matching condition, there was still a very weak OPA effect, and so we locked the pump-seed relative phase to de-amplification of the seed. Optical carrier rejection was engaged for both colours. The homodyne detectors were locked, and spectra of the phase and amplitude quadratures were taken using an electronic spectrum analyser. The red amplitude and phase spectra are shown in Figure 5.1. The amplitude spectrum follows closely the shot-noise limit, except for the roll-up at lower frequencies that is expected from the remnant of the laser relaxation oscillation. The most obvious feature in the phase quadrature spectrum is the set of narrow peaks that rise several dB above the shot-noise level. The widths of the peaks are very narrow compared to their frequencies, they would have a quality-factor of several thousand. There also appears to be a 1/f roll-up below $8\,\mathrm{MHz}$. The results from the green spectra shown in Figure 5.2 are very similar. Indeed, the frequencies of the peaks match up, and their heights are similar. This gives the hint that perhaps the red and green phase quadratures are correlated. In Figure 5.3, we show the sum and difference spectra. There is indeed a correlation, because in the difference, the peaks disappear entirely, leaving only a featureless noise-floor that is $0.5\,\mathrm{dB}$ above shot-noise. This is the excess noise that is left over from the optical-carrier-rejection (OCR) process, and it has not been subtracted here.

Discussion: Our first thought on looking at this data was that the OPA cavity was receiving some kind of RF interference from radio broadcasters in the shortwave band. The PPKTP crystal essentially has the same form as a phase modulator, whose refractive index is modulated according to an electric field that is applied across the crystal. We proceeded to ground the copper cell that contained the crystal, and also shielded the OPA with a grounded aluminium box. The peaks did not change. We also listened to the mixed-down audio signals of the peaks, and their was no discernible information, like speech or music. We concluded that the effect must be optical in nature, but have a common origin since the noise is similar for both the red and green wavelengths. An acoustic source within the crystal seemed like a good candidate.

Temperature dependence: If the PPKTP crystal is really the source of the phase noise peaks produced by some acoustic mechanism, then by changing the crystal length, the frequencies of the peaks might also change. We tested this by measuring the red spectrum for 5 different temperatures, from 30 degrees to 130 degrees Celsius in 20 degree steps, and using the same pump and seed parameters as in the previous section. We zoomed into the region to get a factor of ten better frequency resolution (RBW=$10\,\mathrm{kHz}$). The results are shown in Figure 5.4. Firstly we can see that the narrowness of the peaks are resolved. They have a FWHM of $16\,\mathrm{kHz}$. There appears to be a trend, with the frequency shifting down as the temperature is increased. The value varies from about $-0.7\,\mathrm{kHz}$ to $-1.2\,\mathrm{kHz}$ per degree Celsius, depending on which peak is chosen. The height of the peaks also changes at a rate of about $1\,\mathrm{dB}$ per $100\,^{\circ}\mathrm{C}$. There is also a broad-band excess phase noise that lies between the peaks. This noise-floor rises as a function of increasing temperature.

Discussion: The observations that the peak frequencies and heights depend on the crystal temperature is strong evidence that the cause of the phenomenon is within the crystal, and that the noise is somehow triggered by the temperature.

Conclusion: Taking all of the evidence together: narrow peaks in the phase spectra; the noise is correlated on red and green; the frequency and height of the peaks is dependent on the crystal temperature. Clearly we are dealing with an optical effect within the crystal. A likely candidate is the GAWBS mechanism, where acoustic elastic modes of the crystal cause standing pressure waves to be setup throughout the material. The acoustic modes are excited by the thermal energy of the crystal. The standing pressure waves modulate the phase of the light being transmitted through the crystal. The modulation must have about the same strength for the red and green fields, and this would account for the strong correlation between them.

5.2 GAWBS theory

A model of GAWBS will now be introduced into the OPA model of harmonic entanglement. This breaks down into first identifying the resonant acoustic modes of the PPKTP crystal, and then finding their spatial overlap with the optical mode. The OPA model is

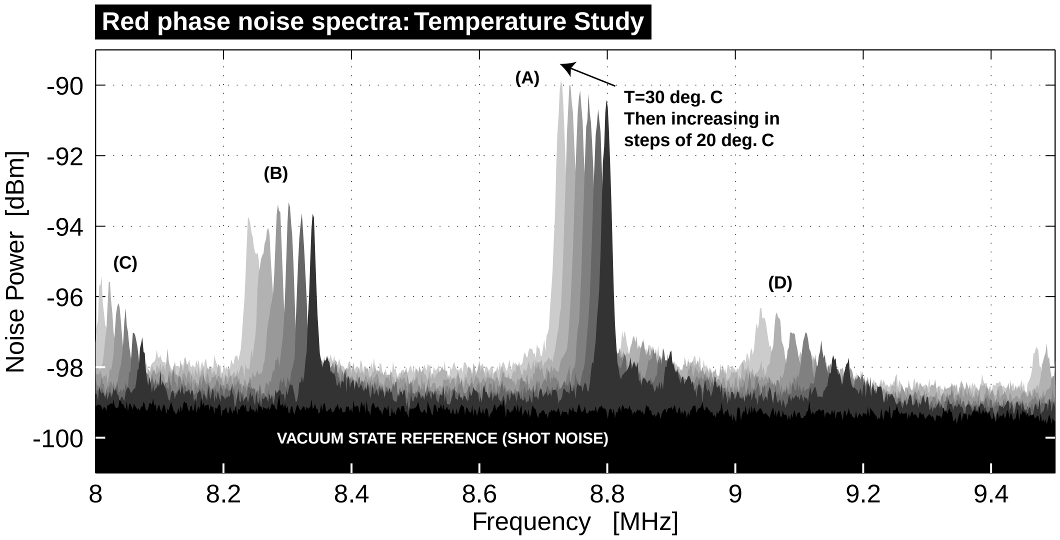

Figure 5.4: A series of phase quadrature spectra of the red field have been overlayed on the same graph. The temperature is varied from 30 deg. C to 130 deg. C (dark grey shading to light grey shading). The shot noise reference is shaded black. The resolution bandwidth is set to $10\,\mathrm{kHz}$. The dark noise (not shown) is approximately $10\,\mathrm{dB}$ below the shot noise level. The frequency shift with increasing temperature for the peaks are: (A) $-0.72\,\mathrm{kHz/K}$; (B) $-1.02\,\mathrm{kHz/K}$; (C) $-0.67\,\mathrm{kHz/K}$; (D) $-1.16\,\mathrm{kHz/K}$.

then extended to include a phase noise term that is common to both the fundamental and second-harmonic fields.

5.2.1 The concept

A bell makes a sound even before it is struck. Each of the mechanical vibrational modes of a solid object in thermal equilibrium at temperature T contains the energy $E = kT$, with k the Boltzmann constant; as ensured by the equi-partition theorem [Reif 1985]. These vibrations cause a strain in the material that modulates the density, and therefore modulates the refractive index as a function of time. As a result, a light beam passing through the object will acquire a phase modulation that has the same frequency as the mode of the mechanical vibration. An equivalent interpretation is that the optical phase modulation is made when light from the carrier is scattered into upper and lower sidebands. One quantises the mechanical vibrations into individual phonons in the sound wave carrying energy $\hbar\omega_a$, and also the photons of the optical beam carrying $\hbar\omega_o$. The photons can be scattered by the phonons and in the process lose or absorb this amount of energy, thus creating upper and lower optical sidebands $\hbar\omega_o' = \hbar(\omega_o \pm \omega_a)$, which give a phase modulation.

This phenomenon was first experimentally observed and interpreted by [Shelby *et al.* 1985b]

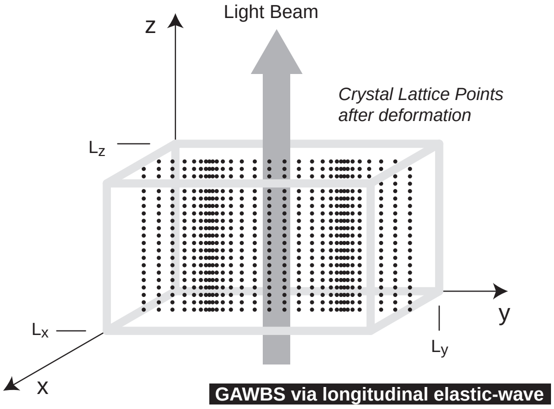

Figure 5.5: Longitudinal elastic waves create a time-varying phase shift for an optical beam. Each standing wave solution creates another GAWBS peak in the phase noise spectrum.

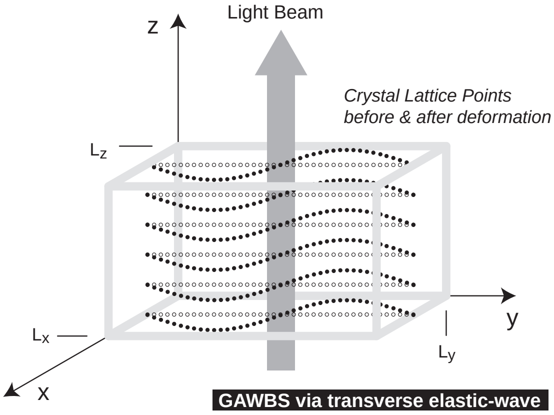

Figure 5.6: Transverse elastic standing waves can also be a source of GAWBS peaks in the phase noise spectrum of the transmitted light beam.

for laser light sent through a single-mode optical fibre. They effectively used an unbalanced homodyne detector to obtain the phase noise spectra. The authors called it guided acoustic wave Brillouin scattering (GAWBS). Note that the mechanism is different to that of stimulated Brillouin scattering (SBS) which depends on the third-order nonlinearity of the medium. Shelby and Poustie got excellent agreement with theory and experiment, for both the frequencies of the excitations and their scattering strengths [Poustie 1992].

5.2.2 Analysis of GAWBS in a block

The aim is to calculate the spectrum of GAWBS peaks and their scattering efficiencies. The analysis is similar to that of an acousto-optic modulator [Saleh and Teich 1991], and is also similar to that of the Debye model of specific heat of a solid crystal [Reif 1985]. The scattering efficiency calculation comes from [Shelby *et al.* 1985a].

Consider an isotropic crystal lattice in the shape of a rectangular block that has length dimensions L_x, L_y, L_z and with one corner lying at the origin of the Cartesian co-ordinate system; see Figure 5.5. An elastic wave propagating through the medium is described by a local displacement of the lattice points from their original positions by an amount given by the vector field $\mathbf{u} = u_x\hat{\mathbf{x}} + u_y\hat{\mathbf{y}} + u_z\hat{\mathbf{z}}$, whose components are functions of space x, y, z and time t. Two kinds of elastic waves can propagate in the medium: transverse waves with speed v_t; and longitudinal waves with speed v_l. Their solutions are found by solving the wave equation:

$$\frac{\partial^2 u_x}{\partial x^2}\hat{\mathbf{x}} + \frac{\partial^2 u_y}{\partial y^2}\hat{\mathbf{y}} + \frac{\partial^2 u_z}{\partial z^2}\hat{\mathbf{z}} = \frac{1}{v^2}\frac{\partial^2 u_x}{\partial t^2}\hat{\mathbf{x}} + \frac{1}{v^2}\frac{\partial^2 u_y}{\partial t^2}\hat{\mathbf{y}} + \frac{1}{v^2}\frac{\partial^2 u_z}{\partial t^2}\hat{\mathbf{z}} \tag{5.1}$$

for a given set of boundary conditions, where v is the speed of propagation. In our case we assume that the surfaces of the crystal are held fixed in the y-direction (because the crystal was held by a clamp in this axis), but they are free to move in the x- and z-directions. Not all elastic waves will couple efficiently into a phase modulation of the optical beam that propagates along the z-axis. The elastic waves that will do well, are those that are analogous to an acousto-optic modulator, i.e. those which create strain or shear (in the form of plane waves) that propagate in the direction perpendicular to the light beam. This means that we have to find solutions to the wave equation that are either the longitudinal plane waves $\{u_x = u_x(x,t), u_y = 0, u_z = 0\}$ and $\{u_x = 0, u_y = u_y(y,t), u_z = 0\}$; see Figure 5.5. Or the transverse plane waves $\{u_x = 0, u_y = 0, u_z = u_z(x,y,t)\}$; see Figure 5.6. I will start with the **longitudinal waves** in the x-axis. The boundary conditions for free ends are $\left.\frac{\partial u_x(x,t)}{\partial x}\right|_{x=0} = 0$ and $\left.\frac{\partial u_x(x,t)}{\partial x}\right|_{x=L_x} = 0$. Applying these and using the method of separation of variables, one obtains the general solution

$$u_x(x,t) = A_m \cos(\Omega_m t)\cos(\frac{\pi m}{L_x}x) \tag{5.2}$$

which is a standing wave. Where m labels the mode, and A_m is a constant that is proportional to the amplitude of the wave. The frequency of the mode depends on the longitudinal propagation velocity v_l and is given by $\Omega_m = \pi v_l m/L_x$. Similarly, applying the free end boundary conditions in the y-axis that are set by $u(y,t)|_{y=0} = 0$ and $u(y,t)|_{y=L_y} = 0$ we get the standing wave

$$u_y(y,t) = B_n \cos(\Omega_n t)\sin(\frac{\pi n}{L_y}y) \tag{5.3}$$

And subscript n labels this mode, with B_n the amplitude. The frequency is given by

$\Omega_n = \pi v_l n/L_y$. The **transverse wave** is like a two-dimensional drum mode. Applying the boundary conditions we get

$$u_z(x,y,t) = C_{mn}\cos(\Omega_{mn}t)\cos(\frac{\pi m}{L_x}x)\sin(\frac{\pi n}{L_y}y) \tag{5.4}$$

The angular frequency is given by

$$\Omega_{mn} = \pi v_t\sqrt{(m/L_x)^2 + (n/L_y)^2} \tag{5.5}$$

Note that it depends both on m and n, which means that compared with the longitudinal modes, the transverse modes can have many more resonance frequencies. In the next step, I would like to know that the amplitudes of the waves will be. I will use the example of the transverse modes, but the analysis of the longitudinal modes follows the same procedure. The energy that is contained in the transverse mode is

$$E_{mn} = \int_0^{Lx}\mathrm{d}x\int_0^{Ly}\mathrm{d}y\int_0^{Lz}\mathrm{d}z\,\frac{1}{2}\rho\Omega_{mn}^2\left[u_z(x,y,t=0)\right]^2 \tag{5.6}$$

where ρ is the density of the material. From the equi-partition theorem, we know that each mode must contain the energy $E_{mn} = k_\mathrm{B}T$, where T is the temperature in Kelvin, and k_B is the Boltzmann constant. Applying the equi-partition theorem is valid because the temperatures are high enough, such that the thermal energy in the mode is much greater than the energy of the phonons ($k_\mathrm{B}T \gg \hbar\Omega_a$. This means that the amplitude of the transverse vibrational mode is

$$C_{mn} = \left(\frac{kT}{\rho\Omega_{mn}^2 L_x L_y L_z}\right)^{\frac{1}{2}} \tag{5.7}$$

Now that we have the displacement, the next step is to find the induced strain within the crystal because it is the strain that determines the change in refractive index. The strain is given by the partial derivative of the mode function in the x-direction:

$$S_{zx} = \frac{\partial u_z}{\partial x} = C_{mn}\left(\frac{\pi m}{L_x}\right)\sin\left(\frac{\pi m}{L_x}x\right)\sin\left(\frac{\pi n}{L_y}y\right) \tag{5.8}$$

and in the y-direction:

$$S_{zy} = \frac{\partial u_z}{\partial y} = -C_{mn}\left(\frac{\pi n}{L_y}\right)\cos\left(\frac{\pi m}{L_x}x\right)\cos\left(\frac{\pi n}{L_y}y\right) \tag{5.9}$$

The photo-elastic constants, otherwise called the strain-optic coefficients, are labelled by P_{zx} and P_{zy}. These values depend on the material, and so they must be found in the literature [Dixon 1967]. The induced change in refractive index is given by

$$\Delta n = n^3 \left(P_{zx} S_{zx} + P_{zy} S_{zy} \right) \tag{5.10}$$

We then have to integrate this change across the beam profile and the beam depth, to get the average refractive index change:

$$\overline{\Delta n} = n^3 \int_0^{Lx} \mathrm{d}x \int_0^{Ly} \mathrm{d}y \int_0^{Lz} \mathrm{d}z \; E_{\mathrm{opt}}(x, y, z) \left(P_{zx} S_{zx} + P_{zy} S_{zy} \right) \tag{5.11}$$

where E_{opt} is the normalised Gaussian beam profile with minimum waist radius W_0

$$E_{\mathrm{opt}} = \left(\frac{\pi}{W(z)^2} \right) \exp \left(\frac{x^2 + y^2}{W^2(z)} \right) \tag{5.12}$$

and where $W(z)$ is the waist as a function of propagation in the z-axis:

$$W(z) = W_0 \left[1 + (z/z_0)^2 \right]^{1/2} \tag{5.13}$$

with z_0 the Rayleigh range: $z_0 = \pi W_0^2 / \lambda$. The change in phase of the light beam is then

$$\epsilon = \frac{2\pi}{\lambda} \overline{\Delta n} \tag{5.14}$$

The final scattering efficiency due to the transverse mode, in units of optical power per unit propagation length, is given by

$$\eta_{mn} = (\epsilon/2)^2 \tag{5.15}$$

The analysis for the longitudinal waves proceeds in a similar manner. Note that for the case of our OPA setup, the presence of an optical cavity ensured that the light beam sampled the same region of the crystal many times. For a finesse of 60, one can assume that the scattering efficiency is simply increased by a factor of 60. This assumption should be valid provided that the frequency of the acoustic mode is much less than the linewidth of the optical cavity.

For our case, the analytical solution for the scattering efficiency for each mode is quite long and unenlightening. So I will proceed with a numerical example that is as similar

L_x	$1.5\,\mathrm{mm}$	
L_y	$1.5\,\mathrm{mm}$	
L_z	$10\,\mathrm{mm}$	
ρ	$2900\,\mathrm{kg\,m^{-3}}$	
n	1.77	Average of all KTP directions
v_t	$5500\,\mathrm{m\,s^{-1}}$	
v_l	$7000\,\mathrm{m\,s^{-1}}$	
α_x	$11 \times 10^{-6}\,\mathrm{K^{-1}}$	
α_y	$9 \times 10^{-6}\,\mathrm{K^{-1}}$	
α_z	$0.6 \times 10^{-6}\,\mathrm{K^{-1}}$	
P_{zx}	0.25	Taken from KDP, not KTP and then assumed isotropic
P_{zy}	0.25	
P_{xx}	0.25	
P_{yy}	0.25	
λ	$1064\,\mathrm{nm}$	
W_0	$40\,\mu\mathrm{m}$	The beam centre was offset by 100 μm in the x-axis

Table 5.1: GAWBS model parameters.

to the experimental OPA setup as possible. The calculation finely samples the acoustic and optical mode functions and performs the integration numerically to get the scattering efficiencies. The parameters for the model are shown in Table 5.1. After an extensive literature search, it was not possible to obtain values for the optic-strain for KTP material, hence data from the structurally similar KDP was used; see [Dixon 1967]. I also assumed an isotropic crystal both for the mechanical (speed of sound) and optical properties (refractive indices). This was to simplify the analysis. The problem is that an anisotropic crystal allows the conversion between longitudinal and transverse modes at the edges of the crystal. To analyse this situation requires a treatment in chaos theory [Ellegaard *et al.* 1996].

In our experiment, we did not directly measure scattering efficiency, but rather we used homodyne detection to measure the phase quadrature which was calibrated to the shot noise of the local oscillator. The calibrated signal is then given by

$$S = 1 + \eta_{mn}\sqrt{\frac{P\lambda}{B\hbar c}} \tag{5.16}$$

with P the optical power in the probe (not local oscillator) light beam in $\mathrm{J\,s^{-1}}$. B the detection bandwidth in Hz, which determines the minimum time integration window.

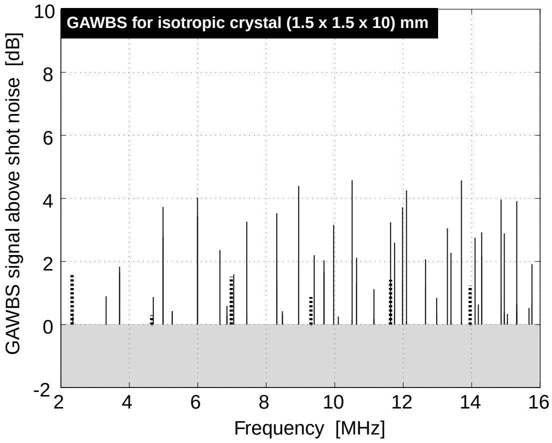

Figure 5.7: Theoretical GAWBS spectrum of signal above shot noise. Red light beam power $240\,\mathrm{mW}$, detection bandwidth $100\,\mathrm{kHz}$. Solid lines are transverse modes up to $(7,7)$. Dashed lines are longitudinal modes up to (7). The grey shaded area is corresponds to the shot noise limit.

Figure 5.7 shows the calculated GAWBS spectrum. Note that (although not visible here) the appearance of the spectrum is highly dependent on the position of the light beam in the crystal. This is because the beam width is on the same scale as the wavelength of the acoustic modes. I have chosen a $100\,\mu\mathrm{m}$ offset in the x-direction to avoid having the optical beam stand in the nodes of the odd acoustic modes. By comparing this graph with the experimental results in Figure 5.1, one can see a good qualitative agreement of the frequencies of the observed and predicted modes, i.e. the spacing of the modes is roughly $0.2\,\mathrm{MHz}$ when looking beyond $10\,\mathrm{MHz}$. The scattering efficiencies themselves are also within an order of magnitude of the experimentally observed values.

I can also build a temperature dependence into the model, where the length of the crystal increases due to thermal expansion. The expansion coefficients for KTP are $10^{-5}\,\mathrm{K}^{-1}$. Figure 5.8 shows a narrower spectrum for the same crystal, but at two different temperatures that are $100\,\mathrm{K}$ apart. One can see that the resonance frequencies drop with increasing temperature, and that the scattering efficiency increases. By comparing this graph with the experimental results in Figure 5.4, one can see that the rate of scattering increase per Kelvin is about the same as that observed in the experiment. But the predicted change in resonance frequency per Kelvin was only about 10% of the value that had been observed. This indicates that the speed of sound for the longitudinal and transverse waves may also be a function of the temperature.

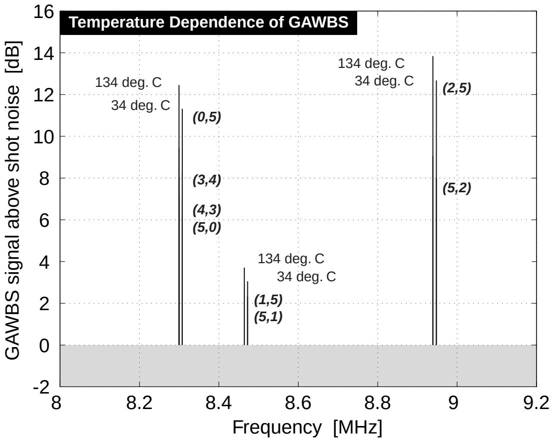

Figure 5.8: Theoretical GAWBS spectrum of signal above shot noise. Red light beam power $240\,\mathrm{mW}$, detection bandwidth $100\,\mathrm{kHz}$. Solid lines are transverse modes that are labelled. The spectrum is re-calculated at a higher temperature. The GAWBS signal increases, and the resonance frequencies decrease.

5.2.3 Mini-conclusion

The GAWBS model produces peaks in the phase noise spectrum. The calculations show good qualitative agreement with the experimental results: in terms of the distribution of resonance frequencies, and also the observed scattering efficiencies. The model is also in agreement with the decreasing resonance frequencies and increasing phase noise, as the temperature of the crystal is increased. Note that the model cannot predict the observed $16\ \mathrm{kHz}$ linewidth of the phase noise peaks. This would depend on the dissipation of mechanical vibration, and the details of how the crystal is held in place.

However, one problem remains: this is to understand the observed broad-band noise between the peaks, that was also seen to increase with increasing temperature. I will choose to consider it as a continuum of modes that arise due to the true mechanical anisotropy of the KTP crystal material. We can then treat this continuum of modes as also causing a phase shift in the light beam. Such a broadband phase noise will be introduced in the next section as a cavity de-tuning noise term in the OPA equations of motion.

5.3 GAWBS-extended OPA model of harmonic entanglement

I would now like to extend my original model of harmonic entanglement from OPA (see Chapter 3) to include a term that describes the effect of guided acoustic-wave Brillouin scattering (GAWBS). What follows is a complete but concise derivation of the OPA cavity transfer functions that include a cavity detuning noise that is common-mode to the fundamental and second-harmonic fields. Consider a mode of light a and its second-harmonic

b, (wavelengths $\lambda_a = 2\lambda_b$), which interact via a nonlinearity of ϵ in a single mode cavity with total decay rates $\kappa_{a,b}$. The intra-cavity fields are coupled to the environment through a mirror $\kappa_{a1,b1}$, and more weakly via other loss mechanisms $\kappa_{a2,b2}$. The system is driven by coherent states of light with steady-state amplitudes of $\alpha_{\text{in}}, \beta_{\text{in}}$; and can be modelled by the coupled set of equations [Drummond *et al.* 1980]:

$$\dot{\hat{a}} = -(\kappa_a + i\delta w_a)\hat{a} + \epsilon \hat{a}^\dagger \hat{b} + \hat{A}_{\text{in}} \tag{5.17}$$

$$\dot{\hat{b}} = -(\kappa_b + i\delta w_b)\hat{b} - \frac{1}{2}\epsilon \hat{a}^2 + \hat{B}_{\text{in}} \tag{5.18}$$

where input fields are denoted by $\hat{A}_{\text{in}} = \sqrt{2\kappa_{a1}}\alpha_{\text{in}} + \sum \sqrt{2\kappa_{a,j}}\delta\hat{A}_{j,\text{in}}$; $\hat{B}_{\text{in}} = \sqrt{2\kappa_{b1}}\beta_{\text{in}} + \sum \sqrt{2\kappa_{b,j}}\delta\hat{B}_{j,\text{in}}$ with $j \in \{1, 2\}$, $\kappa_a = \kappa_{a1} + \kappa_{a2}$ and $\kappa_b = \kappa_{b1} + \kappa_{b2}$. The GAWBS noise terms become $\delta w_{a,b} = (-2\pi c/\lambda_{a,b})\xi_{a,b}\delta P$ which are driven by the dimensionless noise term δP having variance one, but are coupled via the constants ξ_a and ξ_b. For a similar method of introducing de-tuning noise terms one can refer to [Goda *et al.* 2005]. We work in the Heisenberg picture where the annihilation operators $\hat{a}$ and $\hat{b}$ (and corresponding creation operators) evolve, from which the amplitude and phase quadrature operators are constructed: $X^+ = a^\dagger + a$ and $X^- = i(a^\dagger - a)$, respectively (we drop the hat notation). The technique of linearisation is used to obtain the fluctuations $(\delta a, \delta b)$ centered around the classical steady-state solutions (α, β) [Drummond *et al.* 1980]. Fourier transforming into the frequency domain allows one to solve for the driving fields in terms of the intra-cavity fields. This dependence is reversed when the equations are expressed in a matrix whose inverse is found:

$$\begin{bmatrix} \delta X_a^+ \\ \delta X_a^- \\ \delta X_b^+ \\ \delta X_b^- \\ \delta P \end{bmatrix} = \begin{bmatrix} A_- & B & C & D & F_a \\ B & A_+ & -D & C & G_a \\ -C & D & E & 0 & F_b \\ -D & -C & 0 & E & G_b \\ 0 & 0 & 0 & 0 & 1 \end{bmatrix}^{-1} \begin{bmatrix} \delta X_{A,\text{in}}^+ \\ \delta X_{A,\text{in}}^- \\ \delta X_{B,\text{in}}^+ \\ \delta X_{B,\text{in}}^- \\ \delta P' \end{bmatrix}, \tag{5.19}$$

where $\{\delta X_a^\pm, \delta X_b^\pm\}$ and $\{\delta X_{A,\text{in}}^\pm, \delta X_{B,\text{in}}^\pm\}$ are the intra-cavity and accumulated input field quadratures, respectively; and $A_\pm = \kappa_a - i\Omega \pm \epsilon|\beta|\cos\theta_\beta$, $B = -\epsilon|\beta|\sin\theta_\beta$, $C = -\epsilon|\alpha|\cos\theta_\alpha$, $D = -\epsilon|\alpha|\sin\theta_\alpha$, $E = \kappa_b - i\Omega$, $F_{a,b} = 2i|\alpha,\beta|\sin\theta_{\alpha,\beta}(-2\pi c/\lambda_{a,b})\xi_{a,b}$, $G_{a,b} = 2|\alpha,\beta|\cos\theta_{\alpha,\beta}(-2\pi c/\lambda_{a,b})\xi_{a,b}$, with $\theta_\alpha = \text{Arg}(\alpha), \theta_\beta = \text{Arg}(\beta)$; and Ω the sideband frequency. The fields reflected from the resonator can be directly obtained using the input-output formalism, $\delta X^{\pm}_{\rm A1,ref} = \sqrt{2\kappa_{a1}}\delta X^{\pm}_{a} - \delta X^{\pm}_{\rm A1,in}$; $\delta X^{\pm}_{\rm B1,ref} = \sqrt{2\kappa_{b1}}\delta X^{\pm}_{b} - \delta X^{\pm}_{\rm B1,in}$ [Collett and Gardiner 1984]. The resulting bi-partite Gaussian states that are produced, are completely described by the correlation matrix of elements $C^{kl}_{mn} = \frac{1}{2}\langle \delta X^{k}_{m}\delta X^{l}_{n} + \delta X^{l}_{n}\delta X^{k}_{m}\rangle$, arranged in the order:

$$M = \begin{bmatrix} C^{++}_{aa} & C^{+-}_{aa} & C^{++}_{ab} & C^{+-}_{ab} \\ C^{-+}_{aa} & C^{--}_{aa} & C^{-+}_{ab} & C^{--}_{ab} \\ C^{++}_{ba} & C^{+-}_{ba} & C^{++}_{bb} & C^{+-}_{bb} \\ C^{-+}_{ba} & C^{--}_{ba} & C^{-+}_{bb} & C^{--}_{bb} \end{bmatrix} \tag{5.20}$$

where $\{k,l\} \in \{+,-\}$ and the reflected field notation has been simplified with $\{m,n\} \in \{A1_{\rm ref} \mapsto a, B1_{\rm ref} \mapsto b\}$. We use the quantity of inseparability $\mathcal{I}$ as a measure of entanglement, or the EPR criterion; see Chapter 2. For the remainder of this chapter however, I will be concentrating on the individual phase quadrature variances themselves, and the sum and difference of the phase quadratures.

Modelling loss after the OPA: The path from the OPA to the detection is not free of loss. We need to modify the correlation matrix M to take into account the loss η_a on the red path (a), and the loss η_b on the green path (b). This is done by consulting the beamsplitter model (together with a vacuum mode) that was discussed in Section 2.7.2. The elements of the correlation matrix then become:

$$\begin{aligned} M \;=\; & \begin{bmatrix} \eta_a C^{++}_{aa} & \eta_a C^{+-}_{aa} & \sqrt{\eta_a\eta_b}\, C^{++}_{ab} & \sqrt{\eta_a\eta_b}\, C^{+-}_{ab} \\ \eta_a C^{-+}_{aa} & \eta_a C^{--}_{aa} & \sqrt{\eta_a\eta_b}\, C^{-+}_{ab} & \sqrt{\eta_a\eta_b}\, C^{--}_{ab} \\ \sqrt{\eta_a\eta_b}\, C^{++}_{ba} & \sqrt{\eta_a\eta_b}\, C^{+-}_{ba} & \eta_b C^{++}_{bb} & \eta_b C^{+-}_{bb} \\ \sqrt{\eta_a\eta_b}\, C^{-+}_{ba} & \sqrt{\eta_a\eta_b}\, C^{--}_{ba} & \eta_b C^{-+}_{bb} & \eta_b C^{--}_{bb} \end{bmatrix} \\ & + \begin{bmatrix} 1-\eta_a & 0 & 0 & 0 \\ 0 & 1-\eta_a & 0 & 0 \\ 0 & 0 & 1-\eta_b & 0 \\ 0 & 0 & 0 & 1-\eta_b \end{bmatrix} \end{aligned} \tag{5.21}$$

where the first matrix shows the attenuation of the initial state, and the second matrix shows the uncorrelated noise contribution from the vacuum modes that are coupled into the red and green optical paths. The OPA model therefore has another two free parameters (η_a and η_b) that need to be determined from characterisation of the experiment (but not fitted). Setting $\eta_{a,b}$ to unity returns the condition of a lossless detection scheme. From the results collected in Table 4.2 we found that $\eta_a = 0.85(4)$ and $\eta_b = 0.80(6)$. The uncertainties come mainly from estimating the absolute efficiency (quantum efficiency) of the photodiodes used in the homodyne detectors.

Modelling intensity noise on the pump and seed beams: When the OPA model was introduced in Chapter 3, the input pump and seed beams were assumed to be in pure coherent states. Although we used optical filtering cavities, measurements of the input pump and seed beams showed that they carried residual amplitude and phase noise. The amount of excess noise in terms of the quadrature variances, was proportional to the seed and pump powers. The excess noise was approximately equal for both quadratures and both the seed and pump beams. We therefore introduced an extension for the model, where the input variances are given by

$$\langle(\delta^{\pm}_{\mathrm{Ain},1})^2\rangle = 1 + s|\alpha_{\mathrm{in}}|^2 \tag{5.22}$$

and similarly for mode $\mathrm{Bin},1$. Note that all the other input states were assumed to be in the uncorrelated vacuum states. The OPA model therefore has another free parameter (s) that needs to be determined from characterisation of the experiment (but not fitted). Setting s to zero returns the condition that the seed and pump are in (pure) coherent states. From the experiment, we found the value of $s = 10^{-3}$ per mW of optical power, which means that the residual amplitude and phase noise only becomes significant when the OPA is driven near to, or above, the OPO threshold power (85 mW).

5.4 Constraining the GAWBS-OPA model

The aim was to test the GAWBS-extended OPA model against a set of measurements from the harmonic entanglement experiment. In practice, we actually avoided the GAWBS peaks for harmonic entanglement measurements, because they were detrimental to the strength of the entanglement. As mentioned earlier however, there was also broad-band phase noise, that was presumed to have a similar origin to GAWBS, and may arise from a continuum of unresolved GAWBS peaks.

The parameters that were used in our model were determined from characterisation of the experiment. The values for the mirror coupling rates were obtained from the finesse and reflection coefficient measurements in Table 4.1, which gave $\kappa_{a1} = 51$, $\kappa_{a2} = 4.3$,

$\kappa_{b1} = 250$, $\kappa_{b2} = 41$ (in MHz). And the nonlinear interaction strength of $\epsilon = 1.5\,\mathrm{kHz}$ was determined by working backwards from a Boyd-Kleinman model of the OPO threshold power [Kleinman *et al.* 1966].

A set of quadrature measurements of the reflected seed (1064 nm, red) and pump (532nm green) fields from the OPA cavity was made using the harmonic entanglement setup as described in Chapter 4. The measurements were made at the sideband frequency of 7.8 MHz. The amplitudes of the input seed and pump fields were changed so that the total input power to the OPA was held constant at 76% of OPO threshold power, while only their ratios were altered. The ratio is expressed as an angle ϕ in the parameter space of the entanglement maps that are presented in Chapter 3: $\phi = \tan^{-1}(\beta_{\rm in}/\alpha_{\rm in})$. I now refer to three figures which are presented in Chapter 6. Shown in Figure 6.5 are the measurement results for the amplitude and phase quadrature variances of the red field. Figure 6.5 also shows the quadrature variances of the green field. The measurement have been corrected from the excess noise artefacts that come from the optical-carrier-rejection process (see Chapter 4).

The sum and difference of the phase quadratures of the red and green fields is shown in Figure 6.4. The solid and dashed lines in these graphs are the best fit of the GAWBS-OPA model, where only two parameters have been fitted. These are the GAWBS coupling coefficients ξ_a and ξ_b. Although the source of the noise for the red and green fields is identical (coming from a particular acoustic mode), the coupling strength to the optical field may be different, which is due to the different waist-sizes of the two optical fields. The GAWBS coefficients were found by fitting the curves to the set of phase quadrature measurements using the least-squares-method. The results were: $\xi_a = 2.4\times10^{-17}$, $\xi_b = 3.2\times10^{-17}$. All the model parameters are summarised in Table 5.2.

5.5 Summary

We have observed a dense set of narrow-band peaks in the phase spectra from the 1064nm and 532nm light that is reflected from the OPA cavity. These peaks were hypothesised to originate from the guided acoustic wave Brillouin scattering mechanism (GAWBS). We believe that the GAWBS effect is not limited to materials in the optical fibre geometry where

$\kappa_{a1} = 51\ \mathrm{MHz}$	Derived from measurements of cavity finesse and reflection coefficients
$\kappa_{a2} = 4.3\ \mathrm{MHz}$	""
$\kappa_{b1} = 250\ \mathrm{MHz}$	""
$\kappa_{b2} = 41\ \mathrm{MHz}$	""
$\epsilon = 1.5\ \mathrm{kHz}$	Derived from the OPO threshold power
$s = 0.001$ per mW	Derived from measurements of the input pump and seed beam variances
$\eta_a = 0.85$	Estimate of optical losses on the path from OPA to homodyne detection
$\eta_b = 0.80$	""
$\Omega = 7.8\ \mathrm{MHz}$	The chosen sideband frequency for measuring harmonic entanglement
$\xi_a = 2.4\times10^{-17}$	From a least-squares fit with a series of phase quadrature measurements
$\xi_b = 3.2\times10^{-17}$	""

Table 5.2: A summary of all parameters in the GAWBS-extended OPA model of harmonic entanglement.

it has been observed before. A bulk crystal of millimetre dimensions has a GAWBS spectrum shifted to higher frequencies, and lower amplitudes due to the reduced phonon-photon interaction length. However, our experimental setup had a high sensitivity to the phase quadrature that was provided by the combination of the optical carrier rejection technique together with homodyne detection, and it was this that enabled us to observe GAWBS in bulk PPKTP material in a rectangular prism geometry.

We developed a simple model of the GAWBS effect for our crystal geometry, and we could find good qualitative agreement for the scattering efficiencies and also for the density of peaks in the spectrum. Further quantitative comparison was not possible because of the sensitivity of the scattering efficiency due to the exact transverse position of the light beam in the crystal, and other crystal parameters (photo-elastic constants, temperature dependencies etc.). We also extended our model of OPA to accommodate a cavity de-tuning noise term that simulates the GAWBS effect. This model will allow us to make a valid theory-experiment comparison for the harmonic entanglement results that are presented in the next chapter.

Chapter 6

Harmonic Entanglement Experiment: Results

In this chapter I present the main result of harmonic entanglement as measured from an optical parametric amplifier (OPA) with an inseparability measure of $\mathcal{I} = 0.74(1) < 1$. The behaviour of entanglement was also studied as a function of the driving fields to the OPA: for the ratios of seed and pump power, and also the total input power. Good agreement with the theoretical model was found, and the series of measurements as a whole supports the interpretation that a significant exchange of energy between the fundamental and second-harmonic fields is a key requirement in the production of harmonic entanglement from OPA.

The experimental results presented here stem from the collaboration between Syed Assad, Moritz Mehmet and myself. This work has been published under the following reference:

- *Observation of Entanglement between Two Light Beams Spanning an Octave in Optical Frequency,*
  N. B. Grosse, S. Assad, M. Mehmet, R. Schnabel, T. Symul and P. K. Lam,
  Phys. Rev. Lett. **100**, 243601 (2008).

6.1 Main Results

We gathered measurement of the correlation matrix over many points in the two-dimensional parameter space of driving field amplitudes: the seed (fundamental, 1064 nm, red) and the pump (second-harmonic, 532 nm, green). Figure 6.1 shows symbols where the measurements were made in the map of inseparability as a function of the driving fields. The procedure for each measurement was identical to that outlined in the Chapter 4. After an extensive search for many combinations of driving fields, we observed the best harmonic

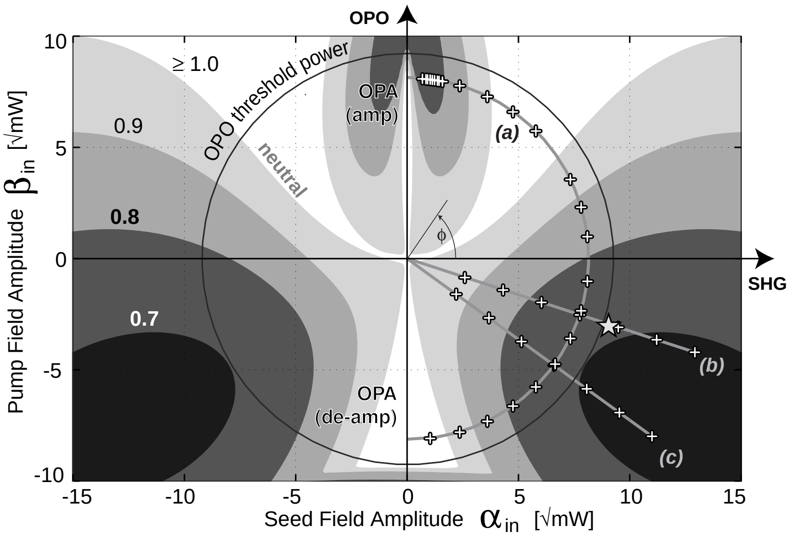

Figure 6.1: Theoretical map of entanglement across the driving fields using experimental parameters in the model. Darker shading means stronger entanglement. Contours are labelled with the inseparability measure. 'Plus' symbols mark the observation points. The arc (a) corresponds to the angle-study, and the radial lines (b) and (c) to the power studies. The star marks the calibration point. The symbol ϕ shows how the angle parameter is defined.

entanglement in the parametric de-amplification region of strong pump-enhancement with powers at $81/\!\!/9$ mW (see the $\star$ in Figure 6.1). Where the notation $/\!\!/$ means parameters for the $\mathrm{red}/\!\!/\mathrm{green}$ fields in that order. For this particular setting of driving fields, we then completed measurements of the correlation matrix for eleven runs over many days. The ensemble average of those matrix elements in linear scale, and their 95% confidence intervals based on the run-to-run variability, are presented here:

$$M_{ab} = \begin{bmatrix} 0.71(1) & 0 & -0.25(1) & -0.02(6) \\ 0 & 2.45(12) & -0.07(10) & +1.42(5) \\ -0.25(1) & -0.07(10) & 0.83(2) & 0 \\ -0.02(6) & +1.42(5) & 0 & 2.56(6) \end{bmatrix}. \tag{6.1}$$

The matrix revealed that both colours were amplitude squeezed with $C_{aa}^{++} = 0.71(1)$ and $C_{bb}^{++} = 0.83(2)$. The phase quadratures showed anti-squeezing of $C_{aa}^{--} = 2.45(12)$ and $C_{bb}^{--} = 2.56(6)$, which imply that the Heisenberg uncertainty relation was satisfied well above the minimum uncertainty bound. These apparent "mixed" state statistics are a requisite of harmonic entanglement. To compute the inseparability, we performed local symplectic transformations $r_a = 0.11(1)$, $r_b = 0.15(2)$ numerically to each mode such that M_{ab} was brought into the standard form. After applying the definition of the inseparability

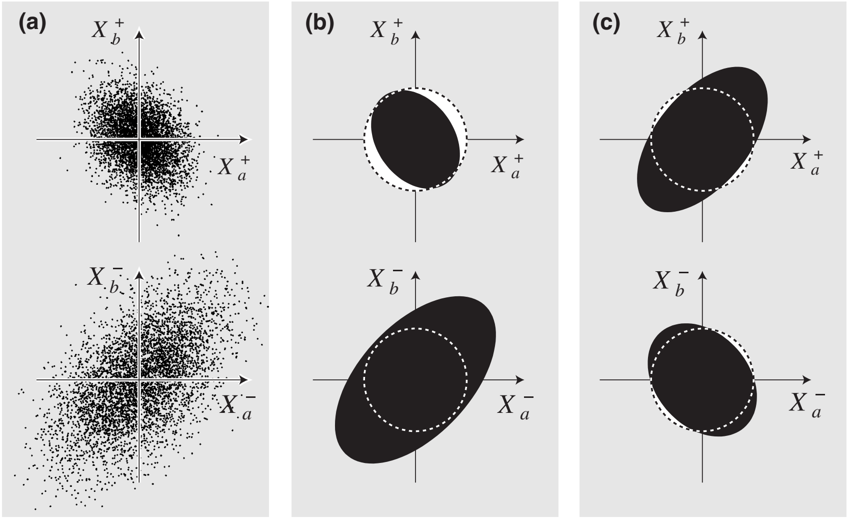

Figure 6.2: **(a)** Time-series quadrature data showing correlations (scaled 50%). **(b)** Shaded ellipses follow a contour of the resulting probability distribution. Dashed circles mark the quantum noise limit. The quantum correlation in amplitude is evident since the ellipse falls within the circle. **(c)** Dual quantum correlations are exhibited by the same data when the correlation matrix is brought into standard form.

criterion to the correlation matrix in standard form (see Chapter 2), we found a value of $\mathcal{I} = 0.74(1)$, which was less than one, and thus confirmed the presence of entanglement.

6.2 Visual representation

A visual representation of the correlations within the entangled state is shown in Figure 6.2, where time-series quadrature data of the second-harmonic field was plotted against the data of the fundamental field. Each dot corresponds to one sample in the recorded quadrature data (note that only the first 10^3 points are plotted here). The ellipse in (b) marks the standard deviation contour of the resulting joint Gaussian probability distribution. The quantum anti-correlation in amplitude is evident as the ellipse falls within the circular boundary that is set by a reference measurement that used vacuum states only. For the phase quadrature, only a classical correlation can be seen, but the proximity of the phase correlations to the classical bound is sufficient for the preservation of entanglement. This feature is symptomatic of biased entanglement [Bowen *et al.* 2003a]. In (c) we performed local symplectic transformations to bring the correlation matrix into standard form. This led to the amplitude quadratures becoming correlated and the phase quadratures anti-correlated by an equal amount, thereby optimally redistributing the quantum correlations over both quadratures.

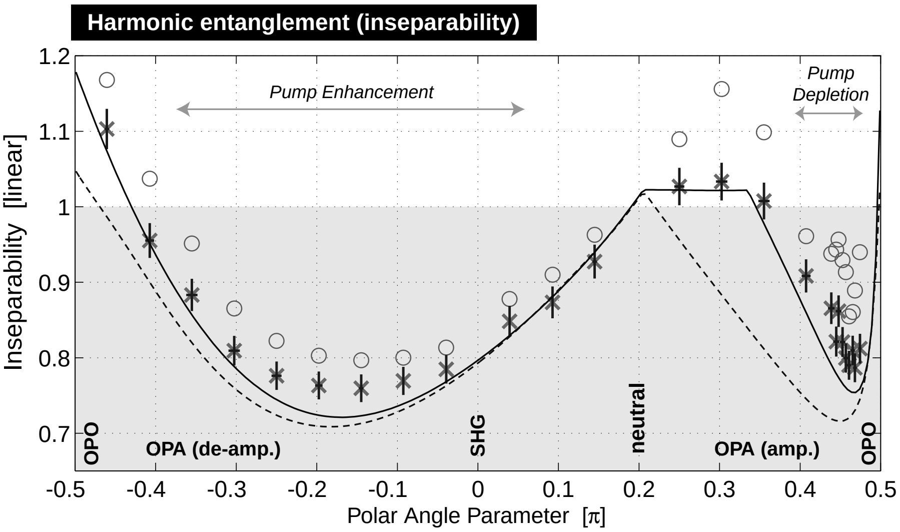

Figure 6.3: Inseparability as a function of angle parameter with the total input power held constant at $65\ \mathrm{mW}$. Entanglement is achieved for values < 1. The solid line is from the theoeretical model with GAWBS term, and the dashed line is from the model without. The measurements marked as crosses are corrected for the noise artefacts from the OCR process. The circles are uncorrected.

6.3 Angle Study

Our aim was to drive the entangler across the whole range of processes: OPO, OPA, and SHG. We set the total input power to $65\ \mathrm{mW}$ (82% of OPO threshold power), and adjusted the balance of power between seed and pump to trace out an arc in the parameter space of Figure 6.1. Limitations of the servo-loops allowed us to only approach true OPO, SHG, and the neutral point. The inseparability results are plotted in Figure 6.3 as a function of polar angle in the parameter space. The raw data is shown as circles, while the crosses show the data corrected for the excess noise from the optical carrier rejection (OCR) process. Entanglement was observed over a broad range of angles $(-0.41, +0.15)\pi$, which covered OPA de-amplification through SHG and almost up to the neutral point. The effect of pump-enhancement in this region was strong, i.e. most of the red was converted into green. By neutral point, we mean the region were net conversion of red to green (and vice versa) is zero, and no squeezing nor correlation can be produced. We also found entanglement in a narrow range $(+0.40, +0.47)\pi$ which corresponded to OPA amplification with weak pump-depletion. The maximum entanglement observed in the broad region ($\mathcal{I}_{\mathrm{opt}} = 0.76(2)$) was slightly better than in the narrow region ($\mathcal{I}_{\mathrm{opt}} = 0.79(2)$). The error-bars plotted were

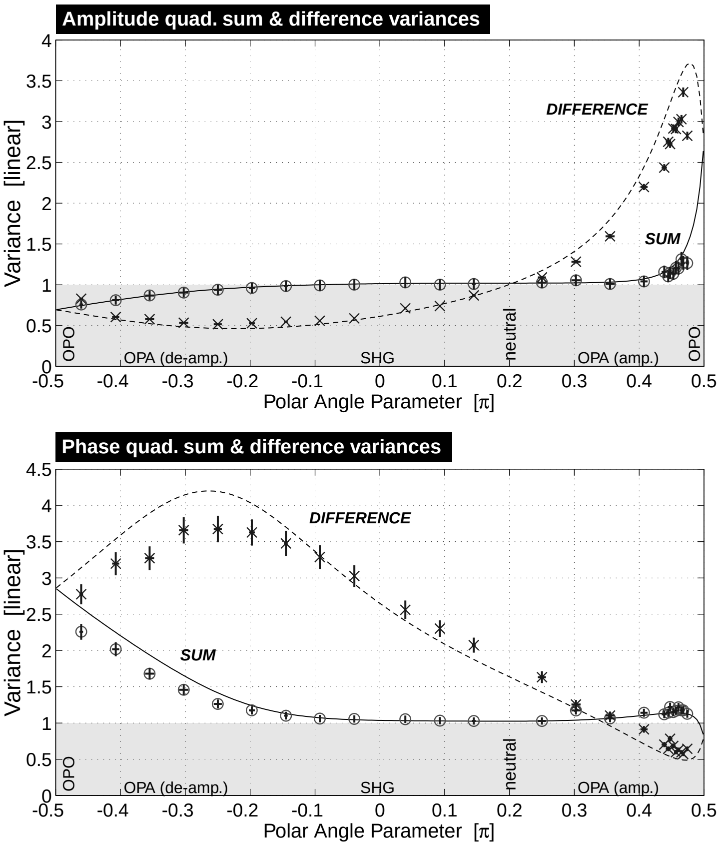

Figure 6.4: Sum and difference variances for the amplitude and phase quadratures as a function of parameter angle. The total input power is held constant at 65mW. The curves are from the theoretical model with GAWBS. The circles and crosses are experimental points that have been corrected for OCR artefacts. A correlation is seen when the gap between sum and difference becomes large. The correlation is quantum when either the sum or difference dips below one.

based on standard deviations that were gathered in the calibration point measurements of Section 6.1. Two theoretical curves are plotted. The dashed line is the original OPA model, while the solid line is the OPA model with the GAWBS phase noise. The coupling strength of the GAWBS have been fitted to the phase quadrature observables alone, and not the inseparability (see Section 5.4). The best agreement between theory and experiment is when the OCR corrections have been made, and the GAWBS-extended OPA model of harmonic entanglement is used. This indicates that GAWBS is indeed a limiting effect in measuring harmonic entanglement from the OPA. Note however, that its effect is minimised in the vicinity of the SHG region.

The behaviour of the sum and difference variances (SDV) are the key to understanding what is happening inside the OPA in its role as a harmonic entangler. In Figure 6.4 we plotted these quantities which were taken from the same data set as the angle study in Section 6.3. The value of the correlation coefficient (multiplied by a factor of 2) can be read directly from the graph by noting the gap between the sum and difference measurements (in linear scale). The nature of the correlation, whether it be quantum or classical, depends

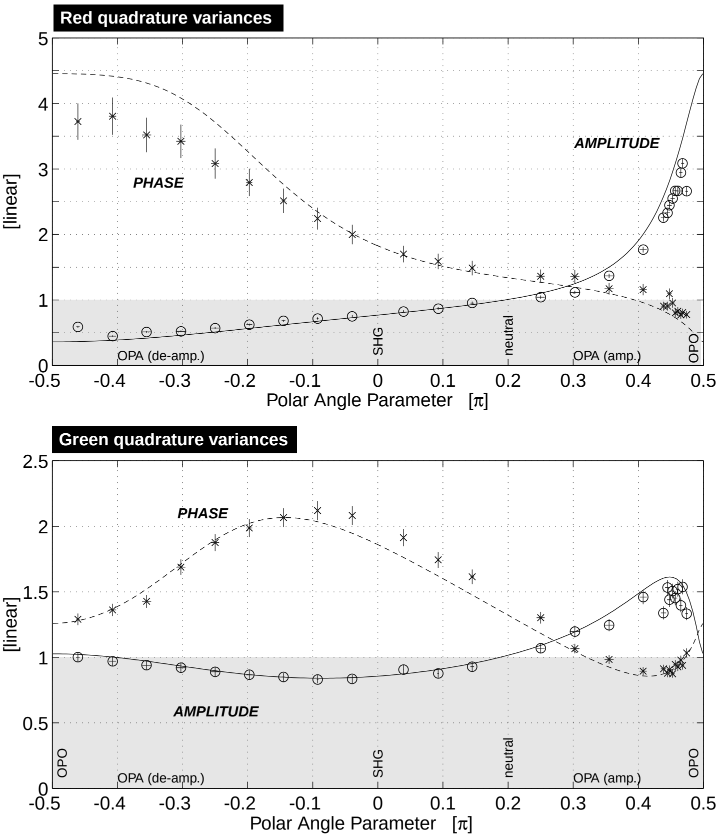

Figure 6.5: Quadrature variances for each colour as a function of parameter angle with the total power held constant at 65mW. The lines are from the model with the GAWBS noise term. The symbols mark the observations. The circles and crosses are experimental points that have been corrected for OCR artefacts. Squeezing is witnessed in the grey shaded region.

on either of the variances dipping or not dipping below one, respectively. Looking qualitatively at the amplitude SDV, starting near OPO (-0.45π) in the de-amplification region and moving toward the neutral point ($+0.20\pi$), one can see that the strength of the quantum correlation gradually turned on but then off. A (classical) correlation then appeared when moving beyond the neutral point and into the amplification region ($+0.45\pi$). This change from a quantum to classical correlation is a consequence of the OPA making the transition from amplitude to phase squeezing on red (and green). Whether or not a correlation is produced relies on there having been some level of pump-depletion or enhancement (which cannot occur in below-threshold OPO). For the phase-SDV, the behaviour was similar, but followed in reverse order. The individual quadrature variances shown in Figure 6.5 complete this picture. Moving across the range of angle parameters, one can see the transition from amplitude squeezing to phase squeezing on the red field. While the green field has its best amplitude squeezing near the SHG point, and its best phase squeezing also near the OPA amplification region. The phase squeezing for both red and green in the latter region indicate that it may be possible to suppress GAWBS phase noise here.

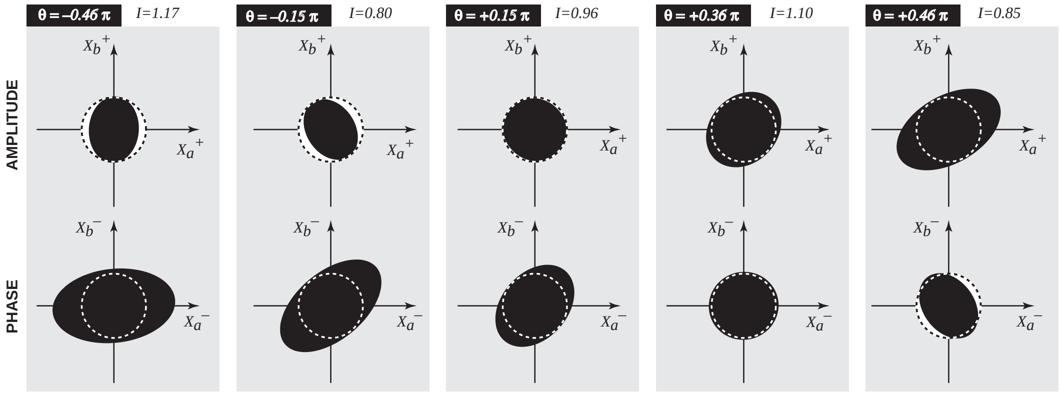

Figure 6.6: A series of five measurements of the quadrature correlations taken at different values of the angle parameter. The total input power was held constant at 65mW. The contours are drawn at the standard deviation of the probability distribution. The dashed circles mark the quantum noise limit. The value for the inseparability is written at the top of each box.

A series of correlation diagrams were prepared from observations along the angle study. Figure 6.6 takes four examples that are set at the parameter angles: $\theta = -0.46\pi$, $\theta = -0.15\pi$, $\theta = +0.15\pi$, $\theta = +0.36\pi$, and $\theta = +0.46\pi$; for which the total input power was held constant at $65\,\mathrm{mW}$. Here the quadratures of the red field are plotted against the quadratures of the green field (in the same manner as Figure 6.2). The symmetry of this plot is striking. The phase quadrature follows exactly the behaviour of the amplitude quadrature, but in the reverse order along the parameter angle. One can see a transition from amplitude squeezing to phase squeezing; and also a transition from a quantum correlation in the amplitude quadrature, to one in the phase quadrature.

6.4 Power Study

The theory predicts that increasing total input power should increase entanglement. We tested this by ramping up the total input power from $10\ \mathrm{mW}$ to $180\ \mathrm{mW}$, which is 10% to 210% of OPO threshold power, while holding the seed:pump power ratio constant at 9:1. This ratio of seed:pump powers corresponds to the region of OPA de-amplification ($\theta = -0.10\pi$). The results for inseparability are plotted in Figure 6.7(left)(a). Initially the entanglement strength increased (appearing lower in the graph) as a function of total input power, but at $P_{\mathrm{total}} = 100\ \mathrm{mW}$ the trend reversed. This is contrary to the theoretical prediction which has the entanglement strength monotonically increasing (appearing

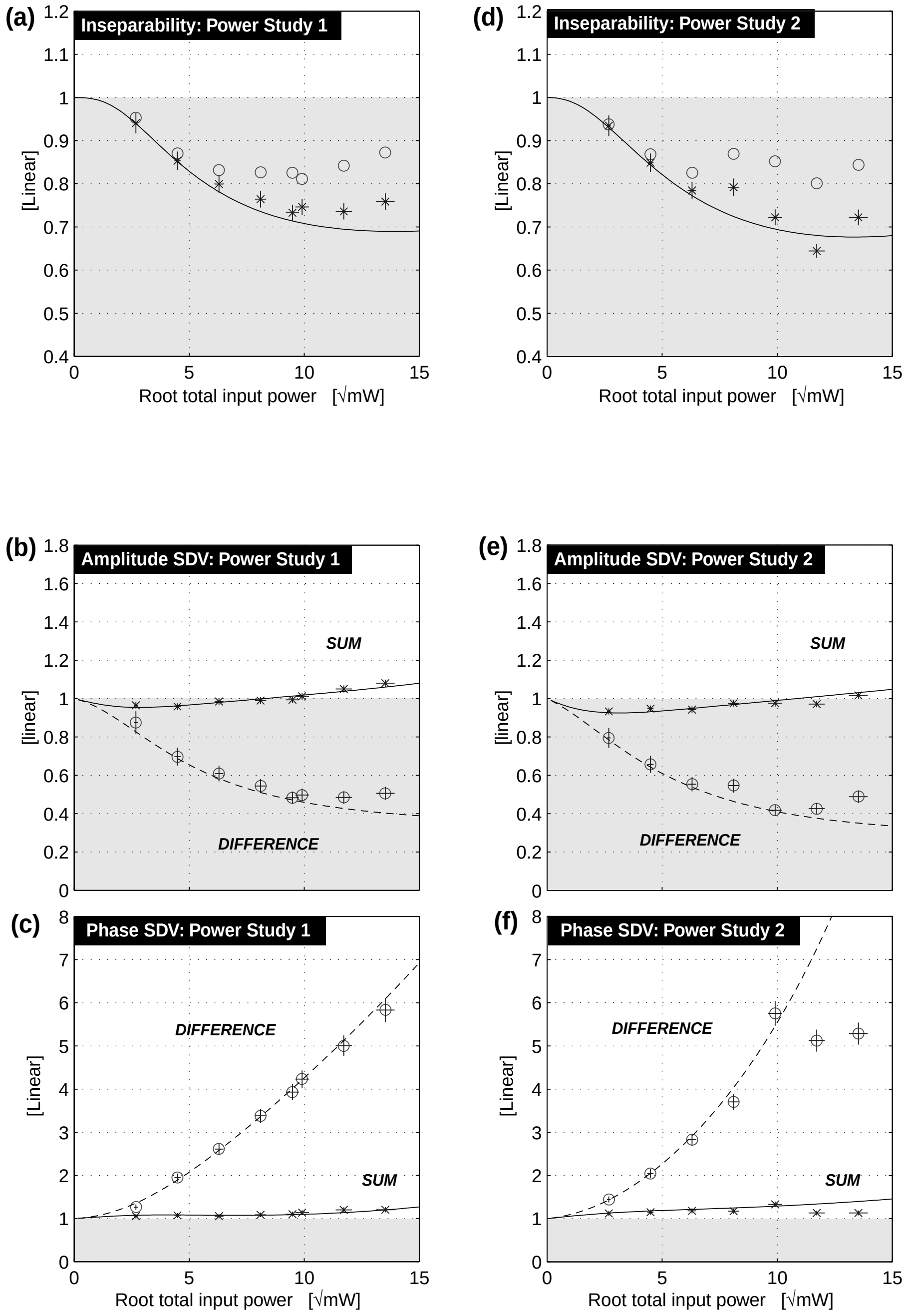

Figure 6.7: (Left) Power Study 1: **(a)** Inseparability as a function of increasing pump power. The angle parameter was held constant at $\theta = -0.1\pi$ which corresponds to a ratio of seed-to-pump power of 9:1 and locked to OPA de-amplification. The solid lines are inseparability from the model with the GAWBS noise term. Symbols are measurements: crosses mark the inseparability corrected for OCR excess noise. Circles are uncorrected. Horizontal and vertical error bar estimates are shown. **(b)** Sum and difference variances for the amplitude quadrature. Measurements are corrected for OCR artefacts. **(c)** Sum and difference measurements and theory for the phase quadrature. Measurements are corrected for OCR artefacts. (Right) Power Study 2: The angle parameter was held constant at $\theta = -0.2\pi$ which corresponds to a ratio of seed-to-pump power of 2:1 and locked to OPA de-amplification. Similar explanations apply to graphs: (d), (e) and (f).

monotonically decreasing in the graph). Lets look at the measurements of the sum and difference variances (SDV) for answers. In Figure 6.7(left)(b) the quantum correlation in amplitude appears to have maximised at $100\ \mathrm{mW}$ (as the separation between the sum and difference has maximised). But after this optimum point, both lines moved higher into the classical regime while keeping their separation constant. This means that the correlation coefficient for the amplitude quadrature is holding steady, while the squeezing is being degraded. Note that the phase sum variance climbed only slightly higher at this point. In Figure 6.7(left)(c), the classical correlation (visible as a gap between the sum and difference) however, grew rapidly. It is primarily the result of the weakening quantum correlation that is the cause of the weakening entanglement. We suspect that excess amplitude noise on the seed and pump (left over from the laser source) are responsible. Other explanations could be phase-jitter in the homodyne detector locking; or competing non-linearities (i.e. competing non-degenerate OPO modes near the 1064 nm wavelengths). This may be reasonable, considering that we are driving the OPA with a total input power that is over 200% of the OPO threshold power. A second power study was made at the parameter angle of $\theta = -0.2\pi$, which corresponds to a seed-to-pump power ratio of 2:1. The results are plotted in Figure 6.7(right). Aside from the highest measured powers where control of the OPA due to thermal effects became difficult, the inseparability graph (d) and the SDV graphs (e) & (f), support the results from the first power study.

6.5 Discussion of EPR

We know that the OPA model predicts harmonic entanglement in the form of both the inseparability and EPR criteria. We have seen from the experiment that the inseparability criterion was satisfied, so what has happened to the EPR criterion? Figure 6.8 shows the experimentally gathered points in the angle study, of the EPR criterion in the red-to-green and green-to-red inference directions. The circles show the raw data, while the crosses are corrected for the excess noise from the optical carrier rejection (OCR) process. Compared with the inseparability results in Figure 6.3, the EPR results are clearly much further away from achieving entanglement (the shaded area). Only at the extreme end of the amplifi-

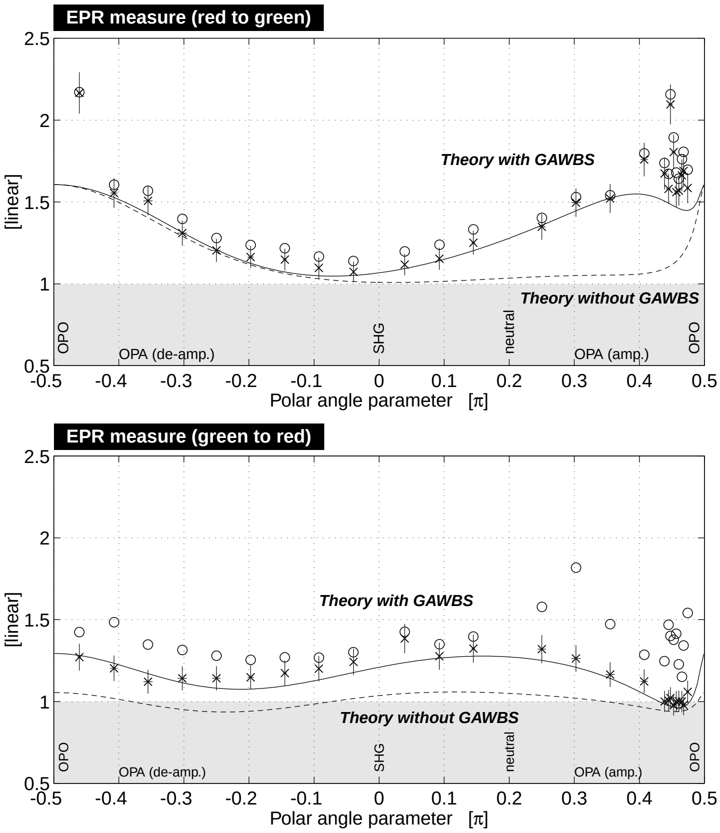

Figure 6.8: EPR entanglement measure for both directions of inference is plotted as a function of angle parameter with the total input power held constant at $65\ \mathrm{mW}$. The shaded area is the entanglement region. The solid line is from the model with GAWBS term, and the dashed line from the model without. The measurements marked as crosses are corrected for the noise artefacts of the OCR process. The circles are uncorrected. Although close to the boundary, measurements of EPR entanglement that were clear of the error bars were not observed.

cation region, do the EPR results dip slightly into the entanglement boundary. The error bars on the measurements however, are too large to make a claim of EPR entanglement here. The reason that the EPR criterion drops at the OPA amplification regime, is that the phase quadrature is de-amplified here. The phase noise arising from the GAWBS mechanism is therefore naturally suppressed. The suppression however, was not sufficient to yield a convincing demonstration of EPR entanglement.

6.6 Entanglement spectra

Harmonic entanglement as produced from an OPA is a broad-band phenomenon. However, the previous results were acquired in a narrow $\Delta\Omega = 22\ \mathrm{kHz}$ bandwidth that was centred at the sideband frequency of $\Omega_0 = 7.8\ \mathrm{MHz}$. This particular sideband frequency was chosen because it yielded the strongest entanglement. We can see this by looking at the spectrum of the sum of the individual sum and difference variances that are shown in Figure 6.9. This quantity is the same as the un-optimised inseparability, and it is a sufficient but not necessary measure of entanglement. Note that the complete matrix of correlation elements, and therefore the optimised inseparability could not be extracted from the spectrum analyser data. The power used was $59/\!\!/6\ \mathrm{mW}$ and locked to de-amplification of the seed. The inseparability spectrum shows a clear minimum in the curve from $6 \rightarrow 8\ \mathrm{MHz}$, but that entanglement could still be observed across the range $4 \rightarrow 16\ \mathrm{MHz}$ with the exception of a couple of spikes at discrete frequencies (of GAWBS origin). To understand why there is an optimum observation frequency, we need to keep in mind that the seed and pump fields still carry some amount of residual noise from the laser relaxation oscillation (at lower frequencies) because the mode-cleaners can only filter so much. And at higher measurement frequencies, one approaches the OPA cavity linewidth, where the entanglement that is produced is degraded because the effective nonlinear interaction strength at those sideband frequencies is not as strong as for frequencies near the carrier. The effects produce a minimum of excess noise in the vicinity of 7 MHz.

Looking at the inseparability spectrum, one may ask, where have the GAWBS peaks of Chapter 5 gone? The answer is that at this combination of seed and pump power, the readout of the phase noise is equal in strength for both the fundamental and second-harmonic fields. So that in the direct subtraction of the two quadratures, the excess phase noise vanishes. Note that this is not the case for the EPR measure. Figure 6.10 shows the spectrum of EPR in the inference direction from red to green. Here, the excess phase noise does not naturally subtract away, because the conditional variance is sensitive to both the correlation strength, and the individual quadrature variances of each mode. The end result is that at no point in the spectrum does the degree of EPR dip below one, which means that although the reflected seed and pump fields were harmonically entangled according to the inseparability criterion, they were not EPR entangled with one another.

6.7 Discussion of experimental limitations

After having observed some harmonic entanglement, the natural question is, how much more can be observed? I could argue that one only needs to turn up the total driving field power to start seeing more entanglement. The problems associated with increased driving field powers are four-fold: (1) The seed and pump fields are no longer shot-noise limited

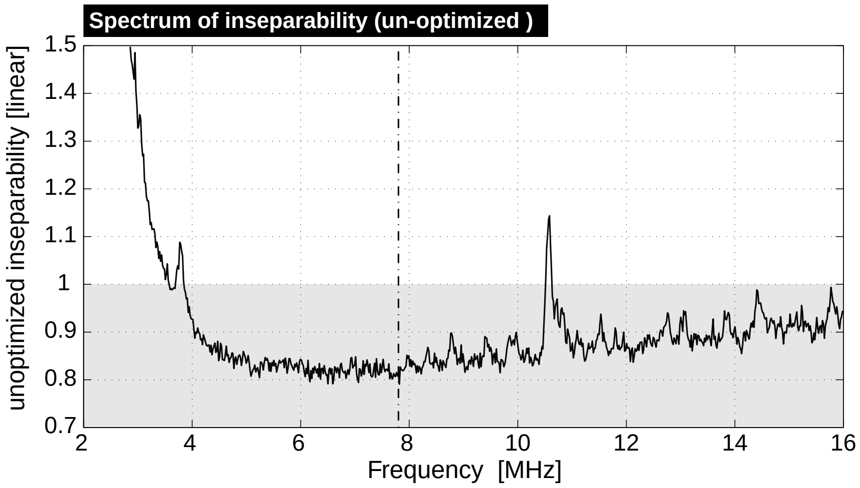

Figure 6.9: Spectrum of the unoptimised inseparability. The measurement has been corrected for OCR noise artefacts. Harmonic entanglement occurs for values less than one. The vertical dashed line is a marker for the narrow-band measurements that were taken at 7.8MHz. The driving field parameters were $59/\!\!/6$ mW and locked to de-amplification of the seed.

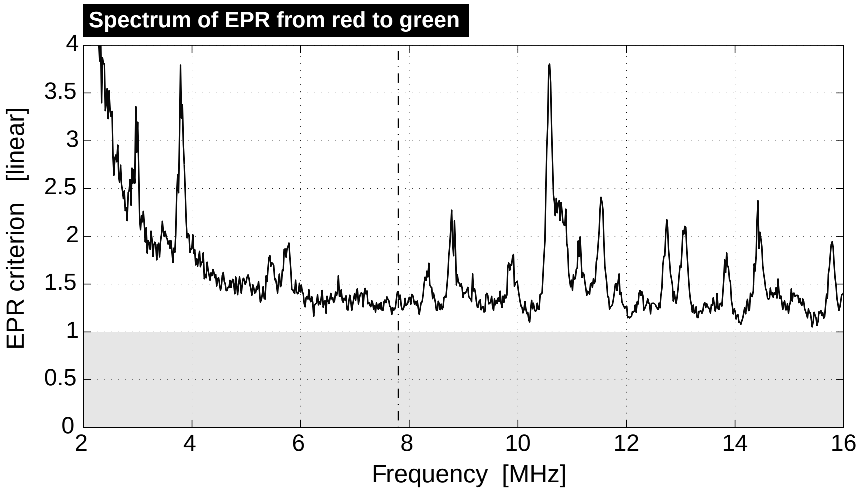

Figure 6.10: Spectrum of the EPR criterion in the inference direction from red to green. The measurement has been corrected for OCR noise artefacts. Harmonic entanglement would be heralded by values less than one, but this does not occur at any point in the spectrum. The vertical dashed line is a marker for the narrow-band measurements that were taken at 7.8MHz. The driving field parameters were $59/\!\!/6$ mW and locked to de-amplification of the seed.

because they retain some of the original laser relaxation oscillation. (2) The OPA cavity becomes increasingly difficult to control due to thermal effects, and the problem of staying on a particular branch of the bi-stable regions. (3) The reflected fields become more difficult to filter using the optical carrier rejection technique, because only a slight misalignment of the optics will cause light to be coupled into higher-order modes, and this amount of light will dominate over the local oscillator power in the homodyne detector. (4) The GAWBS mechanism that produces phase noise becomes more pronounced at higher powers, simply because more light is scattered into the upper and lower sidebands. All of these problems need to be addressed before an increase in entanglement strength can be observed at higher powers. There is however, always room for improvement by reducing optical losses in the experiment. These include: intra-cavity losses in the OPA, losses along the path from the OPA to the homodyne detector, and of course improving the photodiode efficiency.

6.8 Summary

The experimental setup was capable of testing the predictions of harmonic entanglement from the advanced OPA model. We prepared coherent seed and pump beams with powers totalling $200\mathrm{mW}$ and drove our OPA with them. The reflected fields had their optical carriers removed while leaving the sidebands relatively unaffected. Two independent homodyne detectors recorded values of the quadrature amplitudes and the correlation matrix for the combined system was constructed. From this matrix we could show that the fundamental and second-harmonic fields were entangled according to the inseparability criterion. The GAWBS effect, although strong in the individual spectra, was effectively self-cancelled for much of the available parameter angles, so that the inseparability criterion was largely immune to the GAWBS effect. The strength and bias of the entanglement could be controlled by adjusting the ratio of seed and pump powers. The agreement between experiment and GAWBS-extended model was good for a wide range of observables: quadrature variances, sum/difference variances, and inseparability.

Chapter 7

Photon Anti-bunching from Squeezing: Theory

There are two themes in this chapter. Firstly, is the idea that one can use homodyne detection to measure the second-order coherence of an optical field. Secondly, it has often been over-looked that squeezed states can show anti-bunching statistics provided they are appropriately displaced. The statistical property of second-order coherence is not only a tool for measuring the diameters of distant stars, but also of great value in understanding the dual nature of light as a particle and wave phenomenon.

The material that is presented here was part of a collaboration that was initiated by Magdalena Stobińska and Prof. Tim Ralph. Together with the experimental results (see Chapter 8), this theoretical work has been published under the following reference:

- *Measuring Photon Anti-bunching from Continuous Variable Sideband Squeezing,*
  N. B. Grosse, T. Symul, M. Stobińska, T. C. Ralph and P. K. Lam,
  Phys. Rev. Lett. **98**, 153603 (2007).

7.1 Motivation and Review

Fifty years ago, Hanbury-Brown and Twiss (HBT) first demonstrated an optical intensity interferometer [Hanbury-Brown and Twiss 1956b]. Since then, HBT interferometry has been applied to diverse areas such as condensed matter physics [Henny *et al.* 1999], atomic physics [Yasuda and Shimizu 1996, Oliver *et al.* 1999], and quantum optics:

[Arecchi *et al.* 1966]. The HBT interferometer has also become a powerful instrument technique in astronomy, and high-energy particle physics [Hanbury-Brown and Twiss 1956a]. From a historical perspective, HBT reported correlations in the intensity measured at two locations, from light emitted by a thermal source. The effect was interpreted as being either a manifestation of classical wave theory, or due to *bunching* in the arrival time of photons. Such correlations were generalised to *n*th-order by Glauber in a comprehensive quantum theory of optical coherence [Glauber 1963], with the second-order coherence $g^{(2)}$ corresponding to the measurement made with a HBT interferometer. Curiously, the theory predicted that certain states of light would exhibit a photon *anti-bunching* effect, which is the tendency for photons to arrive apart from one another. This is a non-classical phenomenon which violates the Schwarz inequality [Walls and Milburn 1994]. Photon anti-bunching has been observed in resonance fluorescence [Kimble *et al.* 1977]; conditioned measurements of parametrically down-converted light [Rarity *et al.* 1987], [Nogueira *et al.* 2001]; pulsed parametric amplification [Koashi *et al.* 1993], [Lu and Ou 2001]; quantum dots [Michler *et al.* 2000], [Santori *et al.* 2002]; and trapped single atoms/molecules [Lounis and Moerner 2000], [Darquie *et al.* 2005]. Recent experiments have probed the spatial and temporal second-order coherence functions of atomic species in Bose-Einstein-Condensation and atom lasers [Schellekens *et al.* 2005], [Öttl *et al.* 2005]. All of these experiments have relied upon the ability to detect individual particles in a time-resolved measurement.

We apply a technique for measuring the second-order coherence of optical fields, that complements previous studies and provides a link between discrete-variable (DV) and continuous-variable (CV) quantum optics. Our scheme is based on the HBT interferometer, but uses homodyne detection in each arm, to make CV measurements of the quadrature amplitudes over a range of sideband frequencies. The second-order coherence $g^{(2)}$ is then constructed from the set of four permutations of the time-averaged correlations between the amplitude/phase quadratures. At no point is it necessary to make time-resolved detections of single-photons [McAlister and Raymer 1997, Webb *et al.* 2006]. Homodyne detection offers the advantage of high bandwidth, and excellent immunity to extraneous optical modes. We used the scheme to measure the temporal second-order coherence function $g^{(2)}(\tau)$ of a displaced squeezed state.

In contrast to most CV experiments involving squeezed light, is the realisation that

weaker squeezed states can exhibit a greater anti-bunching effect. Some properties of displaced squeezed states in the context of second-order coherence have been investigated before [Koashi *et al.* 1993, Stoler 1974, Mahran and Satyanarayana 1986]. Such states can exhibit behaviour ranging from photon anti-bunching to super-bunching, provided that the state is sufficiently pure, and the squeezing weak. There has also been much interest in the nonclassical properties of displaced Fock states which in addition to showing negativity in the Wigner function, also show oscillations in the number state distribution:
[de Oliveira *et al.* 1990]. An experimental observation of these properties was made by [Lvovsky and Babichev 2002]. Using our modified HBT interferometer, and exploiting the high stability and low optical loss of our experimental setup, we were able to prepare and measure displaced squeezed states that clearly demonstrated photon anti-bunching. In addition, we investigated the immunity of second-order coherence measurements to optical attenuation.

7.2 Ways of measuring coherence

The idea of coherence has its origins in the classical description of light. Early experiments by Grimaldi in 1665 that aimed to prove that light was a wave, failed (see Chapter 9.3.1 in [Hecht 2002]). In such an experiment, a beam of sunlight was allowed to pass through two closely-spaced pinholes. It was expected that the wave nature of light would make itself apparent as an alternating bright/dark pattern (fringes) due to the constructive/deconstructive interference of the wavefronts from each pinhole. However, no fringes were seen. This is because the pinholes were spaced so far apart from one another that they effectively sampled two independent (statistically uncorrelated) sources of light. As seen from earth, the sun has an angular diameter of $0.5°$. And as it is not a point source of light, a sample of the light at one point in space, contains the vector sum from many random emitters across the sun's surface. But if one wishes to sample the light from a second point that is some transverse distance away from the first, then the different arrival times from the emitters of say the western and eastern halves of the sun, will add vectorially to a create a new amplitude and phase for the wavefront. The two pinholes of the experiment did not produce fringes,

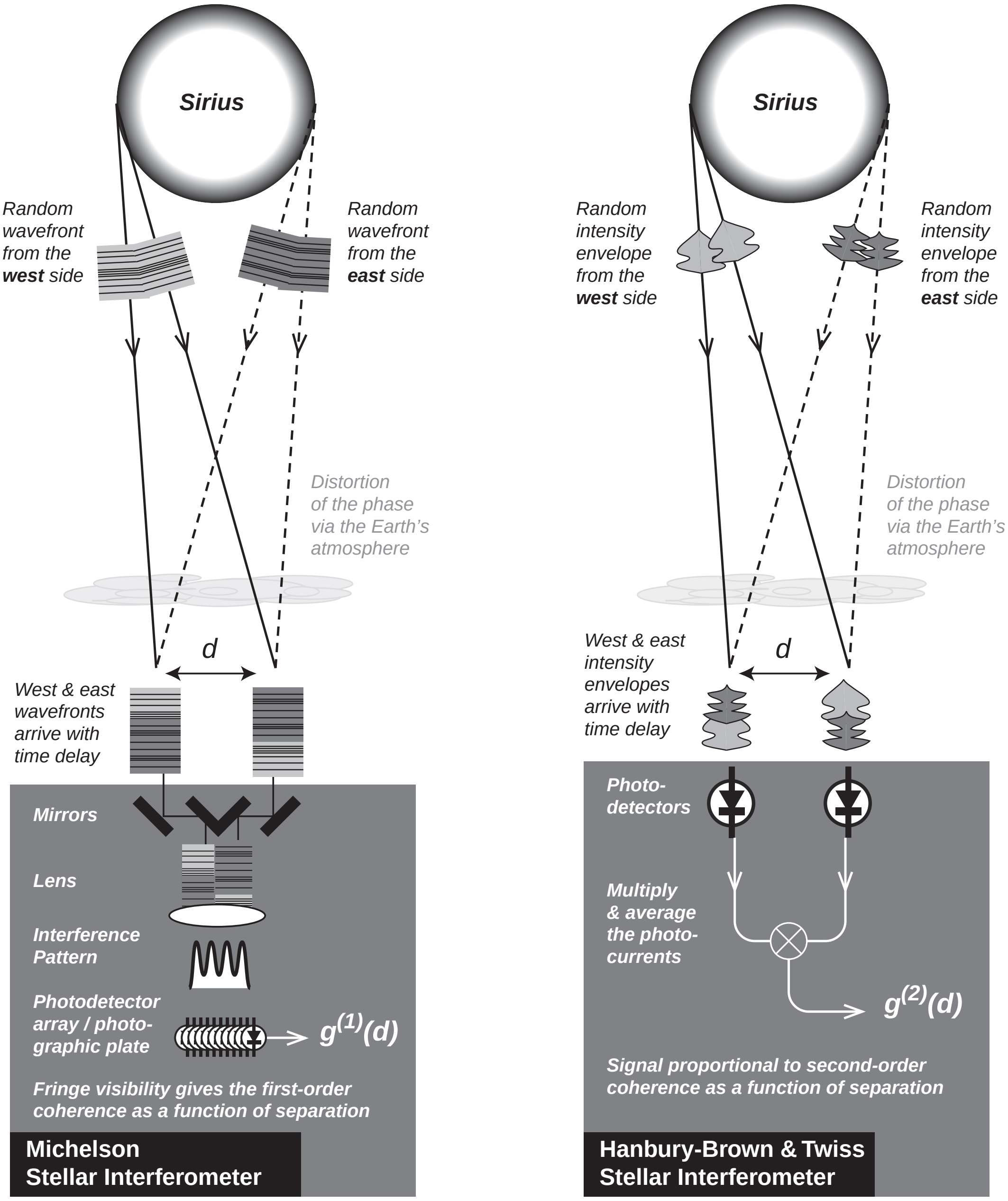

Figure 7.1: Two instruments for measuring the angular diameters of distant stars. (Left) Michelson's stellar interferometer optically interferes the light collected by two mirrors that are spaced by distance d. The interference pattern is similar to that of a double-slit experiment. The fringe visibility gives a reading of the first-order coherence function at the spacing d. When the fringes vanish, the angular diameter of the star is given by $1.22\lambda/d$ where λ is the central wavelength. Note that the measurement is sensitive to phase fluctuations that are induced by atmospheric turbulence. (Right) The stellar interferometer of Hanbury-Brown and Twiss. The light is collected and detected at two points that are separated by distance d. The photocurrents are multiplied and averaged, thus giving the correlation. The signal is proportional to the second-order coherence function that is sampled at the spacing d. When the separation is very large the correlation vanishes because of the time delay of the intensity fluctuations from sources that are on opposite sides of the star. The measurement is insensitive to atmospheric turbulence, thereby allowing much smaller stellar diameters to be measured. The trade-off is that the bandwidth of the photodetectors limits the efficiency of the measurement, which means that integration times are necessarily very long.

because the phases of the two wavefronts were not correlated (not spatially coherent), and therefore the bright/dark fringe pattern averaged out to a uniform intensity. If the pinholes had been separated by less than about $\approx 50\,\mu\mathrm{m}$, then the interference pattern would have appeared; see for example [Hecht 2002]. Young improved on the original experiment by placing a single pinhole (or slit) before the double-slit. This ensured that the light sampled by the subsequent slits was correlated in amplitude and phase, and the appearance of the fringes established the wave nature of light [Young 1804].

7.2.1 Classical definitions and bounds

The original double-slit experiment effectively measures the spatial *first-order* coherence of a light beam. This is defined as

$$g^{(1)}(\mathbf{r}_1, t_1; \mathbf{r}_2, t_2) = \frac{\langle E^*(\mathbf{r}_1, t_1)\, E(\mathbf{r}_2, t_2)\rangle}{\sqrt{\langle E^*(\mathbf{r}_1, t_1)\, E(\mathbf{r}_1, t_1)\rangle}\sqrt{\langle E^*(\mathbf{r}_2, t_2)\, E(\mathbf{r}_2, t_2)\rangle}} \tag{7.1}$$

for the spatial co-ordinates $\mathbf{r}_1$ and at time t_1. Michelson proposed a larger version of the original double-slit experiment that could be used as an instrument to measure the diameters of distant stars [Michelson and Pease 1921]. The pinholes were replaced by two planar mirrors that were spaced several meters apart; see Figure 7.1. The starlight was reflected from these mirror into a parabolic telescope mirror (at the Mt Wilson Observatory), which interfered the light at the focus. A fringe pattern from the star Betelgeuse was observed. The distance between the two planar mirrors was increased until the fringe pattern disappeared. In this way, the angular diameter of Betelgeuse could be resolved, despite it being orders of magnitude much smaller than any telescope of the day could resolve. The difficulty in operating the interferometer, was that atmospheric turbulence induced a randomly varying phase shift of the light received by each planar mirror, and this had the effect of ‘washing’ the interference pattern away. Hence, measurements of more distant/smaller stars was not possible [Mandel and Wolf 1965].

Hanbury-Brown and Twiss thought of another way of measuring the spatial coherence of light. Their idea was to measure the intensity of the star light directly, and not the electric field via an interference fringe; see Figure 7.1 and the equivalent scheme in Figure 7.2. The advantage of doing it this way, is that the relative phase (and therefore atmospheric turbulence) plays a lesser role in the measurement because one does not need to optically interfere two beams on a beamsplitter. With the Hanbury-Brown–Twiss setup, one needs only to detect the starlight on two photo-multiplier tubes that are separated by up to several hundred metres away. The incredible result is that some kind of interference effect still takes place. Hence this setup is often called an intensity interferometer. To create interference, one must divide a signal and combine it again. The division occurs during the sampling process (photo-detection), where only a small portion of the entire wavefront is selected. The combination comes when the photocurrents of the detectors are analysed in the correlator. The interference can be considered to occur not between two monochromatic optical frequencies directly, but between their individual 'beat-notes' which contain a spread over many frequencies. The beat-notes that are sampled at two different delay times, or two different positions, will become less correlated as the delay time or position is increased. The normalised form of the correlation becomes exactly the definition of the *second-order* coherence:

$$g^{(2)}(\tau) = \frac{\langle I(t+\tau)I(t)\rangle}{\langle I(t)\rangle^2} \tag{7.2}$$

The second-order coherence is limited by classical bounds $1 \leq g^{(2)}(0) \leq \infty$ which also have their origins in the Schwarz inequality. Some other properties are: symmetry $g^{(2)}(\tau) = g^{(2)}(-\tau)$; and long time delay $g^{(2)}(\tau) = 1$ for $\tau \gg \tau_c$; and the other limit $g^{(2)}(\tau \neq 0) \leq g^{(2)}(0)$ which says that the coherence finds its maximum at zero time delay. There is a relationship between the first- and second-order coherence functions, namely $g^{(2)}(\tau) = 1 + |g^{(1)}(\tau)|^2$. This relationship was used by Hanbury-Brown and Twiss to analyse the data from their stellar interferometer to infer the diameter of Sirius [Hanbury-Brown and Twiss 1956a]. Their early success led them to build a larger instrument at Narrabri, Australia. Over the course of several years, they measured the angular diameters of 32 stars [Hanbury Brown *et al.* 1974].

7.2.2 Quantum definitions and bounds (single-mode)

When the second-order coherence function is expressed in the quantum theory of light, the measured intensities become normally-ordered products of the creation and annihilation

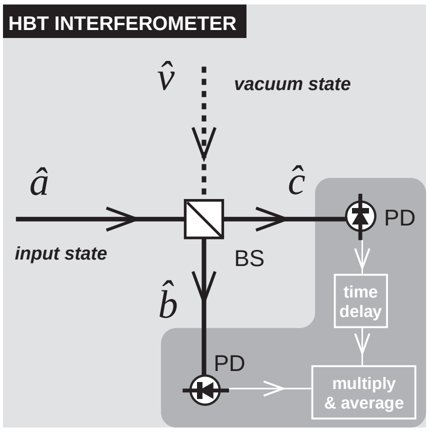

Figure 7.2: The Hanbury-Brown Twiss intensity interferometer is a technique for measuring the intensity correlation function of a light beam. The input state $\hat{a}$ is interfered with a vacuum state $\hat{v}$ on a 50/50 beamsplitter (BS). Each arm is detected by a photo-detector (PD). A time delay is introduced, which can be either optical or electronic. The average value for the product for the intensities is calculated.

operators, which can be interpreted as groupings in the arrival times of photons. As we consider just a single optical mode $\hat{a}$, the second-order coherence is defined as the joint probability of detecting a single photon for time t and at time $t+\tau$ to give

$$g^{(2)}(\tau)=\frac{\langle\hat{a}^{\dagger}(t+\tau)\hat{a}^{\dagger}(t)\hat{a}(t+\tau)\hat{a}(t)\rangle}{\langle\hat{a}^{\dagger}(t)\hat{a}(t)\rangle^{2}} \tag{7.3}$$

where the coherence function has been normalised by the square of the expectation value of the photon number. The equivalent form for classical fields can be made by replacing the creation-annihiliation operators with complex numbers. These can then be re-ordered in such a way, that at zero time delay, we can write $g^{(2)}(0)=\langle I^{2}\rangle/\langle I\rangle^{2}$ with I the field intensity. After applying the Schwarz inequality directly, we can see that the coherence function is bounded below by one. This means that classical fields cannot display anti-bunching which is heralded for values less than one. However, in the quantum expression, the re-ordering of the operators is prevented, and therefore the values of $g^{(2)}(0)$ can take on values less than one.

7.2.3 The two-mode version is identical to single-mode

In practice, second-order coherence is not easily measured in the form of Equation 7.3 because it is not readily possible to detect and resolve n photons. Instead, the single mode is coupled with another mode $\hat{b}$ on a 50:50 beamsplitter. The intensity of the light at each output is then measured. This is the principle of the HBT interferometer.

$$g^{(2)}(\tau)=\frac{\langle\hat{b}^{\dagger}(t+\tau)\hat{b}(t+\tau)\hat{c}^{\dagger}(t)\hat{c}(t)\rangle}{\langle\hat{b}^{\dagger}(t)\hat{b}(t)\rangle\langle\hat{c}^{\dagger}(t)\hat{c}(t)\rangle} \tag{7.4}$$

The amazing thing is that Equation 7.3 and Equation 7.4 become equivalent if the other input to the beamsplitter is in a vacuum mode $\hat{v}$. The contribution from the vacuum state does not appear in the final expression of Equation 7.4, so that one simply gets back Equation 7.3. Formally, the photon anti-bunching effect is witnessed in the coherence function when $g^{(2)}(0) < g^{(2)}(\tau \neq 0)$. On the other hand, photon bunching occurs when the opposite inequality holds true. To make these kind of g2 (pronounced ‘gee’-‘two’) measurements, one needs to have access to the photon number correlations, or in the limit of very weak light beams, to correlate the arrival times of single photons in each arm. This is the most common method of measuring g2.

7.2.4 Re-express coherence with quadrature operators

Experiments in the continuous-variable regime do not have detectors that can resolve single-photon events, but they do use homodyne detection to be sensitive to the quadrature amplitudes of the signal beam. So a connection between the discrete-variable and continuous-variable methods needs to be found. A homodyne detector can be placed at each output port of the 50:50 beamsplitter. The amplitude $\hat{X}^+ = \hat{a}^\dagger + \hat{a}$ and phase $\hat{X}^- = \mathrm{i}(\hat{a}^\dagger - \hat{a})$ quadratures are measured. The dependence can be reversed, so that we get the creation and annihilation operators in terms of the quadrature operators, $\hat{a}^\dagger = (\hat{X}^+ - \mathrm{i}\hat{X}^-)/2$ and $\hat{a} = (\hat{X}^+ + \mathrm{i}\hat{X}^-)/2$, respectively. These forms can be plugged into Equation 7.4 and simplified to give

$$g^{(2)}(\tau) = \frac{\sum_{i,j}\langle \hat{X}_b^i(t+\tau)^2 \hat{X}_c^j(t)^2\rangle - 2\sum_{i,k}\langle \hat{X}_k^i(t)^2\rangle + 4}{(\sum_i \langle \hat{X}_b^i(t)^2\rangle - 2)(\sum_i \langle \hat{X}_c^i(t)^2\rangle - 2)} \tag{7.5}$$

In this compact notation, summations are made over the quadrature indices, $i, j = +, -$ and mode label indices $k = b, c$. This measurement technique is possible only because there do not appear any cross-quadrature terms for a single mode. For example, it is not necessary to measure something like the correlation between the amplitude and phase quadrature for a single mode. The absence of such cross-terms means that each correlation term can be independently measured by recording the output of the homodyne detectors, and then reconstructing $g^{(2)}(\tau)$ according to Equation 7.5. It is therefore possible to measure the second-order coherence function using homodyne detection alone. Homodyne detection has the advantage of being very specific in selecting the mode in terms of polarisation, spatial mode function, and wavelength. The selected mode is always identical to the local oscillator mode.

As an aside, I note that in principle it is possible to reconstruct the complete quantum state in terms of the Wigner function by way of collecting a set of quadrature measurements over a range of quadrature angles. The inverse Radon transformation of that set can then recover the Wigner function [Smithey *et al.* 1993]. From the Wigner function it is possible to calculate many quantities of interest, for example the second-order coherence function to check for photon anti-bunching statistics, and hence test the particulate nature of light. But we can side-step the quantum tomographic procedure by just measuring the contributions that make up Equation 7.5. These contributions are the correlations of squares of the quadrature measurements, so although the individual measurements themselves are linear, the set of measurements are later combined in a nonlinear way in Equation 7.5. In this way, it is possible to extract the particulate nature of light via linear continuous-variable measurements.

7.2.5 Quadrature-angle-averaged measurements

The previous analysis of g2 in terms of quadrature operators does not tell us how to make the measurements themselves, but rather just how to put them together. The simplest interpretation is that one should measure all the combinations of amplitude and quadratures and their correlations between the two modes. This is certainly possible in an experimental setting, however this requires one to control the relative phase of the local oscillator to the signal beam, such that the quadrature measured is precisely X^+ or X^-. But perhaps one can get the same answer by being lazy. We could give the local oscillators a random phase shift, and then averaged the measurements of the signal beam, so as to give a 'quadrature-angle-averaged' measurement.

I start by using the expression for an arbitrary quadrature angle for mode b and c, that are determined by the angles θ and ϕ, respectively, so that

$$\begin{aligned} \hat{X}_b^{\theta} &= \hat{X}_b^{+}\cos\theta + \hat{X}_b^{-}\sin\theta && (7.6)\\ \hat{X}_c^{\phi} &= \hat{X}_c^{+}\cos\phi + \hat{X}_c^{-}\sin\phi && (7.7) \end{aligned}$$

The values for θ and ϕ are drawn from the flat, normalised probability distributions $\Theta(\theta) = 1/2\pi$ and $\Phi(\phi) = 1/2\pi$, respectively. Note that a comparison of the phases θ and ϕ are assumed to show no correlations, hence the joint probability distribution of those two variables is separable into a product $P(\theta, \phi) = \Theta(\theta)\Phi(\phi)$. Next, I would like to calculate the quadrature-angle-averaged variance operator for mode b, which is denoted by an overbar, and becomes:

$$\begin{aligned} \overline{(\hat{X}_b^{\theta})^2} &= \int_0^{2\pi} \mathrm{d}\theta\, \Theta(\theta) \Big\{ (\hat{X}_b^{+})^2 \cos^2\theta + (\hat{X}_b^{-})^2 \sin^2\theta \\ &\quad + (\hat{X}_b^{+}\hat{X}_b^{-} + \hat{X}_b^{-}\hat{X}_b^{+}) \sin\theta\cos\theta \Big\} \\ &= \frac{1}{2\pi}\int_0^{2\pi} \mathrm{d}\theta\, \Big\{ (\hat{X}_b^{+})^2 \cos^2\theta + (\hat{X}_b^{-})^2 \sin^2\theta \\ &\quad + (2(\hat{X}_b^{\frac{\pi}{4}})^2 - (\hat{X}_b^{+})^2 - (\hat{X}_b^{-})^2) \sin\theta\cos\theta \Big\} \\ &= \frac{1}{2}\Big[(\hat{X}_b^{+})^2 + (\hat{X}_b^{-})^2 \Big] \\ &= \frac{1}{2}\sum_i (\hat{X}_b^{i})^2 && (7.8) \end{aligned}$$

where the summation is taken over only the amplitude and phase quadratures $i \in \{+, -\}$. We can see that the quadrature-angle-averaged variance that is measured for one mode is just the same as the average of two measurements: the amplitude and phase quadrature variances. The result for mode c is similar. I now want to analyse the (second-order) quadrature-angle-averaged correlations between the modes b and c. We find that

$$\begin{aligned} \overline{(\hat{X}_b^{\theta})^2(\hat{X}_c^{\phi})^2} &= \int_0^{2\pi}\int_0^{2\pi} \mathrm{d}\theta\, \mathrm{d}\phi\, \Theta(\theta)\, \Phi(\phi)\, (\hat{X}_b^{\theta})^2 (\hat{X}_c^{\phi})^2 \\ &= \left\{ \frac{1}{2\pi}\int_0^{2\pi} \mathrm{d}\theta\, (\hat{X}_b^{\theta})^2 \right\} \left\{ \frac{1}{2\pi}\int_0^{2\pi} \mathrm{d}\phi\, (\hat{X}_c^{\phi})^2 \right\} \\ &= \frac{1}{2}\Big[(\hat{X}_b^{+})^2(\hat{X}_c^{+})^2 + (\hat{X}_b^{+})^2(\hat{X}_c^{-})^2 + (\hat{X}_b^{-})^2(\hat{X}_c^{+})^2 + (\hat{X}_b^{-})^2(\hat{X}_c^{-})^2 \Big] \\ &= \frac{1}{2}\sum_{i,j} (X_b^{i})^2 (X_c^{j})^2 && (7.9) \end{aligned}$$

where the summation is made over the amplitude and phase quadratures, as written by the subscripts $i \in \{+,-\}$ and $j \in \{+,-\}$.

Finally, by way of inspection with Equation 7.5, and combining the two quadrature-angle-averaged operators in Equation 7.8 and Equation 7.9 in the appropriate way, gives back the second-order coherence measurement:

$$g^{(2)}(0) = \frac{\langle\overline{(\hat{X}_b^\theta)^2(\hat{X}_c^\phi)^2}\rangle - 2\langle\overline{(\hat{X}_b^\theta)^2}\rangle - 2\langle\overline{(\hat{X}_c^\phi)^2}\rangle + 2}{\left(\langle\overline{(\hat{X}_b^\theta)^2}\rangle - 1\right)\left(\langle\overline{(\hat{X}_c^\phi)^2}\rangle - 1\right)} \tag{7.10}$$

In principle, this quadrature-averaged scheme will produce the same result as the fixed-quadrature scheme for measuring the second-order coherence function. The only condition that needs to be met, is that the measurement is averaged over all angles in equal time, i.e. over a uniform distribution of angles. This method may be more appropriate for some applications where the relative phase of the local oscillator with the signal beam cannot be controlled, such as when measuring light that originates from a truly thermal source.

7.3 Second-order coherence of displaced-squeezed states

Now that we have a method for measuring second-order coherence from the quadrature amplitudes, we can start investigating sources of light that are non-classical in exactly these observables. Squeezed light is the primary candidate, but as we will see, the displacement of that squeezed state also has an important role to play.

7.3.1 The 'spider' diagram

Let me restrict the analysis for the moment to zero time delays $\tau = 0$. It is already a well known result that a displaced state (coherent state) gives a value of second-order coherence of $g^{(2)}(0) = 1$. Another results is for squeezed vacuum states $g^{(2)}(0) = 3 + 1/\langle n\rangle$, with n the expectation value of the photon number $\langle n\rangle = \sinh(r)$ where r is the squeezing parameter. The interesting theoretical result, and perhaps one that has often been overlooked (an exception is [Mahran and Satyanarayana 1986]), is that the combination of the two processes: a squeezed vacuum that is then displaced, can then take on an arbitrary value of $g^{(2)}(0)$. I want to calculate the second-order coherence of a displaced squeezed state. It turns out to be a simpler calculation if we work in the Heisenberg picture, which means that we start with a mode in the vacuum state, but transform the creation and annihilation operators such that

$$\hat{D}^{\dagger}(\alpha)\hat{r}^{\dagger}(r)\hat{a}\hat{D}(\alpha)\hat{S}(r) = \alpha + \hat{a}\cosh(r) - \hat{a}^{\dagger}\sinh(r) \tag{7.11}$$

where $\hat{D}(\alpha)$ is the displacement operator, and $\hat{S}(r)$ is the squeezing operator. Note that for no other reason than keeping the derivation simple, I restrict the displacement and squeezing parameters to be real quantities: $\alpha \in \Re$ and $r \in \Re$. The second-order coherence for zero time delay then becomes

$$g^2(0) = 1 + \frac{\sinh^2(r)\left(2\alpha^2 + \cosh(2r) - 2\alpha^2\coth(r)\right)}{\left(\alpha^2 + \sinh^2(r)\right)^2} \tag{7.12}$$

The true versatility of this function can only be shown when mapping it out across the variables α and r. The map is shown in Plate 9 where darker colours signify photon anti-bunching statistics, and lighter colours show bunching. Contours are drawn to give the exact values. The horizontal axis corresponds to coherent states, while the vertical axis corresponds to squeezed states. All other points in the graph are a combination of both processes. Immediately we can see the symmetry in positive/negative values of the displacement variable, and the asymmetry in the squeezing variable. Only if the state is amplitude squeezed, and accompanied by at least a small displacement, will the state show photon anti-bunching.

7.3.2 Approaches to the vacuum state 'singularity'

The centre of the diagram in Plate 9, as given by $\alpha = r = 0$ of the displaced-squeezed state, corresponds to the vacuum state. We can see that the contour lines of various g2 values start to crowd together as the origin is approached. Starting with a displaced-squeezed state, it is possible to approach the vacuum state while holding any value of g2 constant. This effect is attributable to the normalisation procedure of g2 as given by the denominator of Equation 7.3, which approaches zero when the expectation value of the photon number of the state also approaches zero. So although the degree of second-order coherence of a vacuum state is defined, its definition is not unique and can therefore be considered to be a singularity.

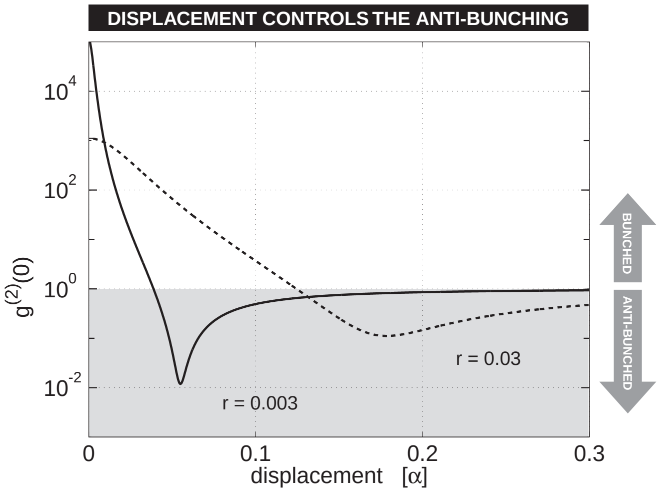

Figure 7.3: The degree of second-order coherence as a function of displacement. The vertical scale is logarithmic. Two curves are shown for a fixed squeezing parameter of $r = 0.03$ dashed line, and $r = 0.003$ solid line. The shaded area corresponds to anti-bunched statistics. Note the large range of values that can be accessed by only slightly changing the displacement.

7.3.3 Displacement controls the anti-bunching

For a given level of amplitude squeezing, the displacement appears to control the anti-bunching behaviour. In Figure 7.3, I have plotted the second-order coherence as a function of the displacement α. For the case of $r = 0.03$ squeezing (solid line), one can vary the degree of second-order coherence by 4 orders of magnitude; while the $r = 0.003$ squeezing case (dashed line) allows a variation of 7 orders of magnitude (from anti-bunching $g^{(2)}(0) = 10^{-2}$ to bunching $g^{(2)}(0) = 10^{+5}$). I could of course obtain a similar kind of behaviour by plotting g2 as a function of the squeezing parameter for a fixed displacement. But squeezed light itself is considered a non-classical effect, and in this sense it is more interesting to see how the displacement affects the degree of second-order coherence (from anti-bunching to bunching) as a function of a ‘classical’ parameter like the displacement.

7.3.4 Invariance to optical loss

No optical measurement is made without introducing at least some optical loss. The loss mechanism could be in the form of scattering from lenses and mirrors; poor mode-matching in a homodyne detector; or simply from the inefficiency of the photodiode itself. These processes can be reduced to a simple model. The loss mechanism couples in new modes other than the original mode of interest. These new modes are usually in the form of a vacuum state, so that the original state, say a squeezed state, becomes mixed and tends to approach the form of a vacuum state, as the level of optical loss is increased. This is most undesirable, because much effort went into making the squeezed state, only for it to become

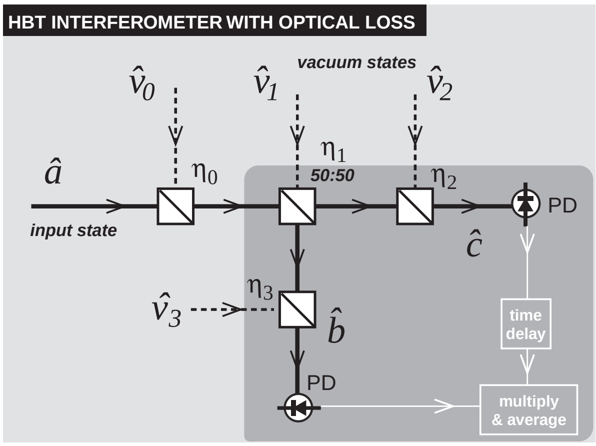

Figure 7.4: The Hanbury-Brown Twiss (HBT) intensity interferometer with optical loss. The coupling of vacuum states via loss is considered prior to, and within, the HBT interferometer.

more 'classical' via the loss mechanism.

It is a rather surprising fact then, that measurements of the second-order coherence are immune to optical loss. Where the loss occurs in the optical path, also does not play a role. This result can be calculated in three separate cases for losses that occur before, during, and after the main beamsplitter. The new setup is shown in the schematic of Figure 7.4. Aside from the original mode a, there are four vacuum modes v_i (where $i = \{0, 1, 2, 3\}$) that enter via various beamsplitters having intensity reflectivities, η_i. The amplitude reflectivities: $\mathcal{T}_i = \sqrt{1-\eta_i}$ and $\mathcal{R}_i = \sqrt{\eta_i}$ allow a more compact description.

The transfer function of this system in the Heisenberg picture for the two modes prior to detection, b and c, becomes

$$\hat{b} = \mathcal{T}_0\mathcal{T}_1\mathcal{T}_2\hat{a} + \mathcal{R}_1\mathcal{T}_2\hat{v}_1 + \mathcal{R}_2\hat{v}_2 \tag{7.13}$$

$$\hat{c} = -\mathcal{T}_0\mathcal{R}_1\mathcal{T}_3\hat{a} + \mathcal{T}_1\mathcal{T}_3\hat{v}_1 + \mathcal{R}_3\hat{v}_3 \tag{7.14}$$

There are similar expressions for the creation operators that have complex conjugated reflection coefficients. Now we choose the initial state of the system to be in the separable state $|\psi\rangle_a|0\rangle_{v0}|0\rangle_{v1}|0\rangle_{v2}|0\rangle_{v3}$. This greatly simplifies the calculation for the coherence function because the cross-terms vanish if they contain only a single entry of a creation or annihilation operator of the vacuum modes. Likewise, terms goes to zero if they contain the mean photon number of one of the vacuum modes. The only part that is tricky, is not to forget the contribution from the anti-normally ordered term: $\langle 0|\hat{v}_0\hat{v}_0^\dagger|0\rangle = -1$. Applying all these rules then gives

$$g^{(2)}_{\text{loss}}(\tau) = \frac{\overbrace{\mathcal{T}_0^4}^{\text{before}}\ \overbrace{(\mathcal{T}_1^2\mathcal{R}_1^2)}^{\text{during}}\ \overbrace{(\mathcal{T}_2^2\mathcal{T}_3^2)}^{\text{after (the beamsplitter)}}}{\underbrace{(\mathcal{T}_0^2\mathcal{T}_1^2\mathcal{T}_2^2)}_{\text{mode } b}\ \underbrace{(\mathcal{T}_0^2\mathcal{R}_1^2\mathcal{T}_3^2)}_{\text{mode } c}}\, g^{(2)}(\tau) = g^{(2)}(\tau) \tag{7.15}$$

The numerator and denominator of the fraction cancel out to give the original coherence function. But if one has not written it out explicitly, then it does not seem possible. I have also identified which terms arise from the loss mechanism before, during, and after the main beamsplitter. Later I will show how this works in the Fock basis as the state is optically attenuated.

7.4 Generalisations

The previous analyses of the second-order coherence have been restricted to zero time delay ($\tau = 0$), and also to *pure* displaced squeezed states. In this section, a finite time window and an extension to *mixed* displaced squeezed states is introduced, in order to make the analysis more applicable to experimental considerations.

7.4.1 Arbitrary choice of the temporal window function

The full expression for the second-order coherence is a function of the time-delay. To get this expression, one needs to go back to Equation 7.3 and repeat the derivation with a time delay τ in mode $\hat{b}(t)$. The result is

$$\begin{aligned} g^{(2)}(\tau) \quad = \quad & \frac{1}{\Big(\sinh^2(r) + \alpha^2\Big)^2}\Bigg\{\Big(\alpha^2 - \frac{1}{2}[\hat{a}(\tau), \hat{a}^\dagger(0)]\sinh(2r)\Big)^2 \\ & + \Big(2 + [\hat{a}(0), \hat{a}^\dagger(\tau)] + [\hat{a}(\tau), \hat{a}^\dagger(0)]\Big)\alpha^2\sinh^2(r) \\ & + \Big(1 + [\hat{a}(0), \hat{a}^\dagger(\tau)]^2\Big)\sinh^4(r)\Bigg\} \end{aligned} \tag{7.16}$$

The final form of the coherence function depends on the commutation relation between the original and delayed versions of the creation/annihilation operators. The commutation relation depends on the shape of the frequency window that is used for the measurement.

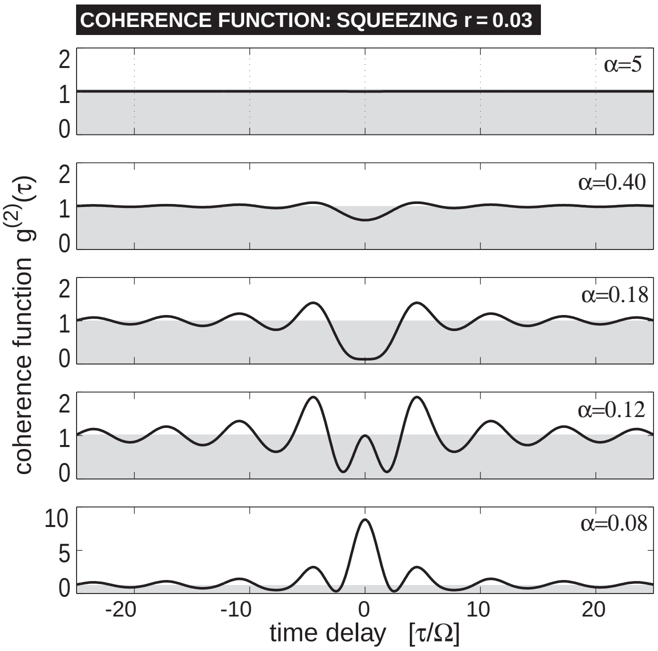

Figure 7.5: The second-order coherence as a function of time delay. Five examples are made with decreasing displacement, but with the squeezing parameter for all of them held constant at $r = 0.03$. (a) Shows a coherent state. (b) and (c) show anti-bunching. (d) appears to be coherent at zero time delay. (e) shows bunching (note change of scale).

7.4.2 Choose top-hat frequency window

Since one can only make measurements in a finite time window, one must choose a corresponding frequency window function. Formally, this means that a filter selects a frequency mode according to $\hat{a}(\tau) = N^{-1/2} \int_{-\infty}^{\infty} \hat{a}_\omega f(\omega) \mathrm{e}^{\mathrm{i}\tau\omega} \mathrm{d}\omega$ where $f(\omega)$ is the filter function and $N = \int_{-\infty}^{\infty} f(\omega)^2 \mathrm{d}\omega$ is a normalisation factor. We already know the commutation relation for the frequency creation/annihilation operators, it is given by $[\hat{a}_\omega, \hat{a}^\dagger_{\omega'}] = \delta(\omega - \omega')$. In many experiments, a flat band-pass filter is chosen to isolate the frequencies of interest. This frequency filter, is described by a top-hat function such that $f(|\omega| \leq \Omega) = 1$ and zero elsewhere. From these, we get the commutation relations for the time-dependent operators to be $[\hat{a}(0), \hat{a}^\dagger(\tau)] = [\hat{a}(\tau), \hat{a}^\dagger(0)] = \mathrm{sinc}(\Omega\tau)$. These results are substituted into Equation 7.16 to give

$$\begin{aligned} g^{(2)}(\tau) \quad = \quad & \frac{1}{\Big(\sinh^2(r) + \alpha^2\Big)^2} \Big\{ \Big(\alpha^2 - \frac{1}{2}\mathrm{sinc}(\Omega\tau)\sinh(2r)\Big)^2 \\ & + 2\Big(1 + \mathrm{sinc}(\Omega\tau)\Big)\alpha^2 \sinh^2(r) \\ & + \Big(1 + \mathrm{sinc}^2(\Omega\tau)\Big)\sinh^4(r) \Big\} \end{aligned} \tag{7.17}$$

It is worth studying the behaviour of this equation. We can take three distinct cases: A coherent state, a bunched displaced-squeezed state, and an anti-bunched displaced squeezed state. I choose the coherent state for $\alpha > 0$ and turn off the squeezing $r = 0$. The equation simplifies to $g^{(2)}(\tau) = 1$ for all τ. This is the expected result for a coherent state, and we note that the form of the filter function does not play a role here. Next, we can choose a bunched state, let us say that we turn off the displacement $\alpha = 0$, and have a large amount of squeezing $r \gg 1$. The result is that $g^{(2)}(0) = 3$ and the function for time delay is $g^{(2)}(\tau) = 1 + 2\mathrm{sinc}(\Omega\tau)$, which means that the time-window, in this case a sinc function, is mapped out over the delay. In Figure 7.5 I have made a set of case studies with a fixed squeezing parameter $r = 0.03$, but with varying displacements. The second-order coherence as function of time delay is plotted for each case. For a large displacement, the function is essentially flat at unity, and this is what one would expect for a coherent state. As the displacement is reduced however, anti-bunching appears as a dip in g2 at zero time-delay. Reducing the displacement further brings the state into something that appears coherent at zero time delay ($g^{(2)}(0) = 1$), but for other time delays, the sinc function behaviour is still visible. As the displacement is turned off completely, we see the bunched state.

7.4.3 The extension to mixed Gaussian states

The previous expression can only handle the class of pure Gaussian states (displaced-squeezed states). It is possible to generalise it for any Gaussian state that has the quadrature variances $V_{\mathrm{in}}^+, V_{\mathrm{in}}^-$ and displacement value α_{in}. We do however restrict α_{in} to be real. The subscript 'in' refers to an ideal measurement of the state that could be made prior to the light entering the HBT interferometer, i.e. before the main 50:50 beamsplitter. The analysis using the top-hat frequency window shows that

$$\begin{aligned} g^{(2)}(\tau) &= 1 + 16\mathrm{sinc}(\Omega\tau)\frac{(V_{\mathrm{in}}^+ - 1)\alpha_{\mathrm{in}}^2}{(2 - V_{\mathrm{in}}^+ - V_{\mathrm{in}}^- - 4\alpha_{\mathrm{in}}^2)^2} \\ &\quad + 2\mathrm{sinc}^2(\Omega\tau)\frac{2 + (V_{\mathrm{in}}^- - 2)V_{\mathrm{in}}^- + (V_{\mathrm{in}}^+ - 2)V_{\mathrm{in}}^+}{(2 - V_{\mathrm{in}}^+ - V_{\mathrm{in}}^- - 4\alpha_{\mathrm{in}}^2)^2}. \end{aligned} \tag{7.18}$$

This expression can also handle thermal and biased thermal states. These do not have squeezing on either the amplitude or phase quadratures, but rather have $V_{\mathrm{in}}^+ = V_{\mathrm{in}}^- > 1$ for the thermal state, and $V_{\mathrm{in}}^+ > 1,\ V_{\mathrm{in}}^- = 1$ for the biased thermal state. There is some surprising behaviour in the second-order coherence function for this state when using the top-hat frequency filter. Depending on the input parameters chosen for the biased thermal states, it is possible to see the coherence function approach a value of zero, for *non-zero* time delays. This feels odd because one would expect only such dips of the coherence function below unity for genuinely non-classical states of light. However, there is no such limitation at non-zero time delays, and one can rest assured that the (classical) thermal and biased thermal states do not meet the criteria for photon anti-bunching.

7.4.4 The inferred state is important

We know that the degree of second-order coherence is independent of loss on the input state both before and during detection in the HBT interferometer. But how does this relate to the generalised g2 expression for arbitrary Gaussian states? The subscript ‘in’ for the quadrature variances and displacement refers to an ideal measurement prior to entering the HBT interferometer. What that means is that there is an entire class of Gaussian states that all have the same value for g2. That class can be traced back to an original state that is pure. To find the pure state, we use the property $V^+_{\mathrm{pure}} = 1/V^-_{\mathrm{pure}}$, and solve the loss transformation equation for the loss η and for one of the variances V^+_{pure}. The solution is

$$\eta = \frac{-(V^+_{\mathrm{in}}-1)(V^-_{\mathrm{in}}-1)}{V^+_{\mathrm{in}}+V^-_{\mathrm{in}}-2} \tag{7.19}$$

$$V^+_{\mathrm{pure}} = \frac{1-V^+_{\mathrm{in}}}{V^-_{\mathrm{in}}-1} \tag{7.20}$$

$$V^-_{\mathrm{pure}} = 1/V^+_{\mathrm{pure}} \tag{7.21}$$

$$\alpha_{\mathrm{pure}} = \sqrt{\eta}\alpha_{\mathrm{in}} \tag{7.22}$$

The range of values for η have to lie within $0 \leq \eta \leq 1$ otherwise the resulting variances are unphysical. The quadrature variances that will be measured after the loss are restricted such that either $V^+_{\mathrm{in}} \leq 1$ or $V^-_{\mathrm{in}} \leq 1$. With the aim of demonstrating large anti-bunching, we know that we need a source of weak squeezed light. However, the result from this analysis is that we cannot cheat by starting with an initially strongly squeezed state, that we then apply an optical loss to. The g2 measurement is sensitive to the state before all loss mechanisms.

7.5 Intuitive interpretations in the Fock basis

We have covered much of the behaviour of second-order coherence for various cases of displaced squeezed states. But what is missing is an intuitive explanation for that behaviour. In the next sections I will search for explanations by relying on expansions in the Fock state basis for various limiting cases.

7.5.1 Relationship of anti-bunching to sub-Poissonian statistics

It is well known [Loudon 2000] that the second-order coherence function at zero time delay can be simply expressed in terms of the mean and variance of the *photon number* of a state:

$$g^{(2)}(0) = 1 + \frac{\sigma_n^2 - \mu_n}{\mu_n^2} \tag{7.23}$$

To show an anti-bunching effect, requires that the second term become negative. This will only happen when the photon number variance is less than the mean. This is exactly the definition of a photon number distribution that is sub-Poissonian $(\sigma_n^2 < \mu_n)$. The negative value term grows when the mean photon number approaches zero. Hence, *the strongest anti-bunching effect occurs for a state that is the most sub-Poissonian for the least number of photons.*

The Mandel factor Q gives a normalised measure for the transition from sub- to super-Poissonian, with $Q = (\sigma_n^2 - \mu_n)/\mu_n$, where $-1 \leq Q < 0$ is sub-Poissonian, and $0 < Q \leq 1$ is super-Poissonian. This means that $g^{(2)}(0) = 1 + Q/\mu_n$. The Mandel factor is easily related to the Fano factor $F = Q + 1$. Note that sub-Poissonian states are sometimes called number-squeezed states, which should not be confused with the quadrature-squeezed states that are referred to throughout this thesis.

For our displaced (quadrature) squeezed states, the most sub-Poissonian statistic is not necessarily generated by the strongest squeezing. Stronger squeezing excites ever higher even photon number states, which causes the photon number variance to increase. However, adding a displacement has the effect of re-distributing the excitation of the photon number states such that the variance of the photon number approaches a minimum, which comes at the expense of increasing the mean photon number. This is why a *displaced* squeezed state

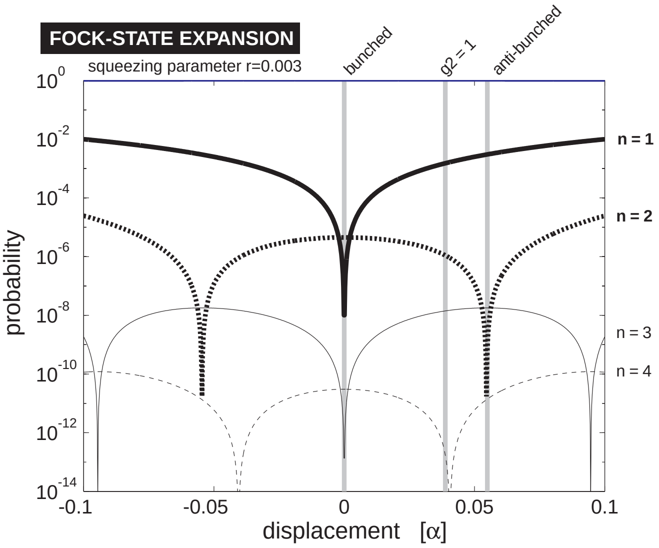

Figure 7.6: A displaced squeezed state with variable displacement, is expanded in the Fock basis for the first few number states. The probability of detecting each state is plotted on the logarithmic vertical axis. For zero displacement, the two-photon state is dominant, and g2 shows bunched statistics. Increasing the displacement then increases the single-photon state until it is dominant, and the two-photon state is suppressed, thus exhibiting photon anti-bunching statistics.

is required to exhibit anti-bunching, and not a squeezed (vacuum) state alone.

7.5.2 An exploration of the 'singularity'

We want to investigate the case of displaced-squeezed states that have quadrature variances and displacements that bring them close to the vacuum state. Weakly displaced squeezed states can be well approximated as a superposition of three Fock states:

$$|\psi\rangle = \Big(c_0|0\rangle + c_1|1\rangle + c_2|2\rangle\Big) \tag{7.24}$$

where $c_{0,1,2}$ can generally be complex coefficients, but I will restrict them to be pure real for this analysis. The second-order coherence from Equation 7.3 can be expressed in terms of the coefficients to get

$$g^{(2)}(0) = \frac{2|c_2|^2}{(|c_1|^2 + 2|c_2|^2)^2} \tag{7.25}$$

We note that the coefficient for the vacuum state does not appear explicitly, but it is hidden within the normalisation restriction. It is important to restrict the coefficients such that the state is normalised. This means fulfilling the condition

$$1 = (|c_0|^2 + |c_1|^2 + |c_2|^2) \tag{7.26}$$

This equation defines the surface of a sphere, so it makes sense to map the g2 function over the surface of a sphere. This is shown in Plate 10. The x-y-z coordinates are scaled by the coefficient for each respective photon number state. The region of validity with weakly displaced squeezed states is only in the immediate vicinity around the $|0\rangle$ 'polar region'. Here, the singularity becomes more pronounced, since the strong cases of bunching and anti-bunching become more densely packed. Furthermore, contours of equal g2 value have another interpretation. Travelling along a line of constant g2 is the same as transforming an initial state by interfering it with a vacuum state on a beamsplitter. This is true since we know that g2 is invariant to optical loss. We can therefore visualise the evolution of a state that is subject to increasing loss. For example, a pure two-photon state will first migrate a fair way toward the single-photon state, before finally plunging into the singularity at the pole.

It is tempting to re-label the axes, such that $|1\rangle$ corresponds to a displacement, $|2\rangle$ to squeezing, and $|0\rangle$ to a loss mechanism. This will only be valid very near to the pole, such that for a squeezing operation, no other even numbered states are excited; and similarly for the higher number states that would surely be excited by a displacement operation. With these caveats in mind, the g2 globe in Plate 10 reduces the system to the essential components that are responsible for the g2 behaviour. For states near the singularity, it is useful to think of the single-photon state as being solely responsible for the anti-bunching; and the two-photon state as being responsible for the bunching. A superposition of the single- and two-photon states (with ample vacuum component) enables us to choose any degree of second-order coherence while approaching the singularity. These ideas can be seen in Figure 7.6. Where Fock state expansion for the first four number states is made for a state that has a fixed (and very weak) squeezing parameter, but as a function of increasing displacement. Where the strongest cases of bunching and anti-bunching occur, supports the idea that for weakly squeezed states, the single-photon state is responsible for anti-bunching, and the two-photon state for bunching.

7.5.3 Another way to approach the 'singularity'

Instead of making a Fock state expansion for displaced squeezed states near the singularity, we can make a series expansion of g2 for weakly displaced squeezed states in terms of small values of α and r. What I am looking for is the relationship between α and r that provides a constant value for g2. Looking at the map of g2 across those parameters in

Plate 10, and looking closely near the singularity, seems to suggest to me that the form of the relationship is quadratic, i.e. something like $r = K\alpha^2$, where K is a constant that needs to be determined. If I plug this form of r into Equation 7.12, and make a series expansion for small $\alpha \ll 1$ up to second order, then we find g2 to be

$$\begin{aligned} g^{(2)}_{\mathrm{lim}}(0) &= (K-1)^2 + (-2K^4 + 4K^3 + 2K^2)\alpha^2 + f(\alpha) && (7.27) \\ &\approx (K-1)^2 && (7.28) \end{aligned}$$

where $f(\alpha)$ contains the terms that are higher than third-order in the expansion, and in the last step I have assumed that the second term can be neglected because α can always be set arbitrarily small. Solving for K then gives $K = 1 \pm \sqrt{g^{(2)}_{\mathrm{lim}}(0)}$ and we have the simple relation

$$r = \alpha^2 \left(1 \pm \sqrt{g^{(2)}_{\mathrm{lim}}(0)}\right) \tag{7.29}$$

which tells us how much squeezing to apply for a given displacement, such that g2 will stay constant. For example, for the state to exhibit complete anti-bunching $g^{(2)}_{\mathrm{lim}}(0) = 0$, then $r = \alpha^2$, and one is free to choose α and make it as small as possible to approach the singularity.

7.6 g2 as a probe for measuring scattering processes

Since g2 is invariant to optical loss, it should make an ideal probe for measuring the optical properties of physical systems. But which properties? A static absorption would not show up in the measurement, nor would a static change of phase. The degree of second-order coherence will only change when the envelope of the wave has been altered through some dynamic process. This occurs for example when coherent light scatters off a collection of small particles that are suspended in a transparent solution. Each particle contributes a small change in amplitude and phase to the original wave. And since the particles are moving randomly under Brownian motion, the amplitude and phase of the light will fluctuate over time. Therefore comparing the intensity at two vastly different times would show less correlation than for a similar measurement that would be made at two closely spaced time intervals. The coherence function over the time delay reveals information about the rate of the de-phasing of the wave, and hence about the physical system that is causing the scattering.

A two-photon absorption process depends on the second-order coherence of the probe beam [Loudon 2000]. The two-photon absorption process is suppressed for anti-bunched light, and enhanced for bunched light, in comparison to a coherent state (and with all three cases having the same mean number of photons in the beam). Perhaps these states could be used to investigate two-photon processes in various system. I can also speculate that anti-bunched light has the potential to improve the performance of optical coherence tomography, compared with the currently used sources such as LEDs.

7.7 Relationship between g2 and entanglement

I want to test the idea of whether g2 and entanglement are properties of light that are related to each other. I will approach the problem from two directions: (1) to study the sources of light, and (2) to examine the measurement instrument.

7.7.1 The instrument: first- and second-order correlations

There is a remarkable similarity between the schematic of an experiment to measure anti-bunching using homodyne detectors, and an experiment to measure biased entanglement from a single squeezed state. For the biased entanglement experiments, a squeezed light source is sent onto a 50:50 beamsplitter to mix it with a vacuum state. The two output beams are then received by two homodyne detectors. The setup for measuring anti-bunching in the second-order coherence of a state likewise begins by mixing the input state (a displaced-squeezed state) on a 50:50 beamsplitter with a vacuum state, and the output light is likewise received by two homodyne detectors. The setups for the two experiments are identical. The difference is how the quadrature information is processed to yield either the degree of second-order coherence, or the inseparability measure.

The difference in the data processing for each experiment, can be summarised in the first- and second-order correlation matrices. For an entanglement measurement, we only need access to the elements of the first-order matrix. The elements of this matrix are for example

$$C_{ab}^{+-} = \langle \delta \hat{X}_a^+ \delta \hat{X}_b^- \rangle = \langle \hat{X}_a^+ \hat{X}_b^- \rangle - \langle \hat{X}_a^+ \rangle \langle \hat{X}_b^- \rangle \tag{7.30}$$

And likewise for the other combinations of the superscripts $+, -$ and subscripts a, b. From these elements it is possible to extract the inseparability criterion for entanglement (see Section 2.9.3). We can compare this situation with the second-order correlation matrix which is made up of the elements:

$$D_{ab}^{+-} = \langle (\hat{X}_a^+)^2 (\hat{X}_b^-)^2 \rangle \tag{7.31}$$

It is these elements that are used to re-construct the second-order coherence function according to Equation 7.5. Unlike the first-order correlation elements, the second-order correlation elements do not have their mean values subtracted. They also lack the positive/negative information, as this is erased when the square of the quadrature amplitudes is taken. However, with the assurance of the similarity of the two experiments (except for the data processing), we can now look for similarities in the states of light themselves.

7.7.2 The source: anti-bunching vs. entanglement

Entanglement is a two-mode phenomenon, whereas second-order coherence is the property of a single-mode. To make a comparison, I need to consider second-order coherence as being measured using a HBT interferometer, with two detectors, which transform the anti-bunched state into a two-mode correlation experiment. So from now on, when I refer to the analysis of anti-bunching as an entanglement, what I really mean is an anti-bunched single mode state that has been transformed into two modes via a 50/50 beamsplitter. Let us choose the extreme anti-bunched case of a super-position of a single photon with vacuum state $|\psi_{\text{in}}\rangle_a \approx (|0\rangle_a + \zeta|1\rangle_a)$, where $\zeta \ll 1$. This could have been prepared by the method of weak squeezing and weak displacements. The state is then coupled with a vacuum state on a 50:50 beamsplitter. The entangled state on modes b and c, will look like

$$|\psi_{\text{out}}\rangle \approx |0\rangle_b|0\rangle_c + \underbrace{\zeta|1\rangle_b|0\rangle_c + \zeta|0\rangle_b|1\rangle_c}_{\text{detectable}} \tag{7.32}$$

where I am ignoring any probability amplitudes or normalisations. The underbrace shows what components can be measured using a pair of conventional single-photon counters. This component is one of the Bell states, which is a maximally entangled state in the Fock basis. However, if we look at the quadrature amplitudes of this state, it is quite unremarkable. The Wigner function would look mostly like the two-dimensional Gaussian distribution of a vacuum state, but the single-photon state component will cause the distribution to be slightly broadened. As such, the quadrature variances for phase and amplitude as measured on each output of the beamsplitter, give values that are greater than one. Correlation measurements made between the two outputs would show only a slight EPR entanglement effect with the degree of EPR being only slightly less than unity (see Chapter 2), nevertheless the two-mode state still shows entanglement. The exact value of the degree of EPR depends on the chosen value of ζ. Note that the inseparability criterion cannot be applied to this state because it has a non-Gaussian Wigner function.

Let us look at the opposite case by starting with a strongly squeezed state that has an appropriate displacement, such that it gives the best anti-bunching statistic possible for the given squeezing factor. The solution for the displacement α that shows the minimum g2 value, when fed with the squeezing parameter r is

$$\alpha = \frac{\sqrt{\exp(r)\sinh(2r)}}{\sqrt{2\cosh(r) - 2\sinh(r)}} \tag{7.33}$$

For example, given $r = 3$ we get $\alpha = 202$. Note that this state has a degree of second-order coherence of $g^{(2)}(0) = 0.999988$ which is only very weakly anti-bunched. An expansion in the Fock basis, before the beamsplitter, reveals almost a complete absence of the single-photon component, which can be considered responsible for the anti-bunching effect. Examining the state after the beamsplitter, reveals a highly mixed state, but one that contains only a minute component of the pure Bell state. From the discrete-variable point of view, this state is not very interesting because it is only weakly anti-bunched, and practically useless for performing Bell tests of hidden variables. On the other hand, the continuous-variable experimentalist who has access to the quadrature amplitudes of the two modes, finds very strong correlations between them. For this particular numerical example,

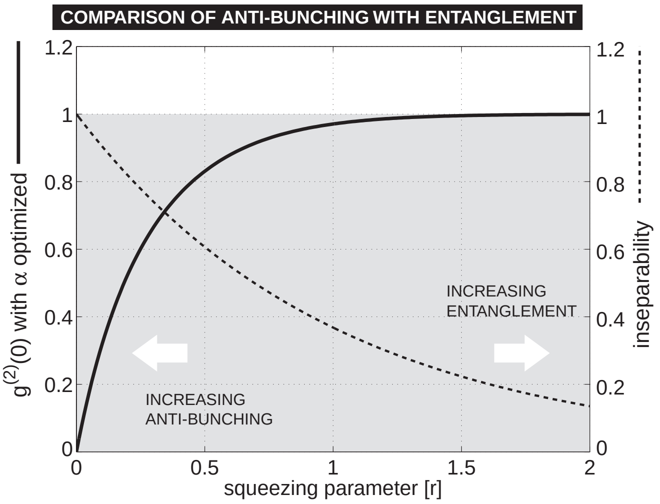

Figure 7.7: A squeezed state is given a displacement that optimises the anti-bunching effect. The second-order coherence is plotted as a function of the squeezing parameter. The same state is sent through a 50/50 beamsplitter. The resulting biased entanglement is confirmed by the inseparability criterion. Notice how the strongest anti-bunching effect occurs for weak squeezing, compared with the strongest entanglement at strong squeezing.

the measured EPR would be $\varepsilon = 0.00991$, which is very close to zero, and is considered to be a very strong level of entanglement.

We have seen two extreme examples for which the anti-bunching and entanglement appear to be disparate. However, I can show that one property cannot appear without the presence of the other, albeit in a very weak degree. I restrict the analysis to the class of pure displaced-squeezed states, so that we can already use the expression for second-order coherence in Equation 7.12. I will assume that the displacement α is made a function of the squeezing parameter r, such that the degree of second-order coherence is minimised. Hence we have only one free parameter, r. The expression for the optimised second-order coherence of this state is

$$g^{(2)}(0) = 1 - 2/\left[\exp(4r) + 2\exp(2r) - 1\right] \qquad (7.34)$$

The state is then sent through the 50:50 beamsplitter where it couples with a vacuum mode, such that two new modes are created. The two-mode entangled state that is created, is Gaussian, and hence we can use the inseparability criterion to check for the presence of entanglement. The expression for inseparability as a function of squeezing parameter is

$$\mathcal{I} = \begin{cases} \sqrt{V_{\min}} & , V_{\min} < 1 \\ 1 & , V_{\min} \geq 1 \end{cases}$$

Where the minimum of either the phase or amplitude quadrature variance is chosen: $V_{\min} = \min\{V^+, V^-\}$. Plotting g2 and inseparability together in Figure 7.7 we can see that both entanglement and anti-bunching is witnessed for all values of r. We can extend the analysis to mixed states by letting the initial state first pass through an optical loss mechanism, which couples in another vacuum mode. For g2 we know that the result is unchanged, however, for entanglement, the degree of inseparability approaches unity in the limit of complete loss. But however much loss we apply, there is still some entanglement remaining. A whole class of mixed Gaussian states can be generated in this way, but they are limited by $V^+ \leq 1$ and $V^- \geq 1$ (or the other way round). We can conclude that for an initial state that is Gaussian, but mixed, having arbitrary $V^+ \neq V^-$, that anti-bunching and entanglement are properties that always occur together.

What about the general case? If the initial state is Gaussian, but not quadrature squeezed, then there can not be any entanglement produced after the beamsplitter. And because we also know that such a state cannot exhibit anti-bunching, we know that the absence of anti-bunching and the absence of an equivalent entanglement go hand in hand.

The conclusion is that anti-bunching and quadrature entanglement are related, but take their place at opposite ends in the limits of small and large mean photon numbers, respectively. We can say, that for every two-mode Gaussian entangled state there is an associated photon anti-bunched state. Or we can say the converse: every Gaussian anti-bunched state will create entanglement when it is sent onto a 50:50 beamsplitter and coupled with a vacuum state.

7.8 Summary

The intensity interferometer of Hanbury-Brown and Twiss can be adapted so as to work using homodyne detection rather than detectors that are sensitive to single-photon counts. The homodyne version has the advantage of being only sensitive to an input mode that is identical to the local oscillator mode: in terms of wavelength, transverse spatial function, and polarisation. The setup is ideal for measuring the coherence of displaced squeezed states of light. These states were characterised for their bunching and anti-bunching behaviour. The behaviour was interpreted using an expansion in the Fock basis, where only the first three members: vacuum, single- and two-photon number states, were needed to explain their behaviour in the second-order coherence. The theoretical results that were gained here, lend themselves very well to an experimental test. Such an experiment is presented in the next chapter.

Chapter 8

Photon Anti-bunching from Squeezing: Experiment

This chapter details an experiment that was conducted to test the two main hypotheses that were proposed in the previous chapter: (1) Second-order coherence can be measured using homodyne detection. (2) Displaced squeezed states can exhibit photon anti-bunching statistics. The construction and operation of the experiment was a collaborative effort between Dr. Thomas Symul and myself. The results showed good agreement with the theoretical predictions, and thereby provided support for the main hypotheses.

Together with the theoretical work already discussed in Chapter 7, the experimental results that are presented here have been published under the following reference:

- *Measuring Photon Anti-bunching from Continuous Variable Sideband Squeezing,*
  N. B. Grosse, T. Symul, M. Stobińska, T. C. Ralph and P. K. Lam,
  Phys. Rev. Lett. **98**, 153603 (2007).

8.1 Overall design considerations

The layout of the experiment can be divided into two parts: preparation of the displaced-squeezed state, and detection using the homodyne version of the HBT interferometer; see Figure 8.1. The source of squeezed light in the experiment was an optical parametric amplifier (OPA). The displacement of the squeezed state was made using the interference with an auxiliary amplitude modulated light beam.

The main challenge in this experiment was subtle. Usually, one seeks to maximise the strength of a squeezed light source, however, the best anti-bunching effect was predicted to occur for the weakest squeezing. Since the source of squeezed light is based on an OPA,

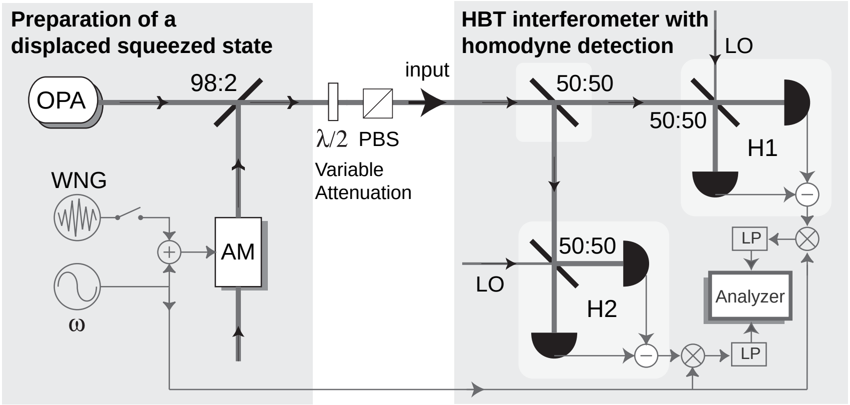

Figure 8.1: Schematic of the experimental setup. OPA optical parametric amplifier, $\lambda/2$ half-wave plate, PBS polarising beam-splitter, x:y beamsplitter with transmission x, H1/H2 homodyne detectors, AM amplitude modulator, ω function generator, WNG white noise generator, $\otimes$ mixer, LP low pass filter.

then this would not normally present a challenge to the experimentalist. This is because one only needs to reduce the pump power to just a fraction of a percent of the OPO threshold power, in order to get very weak (and pure) squeezed light. The main problem associated with doing this, is that one loses the signal-to-noise ratio (SNR) of the error signals that are required to control the phases of the interferometer in the experiment. Without the control, the homodyne detectors would not measure precisely the amplitude or phase quadratures, and an accurate reconstruction of the second-order coherence function would not be possible. The conclusion was to find a compromise between having the OPA operate at the lowest pump power that still enabled an acceptable level of stability in the servo-control loops. Other considerations were to use homodyne detectors that had a good clearance of shot noise above dark noise. This allows one to acquire a good SNR for measurements of the quadrature amplitudes and their second-order correlations.

8.2 Experimental setup

The general experimental techniques were very similar to those described in Chapter 4 on the harmonic entanglement experiment. A major part of the experiment had been constructed by W. P. Bowen and R. Schnabel. They set up the laser and its stabilisation, and the second harmonic generator that pumped the OPA that generated the squeezed light. This setup can be considered as a facility for squeezed light. It is described in detail in

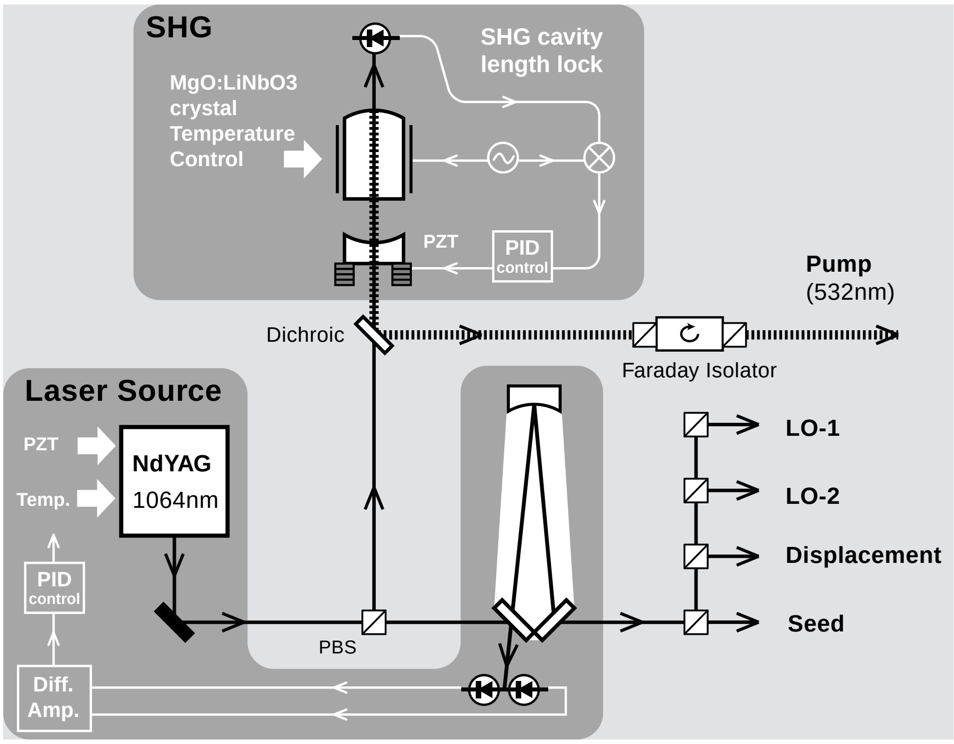

Figure 8.2: A detail of the laser source and the second-harmonic generator (SHG). The laser frequency was held onto the mode-cleaner resonance using tilt-locking, where the error signal was derived from the subtraction of a two-element photodiode. The mode-cleaner provided a TEM00 mode, and also low-pass frequency filtered the light to obtain a shot-noise limited beam above 6 MHz. The SHG was held on resonance using an RF dither-locking technique. The SHG conversion efficiency was maximised by adjusting the phase matching temperature.

[Bowen *et al.* 2002]. The second-order coherence experiment can be considered as an application of the squeezed light source. The off-line displacement to the squeezed light source, the dual homodyne detectors, the extra servo-control loops, and together with the data acquisition system, were built, aligned and operated by Dr. T. Symul and myself.

8.2.1 Preparation of laser light

The experiment was built using all free-space optics that were mounted on an actively damped bench. The source of light for the entire experiment was a Nd:YAG laser operating at 1064 nm and producing 1.5 W of continuous-wave light. The linewidth of the laser was specified by the manufacturer (Innolight) to be 1 kHz. A major fraction of the light was sent to a second-harmonic generator which doubled the frequency to produce about 600 mW of 532 nm light; see Figure 8.2. The 532 nm light was used to pump an OPA. The remaining 1064 nm light was filtered by transmitting it through an optical resonator that had a linewidth of several hundred kHz. This produced a clean TEM00 mode and also provided some filtering of the laser relaxation oscillation. Light from this beam was tapped off to provide the seed beam, displacement beam, and the local oscillators for the homodyne detectors.

8.2.2 The squeezed light source

The OPA was based on a $\chi^{(2)}$ nonlinear crystal of the material $\mathrm{LiNbO_3}$ doped with 7% MgO. One end of the crystal was cut and polished to a convex shape and coated for a high reflectivity (HR) for 532 nm and 1064 nm. The other end was polished flat and was anti-reflection coated for both wavelengths; see Figure 8.3. A stable resonator geometry was formed by the alignment of an external concave mirror (the ‘coupling mirror’), having an intensity reflectivity of 94% at 1064 nm and less than 5% for 532 nm. A ‘seed’ beam of 1064 nm was mode-matched into the 35 micron waist of the resonator through the convex end of the crystal. From the reflected light, a Pound-Drever-Hall type error signal was extracted, which was used to control the round-trip optical path length of the resonator, by way of PZT actuation of the coupling mirror position.

The 532 nm pump beam was mode-matched into the resonator through the coupling mirror. The phase of the pump relative to the seed was controlled via an external PZT actuated mirror. Monitoring the seed beam that was transmitted through the cavity, showed alternating amplification and de-amplification when the phase of the pump was scanned. The relative phase of the seed and pump was locked using a dither lock from a phase modulation on the pump beam. This was measured by using the reflected seed beam from the OPA cavity. The gain of the OPA was maximised by tuning the phase-matching condition of the nonlinear crystal, which was adjusted by an servo-control of the temperature, to a precision of several tens of milli-Kelvin.

The pump power could be set to give a de-amplification factor of the seed beam (measured in transmission) ranging from 0.9 to 0.5. The resulting beam of light had an optical power of $\sim 5\,\mu\mathrm{W}$. Measurement of the quadrature amplitudes using a homodyne detector revealed that the light was amplitude squeezed over a range of sideband frequencies: from 3 MHz up to the OPA cavity linewidth of 15 MHz. The level of squeezing was optimum at

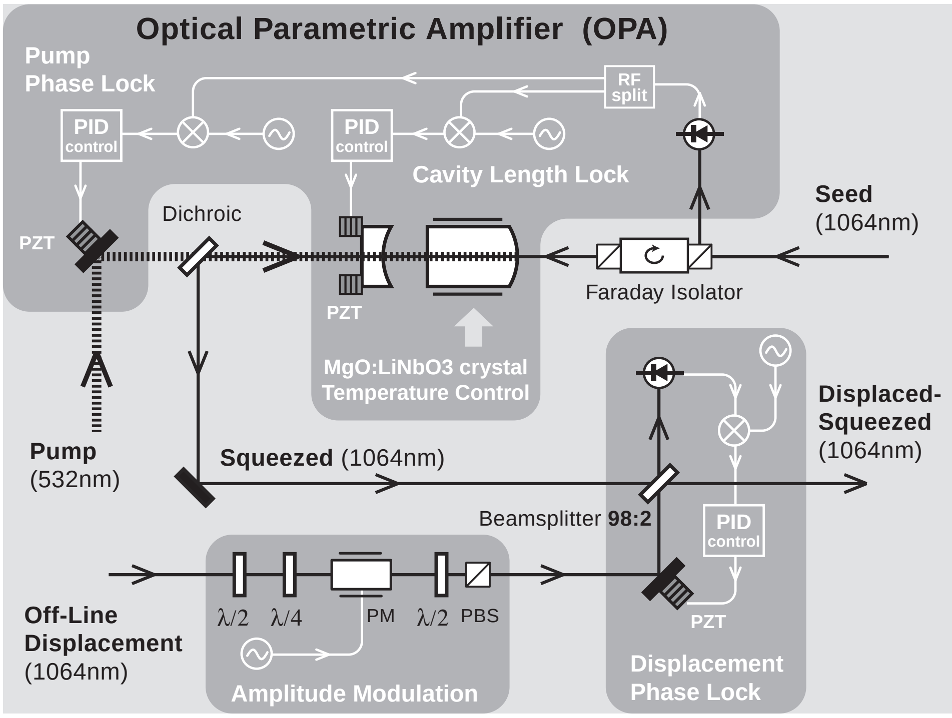

Figure 8.3: A detailed schematic of the generation of the displaced-squeezed beam. The source of squeezed light was based on an OPA that de-amplified the seed beam. The displacement was created 'off-line' by interfering the squeezed beam with an auxiliary light beam that was given amplitude modulation sidebands.

the sideband frequency of 6 MHz, where the level of squeezing could be adjusted via the pump power, to lie in the range of $V_{\rm in}^{+} = 0.89$ to $V_{\rm in}^{+} = 0.55$, with values of the purity of the state $(V_{\rm in}^{+}V_{\rm in}^{-})$ ranging from 1.005 to 1.18, respectively.

8.2.3 Preparing the displacement

An auxiliary beam was prepared with an amplitude modulation using a conventional amplitude modulator. This beam, the displacement beam, was interfered with the squeezed beam on an asymmetric 98:2 beamsplitter; see Figure 8.3. The squeezed beam was transmitted through the beamsplitter with 98% efficiency. The relative phase of the displaced and squeezed beams was actively controlled, such that their coherent amplitudes were in phase, and the angle of the squeezing ellipse remained in the amplitude quadrature. The amplitude modulator could be driven with either a sinusoidal voltage source at 6 MHz, or with a broadband Gaussian noise source. The former gave a displacement in the amplitude quadrature at the 6 MHz sideband frequency, and the latter simulated a biased thermal state.

The state was biased because the phase quadrature was not randomly displaced. The optical power in the displaced beam was chosen, such that it nearly matched the optical power in the squeezed beam, after reflection from the 98% beamsplitter. This reduced the optical power in the squeezed beam to approximately $1\,\mu\mathrm{W}$.

8.2.4 Intensity interferometer using homodyne detection

The displaced-squeezed state was mixed with a vacuum state on a 50:50 beamsplitter; see Figure 8.4. The light from each output port of the beamsplitter was received by two independent homodyne detectors. Each homodyne detector consisted of a 50:50 beamsplitter, on which the displaced-squeezed beam was mode-matched with a local-oscillator (LO) beam to a fringe visibility of 96%. The ratio of optical power in the LO compared with the signal beam was 1000:1. On each output arm of the beamsplitter, the light was focussed down to fill the area of the photodiode (ETX500). The total quantum efficiency of the homodyne detector was estimated to be 86%. The photocurrents from the two photodiodes were subtracted from one another to give a signal that was proportional to the quadrature amplitudes of the signal beam. The quadrature angle was determined by the relative phase of the LO with the signal beam. This was actively controlled by adjusting the optical path length of the LO. An error signal to lock to the phase quadrature was obtained by nulling the difference of the low-pass filtered (DC to 20 kHz) photocurrents. The lock to the amplitude quadrature was accomplished by demodulating the phase modulation that was left over from the PDH locking of the OPA cavity length. The design of the second homodyne detector was identical.

8.2.5 Signal processing

The electronic signals from each homodyne detector were band-passed and amplified, mixed-down at 6 MHz, and low pass filtered with an anti-aliasing filter at 100 kHz; see Figure 8.4. A digital-to-analogue converter then over-sampled the signal at a rate of 240 kS/s and recorded the data as a time series on the computer. The next stage was to apply a digital top-hat filter with a cut-off at 120 kS/s. This was to ensure a flat power spectrum, because it is this filter shape that later determined the form of the $g^{(2)}(\tau)$ function. Next,

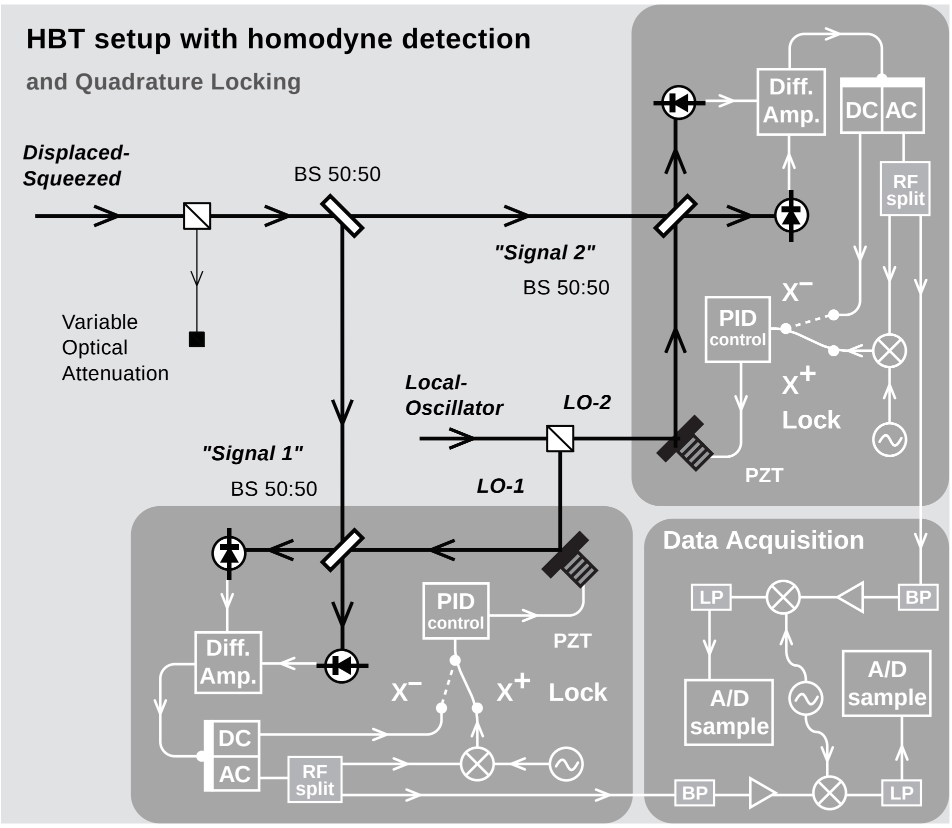

Figure 8.4: A detailed schematic of the HBT interferometer that has been modified for homodyne detection. The local-oscillators were interfered with the 'signal' beams which came from the main 50:50 beamsplitter (BS) that split the displaced-squeezed state. The phases of the local oscillators were controlled such that the homodyne detector was sensitive to either the amplitude or phase quadrature. The resulting signals were mixed-down at a frequency of 6 MHz, before being digitally sampled.

the variances and correlation coefficients of the four permutations of amplitude and phase quadrature measurements were calculated from $\approx 10^6$ data points that were acquired over a total of 10 successive runs. The uncertainty in each measurement, defined at the 68% confidence interval, was calculated using the usual statistical methods of error analysis; see for example [Skoog 1985].

8.2.6 Experimental procedure

The experiment was done according to a strict procedure of alignment and characterisation of the mode-matching or visibility of the beam paths, followed by the data acquisition. The steps in the procedure are given here:

- **Begin the alignment procedure.** Mode-match the 1064 nm laser light into the SHG and mode-cleaner. Lock laser frequency to mode-cleaner resonance, and lock SHG cavity length to laser frequency.
- Maximise the 532 nm power output of the SHG by adjusting the phase-matching temperature of the SHG crystal.
- Align the seed beam into the OPA cavity. Check that the lock-point is centred at the cavity resonance.
- Align the 532 nm pump to the OPA by scanning the phase of the pump and maximising the gain of the seed as observed in transmission. Check that the lock is stable for de-amplification.
- Mode-match each LO with the squeezed beam. Check fringe visibility. Mode-match the off-line displaced beam (squeezed beam blocked) with each LO. Check fringe visibility.
- Null the (DC derived) phase quadrature lock of the homodyne detector by making it immune to intensity fluctuations. Null the (RF derived) amplitude quadrature lock of the homodyne detector.
- Use the homodyne detector to check that the modulation on the displacement beam is a pure amplitude modulation.
- Choose the level of squeezing via the pump power, and the depth of modulation on the displacement beam. Lock all loops in order: OPA cavity, pump phase, displacement beam phase.
- **Begin the measurement sequence.** Lock to amplitude-amplitude quadratures on the two homodyne detectors, record data. Repeat for other quadrature permutations. Take shot noise measurements before acquiring each member of the permutation, and take a dark noise measurement at the conclusion of the run.
- Choose another set of squeezing and displacement settings. Repeat the measurement sequence.

8.2.7 Variable experimental parameters

There was a set of experimental variables that we could choose in a controlled manner. We were free to adjust the amount of displacement or broadband noise that was added to the squeezed beam. The squeezing strength and purity were linked together by the intra-cavity loss and seed-coupling mechanism of the OPA. Some control however, was possible by independently varying the pump and seed powers that were going into the OPA. Additional optical loss could also be introduced to the displaced-squeezed state prior to entering the HBT interferometer. Finally, the electronic signals of each homodyne detector could be given a time delay with respect to one another: both before and after the digital sampling.

8.3 Experimental results

Photon anti-bunching statistics from a displaced-squeezed state were confirmed by the experimental results. Studies were also made for coherent states, and biased thermal states.

8.3.1 Coherence as a function of time delay

The definition of photon anti-bunching is not just $g^{(2)}(0) < 1$ alone, but one also needs to show that $g^{(2)}(\tau) > g^{(2)}(0)$ for all $\tau \neq 0$. Note that for stationary light sources, where the statistical properties remain constant over time, one is guaranteed that $g^{(2)}(\tau) \to 1$ as $\tau \to \infty$. To calculate the coherence over all time is not reasonable, so we tested it over a range of ten units of the inverse measurement bandwidth, which was deemed sufficient.

We prepared a weakly squeezed state that had variances $\{V_{\text{in}}^{+} = 0.902(1); V_{\text{in}}^{-} = 1.137(1)\}$. The state was then displaced by an amount $\alpha_{\text{in}} = 0.257(1)$, which was the amount predicted to minimise $g^{(2)}(0)$ for that particular squeezed state. Figure 8.5(i) shows the measurements over the range of time delays. The minimum value of the coherence was found at zero time delay $g^{(2)}(0) = 0.44(22)$. As τ was increased, the coherence produced some oscillations but approached unity, thereby fulfilling the requirements to demonstrate photon anti-bunching.

8.3.2 Coherence as a function of displacement

As already discussed in the theory (Chapter 7), the photon number distribution of a squeezed state can be manipulated from predominantly even to odd photon number states, simply by changing the displacement. In this sense, it is the displacement that controls the anti-bunching effect for a given squeezing parameter.

For this study, the time delay was set to zero, and a squeezed state was prepared that had $\{V_{\rm in}^{+} = 0.901(3); V_{\rm in}^{-} = 1.136(1)\}$. Measurements of the degree of second-order coherence ('g2') are shown in Figure 8.6(i). Super-bunching statistics of $g^{(2)}(0) = 28(10)$ were found for this state, which had zero displacement (measured to be $\alpha_{\rm in} = 0.001(2)$). The displacement was then increased until the degree of coherence was minimised to $g^{(2)}(0) = 0.41(12)$ thus showing anti-bunching statistics. Increasing the displacement still further, then made the g2 monotonically increase toward one. Therefore by changing only the displacement, we could observe a factor of 70 change in the value of g2: from super-bunching to anti-bunching.

8.3.3 The best anti-bunching statistic

The theoretical predictions tell us that lower levels of pure squeezing should give even stronger anti-bunching statistics. We prepared a very nearly pure state, that had variances $\{V_{\rm in}^{+} = 0.890(2); V_{\rm in}^{-} = 1.129(2)\}$, and a purity of $V_{\rm in}^{+} \times V_{\rm in}^{-} = 1.005(3)$. This was achieved by reducing the optical power of the seed beam that entered the OPA, which helped to de-couple extraneous noise sources. The degree of second-order coherence was measured for a small range of displacements. The results are shown in Figure 8.6(ii). The minimum value for the coherence was found for a displacement of $\alpha_{\rm in} = 0.252(2)$, for which $g^{(2)}(0) = 0.11(18)$. This is a strong anti-bunching statistic. For comparison, a pure two-photon Fock state would be limited to $g^{(2)}(0) = 0.5$.

8.4 Testing the HBT interferometer

Although the results with the displaced squeezed states were adhering to the theoretical predictions, it was good to test our HBT interferometer with two other classes of states, and

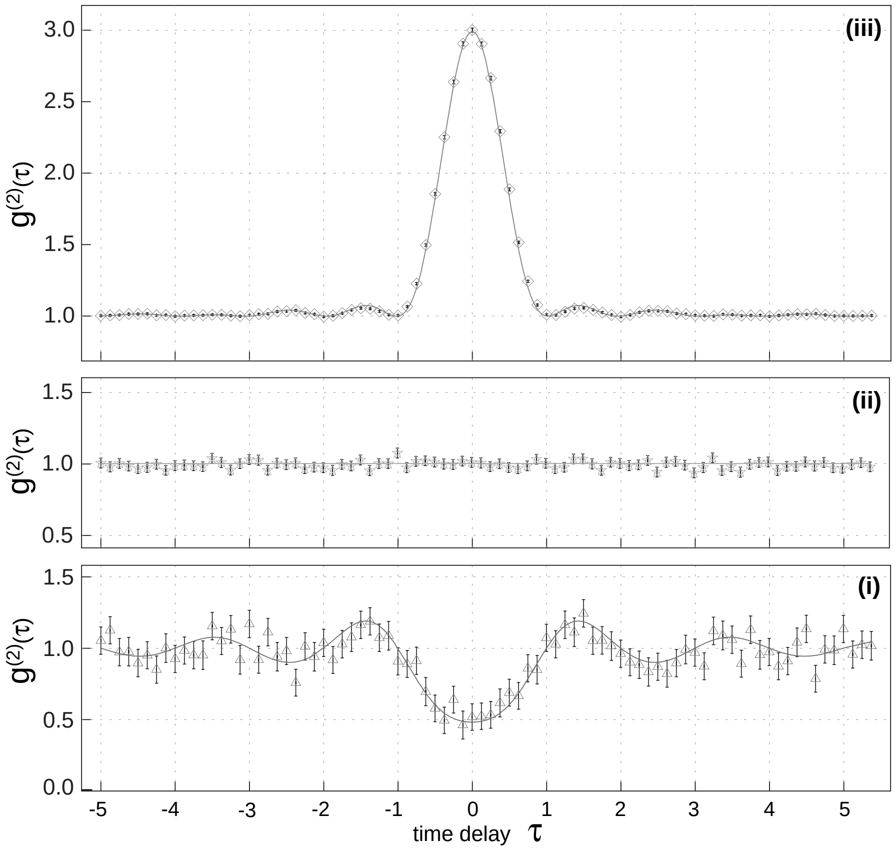

Figure 8.5: Experimental measurement of $g^{(2)}(\tau)$ with normalized time delay τ in units of bandwidth $(\pi/\Omega = 8.3\ \mu\mathrm{s})$. (i) displaced squeezed state, (ii) coherent state, (iii) biased thermal state, curves are theoretical predictions.

also for the property of invariance to optical loss.

8.4.1 A coherent state

The theoretical prediction for a coherent state is $g^{(2)}(\tau) = 1$, regardless of the size of the displacement, and independent of the time delay τ. The experimental results for zero time delay and variable displacement are shown in Figure 8.5(iii), while the results for a fixed displacement and variable time is shown in Figure 8.6(ii). Both sets of measurements yielded a second-order coherence that kept within $g^{(2)}(\tau) = 1.00(6)$, thus confirming the expected value of g2, and therefore validating our experimental setup.

8.4.2 A biased thermal state

A biased-thermal state starts out as a coherent state, but has had its amplitude quadrature modulated with broad-band noise, thus giving $\{V_{\text{in}}^{+} > 1; V_{\text{in}}^{-} = 1\}$, while the displacement α_{in} is allowed to be arbitrary. The prediction for the second-order coherence at zero time delay is $g^{(2)}(0) = 3$ when $V_{\text{in}} \gg 1$ and for small displacements $\alpha_{\text{in}} \approx 1$. We prepared a biased-thermal state that had $\{V_{\text{in}}^{+} = 12.80(9); V_{\text{in}}^{-} = 1.039(1)\}$. The displacement was varied from zero to $\alpha_{\text{in}} = 0.65(1)$. The results are plotted in Figure 8.6(iv). These showed that the second-order coherence adhered to the theoretical prediction by not deviating from $g^{(2)}(0) = 2.98(1)$.

A biased thermal state was also studied under variable time delay. The state had parameters $\{V_{\text{in}}^{+} = 14.60(2); V_{\text{in}}^{-} = 1.025(8); \alpha_{\text{in}} = 0.258(1)\}$. The results are shown in Figure 8.5(iii). At zero time delay, the function was at a maximum $g^{(2)}(0) = 2.98(1)$, but then fell towards unity as τ was increased. The form of the curve followed the sinc-squared curve that comes from the Fourier transform of the top-hat frequency window.

8.4.3 Testing the invariance to optical loss

One of the interesting properties of second-order coherence, is that measurements of it are immune to optical loss both before the measurement instrument, and within the measurement instrument itself. We endeavoured to test this property by introducing a variable loss mechanism in the form of a variable reflectivity beamsplitter; see Figure 8.4.

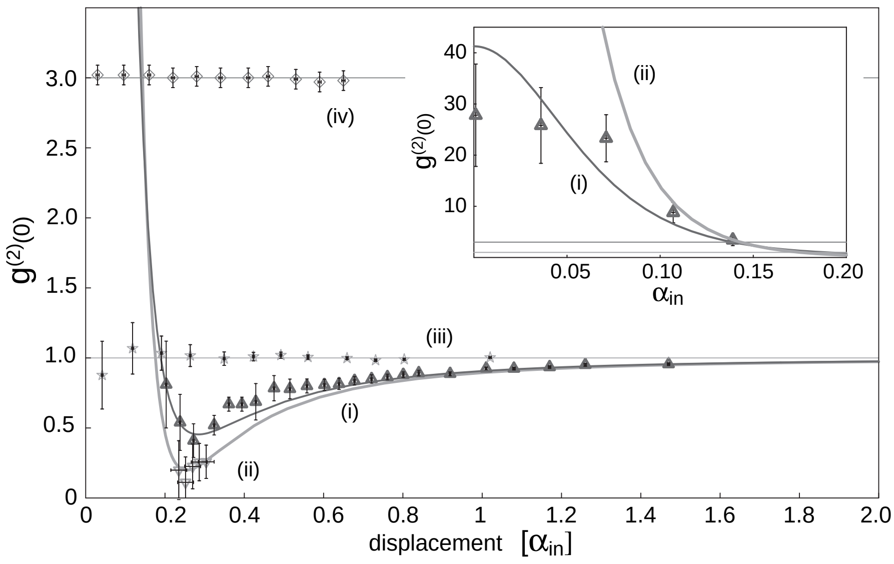

Figure 8.6: Main figure and inset: Experimental measurement of $g^{(2)}(0)$ as a function of displacement $\alpha_{\rm in}$. (i) displaced squeezed state, (ii) weak displaced squeezed state, (iii) coherent state, (iv) biased thermal state, curves are theoretical predictions.

We prepared a displaced-squeezed sate that initially was measured to have $\{V_{\rm in}^{+} = 0.894(2); V_{\rm in}^{-} = 1.139(2); \alpha_{\rm in} = 0.255(2)\}$ using the (maximum available) total detection efficiency of $\eta = 86\%$. Without any optical attenuation, the second-order coherence was found to be $g^{(2)}(0) = 0.67(16)$. The attenuation was increased up to $\eta_{\rm det} = 43\%$ which yielded $g^{(2)}(0) = 0.43(36)$. This showed that at least to the confidence interval of the measurement, $g^{(2)}$ was invariant to optical loss prior to the HBT interferometer. The invariance, however, came at the cost of increasing the uncertainty in the measurement.

8.5 Discussion of results

8.5.1 Adherence to theoretical predictions

One question to address is: do the experimental results agree with the theory for a HBT interferometer that is based on homodyne detection? All the theoretical curves that have been presented alongside the results have not been best fits to the data, but rather, have been curves that were generated by Equation 7.17. The equation was fed with the three measurements that define the displaced-squeezed states: $\{V_{\rm in}^{+}; V_{\rm in}^{-}; \alpha_{\rm in}\}$. These measurements were obtained from one of the homodyne detectors, with an inference made for the (main) 50:50 beamsplitter of the HBT interferometer. Of course the second-order coherence measurement implicitly uses the quadrature variances and displacement, but these were contained in the second-order correlations of the quadrature measurements. We did not have the resources to make an independent test with a conventional HBT interferometer that uses single-photon counting detectors. Actually this would have required the installation of many light baffles and optical frequency filtering, in order to reduce contributions of light from other parts of the lab. Homodyne detection makes these precautions redundant, because the mode of the local oscillator selects these for us. So the best that we could do to test our interferometer, was to get a type of transfer function of our instrument by measuring the second-order coherence for a large range of input states: both classical and nonclassical.

For example, using a squeezed state, we were able to observe the transition from bunching to anti-bunching just by increasing the displacement on the squeezed state. We also demonstrated the time domain behaviour, as evidence by the Fourier transform of a flat pass-band filter, namely, a sinc function. Two other kinds of state were tested, the biased thermal and the coherent state. Like the displaced-squeezed states, these two states also showed good agreement with the theoretical predictions of second-order coherence for those states: both as a function of displacement, and as a function of time. We can conclude then that our version of the HBT interferometer that was based on homodyne detection, was performing well.

8.5.2 Limitations of the experimental setup

If the aim of the experiment was to demonstrate a very large anti-bunching effect, then two limitations of our setup become apparent. The first deals with the generation of the squeezed state, and the second deals with the homodyne detectors.

To show a larger anti-bunching effect with smaller values of $g^{(2)}$ requires squeezed states that are ever weaker and purer. In principle this should not be an issue, because the level of squeezing is set by the pump power of the OPA. But the level of control becomes difficult because the signal-to-noise ratio of the error signals for the control loops (the cavity length, and the pump phase) both scale with the gain of the OPA, which depends on the pump power. So there is a practical limit to the minimum OPA gain that still allows a stable lock of the cavity length and the pump phase. Remember that it is the equivalent pure squeezed state that determines the second-order coherence. What this means is that intra-cavity losses of the OPA do indeed play a role in measuring coherence, but only in the sense that a high intra-cavity loss will require more gain in order to provide an error signal of sufficient strength. The extra gain required by an optically lossy OPA, will then be manifested as an excess noise on the anti-squeezed quadrature, for the chosen level of squeezing. In other words, the state of light that exits an OPA with high loss, has a higher impurity, than for an OPA with low loss, although both OPAs could be set to produce the same level of squeezing.

The issue of the small signal-to-noise ratio of the error signals could be solved by increasing the seed power that goes into the OPA. The problem is that the seed and pump beams are usually not exactly shot-noise-limited (even at 6 MHz sideband frequencies). By turning up the seed power, the noise on the pump and seed beams is coupled ever more strongly into the output squeezed beam. It is therefore wise to keep the seed power low. It is for these reasons that a compromise had to be found for the minimum optical powers driving the OPA and extracting useful error signals.

The second limitation of the experiment was in the homodyne detector itself. In principle, the measurement on a homodyne detector yields the quadrature amplitudes of the signal beam. In a balanced homodyne detector, the noise on the local oscillator beam is cancelled. However, this is only true in the limit that the power in the local oscillator beam is arbitrarily greater than the power in the signal beam. This ratio was 1000:1 in our experiment. For example, the quadrature variance that would be measured on this homodyne detector could be written as $V^+_{\rm meas} = P_{\rm LO}V^+_{\rm sig} + P_{\rm sig}V^+_{\rm LO}$. Even if the LO were shot-noise limited $V^+_{\rm LO} = 1$, this would lead to a minimum variance (normalised to the shot noise level) which could be resolved would be $V_{\rm min} = 1 + P_{\rm sig}/P_{\rm LO}$. In our case, this would have been a variance of $V_{\rm min} = 1.001$. None of the coherent states that we measured fell below this limit.

A technique to circumvent this limitation would be to minimise the optical power in the squeezed beam, but due to the control limitations outlined earlier, this was not possible. An alternative, would have been to choose an interference with the off-line displacement beam, such that the displaced-squeezed beam carried zero optical power. In our experiment this was not possible, because we needed a certain amount of power for the DC-derived phase quadrature lock of the homodyne detector to work. Using an RF-derived error signal would of course remove this limitation, and it would be possible to operate the homodyne detector with a much higher power ratio.

8.6 Summary

In this chapter I have presented an experiment that measured the second-order coherence of optical fields, based on homodyne detection in the configuration of the intensity interferometer of Hanbury Brown and Twiss. We tested our instrument by measuring three classes of states: squeezed-displaced, coherent, and biased-thermal. The results clearly demonstrated photon anti-bunching for the displaced-squeezed state, and also showed good agreement with the theoretical predictions for all the states that were tested.

Chapter 9

Summary and Outlook

9.1 Summary

Harmonic entanglement theory: From a theoretical analysis of an optical parametric amplifier (OPA), I showed that it is possible to entangle light of one wavelength with light that has exactly double that wavelength. This type of entanglement, called *harmonic entanglement,* could be observed by measuring the amplitude and phase quadratures of the fundamental and second-harmonic fields that are reflected from an OPA. Further investigation of the OPA system yielded the following generalisations:

- The OPA needs to be operated in a regime of pump-depletion or enhancement. An exchange of energy between the fundamental and second-harmonic fields is essential for the generation of harmonic entanglement.
- The strength of harmonic entanglement is only limited in principle by the intra-cavity losses of the OPA, and the provision that the OPA be driven with a total input power that is at OPO threshold power or above.
- Biased-entanglement is naturally produced by the OPA. This is a form of entanglement where the inference of the quadrature amplitudes in the direction from the fundamental to the second-harmonic are stronger than the other way around (or vice-versa).
- Squeezed driving fields (instead of coherent fields) for the seed and pump, can increase the strength of the entanglement that is attainable for a given total input power. They can also compensate for the bias in the entanglement to create symmetrically entangled states.

Harmonic entanglement experiment: We built an experiment that was capable of testing the theoretical prediction of harmonic entanglement from OPA. Our methods involved preparing coherent light at the fundamental and second-harmonic wavelengths. The light was aligned into the OPA that consisted of a second-order nonlinear crystal (PPKTP) that was placed at the focus of a resonator/cavity in the bow-tie geometry. The bright reflected fields from the OPA had their carrier fields (but not sidebands) attenuated by filtering the light using narrow-linewidth resonators that were operating near the impedance-matching condition. The filtered light of each of the fundamental and second-harmonic fields was received by two independent homodyne detectors, which could read out the quadrature amplitudes of the light, from which the correlation matrix was determined, and the inseparability criterion calculated. The main results from the experiment are listed here:

- Harmonic entanglement from the OPA was confirmed by the experimental results. The best measurement yielded a degree of inseparability of $\mathcal{I} = 0.74(1)$ which fulfilled the criterion for entanglement ($\mathcal{I} < 1$).

- The phase quadrature spectra showed a dense array of narrow linewidth resonances. We proposed that the phenomenon of Guided Acoustic Wave Brillouin Scattering (GAWBS) was occurring within the nonlinear crystal. A theoretical model of thermally activated GAWBS were in qualitative agreement with the observed spectra. The OPA model was extended to include a GAWBS phase-noise term, and the GAWBS excess noise was shown to be moderately detrimental to the inseparability of entanglement, and severely detrimental to the EPR measure of entanglement.

- The OPA was tested over a large range of operating conditions from amplification to de-amplification (the study across the angle parameter). The results for inseparability and quadrature variances were in good agreement with the GAWBS extended model of OPA.

- Harmonic entanglement was predicted to strengthen with increasing total input power to the OPA. The results from the experiment showed the expected trend, but only up until a point. Beyond about twice OPO threshold power, the entanglement degraded.

The cause of this effect is unclear. It could have been from quadrature noise on the seed and pump beams, or from increased sensitivity from GAWBS. Another explanation may be from competing nonlinearities (other non-degenerate OPO modes).

- Although our results did not allow us to claim a demonstration of EPR entanglement, we can say that the best place to look for the EPR measure of entanglement is in the regime of OPA amplification, where the phase quadratures for both the fundamental and second-harmonic fields are squeezed.

Photon anti-bunching theory: Our group came up with the idea that it was possible to measure the second-order coherence of a light field, by using only homodyne detection of the quadrature amplitudes, instead of the conventional method of single-photon resolution detectors. We also revisited the idea of using displaced-squeezed states to demonstrate photon anti-bunching. The main theoretical results from these analyses are:

- For the purpose of measuring second-order coherence, homodyne detection offers several advantages over the conventional single-photon detectors. The mode that is measured is automatically selected by the mode that the local oscillator is in. This selection includes frequency, transverse spatial distribution, and polarisation.
- Displaced squeezed states can be made to exhibit either super-bunching or anti-bunching statistics, depending only on the amount of displacement that is given to the squeezed state.
- The vacuum state can be considered as a singularity in that sense that the second-order coherence is not defined. The singularity can be approached by making ever weaker displaced squeezed states. Note that it is not possible to approach the vacuum by using optical attenuation. This is because second-order coherence measurements are immune to optical loss, both before and within the HBT interferometer.

Photon anti-bunching experiment: We set up an experiment to test the idea that second-order coherence could be measured using homodyne detection alone, and also to see if displaced-squeezed states could be made to show photon anti-bunching statistics. We modified an existing squeezed light source (based on an OPA) so that it could operate stably in the regime of weak squeezing and low seed powers. The displacement was created off-line using an amplitude modulator, and the displaced and squeezed beams were interfered on an asymmetric beamsplitter. The displaced-squeezed state was sent on to the main 50:50 beamsplitter of the HBT interferometer, after which each beam was received by a homodyne detector that could be locked to either the phase or amplitude quadrature. The signals from the homodyne detectors were digitised and recorded. The second-order coherence was calculated from the correlations of the quadrature data. The main results are summarised here:

- The best anti-bunching statistic was measured from a weakly displaced squeezed state and found to be $g^{(2)}(0) = 0.11(18)$.
- We measured a displaced squeezed state over a range of displacements while holding the squeezing level fixed. We found that the second-order coherence varied from bunching to anti-bunching statistics as the displacement was reduced, which agreed well with the theoretical predictions.
- Measurements of the second-order coherence of coherent states and biased thermal states were in good agreement with the theoretical predictions. These results validated our method of measuring the second-order coherence function using homodyne detection.

9.2 Outlook

What follows are some ideas that can build on the work that we have done so far. There are extensions to the theoretical analyses, and also possible ways to improve the experiments.

Harmonic entanglement: In my theoretical model of OPA, I had restricted the relative phases of the seed and pump beams to be either zero or 90 degrees (as counted in the pump beam frame). This was done for no other reason than to simplify the analysis. The extension would open up a new class of stable classical solutions, which I would expect to have a mixture of properties, for example a bi-stable region that also has non-trivial phase shifts for the reflected fields.

Another class of classical solutions may be opened up by allowing the cavity resonances to be de-tuned from the fundamental and second-harmonic wavelengths. Finally, the phase-matching condition could be tuned, which effectively makes the nonlinear coefficient complex-valued. The classical solutions to the OPA equations essentially drive the quantum fluctuation analysis. New solution sets, could open up new classes of entangled states, for example, where the biasedness of the entanglement is compensated for by a phase-matching de-tuning term. Furthermore, all of these parameters could easily be varied in the laboratory setup. They would involve setting the locking-points for the respective control-loops with an offset from their centred points. The measurement procedure would then proceed in the usual manner. With four extra degrees of freedom, the system should yield some interesting behaviour.

If it is possible to make harmonic entanglement with OPA, is it then possible to undo the process with another OPA, i.e. one that acts as a *dis-entangler*? The OPA process is in principle reversible, but I did not test the dis-entangler idea with the theoretical model. A dis-entangler would complete the analogy with the generating (degenerate) entangled light via two squeezed beams and a beamsplitter, where the beamsplitter process is reversible. To test the idea experimentally, one would take the harmonically entangled light that is reflected from one OPA, and inject this into another OPA, before analysing the reflected light using homodyne detection. The expected null result (no entanglement) however, would not be very exciting.

We had not taken measurements in the bi-stable and complex-valued regions of the OPA stability map. There are some technical issues about how one would control, or even know, on which arm of the bi-stable region the relative phase of pump and seed are locked to. However, if these problems could be tackled, then in it should be straightforward to measure the quadrature amplitudes in the usual way and test for entanglement.

The one thing left to be desired by the experiment was a confirmation of the state of light satisfying the EPR criterion of entanglement. Although inseparability is a necessary and sufficient criterion of entanglement, reaching the EPR criterion is desirable because it is a practical measure for quantum information protocols such as quantum teleportation. I believe that three factors contributed to creating an excess noise in the quadratures of the fields that prevented us from measuring EPR entanglement.

(1) The dominant degradation came from the GAWBS effect that created excess noise in the phase quadratures. Although the noise was correlated for the fundamental and second-harmonic fields, it shows up in the EPR criterion because it degrades the conditional variances that make up that measure. A work-around may be to mount the nonlinear crystal with only a minimum amount of contact to the surface, this should increase the quality factor of the GAWBS resonances, and make it possible to measure entanglement in the gaps between the resonance frequencies. An idea was proposed by Prof. Ping Koy Lam for another work-around to the problem. By moving the measurements to sideband frequencies in the next free-spectral range ($\approx 1\,\mathrm{GHz}$) of the OPA resonator, the GAWBS peaks, which lie predominantly at tens, to hundreds of MHz, would be left behind. The only difficulty is that new detectors would have to be built that have the fast 1 GHz response, while maintaining sufficient clearance above dark noise, and sufficient power handling capabilities.

(2) Our OPA cavity had a great deal of intra-cavity loss. For 1064nm it was measured to be 0.2% and for 532nm it was 7%. The values are per-round-trip. The value for 532nm is quite high. The reason may be grey tracking in the crystal. Grey-tracking is a phenomenon where high intensity light of short wavelengths creates scattering centres due to dislocations of the crystal lattice. PPKTP is famous for grey-tracking at higher powers, especially at blue coloured wavelengths. Another source of intra-cavity loss were the two AR coatings of the dispersion plate, which could be done away with by using a wedged PPKTP crystal. The dispersion compensation would then be done by changing the transverse position of the crystal. Another improvement would come from changing the high-reflectivity mirrors of the OPA cavity, to mirrors of a higher quality, i.e. mirrors of greater reflectivity and lower scattering. Note that this may be accompanied by difficulties in the locking of the cavity using the reverse seed, since from its viewpoint, the cavity would be even less impedance matched.

(3) The theoretical model predicted that driving the OPA with a greater total input power, up to 7 times OPO threshold power, should bring with it more entanglement. The

problem in our experiment, was perhaps that the driving fields were not shot-noise-limited at these higher optical powers. The only solution would be to add more stages of optical filtering prior to the OPA, to make the seed and pump fields shot-noise-limited at the observing frequencies (7.8 MHz).

Further room for improvement could be found by increasing the detection efficiency after the OPA cavity. This could be done by removing the many sets of redundant alignment optics for filter cavities that we had made provision for, but never needed to install. Another improvement would come from reducing the percentage of the light that was tapped-off for the relative phase lock. All of these suggestions should see not only an improvement in the measurements of the inseparability measure, but perhaps also a confirmation of EPR entanglement.

Photon anti-bunching from squeezing: Within the experimental framework of homodyne detection, we had considered only how to measure the second-order coherence function. But there is more information contained in the higher-order coherence functions. For example, the triple intensity correlation (fourth-order coherence) can be measured at three different delay times, and this can be used to extract the phase information of the first-order coherence function. It would be interesting to develop a model to see if one could measure the fourth-order coherence function using homodyne detection alone.

If the aim is to obtain better photon anti-bunching statistics, then there are two aspects of the experiment that could be improved. The first one is the generation of the displaced-squeezed state. As we have seen, the weakness of the squeezing and the purity of the state is paramount. This cannot be faked by optically attenuating a strongly squeezed state. The way to improve this, would be to increase the signal-to-noise ratio of the error signals that control the OPA cavity length, and the pump-seed relative phase. The method may be to introduce an auxiliary control seed beam, this would be a frequency shifted seed, that would act as a single side-band and could be used to derive an error signal for those two locking loops.

Secondly, an improvement can be made at the stage of the homodyne detectors. Here, the limitation came in the form of the signal beams carrying too much optical power. These then created an excess noise when measuring, for example a coherent state, for which the variances were slightly greater than one. A method was proposed by Dr. Thomas Symul to eliminate this problem. One needs to change the locking circuitry of the homodyne detectors to be completely RF-derived error signals, and not reliant on the DC difference of the photodetectors. This could be done by introducing onto the displacement beam a phase modulation at one frequency, and amplitude modulation at a different frequency. The optical beams could then be de-modulated to derive the error signals. In this configuration, one would be free to choose the optical power in the displacement beam, such that the signal beams contained nearly zero optical power. The power would then be limited only by the (interference) fringe visibility between the displaced beam and squeezed beam.

In the theory section, I proposed that the quadrature measurements could be made over an average of quadrature angles, as long as all angles were visited in equal time. This method of measuring would be useful in situations where we cannot extract error signals for the homodyne detectors, or if the source of light is truly chaotic, and has no well defined phase. An experimental test of this proposal would be a simple procedure.

An interesting demonstration of the homodyne technique would be to measure the second-order coherence function of a physical scattering process. The sample could be in the form of a colloidal suspension of microscope particles (scattering objects). These would induce random phase shifts of the light within a certain time frame. Hence, by measuring the second-order coherence of the sample, or how it in-effect de-coheres a coherent laser beam, some dynamics of the physical scattering system could be obtained. Furthermore, by using light beams in a highly anti-bunched or super-bunched state, instead of a coherent state, it may be possible to make measurements at greater sensitivity.

Bibliography

[Arecchi *et al.* 1966] F. T. Arecchi, E. Gatti, and A. Sona. *Time distribution of photons from coherent and Gaussian sources*. Physics Letters, 20(1):27–29, 1966.

[Aspect and Grangier 1987] A. Aspect and P. Grangier. *Wave-particle duality for single photons*. Hyperfine Interactions, 37(1):1–17, 1987.

[Aspect *et al.* 1982] A. Aspect, Ph. Grangier, and G. Roger. *Experimental Realization of Einstein-Podolsky-Rosen-Bohm Gedankenexperiment: A New Violation of Bell's Inequalities*. Phys. Rev. Lett., 49(2):91–94, 1982.

[Bachor and Ralph 2004] H.A. Bachor and T.C. Ralph. *A guide to experiments in quantum optics*. Wiley, 2004.

[Bell 1964] J. S. Bell. *On the einstein podolsky rosen paradox*. Physics (US), 1:195, 1964.

[Bierlein and Vanherzeele 1989] J.D. Bierlein and H. Vanherzeele. *Potassium titanyl phosphate: properties and new applications*. Journal of the Optical Society of America B, 6(4):622–633, 1989.

[Bowen *et al.* 2002] W.P. Bowen, R. Schnabel, H.A. Bachor, and P.K. Lam. *Polarization squeezing of continuous variable Stokes parameters*. Phys. Rev. Lett., 88(9):93601, 2002.

[Bowen *et al.* 2003a] W. P. Bowen, P. K. Lam, and T. C. Ralph. *Biased EPR entanglement and its application to teleportation*. Journal of Modern Optics, 50(5):801–813, 2003.

[Bowen *et al.* 2003b] W. P. Bowen, N. Treps, B. C. Buchler, R. Schnabel, T. C. Ralph, H.-A. Bachor, T. Symul, and P. K. Lam. *Experimental investigation of continuous-variable quantum teleportation*. Phys. Rev. A, 67(3):032302, 2003.

[Bowen *et al.* 2004] W. P. Bowen, R. Schnabel, P. K. Lam, and T. C. Ralph. *Experimental characterization of continuous-variable entanglement*. Phys. Rev. A, 69(1):012304, 2004.

[Casimir 1948] H. G. B. Casimir. *On the attraction between two perfectly conducting plates*. Proc. K. Ned. Akad. Wet., 51:793–796, 1948.

[Cassemiro *et al.* 2007] K. N. Cassemiro, A. S. Villar, M. Martinelli, and P. Nussenzveig. *The quest for three-color entanglement: experimental investigation of new multipartite quantum correlations*. Opt. Express, 15(26):18236–18246, 2007.

[Caves and Schumaker 1985] Carlton M. Caves and Bonny L. Schumaker. *New formalism for two-photon quantum optics. I. Quadrature phases and squeezed states*. Phys. Rev. A, 31(5):3068–3092, 1985.

[Caves 1981] Carlton M. Caves. *Quantum-mechanical noise in an interferometer*. Phys. Rev. D, 23(8):1693–1708, 1981.

[Chaturvedi *et al.* 2002] S. Chaturvedi, K. Dechoum, and P. D. Drummond. *Limits to squeezing in the degenerate optical parametric oscillator*. Phys. Rev. A, 65(3):033805, 2002.

[Chen and Risk 1994] Q. Chen and W. P. Risk. *Periodic poling of KTiOPO 4 using an applied electricfield*. Electronics Letters, 30(18):1516–1517, 1994.

[Cirac and Zoller 1995] J.I. Cirac and P. Zoller. *Quantum computations with cold trapped ions*. Phys. Rev. Lett., 74(20):4091–4094, 1995.

[Collett and Gardiner 1984] M. J. Collett and C. W. Gardiner. *Squeezing of intracavity and traveling-wave light fields produced in parametric amplification*. Phys. Rev. A, 30(3):1386–1391, 1984.

[Darquie *et al.* 2005] B. Darquie, M. P. A. Jones, J. Dingjan, J. Beugnon, S. Bergamini, Y. Sortais, G. Messin, A. Browaeys, and P. Grangier. *Controlled single-photon emission from a single trapped two-level atom*. Science, 309(5733):454–456, 2005.

[de Oliveira *et al.* 1990] F. A. M. de Oliveira, M. S. Kim, P. L. Knight, and V. Buek. *Properties of displaced number states*. Phys. Rev. A, 41(5):2645–2652, 1990.

[Diddams *et al.* 2000] S. A. Diddams, D. J. Jones, J. Ye, S. T. Cundiff, J. L. Hall, J. K. Ranka, R. S. Windeler, R. Holzwarth, T. Udem, and T. W. Hänsch. *Direct Link between Microwave and Optical Frequencies with a 300 THz Femtosecond Laser Comb*. Phys. Rev. Lett., 84(22):5102–5105, 2000.

[DiGuglielmo *et al.* 2007] J. DiGuglielmo, B. Hage, A. Franzen, J. Fiurasek, and R. Schnabel. *Experimental characterization of Gaussian quantum-communication channels*. Phys. Rev. A, 76(1), 2007.

[Dirac 1947] P. A. M. Dirac. *The Principles of Quantum Mechanics*. Oxford University Press, New York, United States of America, 1947.

[Dixon 1967] R. W. Dixon. *Photoelastic properties of selected matierals and their relevance for applications to acoustic light modulators and scanners*. Journal of Applied Physics, 38(11):5149 – 5153, 1967.

[Dmitriev *et al.* 1995] V. G. Dmitriev, G. G. Gurzadyan, and D. N. Nikogosyan. *Handbook of nonlinear optical crystals*. Springer series in optical sciences, 1995.

[Drever *et al.* 1983] R. W. P Drever, J. L. Hall, F. V. Kowalski, J. Hough, G. M. Ford, A. J. Munley, and H. Ward. *Laser phase and frequency stabilization using an optical resonator*. Applied Physics B: Lasers and Optics, 31(2):97–105, 1983.

[Drummond *et al.* 1980] P. D. Drummond, K. J. McNeil, and D. F. Walls. *Nonequilibrium transitions in sub-2nd harmonic generation 1. semi-classical theory*. Optica Acta, 27(3):321–335, 1980.

[Drummond *et al.* 1981] P. D. Drummond, K. J. McNeil, and D. F. Walls. *Non-equilibrium Transitions in Sub/second Harmonic Generation: II. Quantum Theory*. Journal of Modern Optics, 28:211–225, 1981.

[Duan *et al.* 2000] L.-M. Duan, G. Giedke, J. I. Cirac, and P. Zoller. *Inseparability Criterion for Continuous Variable Systems*. Phys. Rev. Lett., 84(12):2722–2725, 2000.

[Einstein *et al.* 1935] A. Einstein, B. Podolsky, and N. Rosen. *Can Quantum-Mechanical Description of Physical Reality Be Considered Complete?* Physical Review, 47:777, 1935.

[Einstein 1905] A. Einstein. *Ü*ber die von der molekularkinetischen Theorie der Wärme geforderte Bewegung von in ruhenden Flüssigkeiten suspendierten Teilchen. Annalen der Physik, 322(8):549–560, 1905.

[Ellegaard *et al.* 1996] C. Ellegaard, T. Guhr, K. Lindemann, J. Nygård, and M. Oxborrow. *Symmetry Breaking and Spectral Statistics of Acoustic Resonances in Quartz Blocks*. Phys. Rev. Lett., 77(24):4918–4921, 1996.

[Fischer *et al.* 2004] M. Fischer, N. Kolachevsky, M. Zimmermann, R. Holzwarth, Th. Udem, T. W. Hänsch, M. Abgrall, J. Grünert, I. Maksimovic, S. Bize, H. Marion, F. Pereira Dos Santos, P. Lemonde, G. Santarelli, P. Laurent, A. Clairon, C. Salomon, M. Haas, U. D. Jentschura, and C. H. Keitel. *New Limits on the Drift of Fundamental Constants from Laboratory Measurements*. Phys. Rev. Lett., 92(23):230802, 2004.

[Freedman and Clauser 1972] S. J. Freedman and J. F. Clauser. *Experimental Test of Local Hidden-Variable Theories*. Phys. Rev. Lett., 28(14):938–941, 1972.

[Fry and Thompson 1976] E. S. Fry and R. C. Thompson. *Experimental Test of Local Hidden-Variable Theories*. Phys. Rev. Lett., 37(8):465–468, 1976.

[Furusawa *et al.* 1998] A. Furusawa, JL Sørensen, SL Braunstein, CA Fuchs, HJ Kimble, and ES Polzik. *Unconditional quantum teleportation*. Science, 282(5389):706, 1998.

[Glauber 1963] R. J. Glauber. *The Quantum Theory of Optical Coherence*. Phys. Rev., 130(6):2529–2539, 1963.

[Glöckl *et al.* 2004] O. Glöckl, U. L. Andersen, S. Lorenz, Ch. Silberhorn, N. Korolkova, and G. Leuchs. *Sub-shot-noise phase quadrature measurement of intense light beams*. Opt. Lett., 29(16):1936–1938, 2004.

[Goda *et al.* 2005] K. Goda, K. McKenzie, E. E. Mikhailov, P. K. Lam, D. E. McClelland, and N. Mavalvala. *Photothermal fluctuations as a fundamental limit to low-frequency squeezing in a degenerate optical parametric oscillator*. Phys. Rev. A , 72(4):043819, 2005.

[Griffiths 1995] D. J. Griffiths. *Introduction to Quantum Mechanics*. Prentice-Hall, New Jersey, United States of America, 1st edition, 1995.

[Gulde *et al.* 2003] S. Gulde, M. Riebe, G.P.T. Lancaster, C. Becher, J. Eschner, H. Haffner, F. Schmidt-Kaler, I.L. Chuang, and R. Blatt. *Implementation of the Deutsch-Jozsa algorithm on an ion-trap quantum computer*. Nature, 421(6918):48–50, 2003.

[Hanbury-Brown and Twiss 1956a] R. Hanbury-Brown and R. Q. Twiss. *A Test of a New Type of Stellar Interferometer on Sirius*. Nature, 178(4541):1046–1048, 1956.

[Hanbury-Brown and Twiss 1956b] R. Hanbury-Brown and R. Q. Twiss. *Correlation between photons in two coherent beams of light*. Nature, 177(4497):27–29, 1956.

[Hanbury Brown *et al.* 1974] R. Hanbury Brown, J. Davis, and LR Allen. *The angular diameters of 32 stars*. Mon. Not. R. Astron. Soc, 167:121–36, 1974.

[Hanbury Brown 1974] R. Hanbury Brown. *The Intensity Interferometer: Its Application to Astronomy*. London: Taylor & Francis, 1974.

[Hecht 2002] E. Hecht. *Optics*. Pearson Education, Addison-Wesley Series in Physics, 2002.

[Henny *et al.* 1999] M. Henny, S. Oberholzer, C. Strunk, T. Heinzel, K. Ensslin, M. Holland, and C. Schönenberger. *The Fermionic Hanbury Brown and Twiss Experiment*. Science, 284(5412):296–298, 1999.

[Hirano *et al.* 2005] T. Hirano, K. Kotani, T. Ishibashi, S. Okude, and T. Kuwamoto. *3 dB squeezing by single-pass parametric amplification in a periodically poled KTiOPO4 crystal*. Optics letters, 30(13):1722–1724, 2005.

[Holzwarth *et al.* 2000] R. Holzwarth, Th. Udem, T. W. Hänsch, J. C. Knight, W. J. Wadsworth, and P. St. J. Russell. *Optical Frequency Synthesizer for Precision Spectroscopy*. Phys. Rev. Lett., 85(11):2264–2267, 2000.

[Horodecki 1997] P. Horodecki. *Separability criterion and inseparable mixed states with positive partial transposition*. Physics Letters A, 232(5):333–339, 1997.

[Horowicz 1989] R. J. Horowicz. *Quantum Correlation between Fundamental and Second Harmonic in SHG*. Europhysics Letters, 10(6):537–542, 1989.

[Jackson 1999] J. D. Jackson. *Classical Electrodynamics*. Whiley, New York, United States of America, 3rd edition, 1999.

[Jaynes and Cummings 1963] E.T. Jaynes and F.W. Cummings. *Comparison of quantum and semiclassical radiation theories with application to the beam maser*. Proceedings of the IEEE, 51(1):89–109, 1963.

[Kimble *et al.* 1977] H. J. Kimble, M. Dagenais, and L. Mandel. *Photon Antibunching in Resonance Fluorescence*. Phys. Rev. Lett., 39(11):691–695, 1977.

[Kleinman *et al.* 1966] D. A. Kleinman, A. Askin, and G. D. Boyd. *Second-harmonic generation of light by focussed laser beams*. Physical Review, 145(1):338–379, 1966.

[Koashi *et al.* 1993] M. Koashi, K. Kono, T. Hirano, and M. Matsuoka. *Photon antibunching in pulsed squeezed light generated via parametric amplification*. Phys. Rev. Lett., 71(8):1164–1167, 1993.

[Kocher and Commins 1967] C. A. Kocher and E. D. Commins. *Polarization correlation of photons emitted in an atomic cascade*. Phys. Rev. Lett., 18(15):575–577, 1967.

[Kwiat *et al.* 1995] P. G. Kwiat, K Mattle, H. Weinfurter, A Zeilinger, A. V. Sergienko, and Y. Shih. *New High-Insensity Source of Polarization-Entangled Photon Pairs*. Phys. Rev. Lett., 75(24):4337–4341, 1995.

[Lamb and Retherford 1947] W. E. Lamb and R. C. Retherford. *Fine Structure of the Hydrogen Atom by a Microwave Method*. Phys. Rev., 72(3):241–243, 1947.

[Lamb and Scully 1968] W. E. Lamb and M. O. Scully. *The photoelectric effect without photons*. Coral Gables, Fla. : Center for Theoretical Studies, University of Miami, 1968.

[Lance *et al.* 2004] A. M. Lance, T. Symul, W. P. Bowen, B. C. Sanders, and P. K. Lam. *Tripartite Quantum State Sharing*. Phys. Rev. Lett., 92(17):177903, 2004.

[Leonhardt 1997] U. Leonhardt. *Measuring the quantum state of light*. Cambridge University Press, Cambridge, England, 1st edition, 1997.

[Li *et al.* 2003] X. Li, Y. Wu, D. Steel, D. Gammon, TH Stievater, DS Katzer, D. Park, C. Piermarocchi, and LJ Sham. *An all-optical quantum gate in a semiconductor quantum dot*. Science, 301(5634):809–811, 2003.

[Li *et al.* 2007] Y. Li, S. Zhang, J. Liu, and K. Zhang. *Quantum correlation between fundamental and second-harmonic fields via second-harmonic generation*. J. Opt. Soc. Am. B, 24(3):660–663, 2007.

[Loudon 2000] R. Loudon. *The Quantum Theory of Light*. Oxford University Press, Oxford, England, 3rd edition, 2000.

[Lounis and Moerner 2000] B. Lounis and W. E. Moerner. *Single photons on demand from a single molecule at room temperature*. Nature, 407(6803):491–493, 2000.

[Lu and Ou 2001] Y. J. Lu and Z. Y. Ou. *Observation of Nonclassical Photon Statistics due to Quantum Interference*. Phys. Rev. Lett., 88(2):023601, 2001.

[Lvovsky and Babichev 2002] A. I. Lvovsky and S. A. Babichev. *Synthesis and tomographic characterization of the displaced Fock state of light*. Phys. Rev. A, 66(1):011801, Jul 2002.

[Lvovsky *et al.* 2001] A. I. Lvovsky, H. Hansen, T. Aichele, O. Benson, J. Mlynek, and S. Schiller. *Quantum State Reconstruction of the Single-Photon Fock State*. Phys. Rev. Lett., 87(5):050402, 2001.

[Mahran and Satyanarayana 1986] M. H. Mahran and M. Venkata Satyanarayana. *Bunching and antibunching properties of various coherent states of the radiation field*. Phys. Rev. A, 34(1):640–643, 1986.

[Mandel and Wolf 1965] L. Mandel and E. Wolf. *Coherence Properties of Optical Fields*. Rev. Mod. Phys., 37(2):231–287, 1965.

[Mandel 1982] L. Mandel. *Squeezing and photon antibunching in harmonic generation*. Optics Communications, 42(6):437 – 439, 1982.

[Maxwell 1892] J. C. Maxwell. *A Treatise on Electricity and Magnetism*. Clarendon, 1892.

[McAlister and Raymer 1997] D. F. McAlister and M. G. Raymer. *Ultrafast photon-number correlations from dual-pulse, phase-averaged homodyne detection*. Phys. Rev. A, 55(3):R1609–R1612, 1997.

[Menicucci *et al.* 2006] N.C. Menicucci, P. van Loock, M. Gu, C. Weedbrook, T.C. Ralph, and M.A. Nielsen. *Universal quantum computation with continuous-variable cluster states*. Phys. Rev. Lett., 97:110501, 2006.

[Michelson and Pease 1921] AA Michelson and FG Pease. *Measurement of the Diameter of Alpha-Orionis by the Interferometer*. Proceedings of the National Academy of Sciences, 7(5):143–146, 1921.

[Michler *et al.* 2000] P. Michler, A. Imamoglu, M. D. Mason, P. J. Carson, G. F. Strouse, and S. K. Buratto. *Quantum correlation among photons from a single quantum dot at room temperature*. Nature, 406(6799):968–970, 2000.

[Myers *et al.* 1995] L. E. Myers, R. C. Eckardt, M. M. Fejer, R. L. Byer, W. R. Bosenberg, and J. W. Pierce. *Quasi-phase-matched optical parametric oscillators in bulk periodically poled LiNbO_3*. Journal of the Optical Society of America B, 12(11):2102–2116, 1995.

[Nielsen 2003] M.A. Nielsen. *Optical quantum computation using cluster states*. Phys. Rev. Lett., 93:040503, 2003.

[Nieto 1997] M. M. Nieto. *Displaced and squeezed number states*. Physics Letters A, 229(3):135 – 143, 1997.

[Nogueira *et al.* 2001] W. A. T. Nogueira, S. P. Walborn, S. Pádua, and C. H. Monken. *Experimental Observation of Spatial Antibunching of Photons*. Phys. Rev. Lett., 86(18):4009–4012, 2001.

[Oliver *et al.* 1999] W. D. Oliver, J. Kim, R. C. Liu, and Y. Yamamoto. *Hanbury Brown and Twiss-Type Experiment with Electrons*. Science, 284(5412):299–301, 1999.

[Olsen 2004] M. K. Olsen. *Continuous-variable Einstein-Podolsky-Rosen paradox with traveling-wave second-harmonic generation*. Phys. Rev. A, 70(3):035801, 2004.

[Öttl *et al.* 2005] A. Öttl, S. Ritter, M. Kohl, and T. Esslinger. *Correlations and Counting Statistics of an Atom Laser*. Phys. Rev. Lett., 95(9):090404, 2005.

[Ou *et al.* 1992] Z. Y. Ou, S. F. Pereira, H. J. Kimble, and K. C. Peng. *Realization of the Einstein-Podolsky-Rosen paradox for continuous variables*. Phys. Rev. Lett., 68(25):3663–3666, 1992.

[Ourjoumtsev *et al.* 2006] A. Ourjoumtsev, R. Tualle-Brouri, J. Laurat, and P. Grangier. *Generating Optical Schrodinger kittens for quantum information processing*. Science, 312(5770):83–86, 2006.

[Paschotta *et al.* 1994] R. Paschotta, M. Collett, P. Kürz, K. Fiedler, HA Bachor, and J. Mlynek. *Bright squeezed light from a singly resonant frequency doubler*. Phys. Rev. Lett., 72(24):3807–3810, 1994.

[Pelton *et al.* 2004] M. Pelton, P. Marsden, D. Ljunggren, M. Tengner, A. Karlsson, A. Fragemann, C. Canalias, and F. Laurell. *Bright, single-spatial-mode source of frequency non-degenerate, polarization-entangled photon pairs using periodically poled KTP*. Opt. Express, 12(15):3573–3580, 2004.

[Planck 1900] M. Planck. *Zur Theorie des Gesetzes der Energieverteilung im Normalspektrum*. Verhandlungen der Deutschen Physikalischen Gesellschaft, 2(17):237–245, 1900.

[Plenio 2005] M. B. Plenio. *Logarithmic negativity: A full entanglement Monotone that is not Convex*. Phys. Rev. Lett., 95(9):90503–90503, 2005.

[Polzik *et al.* 1992] E. S. Polzik, J. Carri, and H. J. Kimble. *Atomic spectroscopy with squeezed light for sensitivity beyond the vacuum-state limit*. Applied Physics B: Photophysics and Laser Chemistry, 55(3):279–290, 1992.

[Poustie 1992] Alistair J. Poustie. *Bandwidth and mode intensities of guided acoustic-wave Brillouin scattering in optical fibers*. J. Opt. Soc. Am. B, 10(4):691–696, 1992.

[Rarity *et al.* 1987] J. G. Rarity, P. R. Tapster, and E. Jakeman. *Observation of sub-poissonian light in parametric downconversion*. Optics Communications, 62(3):201–206, 1987.

[Reid 1989] M. D. Reid. *Demonstration of the Einstein-Podolsky-Rosen paradox using nondegenerate parametric amplification*. Phys. Rev. A, 40(2):913–923, 1989.

[Reif 1985] F. Reif. *Statistical physics*. McGraw-Hill International Editions, 1985.

[Saleh and Teich 1991] B.E.A. Saleh and M.C. Teich. *Fundamentals of Photonics*, volume 4. Wiley-Interscience, 1991.

[Santori *et al.* 2002] C. Santori, D. Fattal, J. Vuckovic, G. S. Solomon, and Y. Yamamoto. *Indistinguishable photons from a single-photon device*. Nature, 419(6907):594–597, 2002.

[Schellekens *et al.* 2005] M. Schellekens, R. Hoppeler, A. Perrin, J. V. Gomes, D. Boiron, A. Aspect, and C. I. Westbrook. *Hanbury Brown Twiss effect for ultracold quantum gases*. Science, 310(5748):648–651, 2005.

[Schiller *et al.* 1996] S. Schiller, G. Breitenbach, SF Pereira, T. Müller, and J. Mlynek. *Quantum statistics of the squeezed vacuum by measurement of the density matrix in the number state representation*. Phys. Rev. Lett., 77(14):2933–2936, 1996.

[Schnabel 2008] R. Schnabel. *Gravitational wave detectors, Squeezing up the sensitivity*. Nature Physics, 4(6):440–441, 2008.

[Schori *et al.* 2002] C. Schori, J. L. Sørensen, and E. S. Polzik. *Narrow-band frequency tunable light source of continuous quadrature entanglement*. Phys. Rev. A, 66(3):033802, 2002.

[Schrödinger 1926] E. Schrödinger. *Quantisierung als Eigenwertproblem*. Annalen der Physik, 4(76):489–527, 1926.

[Shelby *et al.* 1985a] R. M. Shelby, M. D. Levenson, and P. W. Bayer. *Guided acoustic-wave Brillouin scattering*. Phys. Rev. B, 31(8):5244–5252, 1985.

[Shelby *et al.* 1985b] R. M. Shelby, M. D. Levenson, and P. W. Bayer. *Resolved forward Brillouin scattering in optical fibers*. Phys. Rev. Lett., 54(9):939–942, 1985.

[Short and Mandel 1983] R. Short and L. Mandel. *Observation of Sub-Poissonian Photon Statistics*. Phys. Rev. Lett., 51(5):384–387, 1983.

[Skoog 1985] Douglas A. Skoog. *Principles of instrumental analysis*. Holt-Saunders International Editions, 1985.

[Slusher *et al.* 1985] R. E. Slusher, L. W. Hollberg, B. Yurke, J. C. Mertz, and J. F. Valley. *Observation of squeezed states generated by four-wave mixing in an optical cavity*. Phys. Rev. Lett., 55(22):2409–2412, 1985.

[Smithey *et al.* 1993] D. T. Smithey, M. Beck, M. G. Raymer, and A. Faridani. *Measurement of the Wigner distribution and the density matrix of a light mode using optical homodyne tomography: Application to squeezed states and the vacuum*. Phys. Rev. Lett., 70(9):1244–1247, Mar 1993.

[Stoler 1974] D. Stoler. *Photon Antibunching and Possible Ways to Observe It*. Phys. Rev. Lett., 33(23):1397–1400, 1974.

[Su *et al.* 2006] X. Su, A. Tan, X. Jia, Q. Pan, C. Xie, and K. Peng. *Experimental demonstration of quantum entanglement between frequency-nondegenerate optical twin beams*. Opt. Lett., 31(8):1133–1135, 2006.

[Sun *et al.* 2006] F. W. Sun, B. H. Liu, Y. F. Huang, G. C. Guo, and Z. Y. Ou. *Observation of the four-photon de Broglie wavelength by state-projection measurement*. Physical Review. A, 74(3), 2006.

[Suzuki *et al.* 2006] S. Suzuki, H. Yonezawa, F. Kannari, M. Sasaki, and A. Furusawa. *7 dB quadrature squeezing at 860 nm with periodically poled KTiOPO*. Applied Physics Letters, 89:061116, 2006.

[Treps and Fabre 2004] N. Treps and C. Fabre. *Criteria of quantum correlation in the measurement of continuous variables in optics*. Arxiv preprint quant-ph/0407214, 2004.

[Treps *et al.* 2002] N. Treps, U. Andersen, B. Buchler, PK Lam, A. Maitre, H.A. Bachor, and C. Fabre. *Surpassing the standard quantum limit for optical imaging using nonclassical multimode light*. Phys. Rev. Lett., 88(20):203601–203601, 2002.

[Udem *et al.* 2002] T. Udem, R. Holzwarth, and T.W. Haensch. *Optical frequency metrology*. Nature, 416(6877):233–237, 2002.

[Ursin *et al.* 2007] R. Ursin, F. Tiefenbacher, T. Schmitt-Manderbach, H. Weier, T. Scheidl, M. Lindenthal, B. Blauensteiner, T. Jennewein, J. Perdigues, P. Trojek, et al. *Entanglement-based quantum communication over 144 km*. Nature Physics, 3(7):481–486, 2007.

[Vahlbruch *et al.* 2008] H. Vahlbruch, M. Mehmet, S. Chelkowski, B. Hage, A. Franzen, N. Lastzka, S. Gossler, K. Danzmann, and R. Schnabel. *Observation of Squeezed Light with 10-dB Quantum-Noise Reduction*. Phys. Rev. Lett., 100(3):033602, 2008.

[Villar *et al.* 2005] A. S. Villar, L. S. Cruz, K. N. Cassemiro, M. Martinelli, and P. Nussenzveig. *Generation of Bright Two-Color Continuous Variable Entanglement*. Phys. Rev. Lett., 95(24):243603, 2005.

[Villar *et al.* 2006] A. S. Villar, M. Martinelli, C. Fabre, and P. Nussenzveig. *Direct Production of Tripartite Pump-Signal-Idler Entanglement in the Above-Threshold Optical Parametric Oscillator*. Phys. Rev. Lett., 97(14):140504, 2006.

[Walls and Milburn 1994] D. F. Walls and G. J. Milburn. *Quantum Optics*. Cambridge University Press, Cambridge, England, 1994.

[Walls 1979] D. F. Walls. *Evidence for the quantum nature of light*. Nature, 280:451–454, 1979.

[Webb *et al.* 2006] J. G. Webb, T. C. Ralph, and E. H. Huntington. *Homodyne measurement of the average photon number*. Phys. Rev. A, 73(3):033808, 2006.

[White *et al.* 1997] A. G. White, P. K. Lam, M. S. Taubman, M. A. M. Marte, S. Schiller, D. E. McClelland, and H.-A. Bachor. *Classical and quantum signatures of competing $\chi(2)$ nonlinearities* . Phys. Rev. A, 55(6):4511–4515, 1997.

[Winzer 1997] Peter J. Winzer. *Shot-noise formula for time-varying photon rates: a general derivation*. J. Opt. Soc. Am. B, 14(10):2424–2429, 1997.

[Wu *et al.* 1986] L.-A. Wu, H. J. Kimble, J. L. Hall, and H. Wu. *Generation of Squeezed States by Parametric Down Conversion*. Phys. Rev. Lett., 57(20):2520–2523, 1986.

[Yasuda and Shimizu 1996] M. Yasuda and F. Shimizu. *Observation of Two-Atom Correlation of an Ultracold Neon Atomic Beam*. Phys. Rev. Lett., 77(15):3090–3093, 1996.

[Young 1804] T. Young. *The Bakerian Lecture: Experiments and Calculations Relative to Physical Optics*. Philosophical transactions of the Royal Society of London, pages 1–16, 1804.

[Yurke 1984] B. Yurke. *Use of cavities in squeezed-state generation*. Phys. Rev. A, 29(1):408–410, 1984.

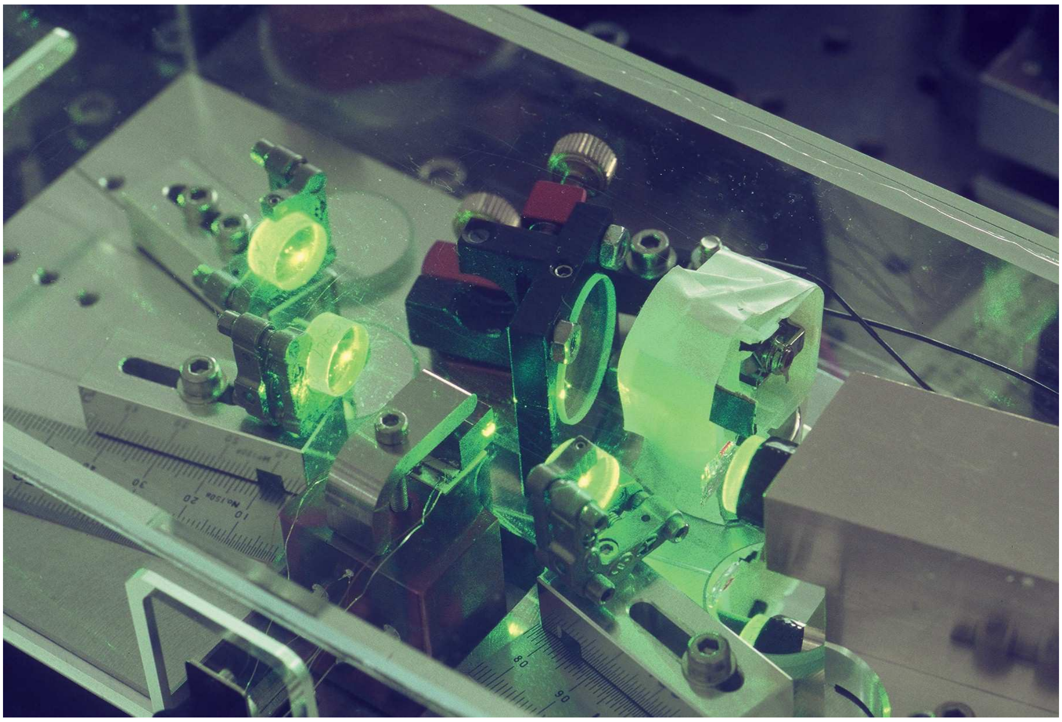

Plate 1: Photograph of the OPA used in the harmonic entanglement experiment. The 532 nm intra-cavity field is discernible as a faint green line due to Rayleigh scattering from air molecules. (see page 121)

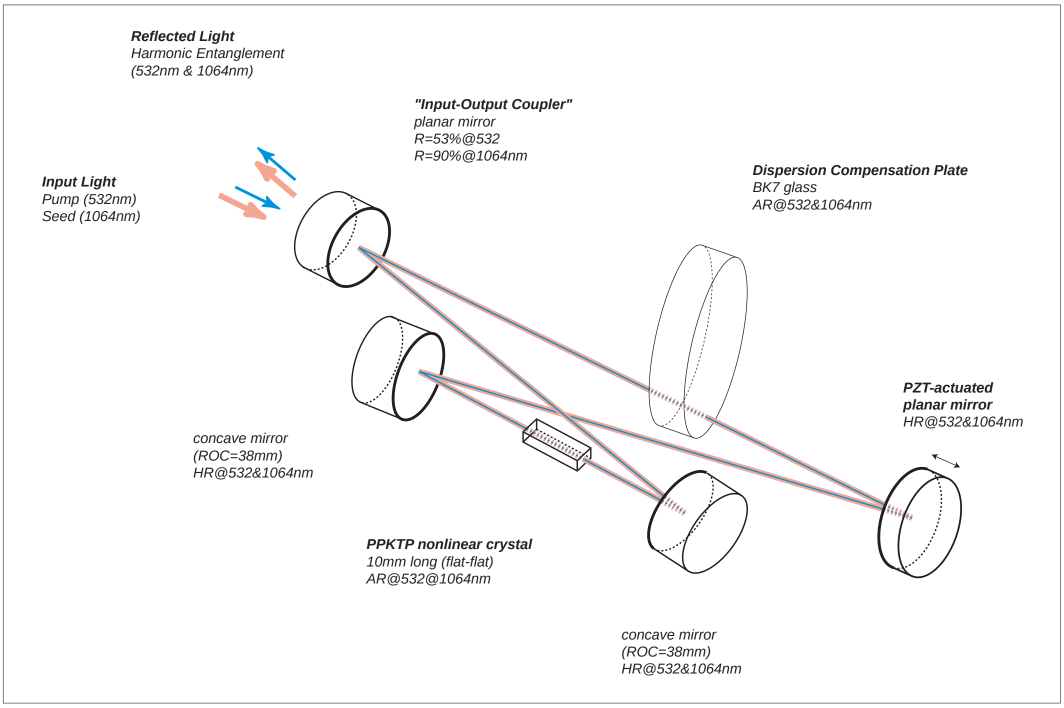

Plate 2: Schematic of the OPA based on the photograph above. PPKTP: periodically-poled potassium titanyl phosphate crystal. AR: anti-reflection coating. HR: high reflectivity coating. ROC: radius of curvature. PZT: piezo electric actuator. (see page 121)

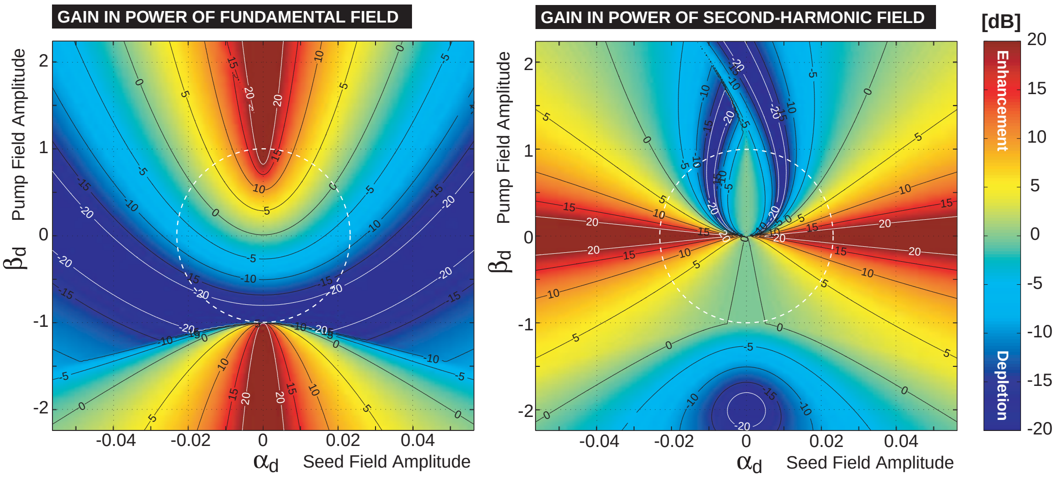

Plate 3: The classical *gain* is the ratio of optical powers of the light incident on, and the light reflected from, one mirror of the *optical parametric amplifier* (OPA). In a lossless OPA, the gain shows how the fundamental and second-harmonic fields have exchanged energy due to the nonlinear interaction. This is referred to as depletion or enhancement of the fields. The gain is expressed in a colour-coded decibel scale, and is mapped as a function of the normalised driving fields: the fundamental *seed*, and the second-harmonic *pump*. **Left:** Gain of the fundamental field. **Right:** Gain of the second-harmonic field. The horizontal axis follows the process of *second-harmonic generation* (SHG), while the vertical axis follows the process of *optical parametric oscillation* (OPO). A dashed circle marks the boundary where the total input power to the system is equal to the power that is required to reach OPO threshold. If the system is driven above OPO threshold, bi-stability in the OPA can be seen as asymmetry when comparing the gain for positive and negative values of the seed amplitude. (See page 103)

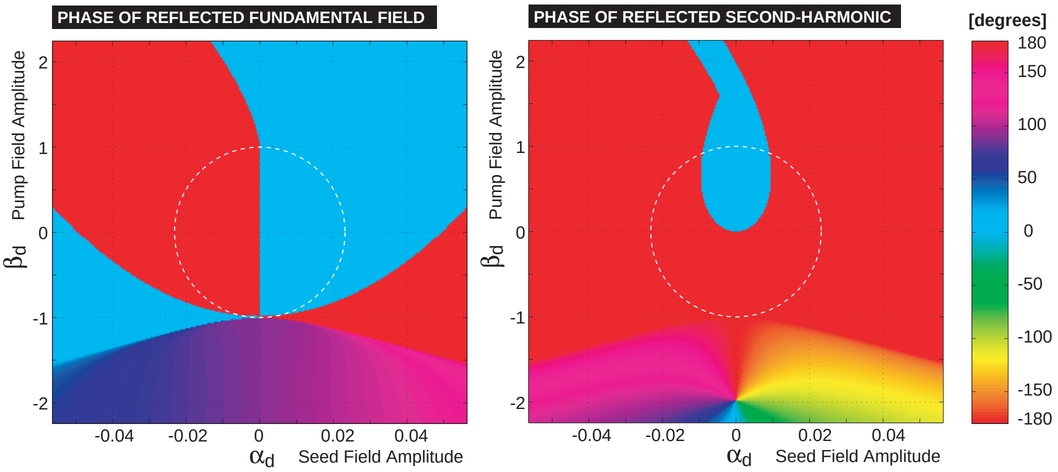

Plate 4: The fundamental and second-harmonic fields can also interact in the OPA in such a way that produces a non-trivial *phase-shift* on the reflected fields. The phase-shift is expressed in a colour-coded degree scale, and is mapped as a function of the seed and pump field amplitudes (similar to Plate 3). **Left:** Phase shift of the reflected fundamental field. **Right:** Phase shift of the reflected second-harmonic field. The most prominent example of a non-trivial phase-shift is found in the complex-value region in the lower half of the diagrams, where for the second-harmonic field, a phase anomaly can be seen. A non-trivial 180° phase-shift occurs along the contours of complete depletion of the pump or seed. (See page 103)

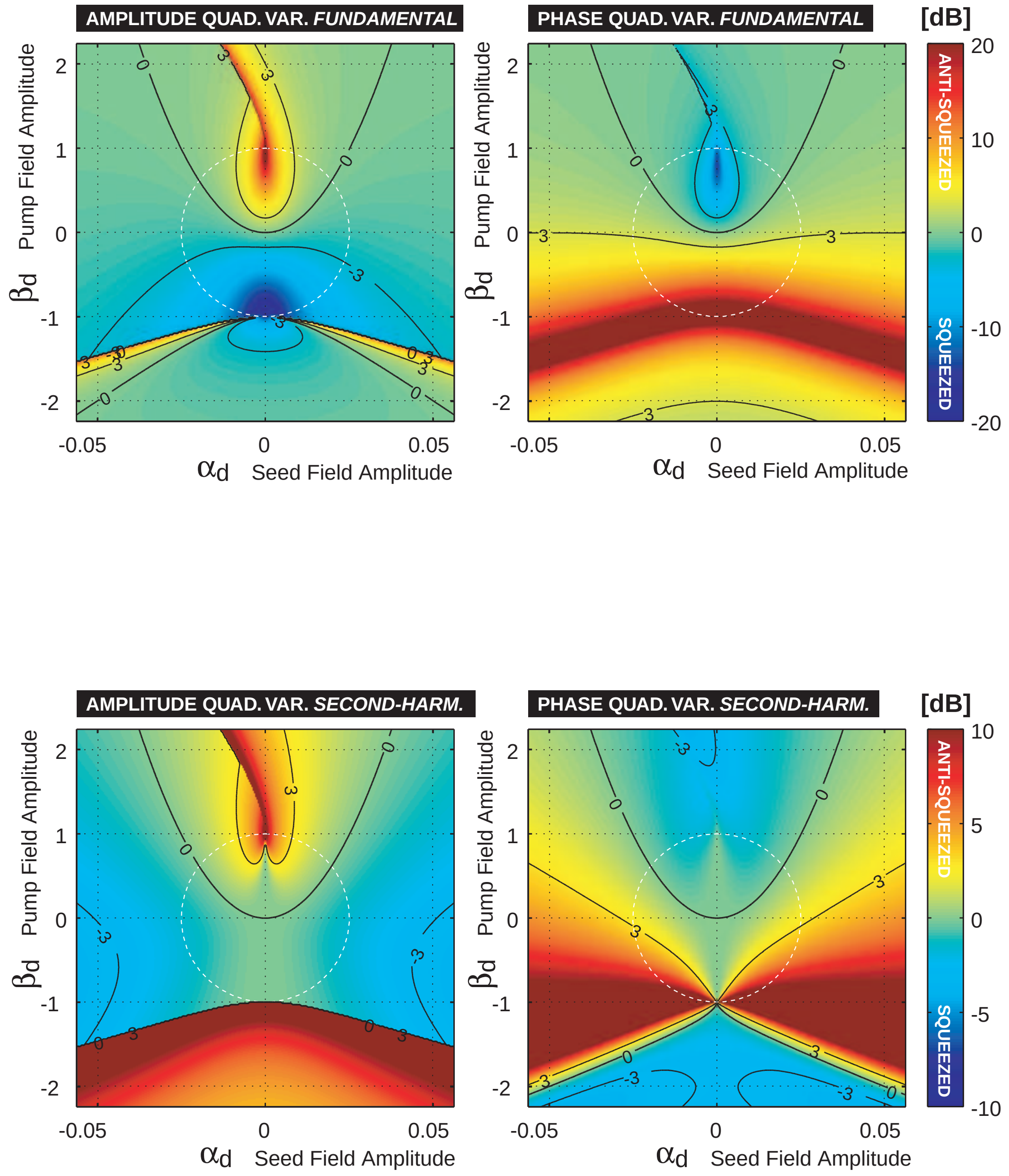

Plate 5: The OPA cavity transforms not only the classical amplitudes of the fields, but also alters their quantum statistics. The variances of the amplitude and phase quadratures of the fields that reflect from the OPA cavity have been mapped as a function of the input seed and pump fields (similar to Plate 3). The *quadrature variances* are shown in a colour-coded decibel scale, where negative values (blue) signify that the state is squeezed. **Top:** The quadrature variances of the reflected fundamental field. **Bottom:** The quadrature variances of the reflected second-harmonic field. The operation of a typical OPA squeezer, with a weak seed and strong pump, would follow a narrow strip along the vertical axis of the diagrams. Here the fundamental field is either squeezed or anti-squeezed depending on the sign of the pump field. The strength of the squeezing increases as OPO threshold is approached (dashed circle), but the quadrature variances of the second-harmonic remain unchanged in this regime. (See page 108)

HARMONIC ENTANGLEMENT AS A FUNCTION OF SEED AND PUMP FIELDS

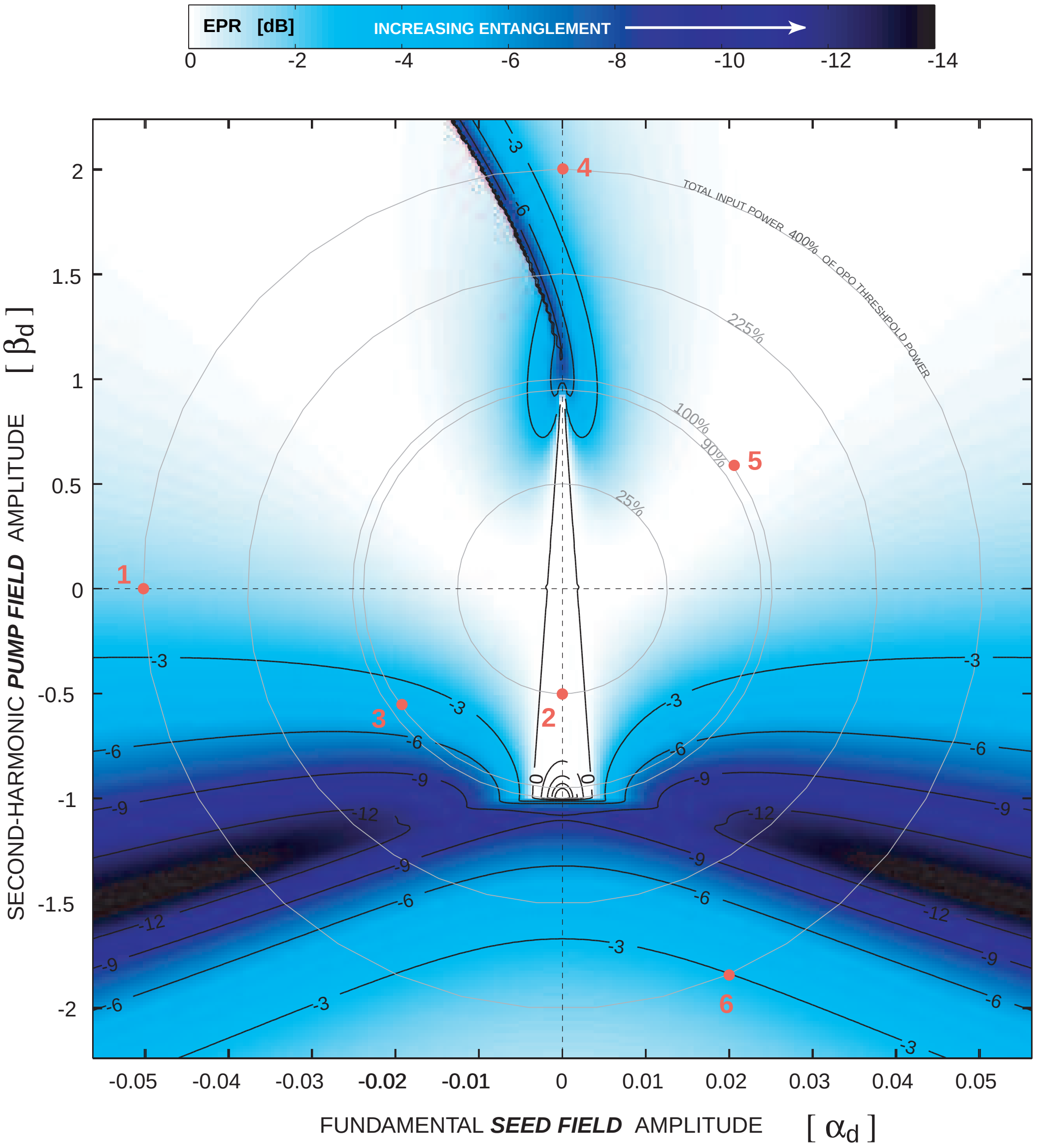

Plate 6: Harmonic entanglement is the entanglement between a fundamental field and its second-harmonic. The OPA alters not only the quantum statistics of the reflected fundamental and second-harmonic fields individually, but also induces correlations between them. As a result, the two-mode states that are produced, are inseparable, and they also demonstrate a violation of the EPR paradox. The EPR measure of entanglement is mapped in a colour-coded decibel scale as a function of the seed and pump fields that drive the OPA (similar to Plate 3). Darker blue signifies stronger entanglement, while contours make these values more precise. Circles of various radii mark paths along which the total input power to the OPA is constant. Red points and numbers refer to the case studies on the opposite page. The strongest harmonic entanglement can be seen on the boundaries to the classical solutions. While the vertical OPO axis for below-threshold pump fields is devoid of entanglement. (See page 109)

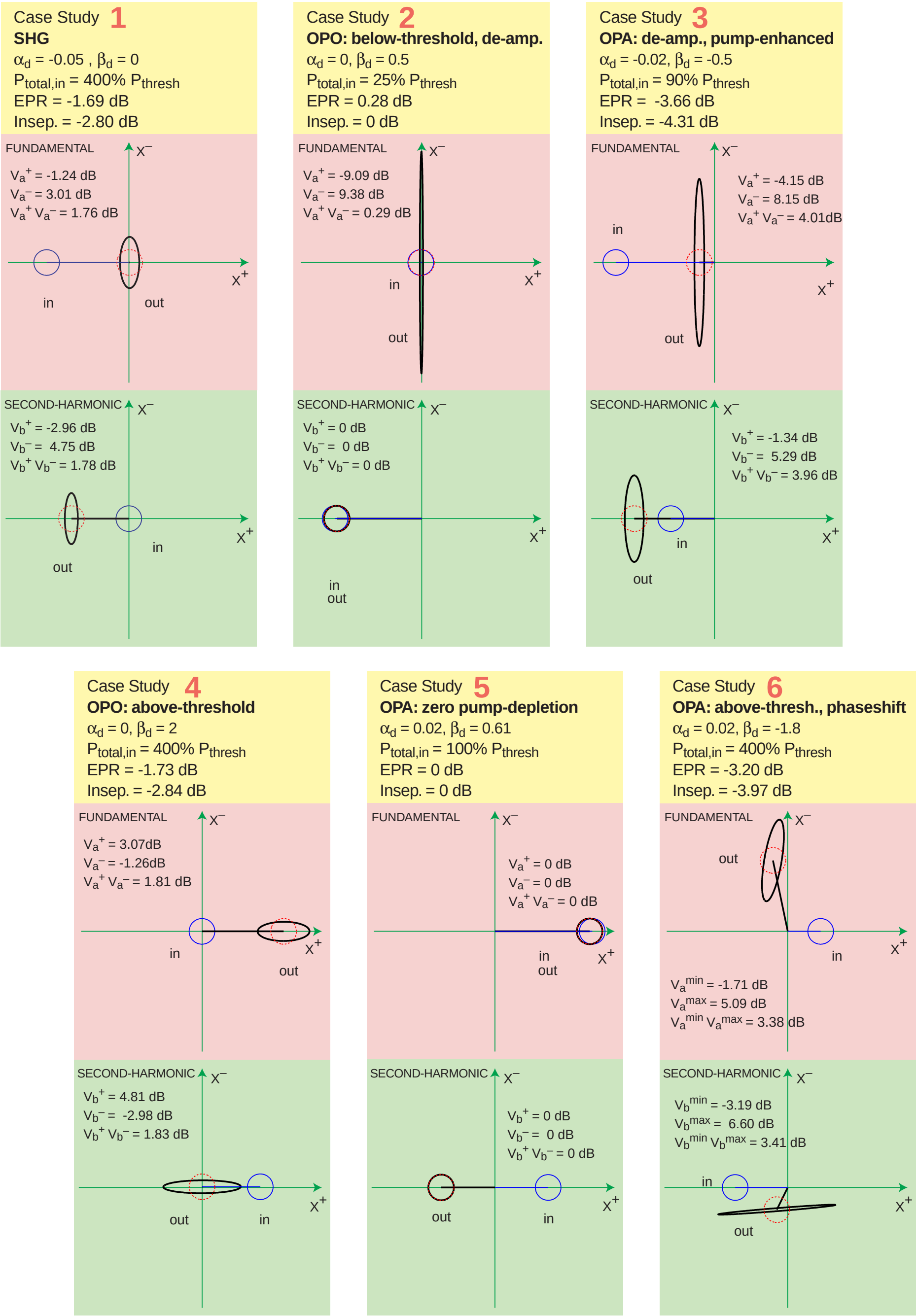

Plate 7: The states produced by the OPA are examined for various points in the map shown in Plate 6. The real and imaginary parts of the classical amplitude are represented as a line from the origin in a phasor diagram, while the quadrature standard-deviations are shown as an ellipse. A dashed red circle is a vacuum or coherent state reference. The fundamental and second-harmonic fields are shown on separate diagrams. The state of the field before and after the OPA are labelled ‘in’ and ‘out’, respectively. **Case 1:** Strongly driven SHG in the regime of complete pump-depletion. The squeezing (*sqz*) and harmonic entanglement (*ent*) are weak. **Case 2:** Below-threshold OPO where there is no pump-depletion shows strong *sqz* but is non-*ent*. **Case 3:** Below-threshold OPA with moderate pump-enhancement shows moderate *sqz* and *ent*. **Case 4:** Above-threshold OPO shows complete pump-depletion but only weak *sqz* and *ent*. **Case 5:** On the neutral-path there is no net interaction between the fields, and therefore no *sqz* nor *ent*. **Case 6:** A point in the complex-value region shows little pump-depletion, but the interaction via a non-trivial phase-shift makes strong *ent*. (See page 114)

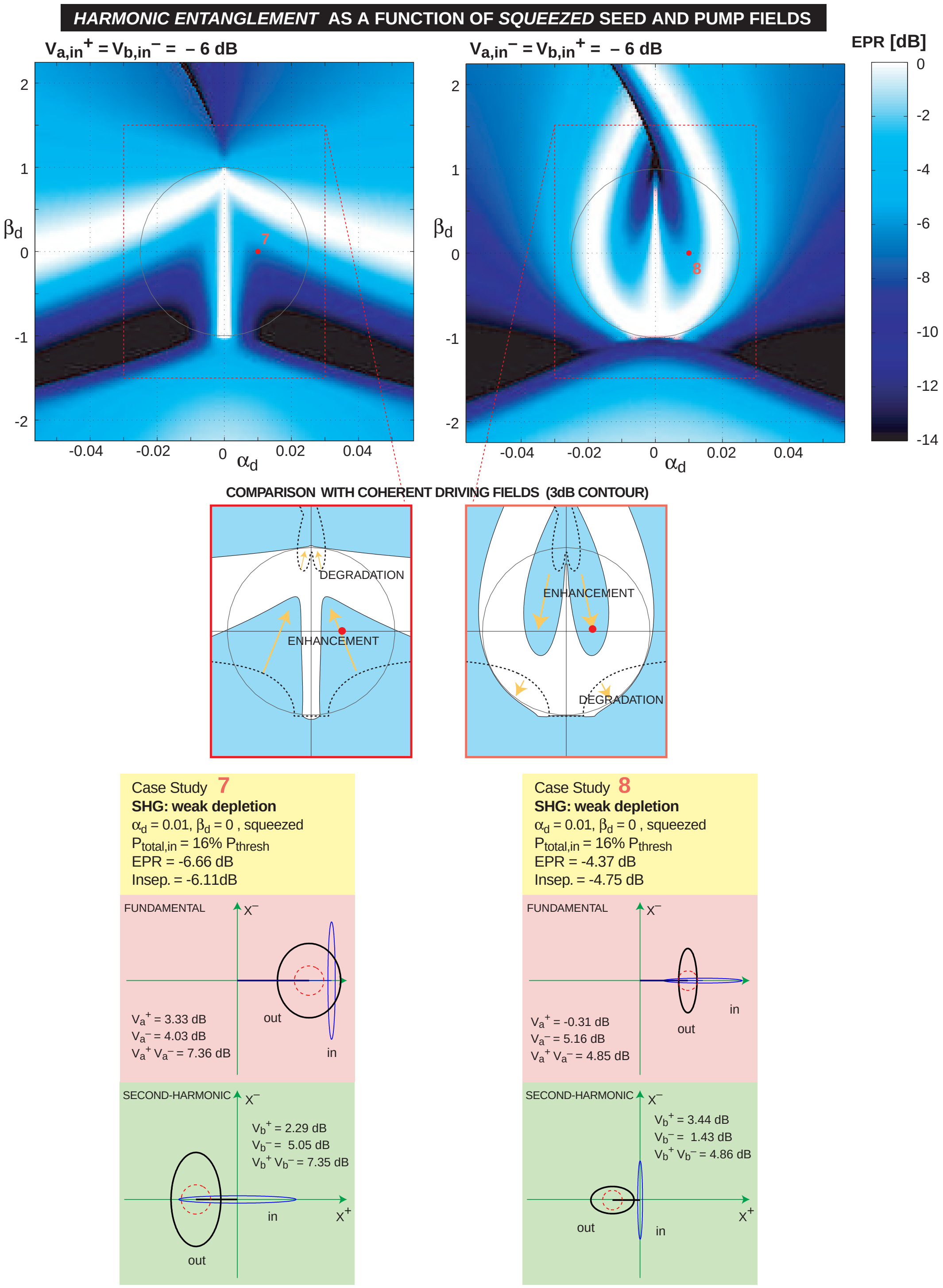

Plate 8: By driving the OPA with *squeezed* seed and pump fields instead of coherent states, the strength, type, and location of harmonic entanglement can be manipulated. **Main:** Two combinations of squeezing for the seed and pump are chosen, which cause the strength and regions of entanglement to grow or shrink. **Inset:** These maps are compared with those having the seed and pump fields in coherent states. The -3 dB contour shows that one region is enhanced, while the other is degraded. **Cases:** The case studies examine weakly-pumped SHG. Initially, the output states are nearly coherent and non-entangled (not shown). Using squeezed fields effectively turns on the entanglement. In case 7, the quadrature variances become nearly symmetric, thereby compensating for entanglement bias. (see page 117)

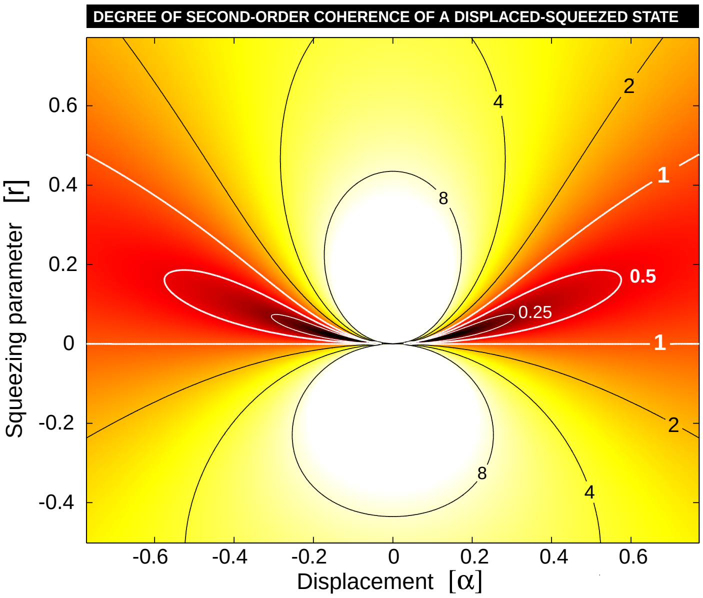

Plate 9: By analysing the *second-order coherence function* $g^{(2)}(\tau)$ of a source of light, its quantum nature can be revealed. The function is a normalised intensity-intensity correlation at two different times, where τ is the delay. An observation of $g^{(2)}(0) < 1$ is a clear signature of the quantisation of the electromagnetic field, here in the form of a *photon anti-bunched state* of light. In the diagram above, a theoretical model was used to investigate the class of displaced-squeezed states for their anti-bunching properties. The *degree* of second-order coherence $g^{(2)}(0)$ as a function of displacement α and squeezing parameter r was plotted as a colour-coded map. Darker colours signify the presence of anti-bunching, while lighter colours signify bunching. Contours mark the exact values. Note the increase in the strength of the anti-bunching and bunching effects as an approach is made to the vacuum state $(r = 0, \alpha = 0)$. (see page 193)

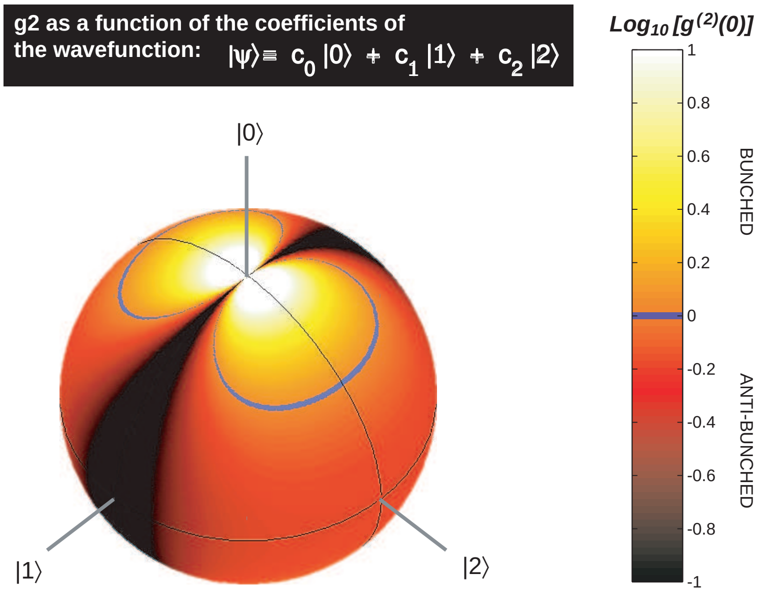

Plate 10: Second-order coherence is mapped onto the surface of the sphere. The co-ordinates of the sphere specify the coefficients of the arbitrary superposition state made up of vacuum, single- and two-photon number states. Darker colours signify anti-bunching statistics. Extreme cases of bunching and anti-bunching occur side-by-side in the area surrounding the vertical axis of the vacuum state. (see page 202)

Preparation of Laser Light

(A) Nd:YAG Laser & Freq. Doubler
(B) "MC1R" (not in use)
(C) "MC2R" (optical filtering via cavity)
(D) "MC1G" (optical filtering via cavity)
(E) "MC2G" (optical filtering via cavity)

← ***Pump*** *(532nm)*
← *Local Oscillator (532nm)*
← ***Seed*** *(1064nm)*
← *Local Oscillator (1064nm)*

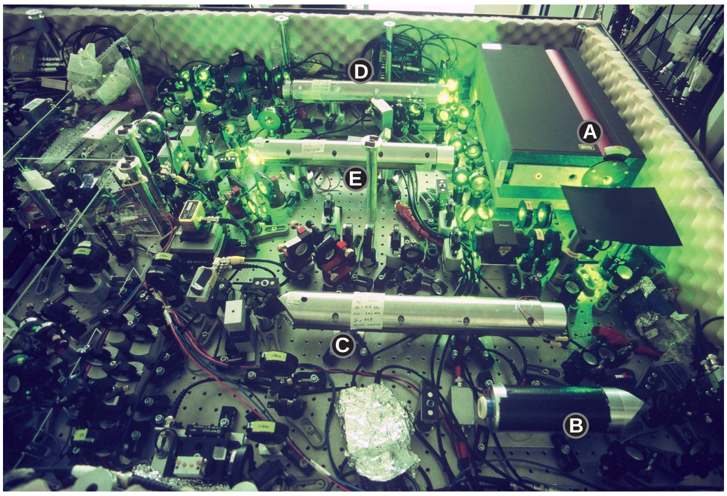

← ***Refl.*** *Pump*
← ***Refl.*** *Seed*

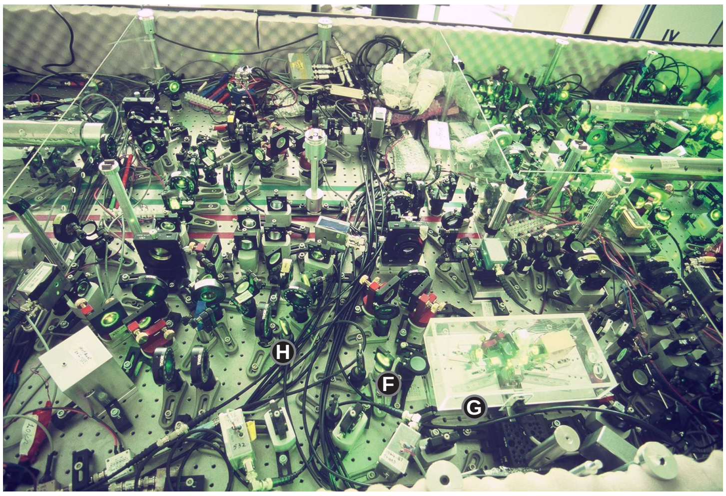

← ***Pump***
← *LO*
← ***Seed***
← *LO*

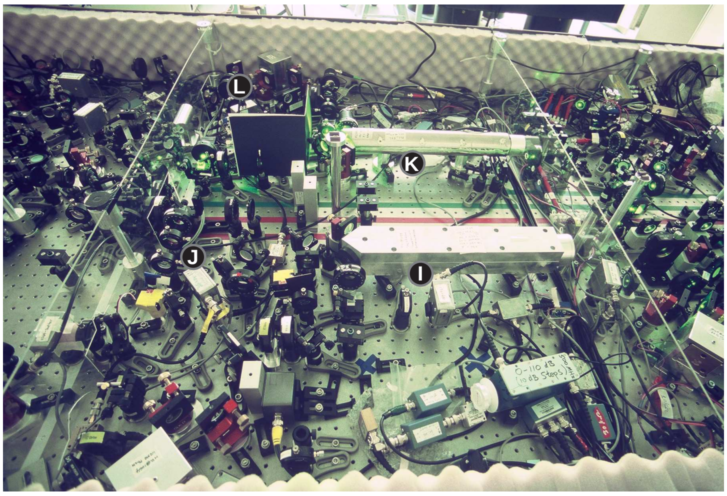

Generation of Entanglement via Optical Parametric Amplifer

(F) Dichroic Beamsplitter to combine seed and pump beams
(G) Optical Parametric Amplifier
(F) Dichroic Beamsplitter to separate reflected seed and pump beams

← ***Reflected*** *Pump (532nm)*

← ***Reflected*** *Seed (1064nm)*

Measurement and Verification of Harmonic Entanglement

(I) "FC1R" (optical carrier rejection)
(J) Homodyne detection (1064nm)
(K) "FC1G" (optical carrier rejection)
(L) Homodyne detection (532nm)

Plate 11: Three photographs that cover the entire setup of the harmonic entanglement experiment.